THE EFFECT OF MICROSTRUCTURE ON FAILURE STRAIN IN PLASTIC DEFORMATION OF LOW CARBON STEEL

by

NURI SABIR M., NURI

A Thesis submitted to the

University of Aston in Birmingham

for the Degree of

Doctor of Philosophy

October, 1977

THE EFFECT OF MICROSTRUCTURE ON FAILURE STRAIN IN IN PLASTIC DEFORMATION OF LOW CARBON STEEL

by

NURI SABIR M., NURI

for the Degree of Doctor of Philosophy

October 1977

SUMMARY

The literature dealing with the process of ductile fracture was reviewed, the two processes of crack nucleation and growth were analysed, and the parts of literature relating fracture to microstructure were highlighted.

Three low carbon steels were tested in tension and compression at room temperature, another range of low carbon steels - with varying proportions of manganese and sulphur - were tested in tension with machined notches of root radii, 0.16 mm, 0.18 mm, 0.26 mm, and 1.00 mm.

The plastic strain distribution in all the specimens deformed in tension and compression were measured using a geometrical method. This method and procedure for strain measurements were comprehensively recorded. The theory of this method was further explored and a possible relationship between necking and dilation was derived.

Stereoscan work provided a detailed quantitative measurement of volume fractions of cracks and voids, during the whole history of deformation to failure. The volume fractions of voids were related to strain.

The results obtained were as expected, they agreed with the theory, and showed that ductile fracture is caused by the growth and coalescence of voids. The beginning of growth was estimated, then the process of growth was followed up, and its early stage was examined. The failure strains were obtained as a measure of ductility, in terms of the volume fraction of voids and the volume fraction of the second-phase which has the most effect on the processes of fracture compared with other metallurgical parameters.

The notch strength ratios were measured and related to the root radii, stress concentration factors and depths. From these results the root radius was found to be the controlling factor that determines the notch ductile behaviour; influence of notch depth and material characteristics were negligible in comparison.

The results provide an adequate formulation of the relationship between fracture and microstructure.

Ductile Fracture
Failure Strain
Growth of Voids
Notches
Steels

I vertify that to the best of my knowledge, no part of the work described in this thesis was done in collaboration unless specifically mentioned, and that the work has not been submitted for any other award.

CONTENTS

CHAPTER I

INTRODUCTION

One of the major preoccupations of both engineering and metallurgy is metal-working; the shaping of functional components in metals. Many techniques are available for metal-working. The method that best adapts mechanical strength to the shape imposed on the metal is forging.

Prior to the advent of the automobile industry, the forging industry was small and of a jobbing nature. The arrival of petrol and diesel engines and the need for highly stressed components within these engines, called for forgings at competitive prices and in large enough quantities to maintain vast industrial development.

Forging is dependent on the automobile industry. Car engines have an average of 50 kgs/unit of forged components. Diesel engines have about 100 kgs/unit. World production of car engines is about 12 million units/annum; (67) diesel engines about 10 million units/annum, so the annual consumption of forgings by the motor industry is about 1.5 million tons. This does not take into account components for transmission and steering.

The automobile industry absorbs about 75% of the forgings produced which emphasises the close economic links between the two industries. Nowadays forgings are also widely used in other major industries, ship and marine engineering, electrical and non-electrical machines, machinery engineering, tools, fittings, fasteners, etc.

1.0 Hot and Cold Forging

Forging operations can be carried out hot or cold. The resistance of steel to deformation is greatly reduced by heating; thus the stresses imposed on tools are similarly reduced and it is possible to achieve much more severe deformation without overstressing the tools

in hot forging. Similarly, hot steel flows more readily into cavities and sustains severe deformation without cracking. Thus hot forging can produce more complex and larger components than cold forging.

On the other hand cold forging which includes many different forming processes, up-setting, reducing, extrusion, die-forming, drawing-out, etc., has found fields of application as a mass production process. The great merit of cold forging is dimensional accuracy which means that little or no machining is required in finishing components. This saves both material and processing costs. The technical and economic advantages and disadvantages of the two forging processes are compared and contrasted.

1.1 Advantages of Hot Forging

(a)Hot forging is used for the production of large components such as pressure vessels, large crankshafts, turbine compressor hubs, turbine rotor shafts, etc., The breakthrough to mass production was associated with the development of closed die drop forging which produces reproducible shapes fairly quickly.

(b)Drop forging is used successfully in the production of complex components such as crankshafts, turbine blades, valve bodies, etc., where the hot steel flows easily to fill the cavities.

(c)For comparable sizes, hot forging requires less deformation energy than cold forging, so a smaller press is needed for the process; hence less capital investment.

1.2 Disadvantages of Hot Forging

The problems of hot forging are:

(a)Human The work is hot, noisy, dangerous, and conditions are uncomfortable. Automation is very difficult and so much handling

and manipulating is involved. Also hot metal is much more difficult to handle and the shapes of hot forged components are more awkward.

(b) Technical To fill the die properly, it is necessary to throw a flash, i.e. not to close the die fully and to let metal escape at joints. This wastes metal and the flash has to be removed by clipping as part of the forging sequence. The parting line and the oxidized surface are machined. This needs additional dies, press locations, labour and handling.

The flash is not accurately reproducible, so the dimension across the parting line is not very accurate. Due to this technical problem, the control of dimensions is difficult to maintain, undersized forgings are scrap, oversize forgings require machining. This results in material loss. According to a report of the Drop Forging Association the total waste of steel in hot forging is up to 40%.

(c) Economic Operating costs continue to rise and eat into profit margins because the major elements of expenses such as labour and fuel are getting progressively more expensive. There are many competitive processes, so that it is not possible always to raise prices in line with costs.

1.3 Advantages of Cold Forging

(a) Less waste of material By 1956-57 the British Motor Corporation moved into the cold forging of components as a result of the very considerable wastage of steel caused by hot forging (62). The saving in material is because cold forging allows accurate control of dimensions so that much less machining is required. This saves both material and processing costs.

(b) Labour The reduction in the machining cost reduces the labour cost. The labour cost may be reduced further by mechanisation.

(c) Cold forging in general allows easy handling, automation, rapid output and low labour content, e.g. the production of 1000 wheel hubs

takes 5 hours by cold forging against 20 hours by hot forging.

1.4 Disadvantages of Cold Forging

(a) In cold forging large components are made on hydraulic presses almost exclusively by extrusion. Small components are made on mechanical presses (crank presses) using upsetting or extrusion as required. Very small components like screws and bolts are made in transfer machines.

In practice, the need for large machines has the effect that there is an upper limit to the size of components that can be cold forged, say 2 - 3 kgs, while drop forging has an upper limit of about 50 - 100 kgs.

Also the need for hydraulic presses raises the equipment cost. Hydraulic presses cost twice as much as mechanical presses, in the case of presses under 1000-ton-capacity, and three times as much in the case of presses over 1000-ton-capacity.

(b) In cold forging, the steel work hardens. In progressive forging operations, the final product is much harder and stronger than the initial feedstock. This increases tool loading and tool wear and also increases the risk of cracking and of minor surface defects opening out into deep cracks.

To minimise these risks, the steel may have to be annealed before cold forging, or at an intermediate stage in the forging sequence, but obviously this adds to the cost.

(c) There are dimensional errors due to tool wear. The need for dimensional accuracy leads to frequent tool changes, sequential tool setting which means long down-time. Because of the high capital cost, the down-time is expensive.

2.0 Economics and Future of Cold Forging

The comparison in the previous section showed that cold forging is characterised by lower labour and material costs, higher tool and capital depreciation costs than hot forging. It is particularly appropriate, therefore, for continuous mass production of simple standard components (33); fasteners are an outstanding example.

With economic growth and a general increase in the production of engineering components, the number of specified components also increases. This leads to increased batch orders and larger production runs. This makes cold forging increasingly viable and explains a tendency for cold forging to grow at the expense of hot forging - at least for components in the range of sizes, shapes and material requirements which do not exclude cold forging. Recent reports (77) showed that cold forging had gained about 10% by value of the traditional hot forging market in the last ten years.

An example was given in a case study (90) for the economics of cold forging compared with other manufacturing processes. This study showed that the two major components of costs were machine-hour and material.

Little can be done to reduce the machine-hour cost, but the material cost was minimised when using cold forging processes i.e. by reducing waste and machining.

Therefore, any further saving in the cost of steel in cold forged components has a very significant economic benefit. Improvements in the quality of the steel can confer considerable economic benefits for the cold forging industry. This means that demand for steels best suited to the cold forging processes is increasing.

3.0 Steels for Cold Forging

The behaviour of steel in cold forging depends on composition and processing. (32, 34)

(a) Composition is largely determined by the properties required in the final forged component.

(b) Processing depends on the severity of forging and the ductility of the steel.

Severe forging affects the properties by work hardening, and imposes a high degree of plastic deformation, where the ductility of the steel is the amount of plastic deformation it can sustain before cracking. The severity of deformation, the ductility and composition of the steel are interrelated, thus the relationship between the ductility of steel and its composition can determine how well the steel is suited to cold forging. Early work carried out in fields relevant to cold forging confirmed that:

(i) Changes in microstructure influence the processing sequences of cold forging and the final properties of the forged components. (Changes in microstructure can be exerted by heat treatment).

(ii) Microstructural discontinuities - such as inclusions, second-phases, grain boundaries, inner and surface defects, flaws, etc. - limit ductility by causing high local stress concentrations, developing triaxial stresses, producing non-uniform strain distribution, and nucleating and propagating cracks.

4.0 The Objectives of the Study

The purpose of this study is to contribute to a deeper understanding of the relation between structure and ductility in the hope that this can eventually lead to improvements in selection, processing and quality control of cold forging steels.

The criterion for ductile fracture was developed in previous work, and the well-established mechanism is that; ductile failure occurs by the nucleation of voids or cracks at the second-phase-matrix interface, then their growth and coalescence.

The first object of this work was to analyse theoretically the formation of the initial void at the particle-matrix interface, and its subsequent growth then coalescence. There is a critical value of strain for each of the above stages, hence the theoretical analysis was to postulate, formulate and relate these critical strain values to microstructural parameters such as volume fraction of voids and second-phases, shape orientation and spacing of second-phase particle and nonmetallic inclusions.

The second object of this work was:

(a)To verify the postulated theory.

(b)To examine the contribution of each of nucleation and growth of voids to the total fracture process at microscopic and macroscopic levels.

(c)To study the conditions favouring each stage of the ductile failure.

(d)To examine the influence of defects present in cold forging steels on the stages of ductile fracture.

This was done through the results obtained from the following experimental programme:-

(a)Correlating strain and work-hardening rate in cold deformation with nucleation, growth and coalescence of void; very simple modes of deformation were employed;

(i) Tensile test (ii) Notch tensile test (iii)Axial compression test

(b)The above tests were carried out at room temperature on different low carbon steels, provided in round rod form. The chemical compositions of the steels used are in the table (1a).

(c) The first three steels A, B and C were annealed to produce the best

possible spheroidization. The other nine types of steel D were vacuum-cast, then hot rolled at 1050°C.

(d) Quantitive data of the microstructure were measured on the QTM as inclusion/particle-size distribution, inclusion spacings, etc.

(e) Specimens of specified sizes and designs were machined off for each test:

* Tensile test specimens were machined from steels A, B and C.
* Notch tensile test specimens were machined from steels A,B and D. The notches had three different root radii.
* Compression specimens were machined from steels, A, B and C.

(f) The strain distribution values were measured in all the specimens deformed in tension and compression. The measurements of the strain on the surface of the deformed specimens were made possible by applying gridmarks and measuring the displacement of their pattern.

The estimation of the strain values in metallographic fields located in the bulk of the specimens from gridmark measurements on the surface required detailed information about strain variations across the section.

The simplest case is uniform strain which can be approximated in compression if barreling is minimised. The method employed was to use conical platens where the value of the angle is selected to compensate for the friction at the ends.

In tensile tests, the strain distribution in the neck is far from uniform, and was derived by treating the deformation as displacements of thin layers of volume.

The strain at any metallographic field within the deformed specimen was calculated from the measured components of strain using invariant functions of the strain.

(g) The deformed specimens were sectioned at different angles and directions, then were prepared for (SEM) to examine the resulting changes

in the distribution of carbides, sulphides, oxides etc.; the incidence of cracking of these particles and inclusions or their decohesion from the ferrite matrix; the probability of cracking with respect to particle and inclusion sizes; the appearance, growth and coalescence of the voids or cracks.

This required detailed quantitative metallography on fields where the localised strain was known with some degree of accuracy.

(h) Steel used in cold forging cannot be free of defects; it is expected that surface defects or even deep defects will be found in such commercial steels. These defects influence the formability of the steel and limit its ductility. The effects of defects were studied through the notch tensile tests. Although the expected defects could not be as large or as deep as the notches introduced in the tests, they all serve as stress raisers, and produce similar effects of stress-strain concentrations and triaxiality.

The introduction of notches meant to speed up the growth of microvoid and micro-cracks and their linking together to initiate and propagate a macrocrack instead of the gradual growth and coalescence of voids in the tensile test : a situation which would be expected in cold forging whenever surface defects were present, but to a small scale. So, the notch tensile tests were employed to explain the initiation and propagation of cracks. In these tests, the notch strength was measured to show the notch ductile behaviour, and was related to ductility and/or crack initiation.

CHAPTER II.

LITERATURE REVIEW

1.0 Introduction

The objective of this work, in general, is to study the limits on formability in cold forging of steels, where the plastic deformation during cold forging is terminated by fracture. In this chapter it is intended to review the types, aspects, theories and mechanisms of fracture, and to present a brief account of the basic theories and mechanisms of fracture established in some early work; which are of interest to this study and can serve as a foundation for a tentative theory of relating microstructure to ductility.

2.0. Types of Fracture

Often the material is expected to sustain moderate nominal stresses, but due to the presence of (often unsuspected) stress raisers, the material is exposed to much higher local stresses. If these high local stresses are relaxed by plastic deformation the structure survives, and deformation continues until it is terminated by ductile fracture. But if plastic flow is restrained (due to geometry or mechanical properties) the material fails in a brittle manner.

Therefore, there are two types of fracture:

Brittle fracture: occurs without plastic deformation, (Fig.1a). There are two separate processes in this type of fracture: crack nucleation and crack propagation. This type of fracture can be expensive and disastrous, because it is unexpected.

Ductile fracture: is the failure at the end of an industrial forming operation, (Fig.1b). The mechanism of ductile fracture consists of three processes: crack or void nucleation, their growth and coalescence.

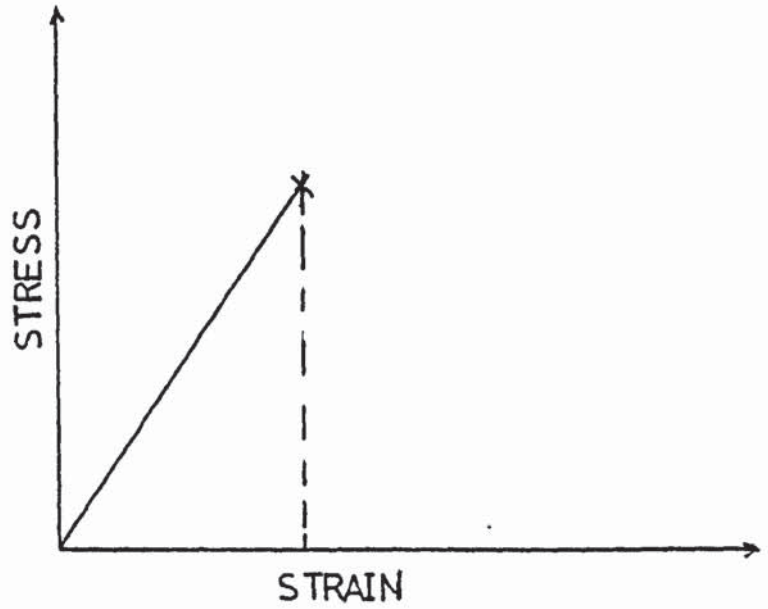

FIG. 1-a.

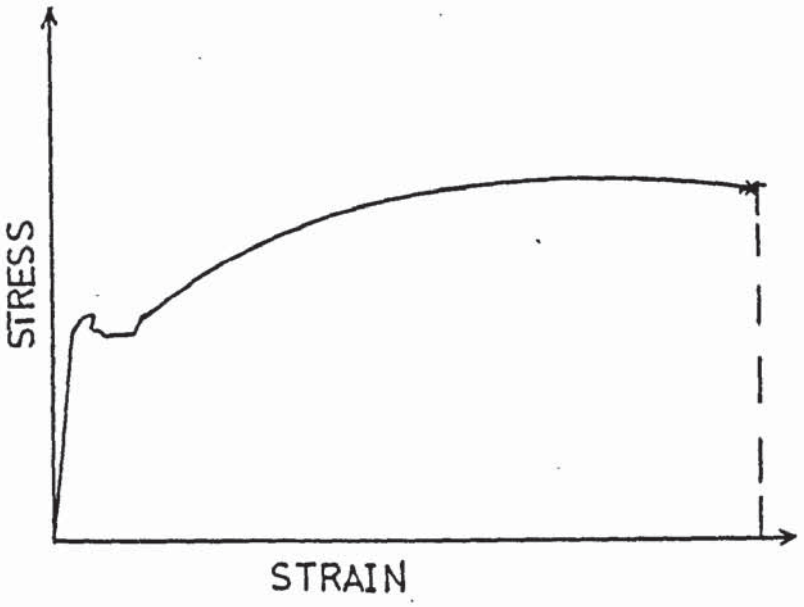

FIG. 1-b.

So, understanding of brittle fracture is important to prevent failure of structures. Understanding of ductile fracture is important to extend cold work - to cold forge more complex shapes, etc.

It needs to be said that ductile fracture is expected to occur at some reasonably high value of strain, and it is desirable to increase the amount of deformation that can be imposed, or at least to understand what determines the limit.

And, therefore, in this work the interest is in the mechanisms of ductile fracture.

3.0. Aspects of Fracture

The general problem of fracture was approached in different dimensional ranges of interest.(95)

(a) Atomic level: where fracture is preceded and initiated by atomic processes; in the dimension of (10^{-10}mm). This stage of fracture mechanism is of interest in nuclear and solid state physics.

(b) Microscopic level: where fracture extends to dimensions of the grain size. At this stage, the deformation at the area near the root of a stress raiser i.e. inclusions, carbides, sulphides, oxides, etc., was studied. This stage of fracture mechanisms is of great interest in the fields of metallurgy and material science.

(c) Macroscopic level: It is the final stage of fracture which leads to complete failure of a structural member. At this stage, fracture extends to dimensions of the size of flaws and notches. This mechanism of fracture is of interest in fracture mechanics, civil and mechanical engineering, etc. Accordingly, ductile fracture is initiated on the atomic level, causes cracks and/or voids at the microscopic level, which grow within the microscopic range, then their

coalescence leads to macroscopic failure.

Similar processes occur in brittle fracture, only faster.

4.0. Mechanisms of Fracture

There are separate processes of fracture: crack nucleation, crack growth and coalescence of cracks.

4.1. Crack Nucleation Process

Crack nucleation in crystalline solids were observed to arise as a consequence of high local stresses generated by inhomogenous plastic flow. The plastic flow in crystals was found to occur by slip or twinning. It was reported that slip occurs first.(86) The atomic processes involved in slip generated dislocations which described the configuration of atoms on the boundary between slipped and unslipped volumes. These dislocations were mobile, so the slipped volume continued to grow.(2,56,73,74,75)

The motion of these dislocations were impeded by barriers such as grain boundaries, second-phase particles, rigid inclusions, etc. So the moving dislocations being blocked piled up at the boundaries of barriers. The effect of these pile-ups on the distribution of stresses had been analysed.(15,16,17,24,87,89,93)

4.1.1. Pile-up of dislocations

Pile-up of n dislocations of the same sign against a rigid barrier, (Fig.2a) was considered, and the equilibrium conditions of dislocations was given by (31)

$$\tau_{yz} = \frac{Gb}{2\pi}\left[\sum_{i=1}^{n}\frac{1}{x_j - x_i} + \sum_{i=1}^{n}\frac{1}{x_j - x_i}\right] \qquad \ldots(1a) \text{ for screw dislocations}$$

$\tau_{xy} =$ ..... (1a)

and

$$\tau_{xy} = \frac{Gb}{2\pi(1-\nu)}\left[\sum_{i=1}^{n}\frac{1}{x_j - x_i} + \sum_{i=1}^{n}\frac{1}{x_j - x_i}\right] \quad \text{...(1b) for edge dislocations}$$

where G = Shear modulus
b = Burger's Vector
ν = Poisson's ratio of the matrix

Again considering a large number of dislocations - ($n >>$) an array of discrete dislocations were replaced by a continuous distribution of dislocations with the same total Burger's Vector, and taking (t) as a function of position. The above equilibrium was expressed by the singular Integral,[15,16,17]

$$\tau(t) = \frac{Gb}{2\pi}\int_{-L}^{+L}\frac{f(x)}{x - t}\,dx \quad \text{..... (2)}$$

where $f(x)$ = unknown distribution function of the array in (-L, + L)

and $\tau(t)$ = stress function, with

$\tau(t) = \tau$ for $t > 0$

and $\tau(t) = -\tau$ for $t < 0$

The solution of this singular integral[68] using the inversion theorem was given as:

$$f(x) = \frac{4\tau}{\pi G b}\cosh^{-1}\left|\frac{L}{x}\right| \quad \text{..... (3)}$$

where L = length of pile-up.

Equation (3) expressed the distribution of dislocations in a pile-up in a heterogeneous medium against the expression:

$$f(x) = \frac{2\tau}{Gb}\left[\frac{L-x}{x}\right]^{1/2} \qquad \ldots\ldots (4)$$

for the pile-up in a homogenous medium.

The range of the array L, from expressions (3) and (4) was (for screw dislocations)

(a) $L = \frac{Gbn}{2\tau}$ ... (5a) for heterogeneous medium

$L = \frac{Gbn}{\pi\tau}$ ... (5B) for homogeneous medium

and $L = \frac{Gbn}{2(1-\nu)\tau}$, and $L = \frac{Gbn}{\pi(1-\nu)\tau}$ for edge dislocations.

Equations (5a) and (5b) showed that, the number of discloations in a constant pile-up due to the same applied shear stress were less in the heterogeneous medium than in the homogeneous medium. This was due to the image dislocations forces which act in opposition to the applied shear stress.

The effective shear stress $\tau_E = \tau_A - \tau_i$

where: τ_A = applied shear stress, τ_i = Lattice friction stress.

4.1.2. Crack Nucleation

In some circumstances, the stresses round a piled-up group of dislocations were found sufficient to generate a crack. A mechanism by which the crack could generate was described as follows:[93,94,95]

An edge dislocation represents a half plane of atoms wedged between two complete planes. Let the leading dislocations of a pile-up group be formed very close together; two dislocations will be as close as possible when the extra half plane of atoms associated with each are adjacent, and in this case there is a wedge two atomic spacings thick between the nearest complete planes of atoms. By forcing more dislocations together a wider wedge can be produced until

ultimately the neighbouring planes are split apart, so that a crack is formed. (Fig.2b). The stress needed to start the crack was found to be the stress which would bring two leading dislocations, of the piled-up group, within one atomic spacing of each other. Accordingly the condition to start the crack was:

$$(3.67\, G\, b)/4\,\pi\,(1-\nu)\tau_E n = b \qquad \ldots\ldots\ldots (6)$$

The circumstances satisfying this condition, hence causing the nucleation of a crack, were analysed.[87,93] The crack was found to initiate inclined at an arbitrary angle ϕ with the plane of the slip.[93] This was suggested to be the inclination of the cleavage planes of the favourably situated barriers which were to break first. The value of angle ϕ was that which gives the maximum values of the stresses in the following equations which were derived for the analysis of crack initiation. The shear stress τ_{12} on the plane OP (Fig.2a)

$$\tau_{12}=(\tau_E/2)(L/r)^{1/2}[2\cos(3\phi/2)+\sin\phi\,\sin(\phi/2)] \qquad \ldots\ldots (7a)$$

and the normal stress σ_{22} on the plane OP

$$\sigma_{22}=(\tau_E/2)(L/r)^{1/2}[3\sin\phi\,\cos(\phi/2)] \qquad \ldots\ldots (7b)$$

The most favourable situation from these equations was seen when $\phi = 70.5^{\circ}$, for which the shear stress became zero.

This analysis was objected to because it neglected the effect of local shear stress in assisting the formation of a crack. The analysis was modified to take this effect into account and a new criterion for crack nucleation was developed.[87] This showed that crack nucleation

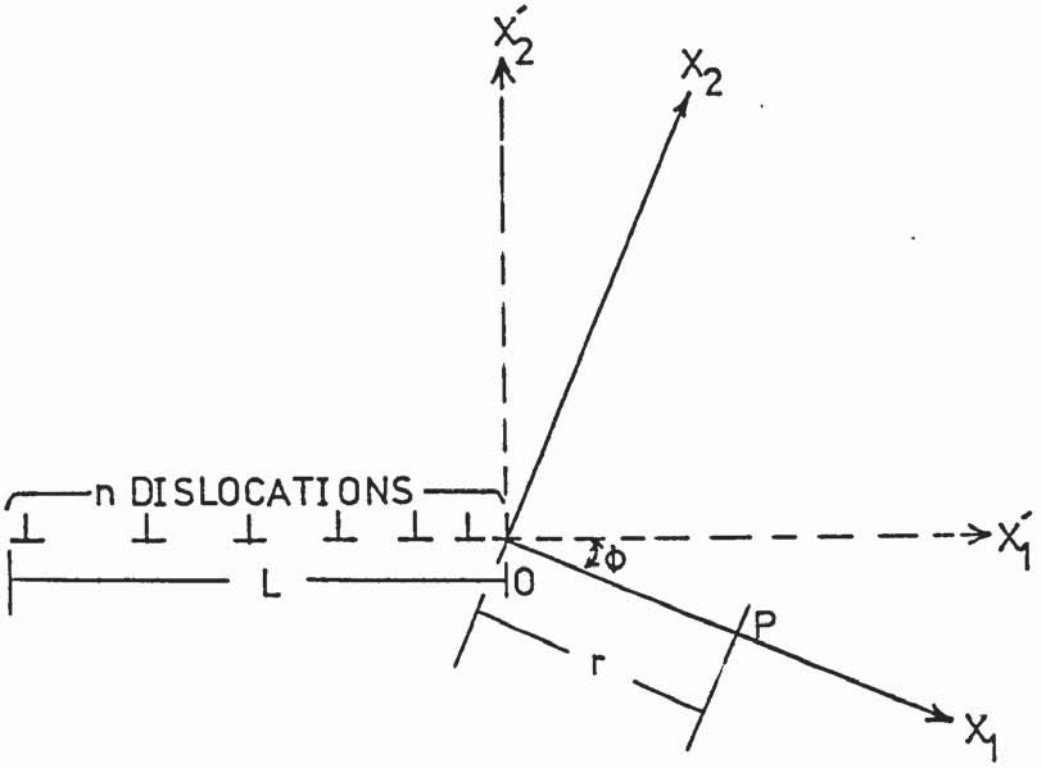

FIG. 2.a.

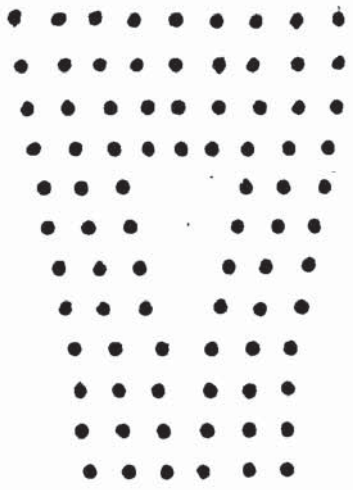

A dislocation with Burger's Vector, 3b, showing an incipient crack

FIG. 2.b.

is much easier and is independent of the orientation of the plane of fracture when $0 < \phi < 90^{\circ}$ This modified criterion was derived following equations (7a) and (7b). above, where shear and normal stresses were given for the model in Fig.(2a) as:

$$\text{Shear stress} = \tau_E (\pi L/2)^{1/2} [2\cos(3\phi/2) + \sin\phi \sin(\phi/2)] \quad \ldots\ldots \text{(8a)}$$

$$\text{normal stress} = \tau_E (\pi L/2)^{1/2} [3\sin\phi \cos(\phi/2)] \quad \ldots\ldots \text{(8b)}$$

whereupon the crack nucleation criterion was expressed in terms of the number of dislocations in the pile-up:

$$n = \frac{\pi^2 \gamma}{2\tau_E b} \times \frac{1}{[F(\phi)]} \quad \ldots\ldots (9)$$

where

$$F(\phi) = (5 + 2\cos\phi - 3\cos^2\phi)/4$$

4.1.3. Dislocations pile-up at Rigid Circular Cylindrical Particles

The second-phase particles in steels concerned were of regular shapes spherical and of finite size. Therefore, the extensions of the above method which treated the pile-ups at hard second-phases particles are reviewed in this section.

In Fig. (3a) a planar array of n dislocations of the same sign (positive), distributed over a length L, piled-up against a rigid spherical particle of radius R, due to a shear stress τ_{yz} The particles situated with its centre at the origin.

In the case of carbide particles in steels there is a perfect bond between the particle and the ferrite matrix, and due to this bond the displacement field w(x,y) and the shear stress τ_{RZ} were

taken as continuous across the interface in the above pile-up. These two boundary conditions required the use of image dislocations of strength [+ nb] located within the particle and image dislocations of strength [- nb] located at the origin.

According to Fig.(3a) above, the equilibrium condition in equation (1a) was modified as:[11]

$$\tau = \frac{Gb}{\pi}\left[\sum_{i=1}^{n}\frac{1}{x_j' - x_j'} + \sum_{j=1}^{n}\frac{1}{x_j' - (R^2/x_j')} - \frac{n}{x_i'}\right] \qquad \ldots\ldots (10)$$

The first term of the sum represented the stress on a pile-up dislocation at x_i' due to other (n - 1) pile-up dislocations at position x_j'.

The second term of the sum represented the retarding stress on the dislocation at x_i' due to n image dislocations at positions (R^2/x_j') (the image positions of the n real dislocations at x_j')

The third term $(-n/x_i')$ which was added to equation (1b) represented the attractive stress acting on the dislocation at x_i' due to the negative image screw dislocation of strength (nb) located at the origin. Again replacing the discrete dislocations in the pile-up by a continuously distributed dislocation array, the above equilibrium condition was given by the singular integral equation,

$$\int_1^{(L+R)/R} \frac{f(t)\,dt}{x - t} + \int_1^{(L+R)/R} \frac{f(t)\,dt}{x - (1/t)} = \frac{n}{x} + \frac{2\pi R\tau}{Gb} \qquad \ldots\ldots (11)$$

where $1 < x < (L+R)/R$

and $\tau = \tau_A[1 - (R/x)^2] - \tau_i$ the term, $\tau_A(R/x)^2$ stood for the perturbation of the applied stress field by the particle.[89]

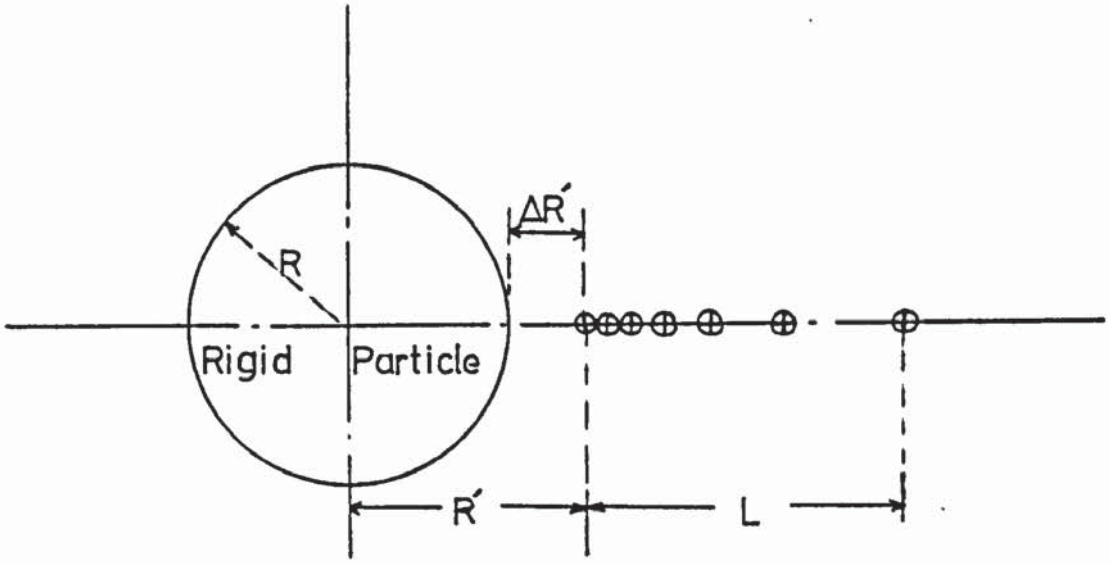

FIG. 3.a.

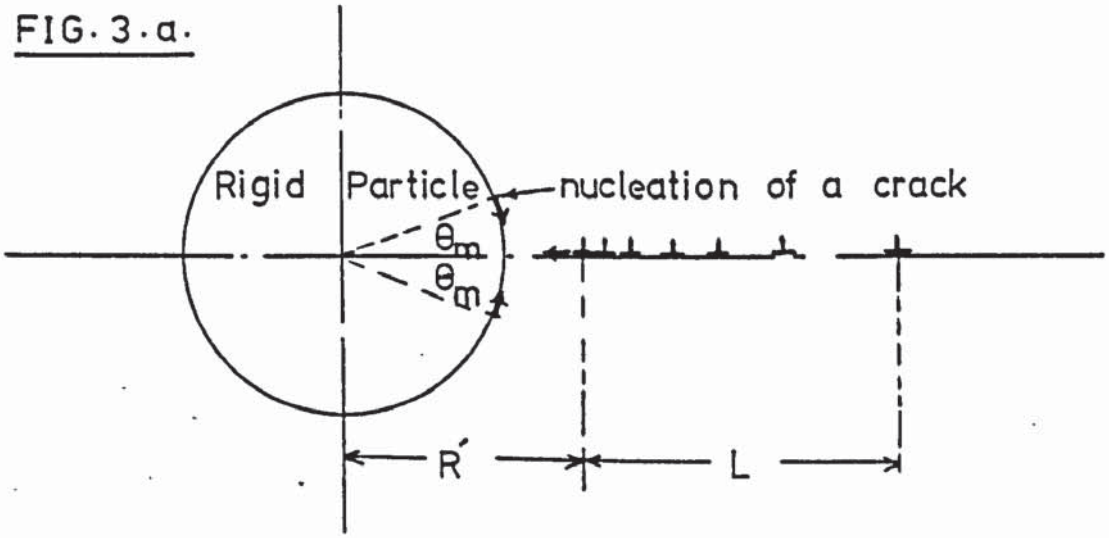

FIG. 3.b.

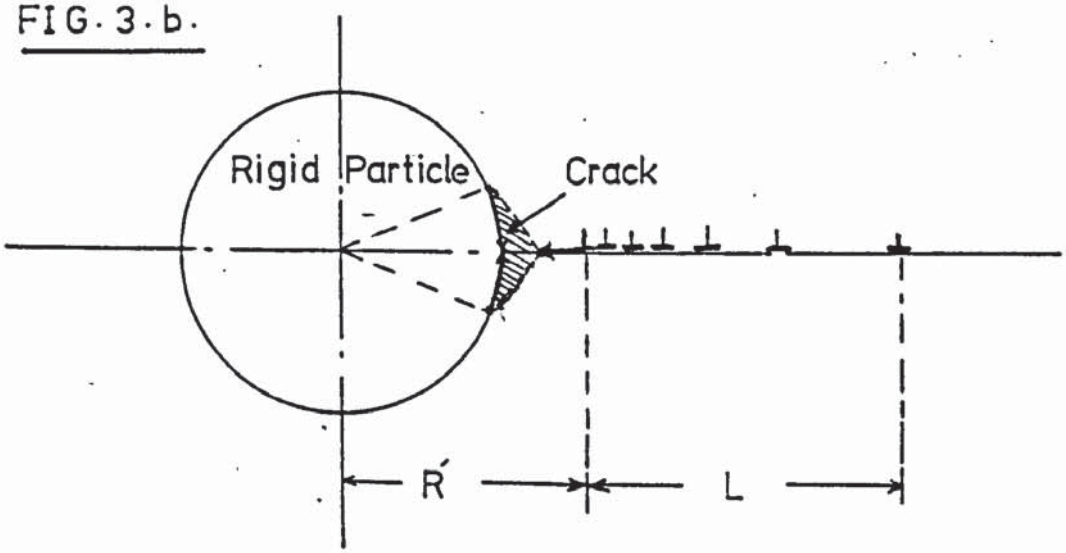

FIG. 3.c.

Equation (11) is not a standard Cauchy kernel, and to solve it, the interval was extended as $\frac{R}{L+R}$ to $\frac{L+R}{R}$, in order to get a simple Cauchy kernel. Also putting $\frac{L+R}{R} = \beta$ slip line length, the equation was solved to give

$$\frac{G b n}{2 L} = \frac{-\tau_i}{(\beta)^{1/2}} \left[\frac{\pi \tau_A (\beta-1)}{2\beta} - \frac{\tau_i (\beta-1)}{2\beta} \left[\frac{\pi}{2} + \sin^{-1}\left(\frac{\beta-1}{\beta+1} \right) \right] \right] \quad \ldots\ldots (12)$$

For $\tau_i > 0$, equation (12) showed that continuously distributed screw dislocations of the same sign were unable to pile up at the boundary of the rigid circular particle. The tip of dislocations distribution was shown to be at a finite distance ΔR from the interface, Fig.(3). This distance was calculated as;[103] Fig.(3a)

$$(\Delta R/R) = 32 \left(\frac{\beta-1}{\beta+1} \right)^2 \exp.\left[- \left\{ \pi \left(\frac{2\tau_A}{\tau_i} - 1 \right) - 2\sin^{-1}\frac{\beta-1}{\beta+1} \right\} \frac{\beta-1}{(\beta)^{1/2}} \right] \ldots\ldots (13)$$

Also from the calculations of the local shear stress on the particle-matrix interface τ_{RZ}, it was predicted that there were dislocations of opposite sign present between the pile-up tip and the particle-matrix interface.

4.1.4. Crack/Void Nucleation

In circumstances similar to those in section (4.1.2), the stresses round the pile-up of dislocations against the circular rigid particles, were found to generate a crack or a void at the interface when the maximum shear stress at this interface reaches the bond strength of the particle-matrix interface. The mechanism of this debonding was described as follows;[103]

(a) The shear stress at the interface was calculated as,

$$\tau_{RZ} = 2\tau_A \left[\frac{\beta^2 - 2\beta\cos\theta + 1}{(\beta)^{1/2}}\right]\cos(\theta/2) \qquad \ldots\ldots (14)$$

and gave maximum value at, $\theta_{max} = \cos^{-1}\left(\frac{(\beta-1)^2}{4\beta}\right)$ Fig.(3b)

(b) Two micro-cracks form on the interface at θ_{max}. At either sides of the slip plane, Fig.(3b), and extend under the initial void/crack formation shear stress along the interface and coalesce at a point on the slip plane. At the same time the pile up tip extends towards the interface and coalesces with the crack, Fig.(3c) to form an arc-shaped crack.

4.2. Crack Propagation

Once a crack is formed the stresses round it are relieved and so make it easy to bring in more dislocations which in turn widen the wedge and cause the crack to spread. The resistance offered to the propagation of the crack due to dislocations interactions was found to be negligible from the following analysis:[37]

(1) The length of the nucleated crack was observed to be much greater than its width ($L \gg h$), so, the state of strain and elastic energy stored in the material around the crack were taken as similar to those around a slip band produced by a pile-up of gliding dislocations. Thus most of the dislocations were to be concentrated at the tip of the crack, and the crack tip was considered as a piled-up group of climbing dislocations.

So, the stress at the centre of the crack $\sigma = \frac{2Gh}{\pi(1-\nu)L}$ and the force/unit length on the leading dislocations at the tip of the crack, $F = \sigma h$.

(2) The stresses produced by dislocations outside the cleavage plane, and dislocations piercing the cleavage plane were found to exert a negligible resistance compared with the line tension, σh.

(3) When the crack crosses a dislocation with Burger's Vector b not parallel to the cleavage plane, a step of height b is produced on the face of the cleavage plane. This step runs normal to the tip of the crack, and increases the resistance to the propagation of the crack. This resistance was also found to be negligible compared with the line tension, σh. The density of these steps do not increase to a level that causes appreciable resistance to propagation because they coalesce quickly. Hence, the crack was to spread.

The condition of spreading the crack was also discussed with the help of the Griffith crack theory.(1) The energy balance was formulated as:

$$\Delta E = \Delta[AL] - \Delta[BL^2\sigma^2] + \Delta[C\, f(L,\sigma,Y)] - \Delta[D \log L] \quad \cdots\cdots \quad (15)$$

where, L = length of the nucleated crack,

Y = yield stress

σ = applied stress

A, B, C & D = constants

The condition for the extension of the crack is $(\Delta E \leqslant 0)$

The four energy terms controlling the growth of the crack were analysed as follows:

(a) The local stress concentration energy, $-[D \log L]$, is due to the pile-up of dislocations under the applied stress at a stage prior to nucleation of the crack, and eventually cause the initiation of the crack.

(b) The surface energy of the crack, which is proportional to its length, is of great importance at the early stages of crack nucleation, and is large compared with the elastic energy available from the reduction of the energy of the applied stress field, $(BL^2\sigma^2)$.

It was also noted that, when the nucleated crack is small and dislocations are widely spaced, the crack grows for some time before its stress field encounters a dislocation. This happens without any plastic deformation and the only energy absorbed is that attributed to the surface energy term. On the other hand when the crack is large and dislocations are closely spaced, dislocations may be included within the region stressed above the yield point and energy is absorbed in plastic deformation.

(c) This energy consumed by the plastic deformation that occurs in the highly stressed region in front of the growing crack, $[Cf(L, \sigma, Y)]$ must be kept very low if the crack is to extend further. It was shown that this energy term is dependent on the strain at the end of the crack at which the force between adjacent atoms reaches its maximum, and more importantly on the concentration of the applied stress around the end of the crack due to the inability of the crack to transmit a tensile or shear stress. This energy term is also governed by the width of slip band swept out by the stress field of the advancing crack.

If the crack is propagating slowly at a constant stress this width increases continuously. The energy available for the crack propagation increases as the length of the crack increases and eventually the crack accelerates; this also raises the effective yield point.

On the other hand the increase in the width of the slip band expands the stress field, hence, increases the energy absorbed in plastic deformation and thus retards and even stops the crack. If the crack stops, the stress may be sufficient to nucleate a fresh crack and the whole process may be repeated several times. Also if the crack moves slowly, the high stresses at the tip of the advancing crack are applied for a long enough time on the same volume of material and thus induce plastic deformation.

To find how slow the crack would advance, the critical velocity of crack propagation was calculated and was found to be equal to the sound velocity and this was also the maximum possible velocity for the crack. So, for a crack to extend it has to propagate at the maximum possible velocity.

4.2.1. Crack Propagation in Ductile Material

It was reported that[1] about the order of 1000 dislocations are required in the pile-up to nucleate a crack. 1000 dislocations are unlikely in one slip line in a ductile material. In this case pile-ups in a slip band were found to co-operate to initiate a crack.[93,94] Once the crack is formed the dislocations on the slip line from which it started can enter it and wedge it open, those dislocations on the other slip lines cannot enter this crack and the crack becomes much smaller than it would have been if nucleated from one slip line, i.e. smaller than the critical Griffith length and so is unable to extend further.

Also in a ductile material having many possible slip systems, there is a cylindrical region of fairly big radius around the tip of the crack where the elastic stresses of the crack have been relaxed.

This stress relaxation makes the piling-up of dislocations of the crack easy, which thus blunts the tip of the crack. The plastic relaxation reduces the stress, σ, at the centre of the crack and widens the crack considerably. This again blunts the tip of the crack.

5.0 DUCTILE FRACTURE

The following can be concluded from the aforementioned discussions:

(1) It is easy to nucleate cracks.

(2) Cracks nucleate at very low strains by the high local stress concentrations due to the pile-up of dislocations.

(3) Plastic deformation stops crack propagation.

(4) It is difficult to propagate a crack in a ductile material (i.e. such as the steels in this study).

Experimental findings also showed that in such ductile metals, ductile fracture occurs only after the onset of necking, during which stress concentrations increase fast enough. The cracks do not develop from the regions of stress concentrations but multiply, and fracture occurs when the cracks link up, then grow and coalesce.

Theories proposed in early work analysed the subsequent growth then coalescence of the nucleated cracks, but overlooked the stage at which nucleation ends and growth begins. The circumstances and conditions which end nucleation and favour the start of growth were not analysed.

So, before reviewing the theories of void growth proposed in early work, it is essential to analyse the transition from the crack nucleation process to the process of growth, to present a coherent picture of the ductile fracture processes.

5.1. Nucleation - Growth Transition

It is aimed here to understand the extent of the two processes of crack nucleation and growth and to predict the stage at which the effective multiplication (i.e. nucleation) of cracks ends and their growth begins. To do this the discussion is picked up from a stage where crack nucleation has already occurred and is still continuing. At this stage also plastic deformation has already occurred and more plastic flow is expected with the increase in strain, until gross plastic deformation occurs.

It is essential, therefore, to discuss in detail the occurrence of this gross plastic deformation and its effect on both the crack nucleation process , and on the growth of critically large nucleated cracks which controls the latter stage of ductile fracture. But first the following assumptions which are characteristic of the steels under study are made:-

(1) The analysis refers to spheroidized low carbon steels of low inclusions, and considers the plastic flow of the soft ferrite matrix surrounding a rigid carbide particle.

(2) The carbide particles are regular spherical or cylindrical and are assumed to be perfectly rigid.

(3) The carbide particles are uniformly distributed and an average mean size of the particles is assumed such that $\lambda \geq 5d_{mean}$ where, λ and d_{mean} = spacing and mean diameter of particles respectively.

(4) The ferrite surrounding the particles is assumed infinite in extent and is subjected to uniform applied stress (σ_N) at infinity.

Beyond the yield stress of the material, the soft ferrite matrix begins to flow plastically. With the increased plastic deformation in the neighbourhood of the rigid carbide particle, no cracks develop and also no cracks can be nucleated because the surface energy of the crack is undoubtedly negligible compared with the energy absorbed in the gross plastic deformation.

But this is not the end of all crack nucleation because while the material surrounding the rigid particles deforms plastically there exist undeformed zones (Z) adjacent to the particles, as in Figs.(4a) and (4b). Such a zone (Z) remains elastic beyond the yield stress due to the triaxiality developing from the high transverse stresses. It is in this zone that cracks continue to nucleate as described in the previous sections.

These cracks nucleated in zone (Z) are also not expected to propagate, either due to their initial length of initiation being smaller than the Griffith critical size, or due to their tips being blunted by plastic flow. It is expected that the nucleation process is repeated in this zone and fresh cracks are produced due to the high local stresses, so, nucleation and multiplication of cracks continue. This nucleation process is ended only when the whole of the zone (Z) deforms plastically and this eventually becomes the end of the effective crack nucleation process and the beginning of the effective growth of large nucleated cracks. This moment when the zone (Z) deforms can be pictured as follows:

(1) Cracks are nucleated due to pile-up of dislocations at the particle-matrix interface.

(2) These cracks are unable to propagate, due to resistance offered

against their spreading as mentioned in the previous sections, so they stop.

(3) More fresh cracks are nucleated due to the high local stresses in front of the "old" cracks.

(4) Such cracks become sufficiently numerous and link by ductile fracture of the bridging material. This in turn produces a large effective crack or void capable of expanding by the plastic flow of the material.

(5) The stresses are relieved and the elastically stressed material is released, and contracts to leave a large void/crack adjacent to the rigid carbide particle as in Fig.(7).

This qualitative description of the end of the crack nucleation process and the start of the growth is analysed quantitatively below:-

(a) While the zones (Z) are still elastic, the forces generated by the plastic flow of the matrix surrounding them cause a uniformly distributed shear stress along the line BC,[18] in Fig.(4a & 4b). Therefore the direction of the shear stress is along this line BC and its magnitude is inversely proportional to the length of this line.

(b) In the absence of the rigid particles, the stress would have been uniaxial with its direction along the tensile X-axis; the zones (Z) would have deformed when the uniaxial tensile stress equalled the yield strength of the soft matrix, and as part of the deformed matrix.

Therefore, analogous with the above, the direction of the tensile flow stress is along the line AB in Figs. (4a & 4b), and is inversely proportional to the length of the line AB.

Plastic Flow around Rigid Particles

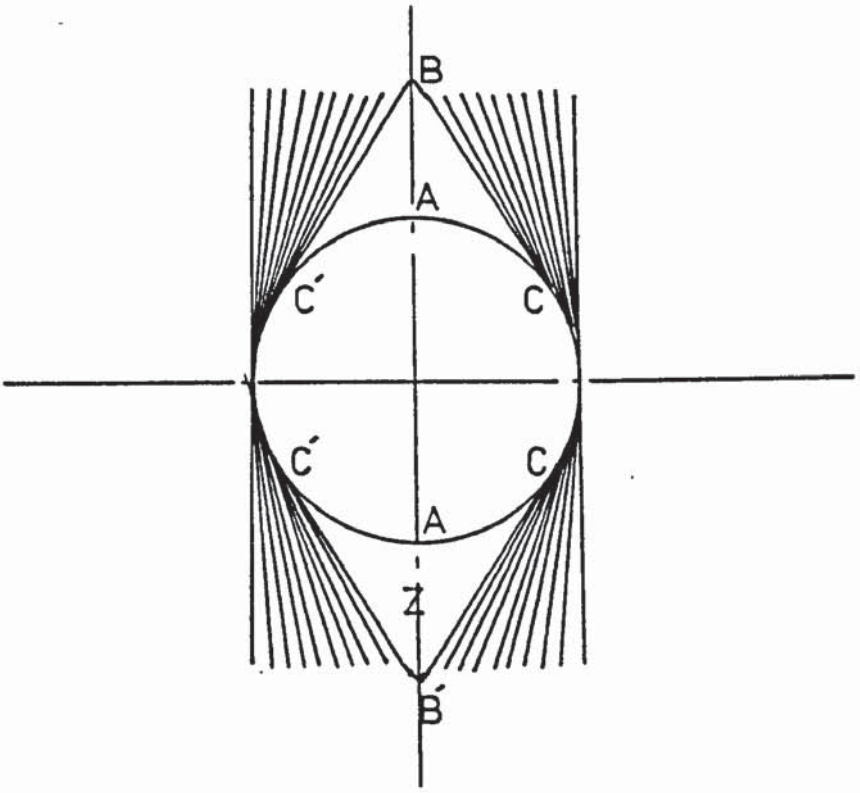

FIG. 4.a. Spherical Particle

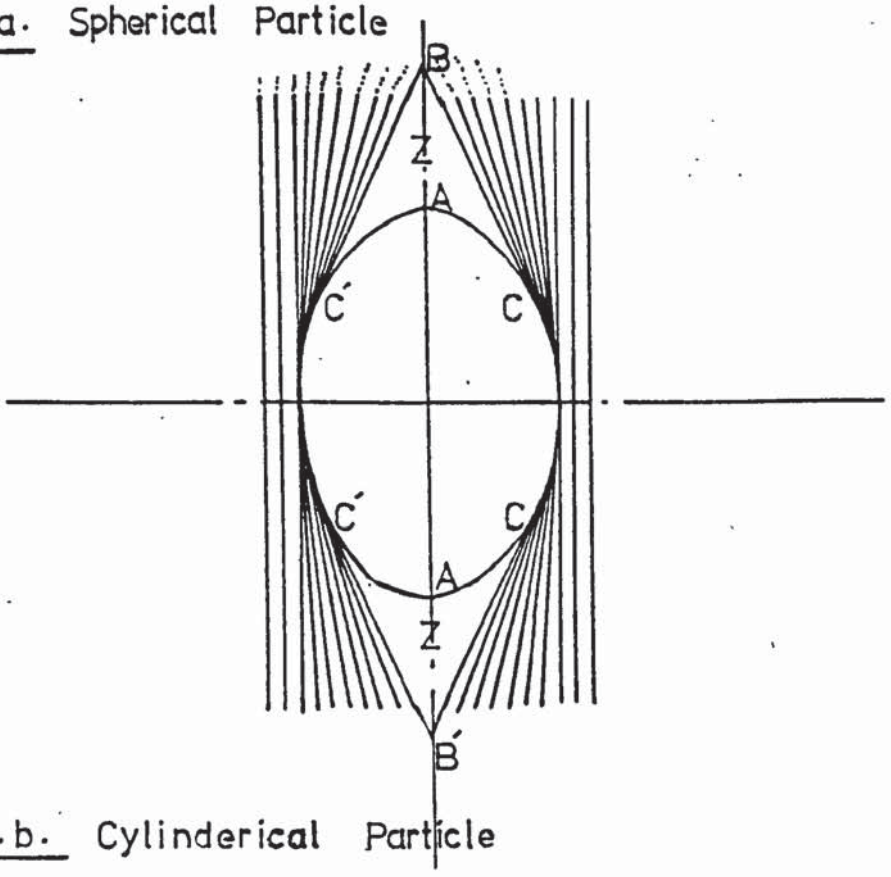

FIG. 4.b. Cylinderical Particle

(c) With this analogy, a ratio of the shear stress, τ , which causes the zone (Z) to deform, to the tensile flow stress of the matrix is obtained from the geometry of the undeformed zone (Z) as:

$$(\tau/\sigma) = (AB/BC) \ldots\ldots \quad \text{FIGS. 4.a. \& 4.b.}$$

(d) Again once the large crack or void forms at the end of the nucleation, the high stresses in the zone (Z) are relieved and the fractured material contracts to leave the crack as in Fig.(7). The material contracts such that the distance from (x,y) to (a,o) reduces to a distance equal to that from (a_o, o) to (a, o), because the stress in the zone when it is released becomes equal to the tensile flow stress of the matrix. Therefore, the ratio of the area occupied by this large crack, (the dashed area in Fig.(7)), to the total area of the zone (Z), is equal to the ratio (τ/σ) above. Hence the size of the crack can be determined from this ratio and the size of the undeformed zone (Z).

The ratio, (τ/σ), can be expressed in terms of the corresponding plastic strain through calculations of the geometry of the zone (Z). To simplify these calculations the shapes of the zone (Z) in Figs. (4 a & 4b) are approximated as in Figs. (5a & 5b) respectively, in order to give standard geometrical shapes. In this approximation the broken lines are assumed as the ellipses into which the particles (solid lines) would have deformed at any value of plastic strain, if they were as soft as the matrix around them.[18] From this approximation the plastic strain of the matrix, ε , is calculated as:

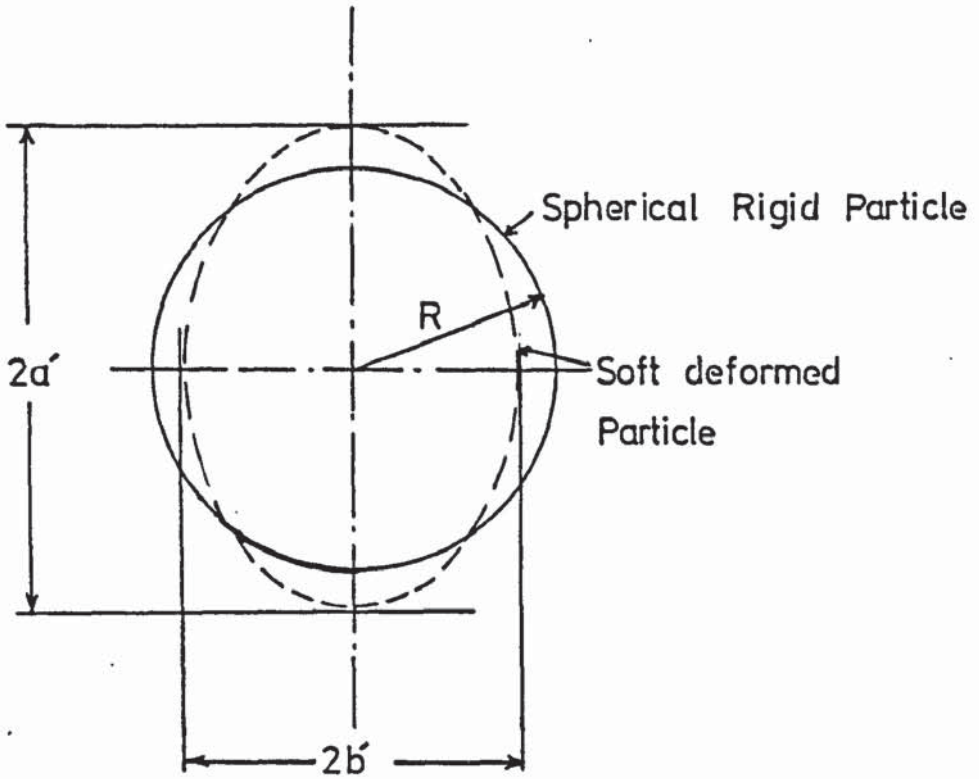
Spherical Rigid Particle
R
2a'
Soft deformed
Particle
2b'

FIG. 5.a.

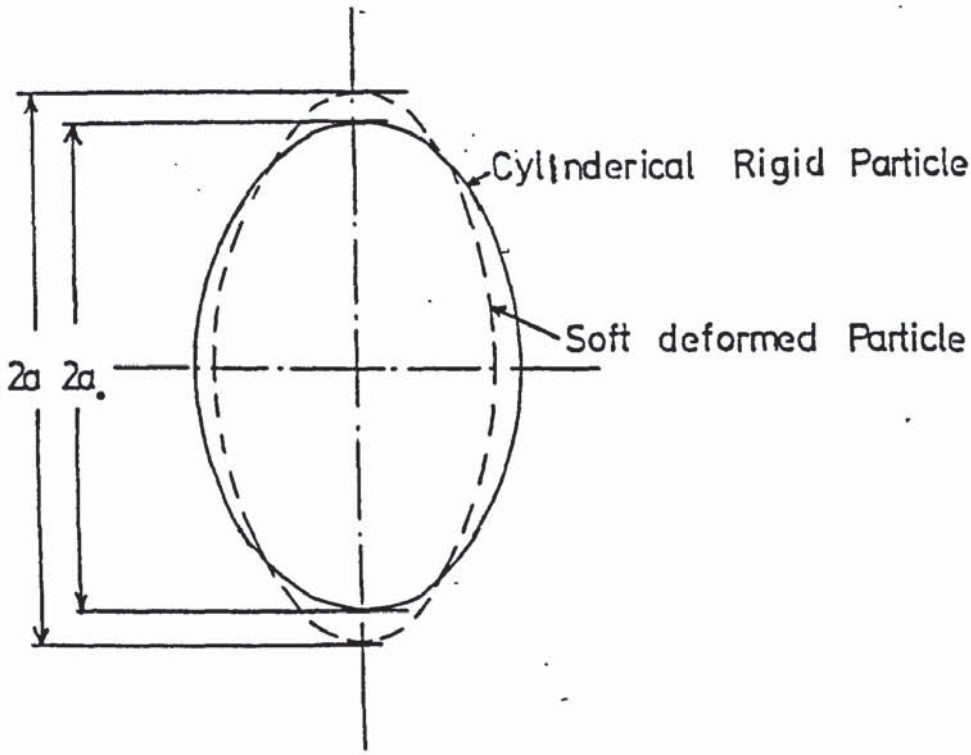
Cylinderical Rigid Particle
Soft deformed Particle
2a 2a.

FIG. 5.b.

$\varepsilon = \log_e (a/a_o)$ and $(\varepsilon/2) = \log_e (b/b_o)$ i.e. $e^{\varepsilon} = (a/a_o)$ and $e^{\varepsilon/2} = (b_o/b)$

(for cylindrical particles)

$\varepsilon = \log_e (a'/R)$ and $\varepsilon = \log_e (R/b')$ i.e. $e^{\varepsilon} = (a'/R)$, and $e^{\varepsilon/2} = (R/b')$

(spherical particles)

The ratio $(\tau/\sigma) = (a - a_o)/l$. from Fig.(6), the straight line $l = [y^2 + (a - x)^2]^{1/2}$

where, $x = [a^2 b/(a+b)]^{1/2}$ and $y = [ab^2/(a+b)]^{1/2}$

Therefore, $l = [a(1 + \frac{b}{a}) - 2(\frac{1}{a/b+1})^{1/2}]^{1/2}$

Substituting the values of the strain ε, with the aspect ratio $r = a_o/b_o$ the straight line l becomes:

$$l = a_o e^{\varepsilon} [(\frac{r e^{3\varepsilon/2} + 1}{r e^{3\varepsilon/2}}) - 2(\frac{1}{r e^{3\varepsilon/2} + 1})^{1/2}]^{1/2}$$

The straight line $(a - a_o) = a_o (e^{\varepsilon} - 1)$

Therefore, the ratio, $(\tau/\sigma) = (a - a_o)/l$ becomes

$$(\tau/\sigma) = \frac{(e^{\varepsilon} - 1)}{e^{\varepsilon} [(\frac{r e^{3\varepsilon/2} + 1}{r e^{3\varepsilon/2}}) - 2(\frac{1}{r e^{3\varepsilon/2} + 1})^{1/2}]^{1/2}} \quad \ldots\ldots \text{(16a)}$$

for cylindrical particles

Substituting $r = 1.0$ for the case of spherical particles

$$(\tau/\sigma) = \frac{(e^{\varepsilon} - 1)}{e^{\varepsilon} [(\frac{e^{3\varepsilon/2} + 1}{e^{3\varepsilon/2}}) - 2(\frac{1}{e^{3\varepsilon/2} + 1})^{1/2}]^{1/2}} \quad \ldots\ldots \text{(16b)}$$

To calculate the size of the crack/void, the area of the zone (Z) is calculated first. This area is calculated for the case of the cylindrical particles then the aspect ratio ($r = 1.0$) is substituted for the case of spherical particles.

From the equation of the ellipse $\frac{x^2}{a^2} + \frac{y^2}{b^2} = 1$ the equation

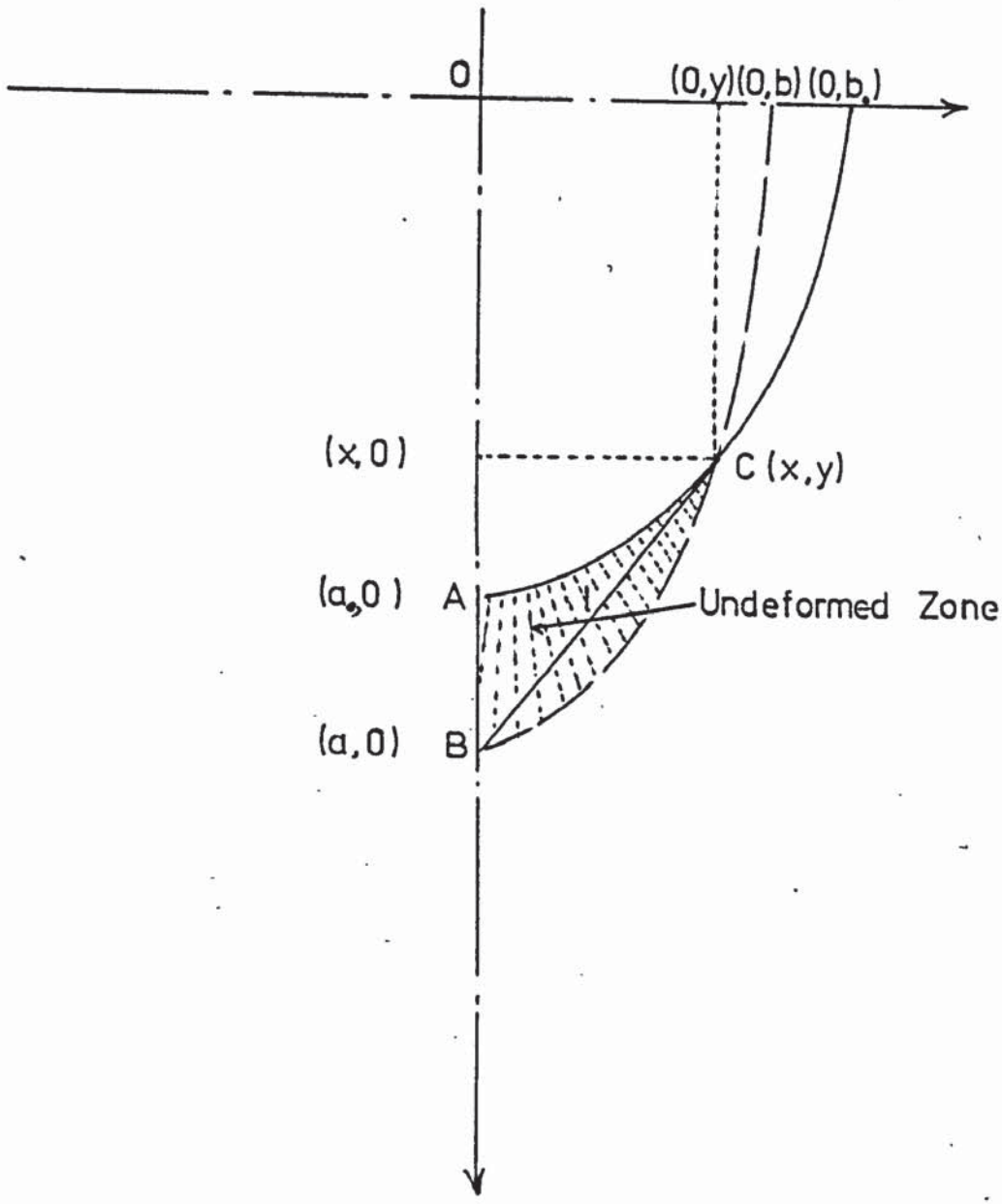

FIG. 6.

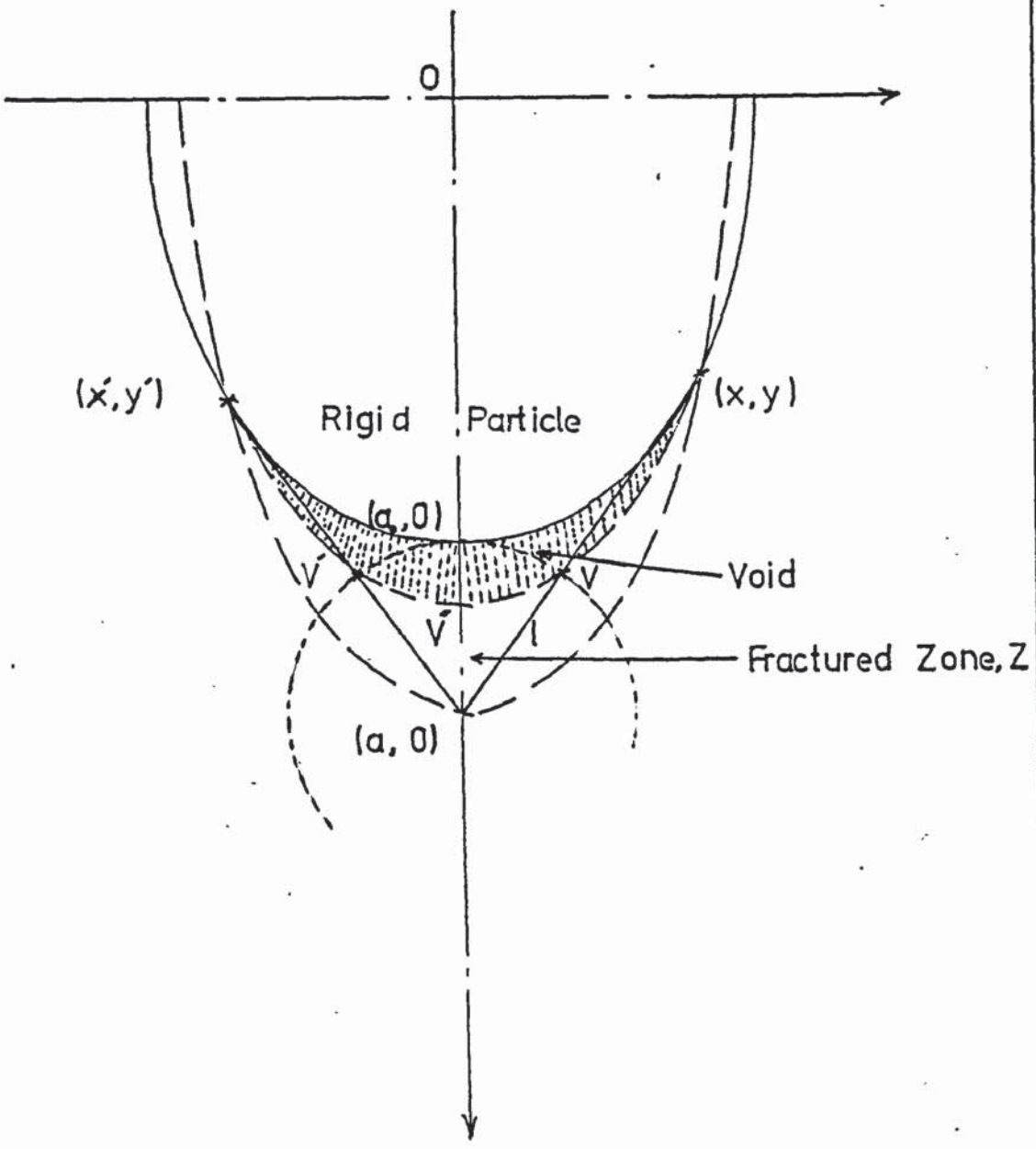

The linking of small nucleated cracks to form a large void.

FIG. 7.

for the first quadrant in Fig.(6) is $y = b\left(1 - \frac{x^2}{a^2}\right)^{1/2}$

The equation for the solid line is, $y_o = b_o\left(1 - \frac{x^2}{a_o^2}\right)^{1/2}$

for the broken line, $y = b\left(1 - \frac{x^2}{a^2}\right)^{1/2}$

The area of the zone (Z) is four times the dashed area in Fig.(6)

and is, $4\left[\int_x^a y\,dx - \int_x^{a_o} y_o\,dx\right]$

~~The area (Z) =~~

The area (Z) $= 4\int_x^a b\left(1 - \frac{x^2}{a^2}\right)^{1/2} dx - 4\int_x^{a_o} b\left(1 - \frac{x^2}{a^2}\right)^{1/2} dx$

integrating; the area (Z) becomes, $2a_ob_o\left[\sin^{-1}\left(\frac{ab}{ab_o}+1\right)^{-1/2} - \sin^{-1}\left(\frac{ab_o}{a_ob}+1\right)^{-1/2}\right]$

Substituting for the value of the strain, ε , the area of the zone,

$$Z = 2a_ob_o\left[\sin^{-1}\left(e^{-3\varepsilon/2}+1\right)^{-1/2} - \sin^{-1}\left(e^{3\varepsilon/2}+1\right)^{-1/2}\right] \qquad \ldots\ldots \text{(17a)}$$

putting aspect ratio (r = 1.0), and $a_o = b_o = R$, the area of the zone for the case of spherical particles is

$$Z = 2R^2\left[\sin^{-1}\left(e^{-3\varepsilon/2}+1\right)^{-1/2} - \sin^{-1}\left(e^{3\varepsilon/2}+1\right)^{-1/2}\right] \qquad \ldots\ldots \text{(17b)}$$

recalling the ratio,

$$\frac{\text{area of the large crack}}{\text{area of the zone (Z)}} = (\tau/\sigma)$$

$$\frac{\text{area of the large crack}}{\text{area of the rigid particle}} \times \frac{\text{area of rigid particle}}{\text{area of the zone (Z)}} = (\tau/\sigma)$$

$$\frac{\text{area of the large crack}}{\text{area of the rigid particle}} = (\tau/\sigma) \times \frac{\text{area of the zone (Z)}}{\text{area of rigid particle}}$$

Since regular sizes of carbide particles of uniform distributions are assumed, then

$$\frac{\text{area of the crack}}{\text{area of the rigid particle}} = (f_v/f_c)$$

where f_v and f_c = volume fraction of cracks/voids at the end of crack nucleation process or at the start of void growth, and volume fraction of carbides respectively. Therefore,

$$(f_v / f_c) = (\tau / \sigma) \times \frac{\text{area of zone Z}}{\text{area of rigid particle}}$$

$$(f_v/f_c) = \frac{2(e^{\varepsilon}-1)[\sin^{-1}(e^{-3\varepsilon/2}+1)^{-1/2} - \sin^{-1}(e^{3\varepsilon/2}+1)^{-1/2}]}{\pi e^{\varepsilon}[(\frac{e^{3\varepsilon/2}+1}{re^{3\varepsilon/2}}) - 2(\frac{1}{e^{3\varepsilon/2}+1})^{1/2}]^{1/2}} \quad \ldots\ldots (18a)$$

and putting r = 1.0 for spherical particles,

$$(f_v/f_c) = \frac{2(e^{\varepsilon}-1)[\sin^{-1}(e^{3\varepsilon/2}+1)^{-1/2} - \sin^{-1}(e^{3\varepsilon/2}+1)^{-1/2}]}{\pi e^{\varepsilon}[(\frac{e^{3\varepsilon/2}+1}{e^{3\varepsilon/2}}) - 2(\frac{1}{e^{3\varepsilon/2}+1})^{1/2}]^{1/2}} \quad \ldots\ldots (18b)$$

Equations (18a) and (1.8b) give the values of the strain, ε at which effective growth of cracks and voids start; in terms of the volume fractions of cracks/voids formed at that stage and the volume fraction of the second-phase. This equation satisfied the requirements of the first objective of this study.

The values of strains obtained when applying these equations to the experimental results later, can be compared with the corresponding strain values obtained from some of the proposed theories of ductile fracture,[43,57,64,95] which stand on the assumption that void growth starts at a very low negligible strain, either from the growth of cracks already existing before deformation or from the growth of cracks initiating before hardly any strain.

The mechanism of initiation of cracks and voids in these theories was due to the cracking of second-phase particles or the decohesion of the particle-matrix interface, as shown by the models in Figs.(8a & 8b).[40]

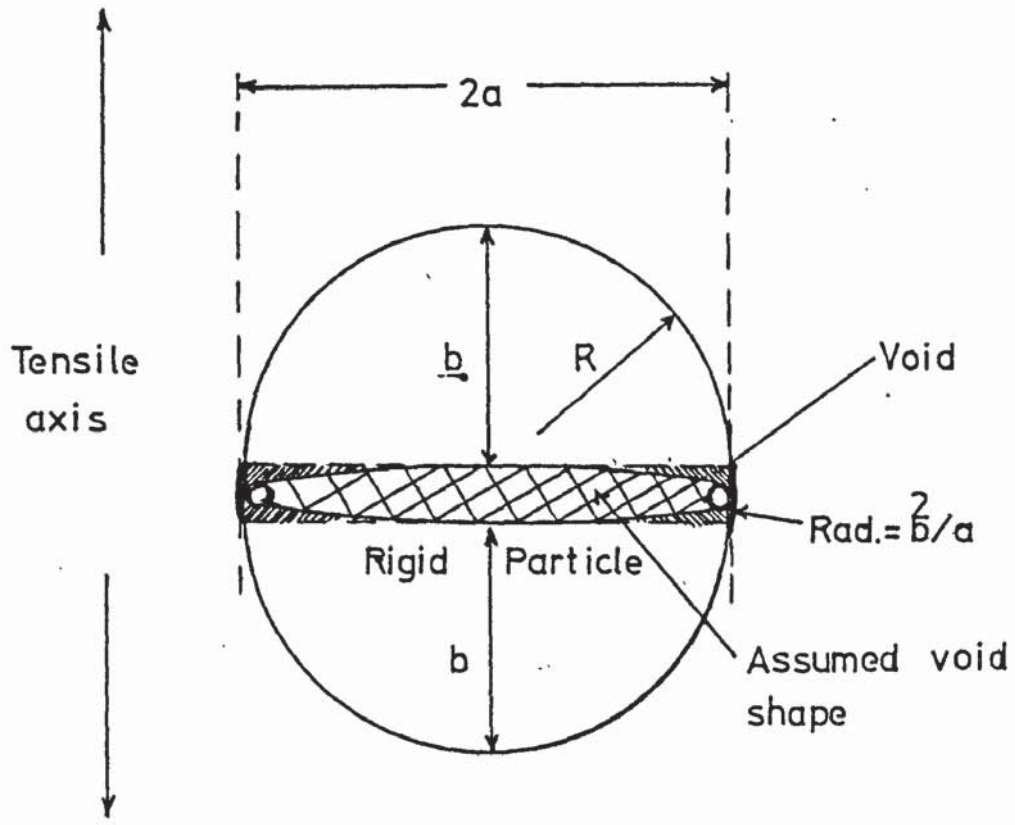

FIG.8.a. Cracking

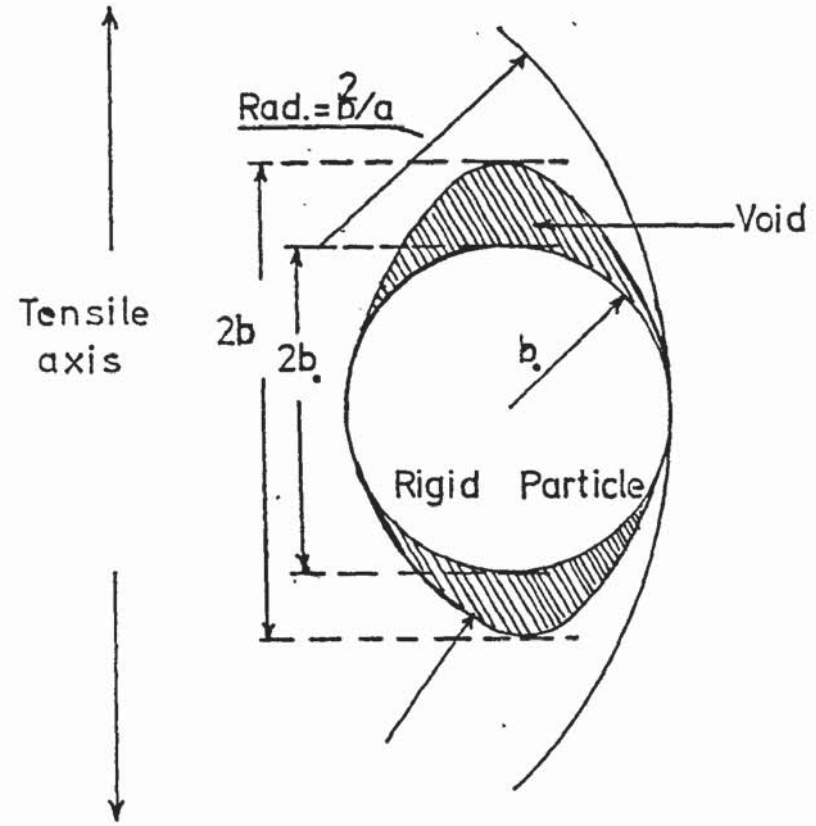

FIG.8.b. Decohesion

The strain at which cracks initiate was given as zero especially in the case of particle cracking where it was expected that effective crack growth starts immediately at the moment when the particle cracks.

5.2. Void Growth

The large cracks/voids formed as described in the previous sections, grow in a ductile manner, i.e. increase in volume gradually with the progress of plastic deformation. Equations (18a) and (18b) mark the beginning of this growth but do not describe its range, because the circumstances and physical and mechanical conditions during this range of growth were found to be different from those which were prevailing during the crack nucleation process and those at the stage of transition from nucleation to growth.

The circumstances associated with growth process were analysed and two cases of void growth were explained as below.

5.2.1. Case (a) Void Growth and Strain Concentration

It was shown that[43,40] with the shapes of cracks and voids formed at the beginning of growth, being as in Fig.(7) and Fig.(8a and 8b), their radius of curvature was low, thus high strain concentrations were expected at their edges.

It was also shown that these cracks changed shape more than they changed volume at the early stage of growth; hence their growth was dependent on the strain concentration as:

$$C = (d\varepsilon_v/d\varepsilon) > 1$$

where c = strain concentration factor which accounts for the change in the shape of the crack or void

$d\varepsilon_v$ = relative strain increment of void corresponding to a given increment in macroscopic strain

$d\varepsilon_v = (db/b)$ from Figs. (8a & 8b).

The strain concentration was found to be inversely proportional to the frontal radius of curvature of the void. And for homogeneous matrix, the strain concentration near the edge of the void was to be distributed over a zone of dimensions depending primarily on $(a/_{Rad.})$, thus the strain concentration factor was given as:

$$C = 1 + k\,(a/_{rad})$$

where K = constant

and Rad = radius of curvature $= (b^2/a)$ from Figs.(8a & 8b)

Therefore

$$C = 1 + k\,(a/b)^2$$

equating both values of the strain concentration factor,

$$(db/b) = [1+k(a/b)^2]\,d\varepsilon$$

Re-arranging, and integrating between ε_o to ε and b_o to b it becomes

$$b = [(b_o^2+ka^2)\exp.(2\varepsilon-2\varepsilon_o) - ka^2]^{1/2} \qquad \ldots\ldots (19)$$

where b_o and ε_o = size of void and strain before growth respectively,
$b_o = 0$, in the case of nucleation by carbide cracking.

This equation was extended for all voids, assuming that all the second-phase particles behave in an identical manner,[40] to give:

$$f_V = f_o \times (3/2)[(k^{1/2}/r)[\exp.(2\varepsilon-2\varepsilon_o) - k/r^2]^{1/2} \qquad \ldots\ldots (20a)$$

when cracks nucleate by particle (carbide) cracking, and when cracks nucleate nucleate by decohesion.

$$f_V = f_o\,[(1+k/r^2)\exp.(2\varepsilon-2\varepsilon_o) - k/r^2]^{1/2} \qquad \ldots\ldots (20b)$$

where f_V = volume fraction of voids
f_o = volume fraction of second-phase
r = length to width ratio of particle

Equations (20a and 20b) were extended further - to express the process of void coalescence and the failure strain - to equations (21a & 21b) respectively.[40]

$$\phi = (2/3)(R/\lambda)^2 = f_o\,[(1+k/r^2)\exp.(2\varepsilon_f - 2\varepsilon_o) - k/r^2]^{1/2} \qquad \ldots\ldots (21a)$$

$$\phi = (R/\lambda)^2 = f_o \times (3/2)[(k^{1/2}/r)[\exp.(2\varepsilon_f - 2\varepsilon_o) - 1\,]^{1/2} \qquad \ldots\ldots (21b)$$

where ϕ = constant

R = particle radius

λ = interspacing of near, neighbouring voids, centred in the same plane.

ε_f = total failure strain

5.2.2. Case (b) Void Growth and Triaxial Stresses

In this case of void growth, the void was assumed to elongate under the effect of the applied tensile stress, until its length equals the spacing of the neighbouring voids centred on the same plane.[21] This assumption gave the expression , $2R(1+\varepsilon_g) = \lambda$

where ε_g = strain during growth,

and substituted into equation $\varepsilon_f = \log_e (1+\varepsilon_o + \varepsilon_g)$ this gave

$\varepsilon_f = \log_e [(\lambda/2R) + \varepsilon_o\,]$ substituting again for $(\lambda/2R)$ from Appendix I.3).

$$\varepsilon_f = \log_e [(\pi/6f\,)^{1/2} - (2/3)^{1/2} + \varepsilon_o\,]$$

But voids change both volume and shape during growth, and not just elongate; thus the above relationship was challenged[64,79] and was considered inadequate.

Further investigations on void expansion[64,65] showed that the process of growth was enhanced by the superposition of hydrostatic tensile

stress on a plastic deformation. Therefore, the effect of the principal components of the triaxial stresses on void growth was considered, assuming incompressible material and neglecting the interaction of voids with each other.

This indicated that, when sperical voids were pulled in the direction of the tensile axis, while being subjected to transverse stresses, the relative void increment per unit applied strain increased exponentially with transverse stresses as:

$$\bar{\varepsilon}_f = \frac{(1-n)\log(\lambda/2R)}{\sinh[(1-n)(\sigma_a+\sigma_b)/(2\bar{\sigma}3^{1/2})]} \qquad \ldots\ldots (22)$$

where n = strain hardening coefficient

σ_a, σ_b = transverse stress components

$\bar{\sigma}$ = effective stress (Appendix II. 3.0)

$\bar{\varepsilon}$ = effective strain at fracture

With the same void growth analysis and triaxial stresses, it was also shown that[22,52,79] the volume changing part of the void growth, far overwhelms the shape changing part when the hydrostatic tensile stress becomes large. This also gave an exponential dependence of the volume increments of voids on the triaxiality as[22]

$$\Delta R// = R_v[2+0.56\sinh(3^{1/2}/2\times\sigma_{hyd.}/\tau_o)] \qquad \ldots\ldots (23a)$$

$$\Delta R_\perp = R_v[-1+0.56\sinh(3^{1/2}/2\times\sigma_{hyd.}/\tau_o)] \qquad \ldots\ldots (23b)$$

where

$\Delta R//, \Delta R_\perp$ = elongation increments of the void parallel and transverse to direction of strain

R_v = radius of the expanding void

$\sigma_{hyd.}$ = hydrostatic component of stress

τ_o = yield stress in shear

So, different formulations, expressing the process of void growth. were proposed. The idealpresentation of the process of growth of voids for the purpose of this study are the formulae which express the extent of deformation (strain) in direct relation with the parameters of the microstructure.

The parameter inflicting the most pronounced effects on microstructure is the volume fraction of the second-phases i.e. in this case the volume fraction of carbides.

Therefore, the expressions best suited to describe the range of void growth are equations (20a & 20b). Equations (22 & 23) have limitations. Equation (22) gives the strain values in terms of the stress system. It excludes the parameters of microstructures except for the interparticle spacing, λ , which accounts for little description of the microstructure. The equation also neglects the sizes of the cracks and voids which are responsible for fracture.

Equation (23) does not provide any measure of the extent of deformation which is required in this study. It also neglects the parameters of microstructure. It only gives the longitudinal and transverse increments of void in relation to the stress system.

Equation (20) can be used to extend the theoretical hypothesis of equation (18) to describe both the beginning and duration of void growth. And since it is needed, later, to verify equation (18) by experimental results, it is useful to re-arrange equation (20) into a form which can facilitate the direct addition of the experimental results obtained from both equations.

To do this equation (19) is squared and divided by, b^2,

$$1 = [(b_o/b)^2 + k(a/b)^2] \exp.(2\varepsilon - 2\varepsilon_o) - k(a/b)^2$$

where, ε_o and b_o, can be defined for the purpose above as the strain and

size of void at the start of void growth. b = size of the growing void at strain $\varepsilon > \varepsilon_o$: and assuming unifromly distributed regular shapes of carbide particles b_o, b can be replaced by f_{V_o}, f_V, the volume fractions of voids at the start of growth and at strain $\varepsilon > \varepsilon_o$ respectively.

Therefore, $(b_o/b) = (f_{V_o}/f_V)$ and substituting in the above equation,

$$1 = [(f_{V_o}/f_V)^2 + k(a/b)^2] \exp.(2\varepsilon - 2\varepsilon_o) - k(a/b)^2$$

(f_{V_o}/f_c), is the ratio of volume fractions of voids and carbides, at the beginning of growth, at ε_o, and can be calculated from equation (18); and dividing the above equation by the square of this ratio, $(f_{V_o}/f_c)^2$

$$\frac{1}{(f_{V_o}/f_c)^2} = \left[\frac{1}{(f_V/f_c)^2}\right] \exp.(2\varepsilon - 2\varepsilon_o) + \left[\frac{k(a/b)^2}{(f_{V_o}/f_c)^2}\right][\exp.(2\varepsilon - 2\varepsilon_o) - 1]$$

re-arranging

$$\left[1 - \frac{(f_{V_o}/f_c)^2 \exp.(2\varepsilon - 2\varepsilon_o)}{(f_V/f_c)^2}\right] = k(a/b)^2 [\exp.(2\varepsilon - 2\varepsilon_o) - 1] \quad \ldots\ldots \text{(24a)}$$

This equation expresses the beginning of void growth and extends further throughout the process of void growth. This equation also gives the change in the strain concentration factor, $C = +k(a/b)^2$ during the growth of voids as,

$$1 + k(a/b)^2 = 1 + \left[1 - \frac{(f_{V_o}/f_c)^2 \exp.(2\varepsilon - 2\varepsilon_o)}{(f_V/f_c)^2}\right]\left[\frac{1}{\exp.(2\varepsilon - 2\varepsilon_o) - 1}\right] \quad \ldots\ldots \text{(24b)}$$

5.3. Void Coalescence

Void coalescence was analysed as the result of internal necking of the matrix between the voids.[98] It was stated that this type of coalescence is possible when:

a) The transverse stress components are tensile.

b) The ratio of the tensile stress to cause plastic flow to the true yield stress becomes small.

The condition for void coalescence by internal necking of the matrix was derived as:

$$(\sigma_n/Y)(1 - f_v^{1/2}) \leq 1/2 + (\sigma_{hyd.}/Y)$$

where σ_n = flow stress

Y = true yield stress

$\sigma_{hyd.}$ = hydrostatic component of stress

f_v = volume fraction of voids

This equation does not include a contribution to failure strain and, therefore, is inadequate for the purpose of this study. Equations (21a and 21b) which were derived as an extension of equations (20a and 20b) respectively, satisfy the purpose for void coalescence. They express failure strain, ε_f , in terms of volume fraction of carbides, sizes of carbide particles and their distributions.

So, the main objective of this study, - to relate the fracture strain to microstructure, - is completed when equations (20) and equation (21) are added to equation (18), and it remains to verify these equations by experimental results.

6.0. The Effect of Notches on Fracture

It is not desirable that a steel fails in a brittle manner during a cold forging operation. This can occur due to certain defects which restrain plastic flow, increase very much the local stress concentrations, and hence nucleate cracks and allow them to propagate.

These adverse effects of defects were dealt with, in early work, they were analysed both qualitatively and quantitatively in an attempt to avoid them or at least to minimise them.

The analysis was carried out by introducing notches of different geometries which resemble various expected deep and surface defects, hence, serve the same purpose of stress raisers. It was found that notches of various sharpness and depth produce different states of stress, stress concentrations, strain concentration, and triaxiality.[27,71,81, 82,83,92].

Some of the early work covering this analysis is summarized in this sectiom.

6.1. Notches and the State of Stress

The introduction of a notch produces a condition of biaxial stress at the root of the notch (i.e. transverse stress σ_T, longitudinal stress σ_L - and radial stress $\sigma_r = 0$), - and triaxial stress (σ_T, σ_L and σ_r) at the interior of the specimen, when the specimen is pulled in tension. (Fig.(9a).

The occurrence of this state of stress was explained by the constraints to plastic flow w hich a notch sets up[27]. For an equilibrium of forces to be maintained in the notched bar, it is necessary that:

a) No stresses act normal to the free surface of the notch.

b) All the tensile load must be taken by the metal core of the notch.

c) Therefore, a relatively large mass of unstressed metal exists around a central core highly stressed.

d) The central core tries to contract laterally because of the Poisson effect, but it is restrained by what amounts to a hoop of unstressed material around it. This resistance of unstressed material to the deformation of the central core produces the radial stress (σ_r) and the transverse stress (σ_T).

The average transverse stress σ_T was determined from the elastic characteristics of the notched section of the test bars according to the following relations for the elastic transverse strain(e_T).[82]

$$e_T = -\frac{\sigma_L}{E_T} = \frac{1}{E}(\sigma_T - \nu\sigma_L - \nu\sigma_T)$$

where ν = Poisson's ratio

E = Elastic modulus of unnotched bars

E_T = transverse elastic Modulus.

From the above equation the triaxiality ratio (σ_T/σ_L) was ;

$$(\sigma_T/\sigma_L) = \frac{1}{1-\nu}(\nu - E/E_T)$$

The triaxial state of stress raises the values of the longitudinal stress at which yielding occurs compared to yielding for unnotched specimens. The entire stress-strain curve for notched specimen is raised over that for unnotched specimens by the amount known as the plastic constraintfactor (q), as in Fig. (9b).

Yielding of a notched specimen occurs when ,

$$\sigma_L - \sigma_T = 2\tau_o$$

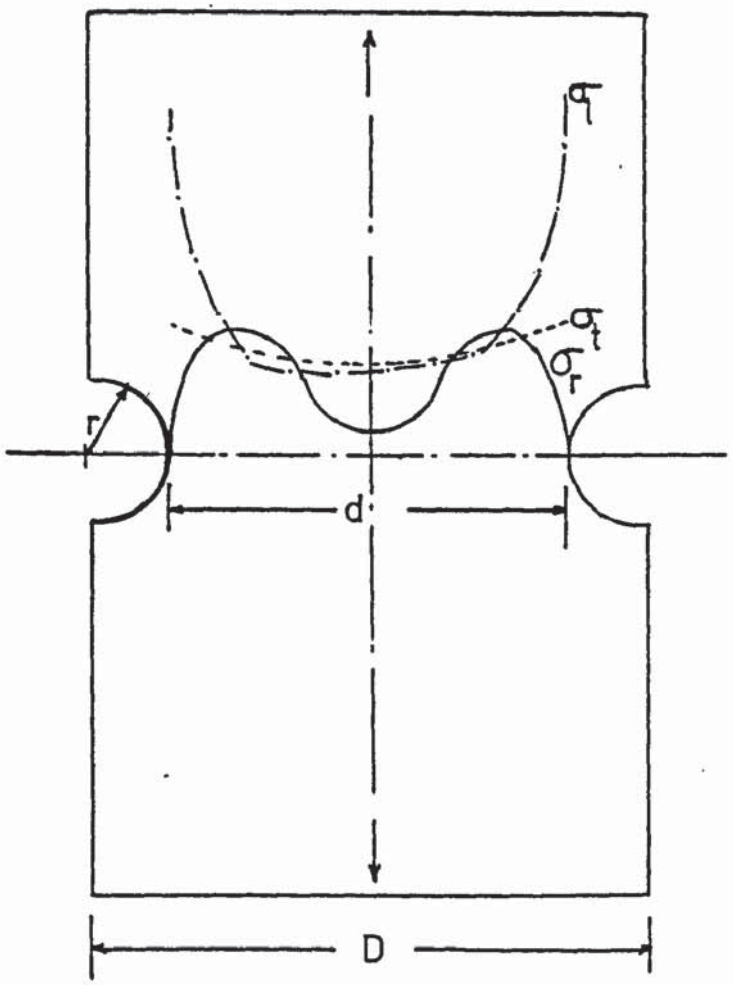

The distributions of elastic stresses in the notch section.

FIG.9.a.

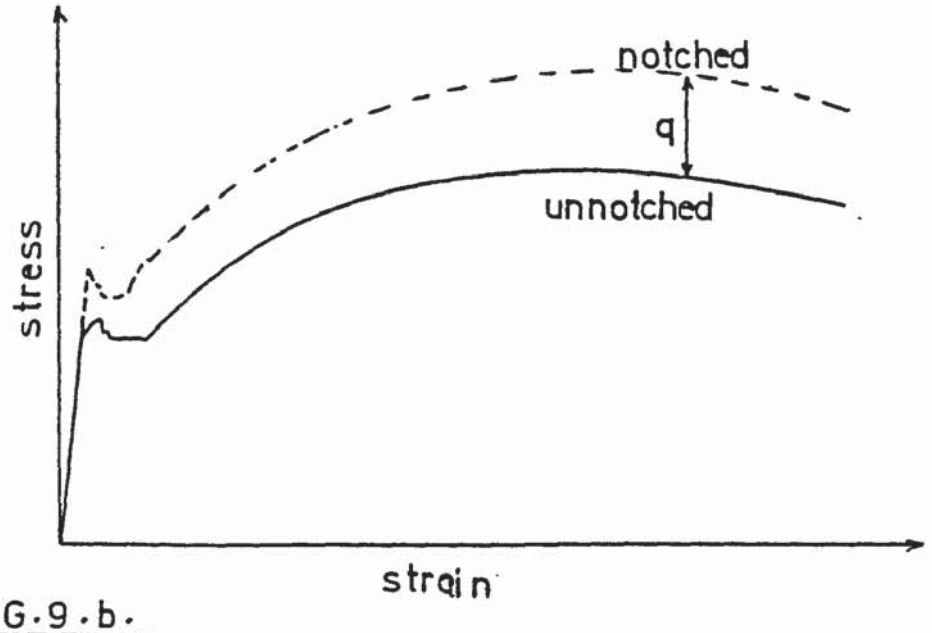

FIG.9.b.

When yielding occurs the elastic stress concentration factor, K_t, reduces and plastic constraint is produced.

The elastic stress concentration factor (K_t) is the ratio of the maximum value of the longitudinal stress to the applied stress at the section of the notch: ($K_t = \sigma_{max.}/\sigma_N$)

These changes in the state of stress, stress concentration, the raising of the yield point and the plastic constraint, have their effects on the energy balance of crack nucleation and propagation. The raising of the yield point and the high stress concentration increase the energy available for the crack propagation. Also the plastic constraint factor favours the propagation of the crack, because low plastic flow means little energy being absorbed in plastic deformation which means more energy for the cracks to propagate without their tips being blunted.

6.2. Notch Stress Analysis of Fracture

For a particular material, the above changes in the state of stress, stress concentration triaxiality, yield point and plastic constraint, are dependent on the notch geometry, its root radius, depth and width. Sharp deep notches produce high elastic stress concentration factors. This dependency of elastic stress concentration factors and triaxiality on the notch geometry were analysed.[71,78,105] The relationships derived from these analyses are summarised in this section.

6.2.1. Elastic Stress Concentration Factors (K_t)

The elastic stress concentration factor is:

$$K_t = \sigma_{max.} / \sigma_N$$

where, $\sigma_{max.}$ = maximum stress which develops at the root of notches (longitudinal or circumferential)

σ_N = nominal stress on the net section of the notch

$$\sigma_N = \frac{\text{Applied load}}{\pi d^2}$$

d = diameter at notch section

A comprehensive treatment of the elastic stress distribution in the vicinity of notches (71,105) was used to derive basic formulae for the values of the elastic stress factors, K_t , for deep circumferential notch as:

a) <u>in the case of the longitudinal stress</u>

$$K_t = \frac{(d/r)(d/r+1)+0.8\,d/r+1.3[(d/r+1)^{1/2}+1]}{d/r+0.6(d/r+1)^{1/2}+2} \qquad \ldots\ldots(25a)$$

where a Poisson's ratio of $\nu=0.3$ was assumed. For a very sharp notch, , $d/r \gg 1$, the formula reduces to $K_t = (d/r)^{1/2}$

b) <u>in the case of the circumferential stress</u>

$$K_{t_{cir.}} = (d/r)\left[\frac{1}{d/r+0.6(d/r+1)^{1/2}+2}\right][0.6(d/r+1)^{1/2}+0.5] \qquad \ldots\ldots(25b)$$

where again a Poisson's ratio of $\nu=0.3$ was assumed.

The stress in the notch plane normal to the notch front has its maximum at some distance, y , below the notch root at, $y = d\left\{1-[(d/r-2)/(d/r-1)]^{1/2}\right\}$ ..... (26)

For very sharp notches, $y \simeq 0$, i.e. the maximum stress, is at the notch root.

Away from the notch root the maximum stress decreases in proportion to ($1/y^2$) which is a steeper gradient compared with the decrease of the maximum stress in case of sharp notches in sheets or plates.

Extending the analysis further an approximate solution of the maximum elastic stress distribution near the notch root was proposed as(105),

$$(\sigma_x/\sigma_N) = K_t\left[\frac{r}{(r+4y)}\right]^{1/2} \qquad \ldots\ldots (27)$$

Equations (25, 26 & 27) in comibation give a good indication of the distribution of the maximum stress in the immediate vicinity and further away from the notch root.

The characteristics of the elastic stress field in the vicinity of the notch create a zone in which the stress distribution in not uniform. The extent of this zone was found to depend on the elastic stress concentration factor, K_t , the notch root radius, r , the width of the notch, the properties of the material and the loading condition.

Two extreme cases for the length of this zone are:[51]

1) When the notch is sharp, the zone is small but it may be greater than the notch width, Fig.(10a)
2) For a superficial notch the disturbed zone is smaller than the notch width, Fig.(10b).

The length of this zone of non-uniform stress distribution was found experimentally to be:[51]

$$Z_l = r \times (K_t - 1)$$

6.2.2. Triaxiality

In the application of notch analysis to design and fracture problems, it is important to consider the multiaxial stress states (biaxiality and triaxiality). For fairly deep notches the degree of triaxiality was determined in terms of the notch depth (the fraction cross-section removed by the notch, $\left(\frac{D-d}{D}\right)^2$.[78,81,83] For such a deep notch, it was shown that the fracture stress approximately equals the notch strength and that both stresses increase in the same manner with increase in the notch depth,[84] following this relationship:

Comparison of the value of Z and the plastic zone around a notch.

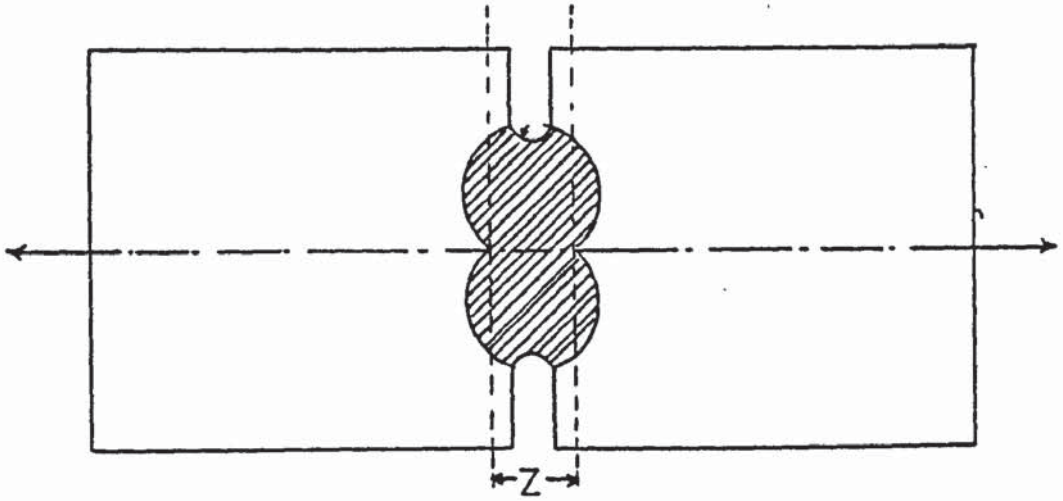

FIG. 10.a. for a sharp notch.

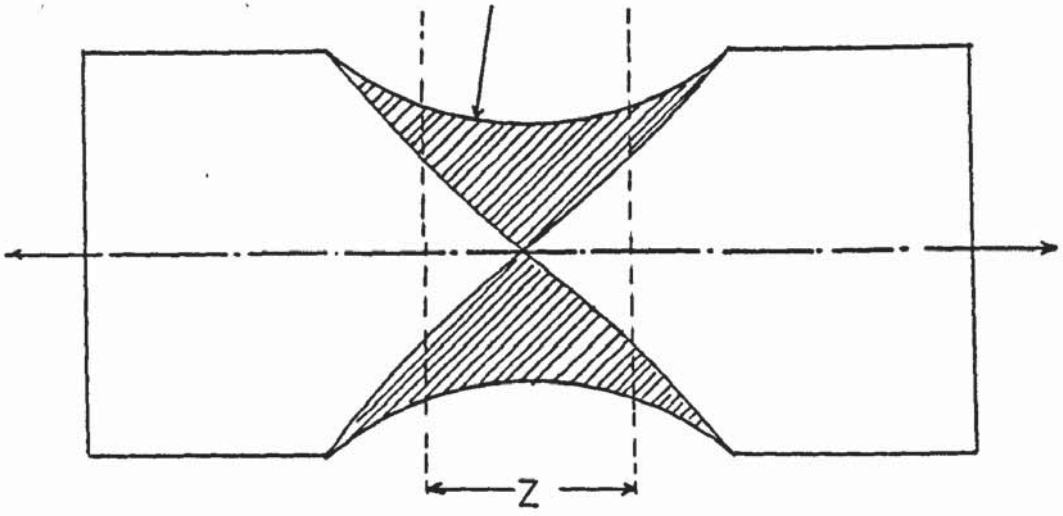

FIG. 10.b. for a shallow notch.

Fracture stress $\sigma_f \approx$ notch strength $\sigma_L = \sigma_{U.T.S.}[1 + (\frac{D-d}{D})^2]$

where $\sigma_{U.T.S.}$ = tensile strength of unnotched specimen.

From the flow curve Fig.(9b), considering the plastic constraint factor constant, the transverse stress, $\sigma_T = \sigma_L - \sigma_{U.T.S.}$

Therefore, the triaxiality degree, (σ_T/σ_L) was calculated as:

$$(\sigma_T/\sigma_L) = 1 - (\sigma_{U.T.S.}/\sigma_L) \qquad \text{i.e.}$$

$$(\sigma_T/\sigma_L) = \left[\frac{(\frac{D-d}{D})^2}{1 + (\frac{D-d}{D})^2}\right] \qquad \ldots\ldots (28)$$

where D = diameter of the unnotched section of specimen.

6.3. The Notch Ductile Behaviour

It is recalled that crack propagation was believed to be difficult in ductile steels (such as those used for the purpose of this study); but the introduction of notches produce circumstances which favour crack propagation very much. Thus it is necessary to determine how high local stresses, elastic stress concentration factors and surface energy are needed to overcome the resistance offered against the rapid propagation of cracks in these ductile steels. In other words it is needed to determine the geometry of the notch that can produce high enough stress concentrations to cause crack propagation, hence, promote brittle behaviour.

Two situations arise:-

1) A certain sharp notch gives high elastic stress concentration factors, where high local stresses at the notch root are likely to nucleate and propagate cracks in such a way that cracks start at the notch root and spread rapidly inwards to cause the complete failure of the specimen.

2) A moderate notch gives lower values of the elastic stress concentration factors hence the local stresses are not high enough to propagate cracks. But the triaxiality due to the

presence of this notch can enhance the growth of the cracks nucleated within the bulk of the material below the root of the notch. This fast growth of cracks, speeds-up their linking together and produces large cracks which move outwards.

To determine what notch geometry produces either of these two types of fracture, the term "notch strength ratio, N.S.R."[60] was introduced as a measure of the notch sensitivity. This "N.S.R." is the ratio of the notch strength to the ultimate tensile strength. The notch strength is the maximum load divided by the notch section area.

The relationship between experimentally measured values of "N.S.R." and K_t, produced a family of curves; different curves for various values of the notch root radius. The analysis of these curves, combined with the fact that the extension of the zone, $[r \times (K_t - 1)]$ is limited by crack opening, gave the expression:[51]

$$N.S.R. = \exp.[A(r) \times (K_t - 1)^3] \qquad \ldots\ldots (29)$$

where, $A(r)$ = third degree polynomial, which depends on the characteristics of the material.

Another expression used here, and which shows the effect of triaxiality on notch ductile behaviour, is

$$N.S.R. \geq 1 + \left(\frac{D - d}{D}\right)^2 \qquad \ldots\ldots (30)$$

Equations (29 & 30) show how the notch geometry affects the manner of fracture.

CHAPTER III

EXPERIMENTAL PROCEDURE

1.0. Introduction

The theoretical analysis of the stage at the beginning of void growth (in chapter 2, section 5.1), was to bridge the gap between the reviewed theories of crack nucleation and those proposed for the next process of void growths, in order to present an integrated description of the mechanisms of ductile fracture. And the purpose of the experimental work in this chapter is:-

1) To test this theoretical hypothesis and to compare the values of the strain at the beginning of void growth calculated from the theoretical equations (18a & 18b) with the experimental findings.
2) To test whether the calculations of the failure strain based on the strain at the beginning of void growth calculated from equations (18a & 18b) added to the strains for void growth and coalescence calculated from equations (20a & 20b) and equations (21a & 21b) respectively, agree in practice.
3) To verify the analysis of the notch ductile behaviour, through the results from experiments on notches of different root radii and steels of varying contents of carbides, oxides and sulphides.

The data required to fulfil these purposes are detailed description of the deformation, and the changes of the microstructure of the steels during this deformation in relation with the fracture processes.

So, experiments were carried out on four types of steels. Three

of the steels, - provided in rod form, - were heat treated to distribute the carbides present as dispersed spheroids. The fourth steel (nine different alloys) were made in the laboratory to provide varying oxide and sulphide contents.

These experiments were carried out at room temperature using mechanical testing methods of simple modes of deformation, i.e. tensile and notch tensile tests and axial compression. The major advantage of the tensile and notch tensile tests is that the state of stress can be defined precisely. The results obtained from compression are not as useful as the ones from the tensile test, but compression gives a different strain distribution which is important in studying some cold forging operations which are bascially compressive such as upsetting.

The necessary measurements carried out in this respect were:

1) Measurements on the QTM to quantitatively characterize the microstructure of the steels.
2) Measurements of the distribution of the strain imposed due to the tensile and compression tests, from the grid marks.
3) Measurements of the void volume and distribution in areas of known strain.
4) Measurements of the geometry of notches, (elastic stress concentration factors), and the notch strength.

2.0. <u>The Steels used</u>:

The three steels A, B and C were provided in round rods of 12.50 ± 0.005 mm diameter. They were annealed to adjust the microstructure and to provide the best possible spheroidization. In practice, a wide range of annealing treatments are used depending on the ductility needed and the cost. For the purpose of this work, the following four annealing treatments were used.

1. The steels were spheroidized at 670°C for 6 hours, then air cooled; heated for 5 minutes at 900°C; then transferred to 670°C, then transferred to 670°C for 6 hours; and finally air cooled to room temperature.
2. The steels were spheroidized at 700°C for 7 hours, then air cooled; heated for 6 minutes at 900°C, then transferred and held at 700°C for 5 hours, and finally furnace cooled to room temperature.
3. The steels were heated for 15 minutes at 750°C, then cooled down to 670°C in 8 hours, and finally air cooled to room temperature.
4. The steels were heated for 15 minutes at 750°C, then cooled down to 670°C in 8 hours; air cooled to room temperature; heated again and held at 720°C for 8 hours; and finally furnace cooled to room temperature.

The nine types of steel D were produced as follows - 1.5 kg of Japanese electrolytic iron contained in an alumina crucible (Fig.11) were melted under Argon gas to prevent oxidation. The melt was held at 1600°C superheat and the first sample was taken to get the oxygen level. Ferric oxide (Fe_2O_3) and ferrous sulphide (FeS) were added to bring the oxygen and sulphur to their required levels, and the second sample was taken. Then a deoxidizing alloy was added and the melt was sucked into a silica tube and was left to air cool. Three different deoxidizing alloys D1, D2 and D3 were used. Each deoxidztion alloy was used with three different percentages of sulphur, 0.02%, 0.1% and 0.2% to give nine different compositions of steel.

Furnace Assemply

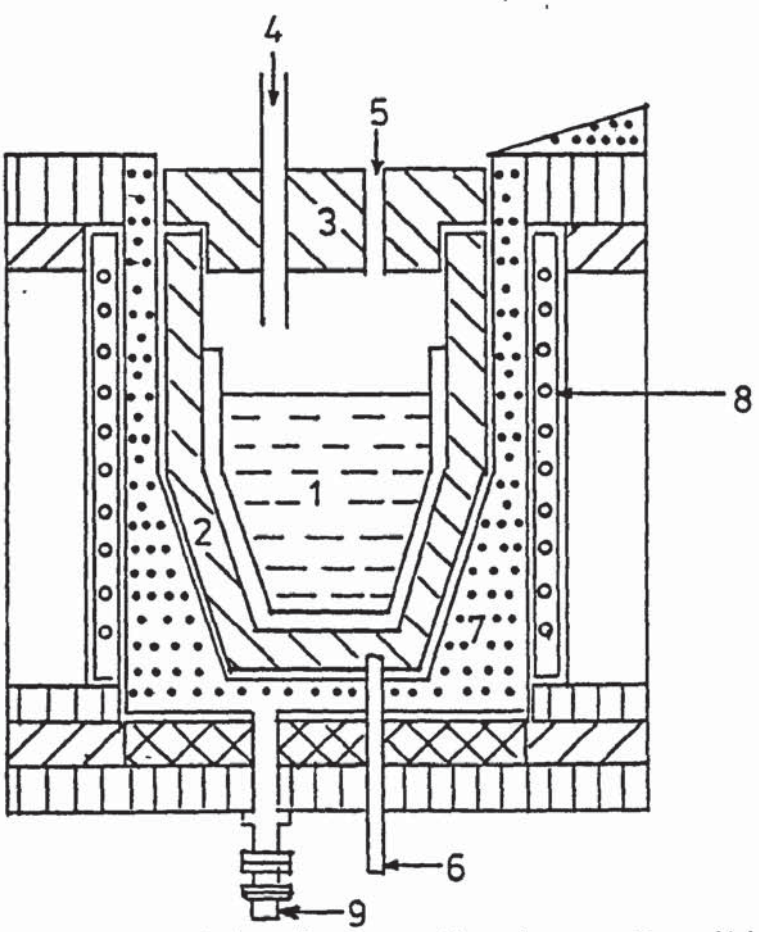

1 Iron Melt Contained in Alumina Crucible
2 Graphite Susceptor
3 Graphite Susceptor Lid
4 Argon Inlet Tube
5 Thermocouple and Sampling Hole
6 Thermocouple
7 Furnace Lining
8 Water Cooled Induction Coil
9 Earth Leakage Spider

FIG.11.a.

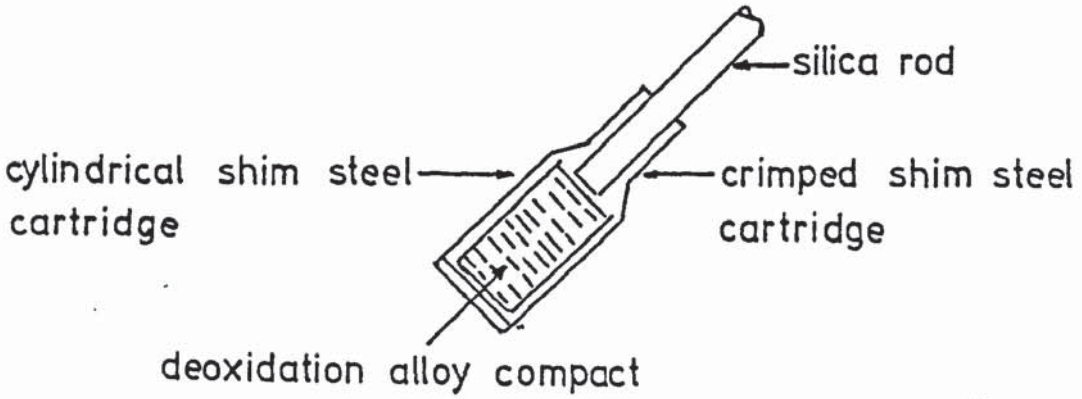

FIG.11.b.

3.0. Quantitative Measurements of the Microstructure

In order to obtain details of the microstructure produced in the above preparation of steels as measurable quantities, quantitative metallography techniques were employed. It was necessary to measure the sizes of the inclusions and particles, carbides, sulphides, oxides, silicates, etc., and their distributions. To do this, small specimens of the above steels were prepared and examined under the Quantitative Television Microscope (Q.T.M.). The Q.T.M.720 was used to identify different types of inclusions and particles, count them and measure their sizes.[38,46,91]

The microstructural quantities measured for steels A, B and C were: the percentages of pearlite and cementite, - the volume fraction of carbides, - the ferrite grain size, - the interparticle spacing, - and the size-distribution of carbide particles.

The microstructural quantities measured for steels type D, were:- the size-distribution of sulphides and oxides.

The procedure and calibration of the Q.T.M. for these measurements are in Appendix I.

4.0. The Tensile Test

Specimens for the tensile test were prepared from steels A, B and C (20 specimens from each steel). These specimens were machined axially from the round rods provided according to the B.S.18, part 2, 1971. The dimensions of the tensile specimen are in Fig.(12).

To calculate the circumferential and longitudinal strains on the surface of the specimens after deformation, it was required to measure the relative displacements that occurred on the outer surface. To do this circular gridmarks of diameters 2.5 mm were printed on the surface of specimens. The changes in the pattern of these circular gridmarks during deformation were measured as the relative displacements. These displacements were used to calculate the longitudinal and circumferential logarithmic strain values on the outer surface of the deformed specimens.

The equipment in Fig.(13) was used to print the gridmarks on the surface of the specimens as follows:[19,23,81,92]
The holder was used to roll the specimens on the stencil. The electric circuit was closed and alternating current from the power unit was carried by the electrolyte through the stencil to the specimen. The pattern of circles on the stencil was then printed as black iron oxide markings on the surface of the specimens due to chemical reactions between the specimens and electrolyte. These oxide markings were printed to a depth of 0.005 mm.

The tensile test was carried out on a Mand Precision Tensile machine of load range (0 —1,000 kgf).

The crosshead speed was - low gear 400 r.p.m., i.e. 0.83 mm/min. The extension of the specimens during the test was measured by an

electronic strain gauge. This extension was recorded against the corresponding applied load on a chart recorder.

During pulling to fracture each specimen changed shape as illustrated below: (see Fig.(14)

(a) The machine was loaded to a load value corresponding to the yield stress value without any appreciable change in the shape of the specimens.

(b) When the machine was loaded further, the specimens elongated uniformly with uniform reduction in its diameter up to a moment when the load of the machine began to drop from a maximum. A neck began to form on the specimens.

(c) The specimens continued to elongate non-uniformly only in the region of the neck.

(d) Finally the specimens separated (fractured) at the narrowest part of the neck.

The gridmark circles printed on the surface of the specimens changed shape in stages corresponding to the changes of the specimens as illustrated below:

(a) The grid circles remained unchanged.

(b) The grid circles changed into ellipses.

(c) The ellipses in the region of the neck changed into ovals.

The above changes in shape and relative positions were measured by a travelling microscope. These measurements were corrected for the curvature of the surface of the specimens, by graphical methods.

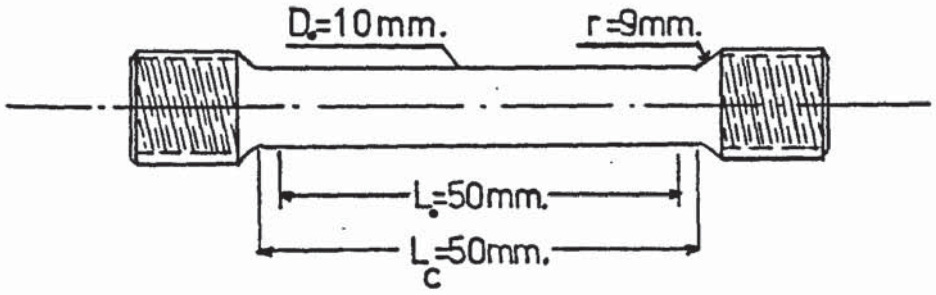

Tensile specimen

Scale = 1 : 1

Dimensions : mms.

FIG. 12.

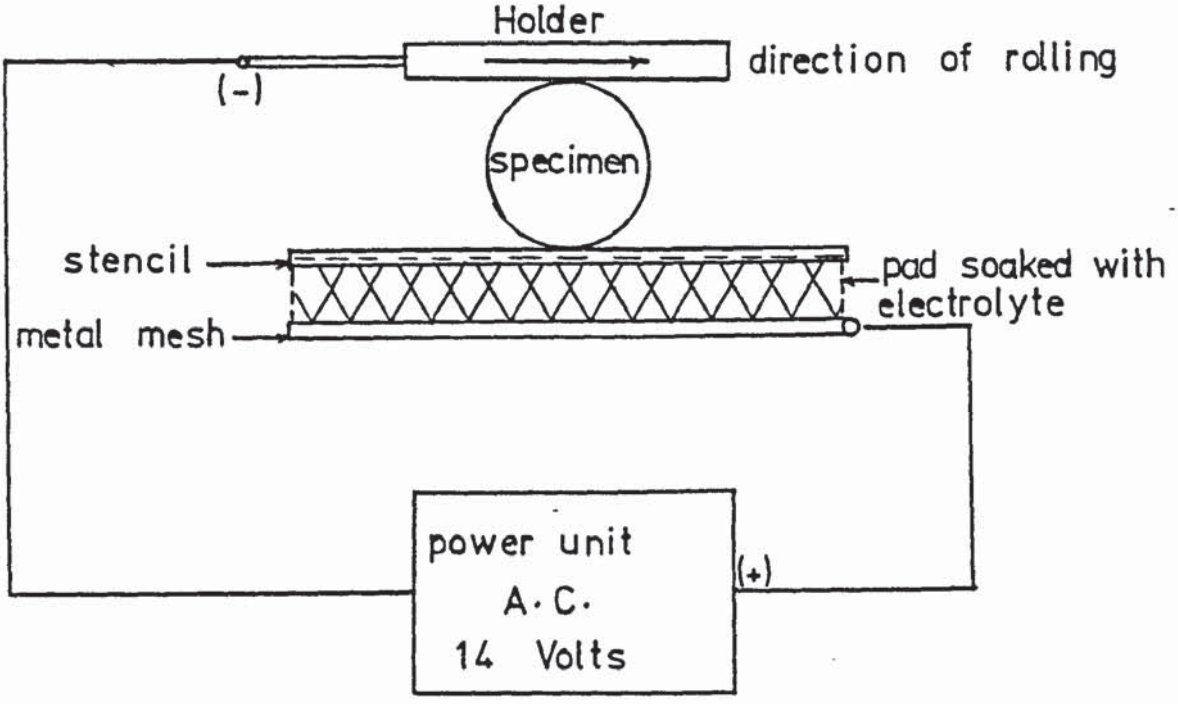

Electrochemical Printing Equipment

FIG. 13.

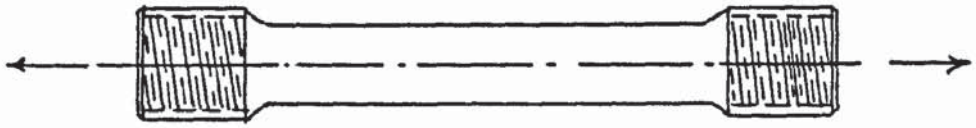

(a) original tensile specimen before pulling

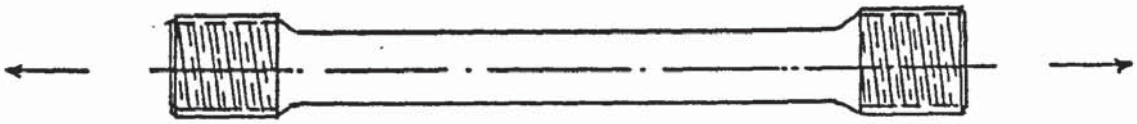

(b) during uniform elongation

(c) after necking

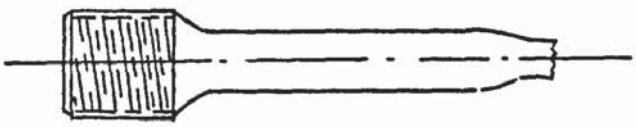

(d) after fracture

FIG.14.

4.1. Strain Measurements

4.2.... Axial and Radial Strains, (3,20)

The axial strain along the tensile axis was calculated from the reduction of the diameter of specimen during deformation, as:

$$\text{Axial Strain } \varepsilon_x = \log_e (D_o / D_i)^2$$

where, D_o , D_i are the original and instant diameters of specimens. The radial is negative and is normal to the axial strain, it was calculated as:

$$\text{Radial, Strain } \varepsilon_r = \log_e (D_i / D_o)$$

4.3.... Strains on the Outer Surface of the Specimen

The calculation of the circumferential negative strain ε_θ and the longitudinal strain ε_L on the outer surface of the specimens required the location of the corresponding points on the circumference of the changing gridmarks, then the displacements of the oo-ordinates of these points were measured.

To do this, points were chosen on the circumference of the original circles, then their corresponding final locations on the circumference of the ellipses and oval curves were found using the properties of these three shapes and the theories relating them (as in Appendix III)

The corresponding points were located graphically as follows:

Uniform Deformation

(a) The deformation was seen as displacement of consecutive layers of volumes as in Fig.(15).

(b) The volumes after deformation were equal to the corresponding ones before deformation, in Fig.(15a) and (15b). (Area 1 = Area 1' and Area 2 = Area 2').

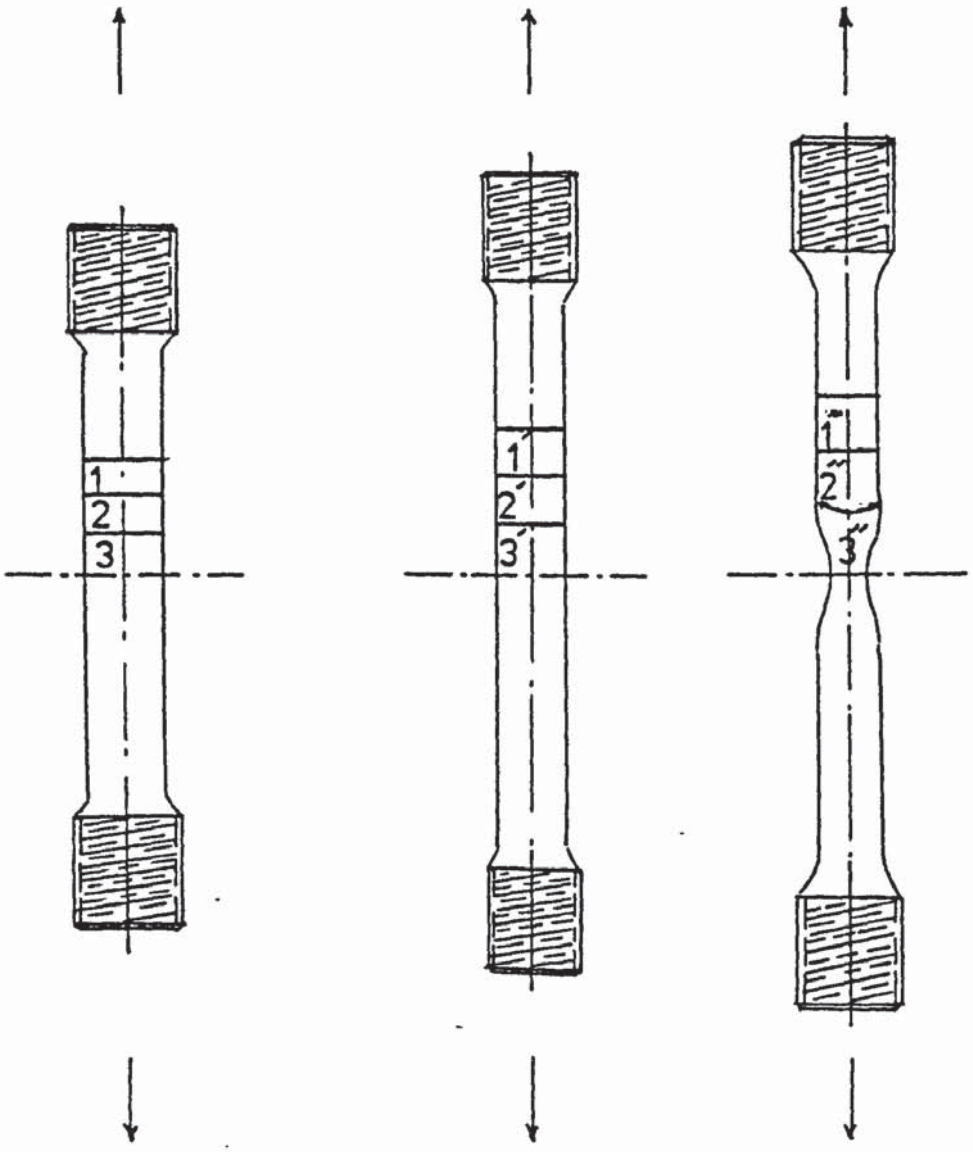

(a) Before Pulling (b) At Necking (c) Beyond Necking

FIG. 15.

(c) Accordingly the gridmark circles on the outer surface of the specimens were divided into ten equal area strips. The areas represented equal volumes. Ten points, P1, P2, ... P10, were taken on the mid-ordinates of these area strips as in Fig. (16) drawn at (40X) scale.

(d) The ellipse at any uniform deformation (for this case at the point of necking) was drawn to the same scale above, an example measured from the experiments on Steel A is in Fig.(17). The points and area strips, corresponding to those on the original gridmark circle were located on this ellipse using the auxiliary circle as in Appendix III. The area strips were still equal.

(e) The strains during uniform deformation were calculated from the displacements of these points on the above Figs.(16 & 17) as follows:

Longitudinal strain on the outer surface of the specimens ε_L at M,

$$\varepsilon_L = \log_e \left(\frac{ON_1'}{ON_1}, \frac{N_1'N_2'}{N_1N_2}, \ldots\ldots, \frac{N_9'N_{10}'}{N_9N_{10}}\right)$$

Circumferential Strain ε_θ at M,

$$\varepsilon_\theta = \log_e \left(\frac{b_1}{r_1}, \frac{b_2}{r_2}, \ldots\ldots, \ldots\ldots, \frac{b_{10}}{r_{10}}\right)$$

Non-uniform Deformation

(a) The above ellipse at the necking point, representing the end of uniform deformation, was taken as a reference.

(b) The oval closest to the fracture edge was selected and drawn to to the same scale above. An example measured from the experiments on the same specimen of steel A above, is in Fig.(18).

The corresponding ten area strips and their mid-ordinates were located by the method of non=uniform compression of ellipses as in Appendix III.

This was done as follows:

1) An ellipse similar to that in Fig.(17) was drawn with the axial length of the oval curve as its major axis as in Fig.(18), The points on the circumference of the ellipse in Fig.(17) were located on this large ellipse by similarity.

2) The ordinates were dropped from these points on the large ellipse onto the circumference of the ocal curve.

3) The compression ratios, $k_1<k_2<k_3<\ldots\ldots<k_{10}$, were calculated.

4) Since the volume layers in Fig.(18) increased with non-uniform elongation and reduction of cross sectional area, the total area of the oval curve was divided in ratios of the reciprocals of compression ratios as:-

$$\frac{\text{Area of strip (1)}}{\text{of the oval curve}} = \frac{\text{Total Area of the oval curve}}{[1/k_1+1/k_2+\ldots\ldots+\ldots\ldots+1/k_{10}]} \times (1/k_1)$$

$$\frac{\text{Area of strip (2)}}{\text{of the oval curve}} = \frac{\text{Total Area of oval curve}}{[1/k_1+1/k_2+1/k_3+\quad+1/k_{10}]} \times (1/k_2)$$

$$\frac{\text{Area of Strip (10)}}{\text{of the oval curve}} = \frac{\text{Total Area of oval curve}}{[1/k_1+1/k_2+\ldots\ldots+\ldots\ldots+1/k_{10}]} \times (1/k_{10})$$

5) So, the corresponding areas of strip and their mid-ordinate points were located on the circumference of the oval, as in Fig.(18).

(c) The strains were calculated from the displacements of these points as:

$$\text{Longitudinal Strain } \varepsilon_L \text{ at } Q = \log_e \left[\frac{ON_1}{ON_1}, \frac{N_1N_2}{N_1N_2}, \ldots\ldots, \ldots\ldots, \frac{N_9N_{10}}{N_9N_{10}}\right]$$

$$\text{Circumferential Strain } \varepsilon_\theta \text{ at } Q = \log \left[\frac{w_1}{b_1}, \frac{w_2}{b_2}, \ldots\ldots, \ldots\ldots, \frac{w_{10}}{b_{10}}\right]$$

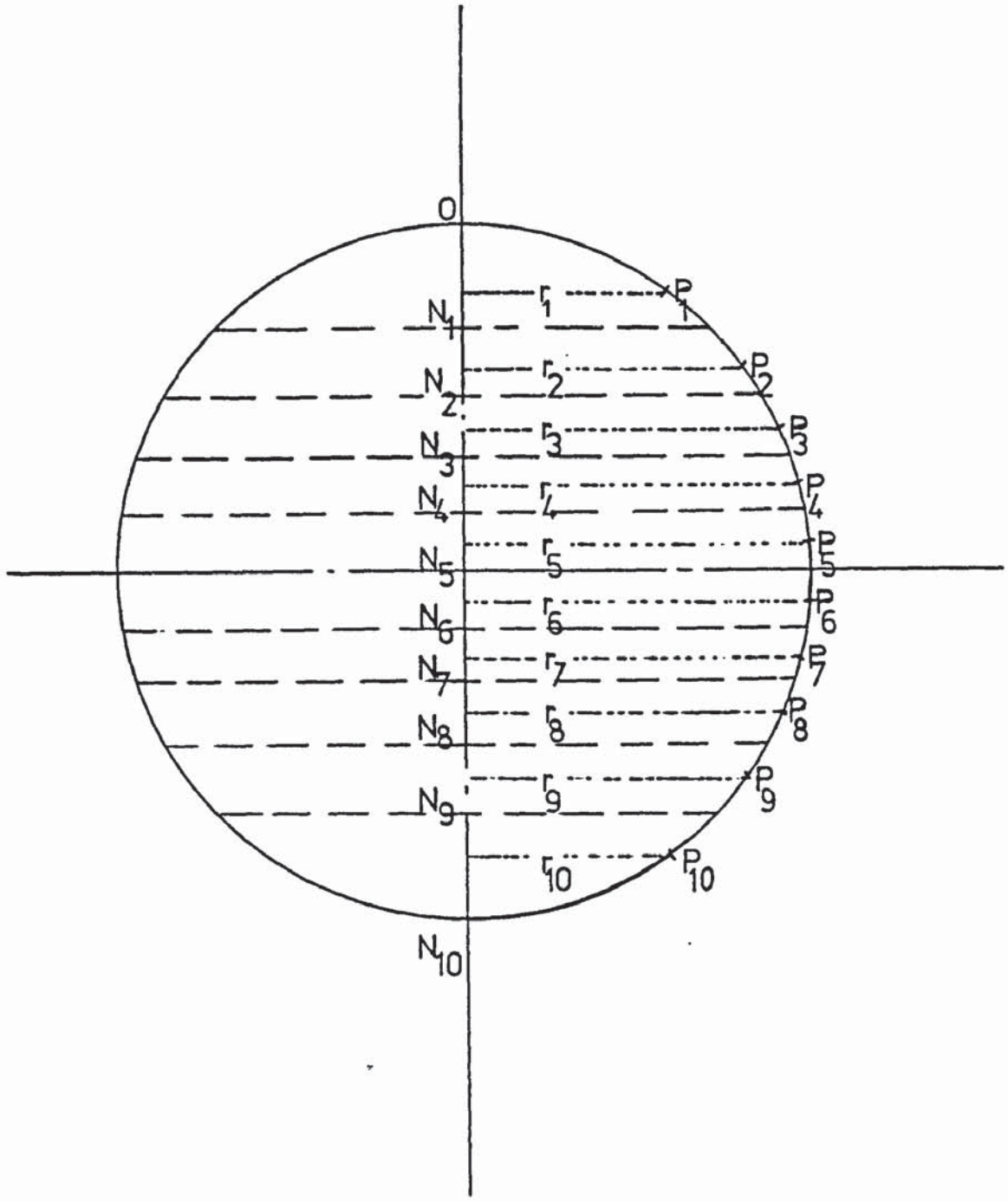

Original gridmark circle
Scale = 40 : 1
Dimensions: mms.

FIG. 16.

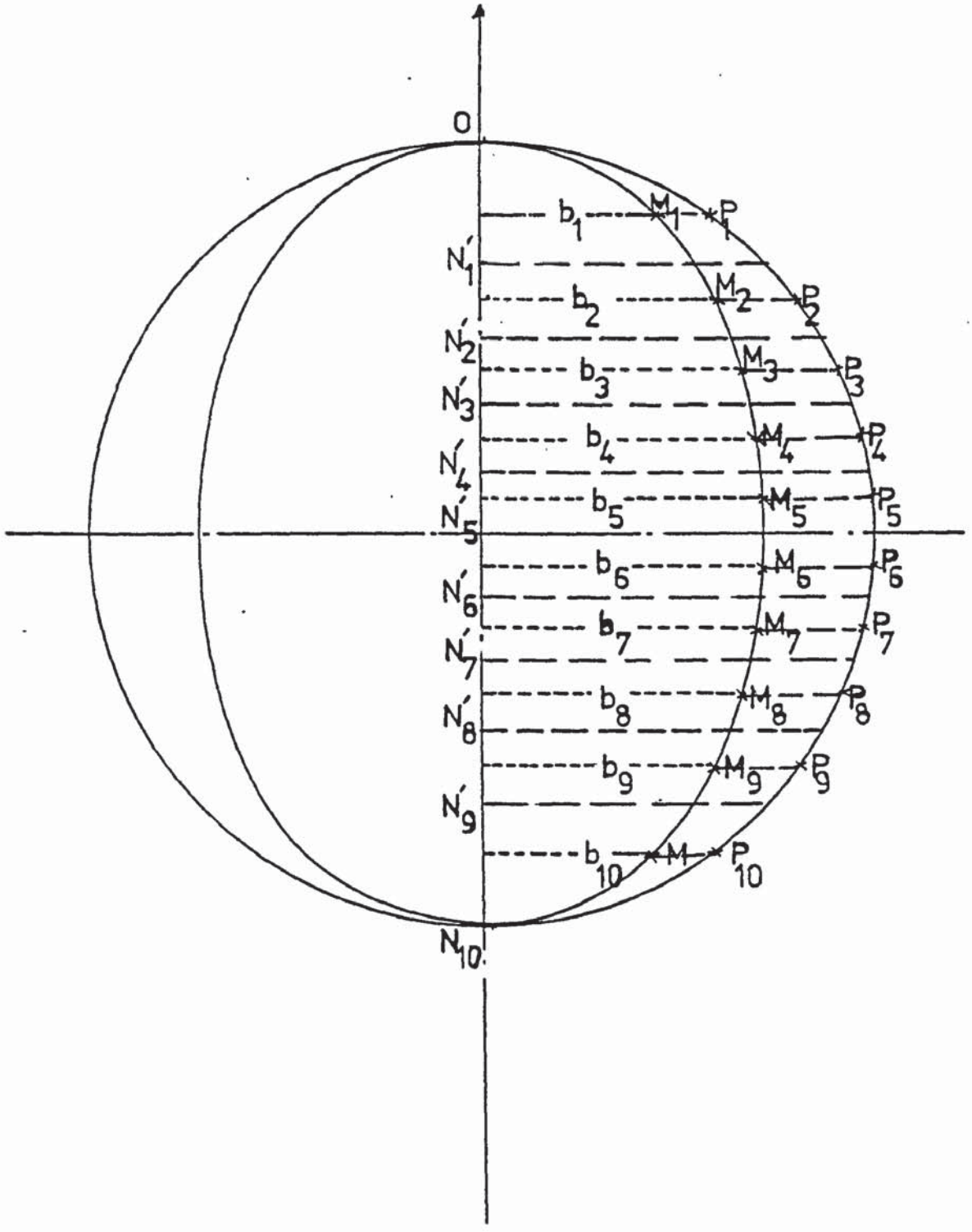

The ellipse at necking and an auxiliary circle.
Scale = 40 : 1

FIG. 17.

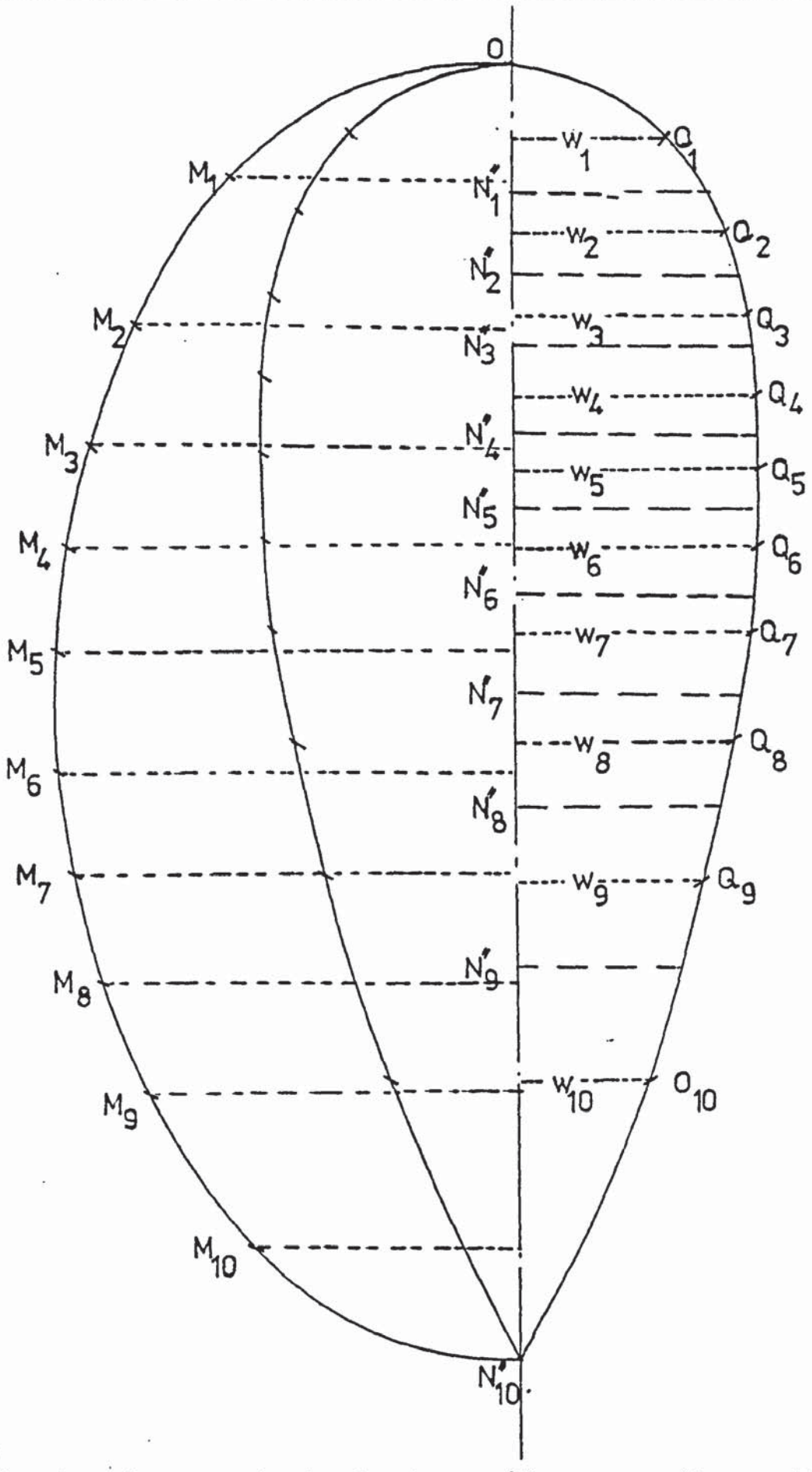

The teardrop oval at fracture with an auxiliary ellipse similar to that at necking.

Scale = 40 : 1

FIG.18.

An alternative and more convenient method of locating the points Q_1, Q_2..... Q_{10}, on the circumference of the tear drop oval" is based on the construction of the negative pedals described in Appendix III.F.

(1) From the construction of the negative pedals in (Fig. 91)
angle FMP = angle FQM. = ϕ

(2) Therefore, when the example in Figs.(17 & 18) was drawn as in Fig.(19) the corresponding points on the circumferences of the original circle, the ellipse at necking and the tear drop oval, were colinear. And with two of the three points located as in Fig.(17) the straight line joining them was extended to intersect the circumference of the oval curve hence locate the third point. The straight line joining these construction points is a good approximation to the real movements of the points on the original grid circle during deformation.

The corresponding points from the regular ellipse at necking to the teardrop oval were located by two methods for the same example in Figs.(18 & 19), and gave the same results. The two methods gave the same results for other measured examples.

The procedure of locating the corresponding points by the method of the construction of negative pedals, is easier, direct and less time consuming compared with the method of the non-uniform compression of ellipse. Moreover it gives a better approximation to the actual measurement of points on the surface. For this reason it was used to calculate the strains on the surface of deformed specimens in this work.

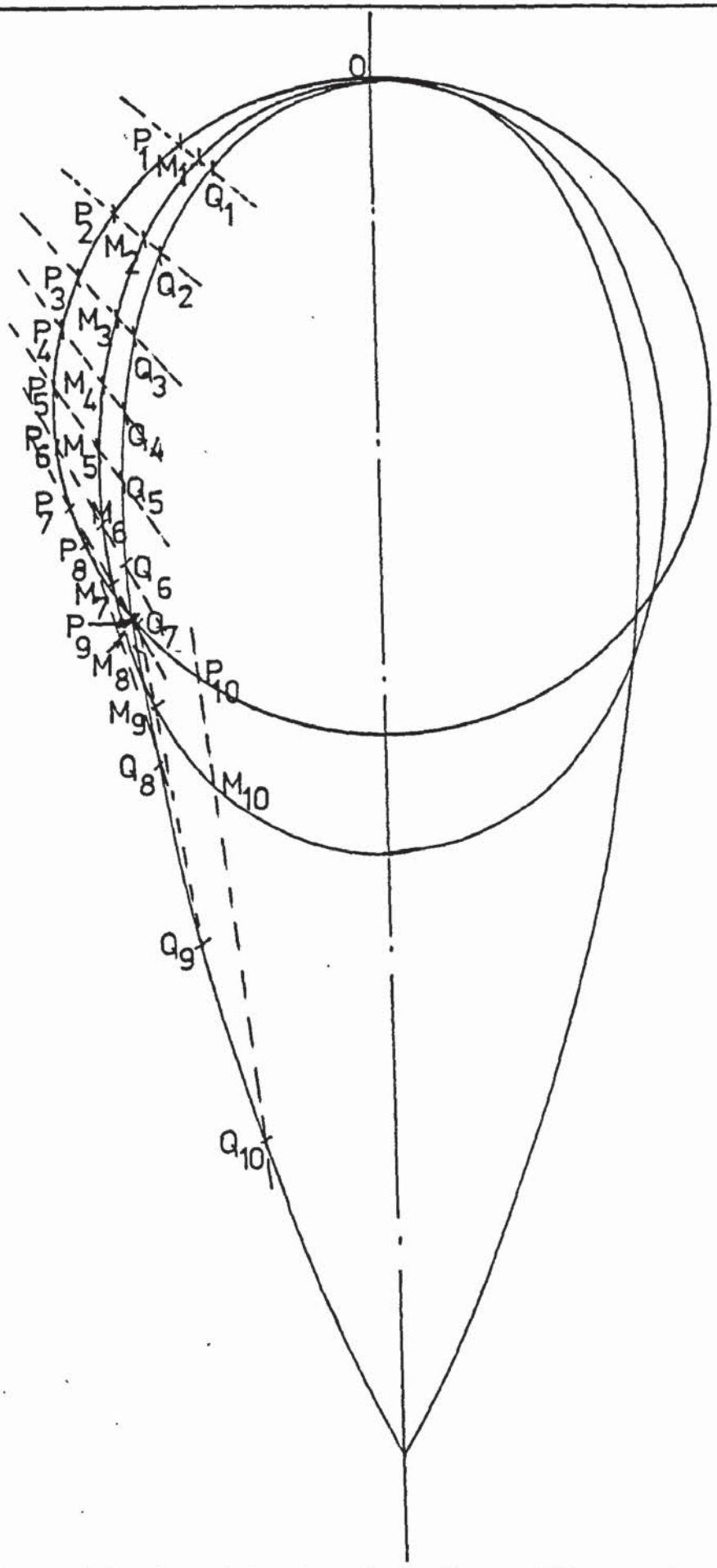

The original gridmark circle, the ellipse at necking and the teardrop oval at fracture.
Scale = 40 : 1

FIG.19.

4.4. Measurements of Volume Fraction of Voids and Particles

With the strain distributions within the deformed specimens calculated, the next step was to measure the metallurgical variables - the volume fractions of voids and carbide particles - at different fields located within these specimens. These volume fractions for each field were then related to their measured strain values.

The volume fraction of voids and carbides were measured by scanning parts of the fractured specimens, photographing fields of interest, and measuring the volume fractions from these photographs.

The Scanning Electron Microscope Cambridge SEM 2a and Cambridge Stereoscan 600 were used to scan sectioned planes of the specimens. The specimens were mounted on a travelling micrometer within the stereoscan which made it possible to locate the co-ordinates of the fields of interest along and across the axes of the specimens. This location was used to determine the strain values at any particular field. The fields scanned were photographed by means of a camera mounted on the Scanning Electron Microscope.(86)

From these photographs the volume fractions of voids and carbides were measured by a real analysis. The two dimensional random point count method(46) was used by superimposing a grid of fine spacing and counting the intersections falling on second phase particles or voids.

The measurements from the photographs were carried out as follows:(46)

(a) The number of all voids/particles whether circular, rectangular or irregular were counted as Ma.

(b) For each individual void or particle the radius, R, in the case of sphericals and the largest diagonal, Rm in the case of irregulars, were measured.

(c) Using the transparent fine grid the points falling on either particles or voids were counted as Np and Nv respectively.

These measurements were corrected for the statistical errors which resulted from the deviation of the areal fraction from the true volume fraction and from the use of point count in place of a direct measurement of the areal fraction by the method in Appendix IV.

In the fields scanned the size of the smallest cracked particle, if any, was measured and related to the corresponding effective strain. Similarly the size of the particle associated with the smallest void was measured and related to the corresponding effective strain.

5.0. Notch Tensile Test

Specimens for the notch tensile test were prepared from steels A, B, and the nine types of steel D, i.e. D10, D11, D12, D20, D21, D22, D.30, D31 and D32. Three different notches were machined from each type of steel : three specimens for each notch, i.e. a total of nine specimens of each steel; a grand total of 101 notch tensile specimens. These specimens were machined, with three notches of different root radii, to the dimensions shown in Fig.(20)

The initial diameter of the specimens (D) and the diameter of the notch cross section (d), the notch root radii (r) and the depth of each notch $(\frac{D-d}{D})^2$ were measured. The elastic stress concentration factors (K_t) were found from standard curves. (78)

The tests were carried out on the same Mand Precision Tensile machine used for the tensile test. The crosshead speed was : -low gear, 100 r.p.m. - i.e. 0.2mm./min. The extension of the specimens was measured by an electronic strain gauge and was recorded against the corresponding applied load on a chart recorder. The maximum load and the load at fracture were recorded.

The fractured sections of the specimens were examined under the Scanning Electron Microscopes (Cambridge SEM 2a and SEM 600) for the types of fracture, the appearance of cracks and voids, and for the growth of voids.

6.0. The Compression Test

Specimens for the compression test were prepared from steels A, B and C. These specimens were machined from the provided round rods. The dimensions of the specimens were 10mm. to 12mm. in diameter and height varying from 27mm. to a maximum of 38mm. Heights greater

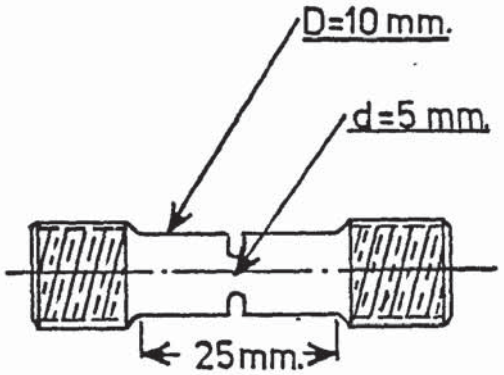

(a) A Notched Tensile Specimen.

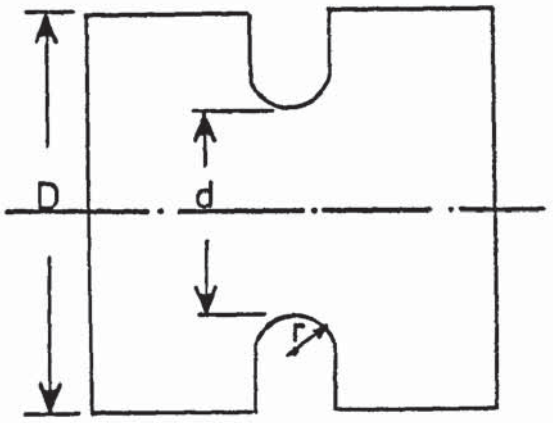

(b) r=1.00mm.

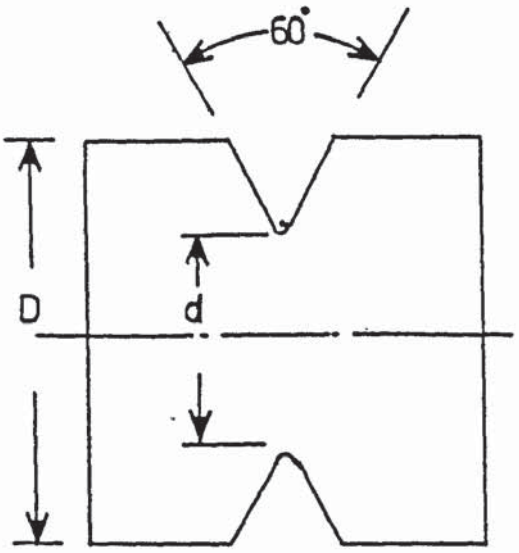

(c) r=0.26mm.

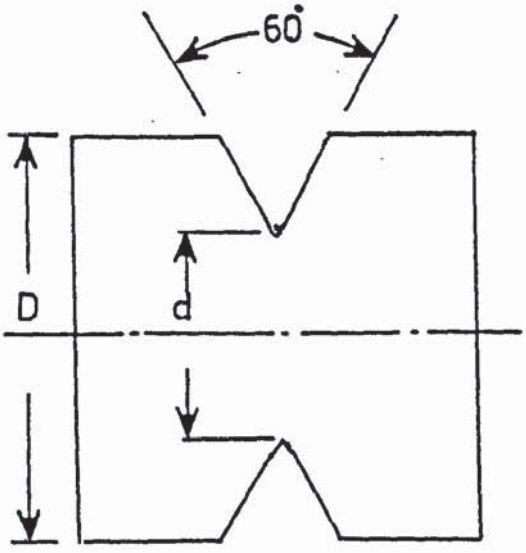

(d) r=0.16 mm.

FIG. 20.

than 38mm. were not chosen to avoid the buckling of the specimens during compression.

Some of the specimens were machined with flat top and bottom, others with cone angles of 10° and 30°. The cone angle was used to minimise barreling during compression. Top and bottom compression plates were used; they were made of die steel and heat treated to a hardness of 62 Rockwell. These compression plates also were flat, with a cone of 10° and a cone of 30°. These plates were repeatedly lubricated before the test.

Circular gridmarks were printed on the surface of the specimen by the same technique used for the tensile specimens.

The compression tests were carried out on a 50-ton capacity Instron Universal Testing Machine (1197).

The crosshead speeds used were 0.5 mm./min., 1.0 mm./min. and 2.0 mm./min.

After compression, the components of the strains were measured. The axial compressive strain(ε_c) and the radial strain(ε_r) were measured from the changes in the geometry of the specimens.

The average longitudinal strain(ε_L) and the circumferential strain (ε_θ) were measured from the change of the gridmarks at the maximum diameter of the bulging surface. From these measurements the logarithmic strain components were calculated as (20, 54, 55, 97, 99)

Longitudinal strain $\varepsilon_L = \log_e (b/r)$

Circumferential strain $\varepsilon_\theta = \log_e (a/r)$

Where a, and b = semi-major and minor axis of the ellipse at the maximum bulging surface.

r = radius of the original grid circle.

Axial compressive strain ε_c = loge $(^{Hi}/_{H_o})$

Radial strain ε_r = loge $(^{Di}/_{D_o})$

Where H_o and H_i = initial and final heights of specimens

D_o and D_i = initial and final diameters of specimens.

The compressed specimens were then sectioned and the sectioned planes were scanned under the Cambridge SEM 2a and SEM 600, to detect microvoids, cracks and cracked particles and photograph them in the same way as in the tensile test. Also measurements on the photographs were carried out to determine the volume fractions of the voids and cracks by the same method used in the tensile test.

CHAPTER IV

4.0 Results

The results of the measurements and calculations from the experimental work in Chapter III are presented in this Chapter.

1.0 The microstructure of steels

The chemical analysis showed that steels A and B were of low carbon and inclusion content; steel C was pure iron of very low carbon, and alloys of steel D were of very low carbon content and varying percentages of manganese and sulphur, as in table (1.a)

The data obtained from the measurements on the Quantitative Analysing Television Microscope (QTM) were :

for steels A, B and C

1. The percentage of pearlite, about 20% for steels A and B, and 2% for steel C, as in tables (2, 3 and 4)
2. The ferrite grain size, about 18 - 20 μm. for steels A and B, and 125 μm. for steel C, as in tables (2, 3 and 4) Similar values of the ferrite grain diameter were obtained from the measurements of grain sizes from photographs of the microstructure such as Figures(21a and 21b.)
3. The average interparticle spacing was in the range 8 - 15 μm. for steels A and B, in tables (2 and 3)
4. The carbide particles size-distributions were given in tables (5, 6 and 7) and the histograms in Figs. (22a, 23a and 24a) these size distributions corrected in terms of volume, were as in Figs. (22b, 23b, and 24b)

All four annealing treatments gave similar microstructures.

For the alloys of steel D

5. The size distributions of sulphides and oxides were given, as in tables (8a and 8b) respectively, and by the histograms in Figs. (25a — 33a.) and Figs. (25b — 33b) respectively.

2.0. The Tensile Test

2.1. The Strain Distributions

The components of strains ε_x, ε_r, ε_L and ε_θ were calculated from the measurements of the displacements of the specimens and the patterns of the gridmarks, for steels A, B and C. The components of strains were simplified by means of an invariant function of strain, the effective strain $\bar{\varepsilon}$ as :

$$\bar{\varepsilon} = (2^{1/2}/3)[(\varepsilon_x-\varepsilon_r)^2 + (\varepsilon_r-\varepsilon_\theta)^2 + (\varepsilon_\theta-\varepsilon_x)^2]^{1/2} \quad \text{.....Appendix II.}$$

These components of strains were given with respect of their location within the specimen, in tables (12, 13 and 14)
The variations of the components of strain ε_L and ε_θ with respect to the axial tensile strain were shown in Figs. (34 - 36)

The values of the strain at necking for steels A and B were similar and the average $\bar{\varepsilon} = 0.21$ as shown in tables (9 and 10)
The fracture strains were also similar and of the range $\bar{\varepsilon}_f = 1.25 - 1.50$
The corresponding values were high for steel C which showed more ductility compared to steels A and B. The average strain at necking was $\bar{\varepsilon} = 0.22$ for steel C, as in table (11) and the fracture strain was $\bar{\varepsilon}_f = 2.50$.

The variations of the invariant function $\bar{\varepsilon}$ with the location were plotted in Figs. (37, 38, 39) These were used to calculate the volume fraction of voids in relation to the locations of metallographic fields on scanning Electron Microscopes; hence to relate the volume fractions of voids to the strains.

2.2 Voids Formation in steels A and B

2. The volume fractions of voids fv, and carbides fc were calculated for each metallographic field from the photographs obtained from the Scanning Electron Microcopes, using the method in Appendix IV.

The values of these volume fractions, fv, fc, are given in tables (15 and 16.) The ratios of the volume fractions of voids to carbides (fv/fc) in the same fields were related to the corresponding values of the effective strain $\bar{\varepsilon}$ in Figs.(40 and 41) for steels A and B respectively.

2.3 Void Growth in steels A and B

The values of the theoretically postulated equation [18] were superimposed on Figs. (40 and 41) to give values corresponding to the beginning of voids growth.

Moreover, results that yield values of the strain at which void growth began were obtained when fields were scanned at low values of strain to examine the mechanisms of formation of cracks and voids. These results were :

in the case of carbide cracking : the sizes of the smallest particles cracked and the strains at which they cracked were shown in Figs. (42 and 43) for steels A and B respectively.

in the case of the decohesion of particle-matrix interface the sizes of the smallest particles associated with the smallest crack or void, and the strains at which they occurred were shown in Figs. (44 and 45) for steels A and B respectively.

The values of the volume fractions of voids divided by the number of the voids present in the same fields (fv/M_{av}) were related to the corresponding effective strain $\bar{\varepsilon}$ in Figs. (46 and 47) for steels A and B respectively. These figures described the beginning

and duration of void growth.

Figs. (48 and 49) show the change of the strain concentration factor $C = 1 + k (a/b)^2$, with(the growth of voids) the increase in the effective strain.

2.4. Voids Formation in steel C

Very few cracks and voids were detected on the scanned sections of specimens of steel C, as in table (17) Most of the cracks were found close to the fractured edge, Fig. (50) Many of the voids and cracks were identified as cracks at the grain boundaries.

3.0 The Notch Tensile Test

The measured values of the notch geometry were used to calculate the notch depth and the elastic stress concentration factors (k_t) using standard curves (78).

The notch strength was calculated as the maximum load divided by the cross-sectional area of the notch section. The ratio of the notch strength to the ultimate tensile strength gave the notch strength ratio (NSR). The ultimate tensile strength for steels A and B was calculated from the tensile test, while the ultimate tensile strength for the alloys of steel D was obtained from the tensile tests carried out on unnotched tensile specimens, using the Hounsfield Horizontal tensile machine, and the values were as in table (18)

The data calculated above are in tables (19 - 29)

The notch strength ratios (NSR) were related to the stress concentration factors. These relationships were given in Figs. (51— 61) as the plot of loge (NSR) against $(k_t - 1)^3$ in the expression given by equation (29). The relationships were linear.

For a particular notch root radius, the slopes of the curves in the above Figures were functions of the notch root radii, i.e. a polynomial which is dependent on the metallurgical properties of the steel. The values of this polynomial as obtained from the above figures were different for the different types of steel (as in table 30). These differences in the values obtained for this polynomial were related to the characteristics of the different alloys of steel D in terms of the ratio of Mn% to S%, in figs. (62, 63 and 64)

The notch strength ratio was also related to the notch depth, which also has an effect on the state of the stresses produced, because the variation in the notch depth changes the triaxiality. It was useful to determine when this effect on triaxiality becomes more important than the stress concentration. To show this, the notch strength ratio was plotted against the variation in the notch depth for different notch root radii; this is in Figs.(65-75)

4.0. The Compression Test

Barreling occurred in most of the compressed specimens from steels A, B and C. It seemed to be greater in the case of flat specimens compared with those specimens with cone angles. This barrelling was due to the friction between the surfaces of the specimens and the compression platens. The use of the grease lubricant was meant to reduce this friction.

Due to barrelling, the strain components calculated in tables (31, 32 and 33) , were related as follows : (14)

$$\varepsilon_c = -5/3\ \varepsilon_\theta$$

$$\varepsilon_r = 2/3\ \varepsilon_\theta$$

and from Appendix II.3., $\bar{\varepsilon} = 1.678\ \varepsilon_\theta$

From these relations the circumferential strains were plotted against the effective strains in Figs. (76, 77 and 78) to show the barreling and the effect of the cone angles on the barrelling.

Fracture was expected at around the circumference of the bulge surface, but it did not occur, because the maximum load on the Instron machine was reached before enough compression was attained. Also the different rates of compression using different crosshead speeds did not show any varying effects nor did they give external fracture. However, internal necking and localised fracture at the circumference of the bulging surface, especially with more barreling, were investigated.

Internal necking was not useful in determining the formability, and the effect of the hydrostatic stress component was ignored (14) so that the flow stresses were related to the microstructure in the same way as the tensile flow stresses. In this case, the formation and growth of the voids were affected only by the changes in the ratios of the principal strains.

The volume fractions of voids measured in relation with the strains were given in tables (31 and 32) for steels A and B respectively. The same relations were also shown in Figs. (79 and 80) for steels A and B respectively.

No voids could be detected in specimens of steel C.

CHAPTER V

Discussion

1.0 The Microstructure of Steels

1.1 Steels A and B

These two types of steels were found to be similar in microstructure. Corresponding to their carbon contents, these steels were found to contain about 20% pearlite, the remainder of the structure being ferrite. After annealing, all the pearlite had broken down to a dispersion of spheroidal carbides in ferrite. These carbide particles were, in the range 0.5 µm - 7.0 µm in diameter, as in Figs. (22a. and 23a) The carbide particles of sizes greater than 1.0 µm. diameter, constituted about 90% of the volume fraction of the second-phase as computed from the area under the curves in Figs. (22b and 23b) Generally, the carbide particles were evenly spaced; the interparticle spacings were measured at about 8 - 15 µm. The two types of steels also had uniform ferrite grains of about 20 µm. in diameter.

These steels were observed to be clean of [illegible] inclusions such as oxides, sulphide etc. The microstructure of these steels was found to be uniform enough to satisfy the assumptions made for the theoretical hypothesis, section 5.1, Chapter II.

1.2. Steel C

This steel was found to be very pure of very low carbon content, hence a low percentage of pearlite, about 2%, and the structure was all ferrite with large grains of about 150 µm - 200 µm. Some carbides were precipitated within the grains and more particularly at grain boundaries as carbide films.

1.3 Steels D

All the nine alloys were prepared from electrolytic iron. They were melted in an alumina crucible under argon. Material was taken for chemical analysis of each alloy. The chemical analysis is shown in tables (1a. and 1b) The oxygen contents in table (1b.) were found enough to precipitate type I manganese sulphide inclusions (7, 8, 35, 36, 61). With the compositions used, it was clear that most of the non-metallic inclusions should be sulphides, and were identified as type I, Figs. (84) Some of these sulphides in alloys D21, D22, D31 and D32 contained concave cavities as in Fig. (84d.) These cavities are generally caused by the contraction of the sulphides during solidification; the cavities include metallic inclusions (35, 36, 61).

The alloys with high manganese and sulphur contents, D22, D31 and D32 contained more fine sulphides of sizes less than 10 μm., as shown by the histogram in Figs. (25a - 33a). The large sulphides were mostly Oxy-sulphides. All nine alloys contained oxides as in histograms, Figs. (25b. - 33b.)

2.0 Strain Distributions

Typical micrographs for inclusion, carbide and void counts are shown in appendix V.

During the uniform deformation, the longitudinal strain on the surface was approximately equal to the axial strain in magnitude, but was larger than it is in the region of the neck.

The circumferential strain was a negative value, approximately equal to the radial strain, hence equal to half the axial strain in magnitude. But at large strains it deviated in the case of steels A and C, Figs. (34 and 36) the circumferential strains

showed deviations of opposite signs from the straight line, $\varepsilon_\theta = |\varepsilon_x/2|$. In the case of steel A the values $\varepsilon_\theta > |\varepsilon_x/2|$ while in the case of steel C $\varepsilon_\theta < |\varepsilon_x/2|$ These deviations indicated dilatation, where $\varepsilon_\theta > |\varepsilon_x/2|$ means a decrease in volume, and $\varepsilon_\theta < |\varepsilon_x/2|$ means an increase in volume.

So, such changes in the circumferential strain ε_θ close to the fracture strain produce dilatation, and since the circumferential strain itself depends on the manner of the change of the teardrop ovals therefore, it is useful to study the possible changes of these ovals. If this leads to different ways of change of ovals for different steels A, B and C then the conditions of volume constancy and dilatation can be related to microstructure.

The observed changes in the pattern of the gridmarks showed that the circle started to change into an ellipse at the yield point, and that the necking point is the end of the change of the circle into a proper ellipse, and the beginning of the change of the proper ellipse into an oval.

The construction of the negative pedal of the ellipse, Appendix III.F, gave two different shapes of ovals, depending on the eccentricity of the proper ellipse at necking. And the ovals produced by the gridmarks in the region of the neck of tensile specimens of the three steels A, B and C must follow one or the other of the patterns of these two ovals that resulted from the construction. Therefore, the explanation of the properties of the two shapes of ovals can be used to help analyse the manner of the deformation of the steels at large strain values in the necked region.

The conditions for the two shapes of ovals are :

(i) when the eccentricity of the ellipse $e > 0.5$

(ii) when the eccentricity of the ellipse $e \leqslant 0.5$

The eccentricity of the ellipse is $e = [\,1 - (b/a)^2\,]^{\frac{1}{2}}$, and from the construction of the negative pedals of the circle, the major axis of the ellipse is equal to the diameter of the circle; therefore,

$$a = r$$

and the eccentricity of the ellipse becomes

$$e = [1 - (b/r)^2\,]^{1/2}$$

from the strain calculations, $(b/r) = \exp.(\varepsilon_\theta)_n$ where $(\varepsilon_\theta)_n$ = circumferential strain at necking.

The above conditions become :

(1) $[1 - \exp.(2\varepsilon_\theta)_n]^{1/2} > 0.5$

(2) $[1 - \exp.(2\varepsilon_\theta)_n]^{1/2} \leqslant 0.5$

From the calculations of the average strain components at necking, tables (9, 10 and 11) it can be seen that steel A satisfies condition (i) while steel C satisfies condition (ii).

So, to understand how these two steels are expected to behave close to fracture, it is necessary to interpret the meaning of the two shapes of the ovals.

Shape (1) when the eccentricity $e > 0.5$

In this shape, the oval has a node N and two cusps C and C' The zone (area) bounded by NCC' did not appear on the actual grid-marks on the surface of any of the steels A, B and C. And for the actual oval on the surface of the necked specimens of steel A,

to be of this shape of oval, is only possible if material corresponding to the area of this zone NCC' is assumed to be squeezed from the outer surface of the specimen into the bulk. That is, atoms of the material escaping from the outer surface into the inner bulk of the specimen during deformation. To say that the deformation of the specimens of steel A were under decreasing volume with negative dilatation and with Poisson's ratio greater than 0.5 is not possible.

But this can be explained as metal being extruded from the neck towards shank due to a change in the radius of curvature of the neck. The change in the radius of curvature can be discussed as to its effect on the distribution of plastic strain and hydrostatic tensile stress, which was given by the equation, (20,4)

$$(\sigma_{hyd.}/Y) = 1/3 + \log_e\left(1 + \frac{d/2}{2R}\right) - 2\log_e\left(1 + \frac{x^2}{d/2(d/2 + R)}\right) \ldots\ldots \quad (31)$$

where

Y = yield stress

R = minimum longitudinal radius of curvature

d = diameter of narrowest portion of the neck

x = distance away from the plane of the neck

The radius of curvature in the neck for steel A is smaller compared with steels B and C, and the situations arising from such changes of radius of curvature can be compared with those arising due to the presence of notches, where the above equation can be compared with equations (25). Thus in the case of steel A, where the radius of curvature decreases very much, the voids/cracks are expected to grow (propagate) fast, then link together rapidly, hence to cause fracture.

Shape (2) when the eccentricity $e \leq 0.5$

This gives an oval only without node or cusps. The actual oval on the surface of the specimens can be of this type. To prove this it is useful to describe the changes occurring on the gridmarks during deformation.

(1) The area included within the dark marking of the grid circle increases with deformation.

(2) Since, of all the closed curves of equal circumferences the circle encloses the greatest area (76) therefore for the ellipse and oval to enclose areas equal or greater than the original grid circle, their circumferences must be greater than that of the circle. This means that the circumferences of the ellipse and oval increased with deformation. Thus the gridmarks expanded; in doing so the dark markings became less dark, less sharp and eventually they grow fainter with increased deformation.

(3) Figs (81.a.) and (b.) of the expanding gridmarks for steels A and C showed that this was the case. The figures showed that the gridmarks became more faint in steel C compared to steel A where the gridmarking of the teardrop oval in steel C nearly disappeared, Fig. (81.b.) i.e. the markings expanded more in this area. This increased expansion caused material movement from the bulk on to the outer surface of the specimen, contrary to the first case above. This reverse movement of material means that the deformation of steel C was under increasing volume, i.e. positive dilatation with Poisson's ratio of less than 0.5. This type of dilatation is possible.

This discussion shows that the shape of the ellipse at necking indicates the extent of dilatation which the specimens are expected

to experience when pulled to fracture. This can also describe the increase of Poisson's ratio to $\nu = 0.5$ and its decrease to $\nu < 0.5$ as :

(1) $\nu < 0.5$ dilation

(2) $\nu = 0.5$ constant volume deformation

Where the eccentricity of the ellipse is replaced by Poisson's ratio, therefore, Poisson's ratio can be expressed in terms of the circumferential strain ε_θ as;

$$\nu = [1 - \exp.(2\varepsilon_\theta)_n]^{1/2} \quad \ldots\ldots \quad (32)$$

This highlights the importance of the necking phenomena. At necking, the effective strain is equal to the strain-hardening index;

$$\bar{\varepsilon} = n$$

The effective strain depends on the circumferential strain; thus the Poisson's ratio is related to the strain-hardening index.

The extent of dilatation in steels A, B and C is shown in Fig. (81.c) In this figure the horizontal error bars are a measure of the experimental errors. These errors resulted from the experimental measurements of the average strains, due to some experimental techniques, such as :

(1) The printing technique :-

when printing the circles on the outer surface of the round specimens, the holder in Fig. (13) was moved manually to roll the specimen on the stencil. The pressure applied to the specimen was not constant, so the friction between the specimen and stencil was variable; the stencil was stretched sometimes. This resulted in some circles of slightly varying diameters.

(2) Measurement of the deformed gridmarks :-

(a) The dark marking lines spread and became faint during deformation. This made it difficult to focus exactly on the gridmarks because they were not sharp, and resulted in errors in the measurements.

(b) Also the circles, ellipses and ovals were measured on the curved surfaces of the round specimens using a travelling microscope which measured chords. These cords were corrected for the curvature of the specimens to obtain the lengths of the actual arcs.

(c) The measurements were also corrected for the curvature of the profile of the neck.

All the above measurements were corrected by graphical methods.

Average values were taken for four or five measurements for each location in order to minimise the experimental errors.

3.0 Voids Formation in steels A and B

3.1. The beginning of the Growth Process

Decohesion was observed to be the controlling mode of voids nucleation in these spheroidised steels A and B. In most cases voids appeared in association with the carbide particles; thus the ratio of the volume fractions of voids to that of the volume fractions of carbides, (f_v/f_c), - related to the strain - was a good measure of the void growth. These representations were given in Figs.(40 and 41)

The value of the strains obtained from the theoretical equation (18) were superimposed on the experimental results in

Figs. (40 and 41) The first intersections which these theoretical curves make with the experimental points were taken as the average values at the beginning of the void growth process. i.e. (fvo/fc), as the volume fraction of voids at the beginning of growth to the volume fraction of carbides, $\bar{\varepsilon}_o$, as the effective strain at which growth begins. These values of the strain were $\bar{\varepsilon}_o = 0.5 — 0.6$ for both steel A and B. These theoretical strain values were compared with the corresponding experimental values.

The method to evaluate the experimental values of the strain at which growth begins in steels A and B was to consider Figs. (42 and 43) in the case of the formation of voids by particle cracking and Figs. (44 and 45) in the case of the formation of voids by the decohesion of particle-matrix interface. In these figures, the range of strains at which the cracks and/or voids are in association with the mean size of the particles were taken as the average strains at which growth begins. The mean size of carbide particles for both steels A and B was $d = 1.0\,\mu m$. from Figs. (22a. and 23a.) and the average strains were as follows:-

(1) steel A $\bar{\varepsilon}_o = 0.45$ —— 0.60 for carbide cracking
and $\bar{\varepsilon}_o = 0.55$ —— 0.60 for decohesion

(2) steel B $\bar{\varepsilon}_o = 0.50$ —— 0.60 for carbide cracking
and $\bar{\varepsilon}_o = 0.55$ —— 0.60 for decohesion

An alternative approach to evaluate this strain at which void growth starts was to relate the values of the volume fractions of voids divided by the number of voids in the same field (fv/Mav) to the corresponding values of the effective strains as in

Figs. (46 and 47). This relationship described the whole processes of fracture nucleation, growth and coalescence.

At the start of voids formation, these voids were small in volume, hence the ratio ($fv/_{Mav}$) was small, and was to increase gradually, i.e. increase in volume due to the number of freshly nucleated voids.

The beginning of the stage of voids growth was recognised by the fact that the already formed voids began to expand and increase in volume irrespective of the increase in their number. This resulted in a continuous increase in the volume fractions of voids fv, hence a rapid increase in the ratio ($fv/_{Mav}$). This change in the rate of the increase of the ratio ($fv/_{Mav}$) marked the end of the voids and cracks nucleation process and the start of void growth.

Sharp increases in the ratio ($fv/_{Mav}$) were observed at strains in the range of :

$\bar{\varepsilon}_o = 0.50$ —— $\bar{\varepsilon}_o = 0.60$ in Fig. (46) for steel A and at $\bar{\varepsilon}_o = 0.60$ in Fig. (47) for steel B.

It can be seen from the above that the theoretical strain values at the beginning of the growth process agreed with the strains obtained from experiments for the same stage. This agreement between the theoretical calculation and the experimental measurements was because the steels were heat-treated to produce second-phase particles of regular shapes and uniform distributions.

These strain values, $\bar{\varepsilon}_o$ obtained were high enough not to be ignored when formulating the failure strains. These values are

considerably high compared with the values obtained or suggested earlier (43, 57, 64, 95). In the early work, void growth was believed to begin at zero volume fractions of voids, which would have yielded values of $\overline{\varepsilon}_o = 0.4$, for steel A, and $\overline{\varepsilon}_o = 0.3$ for steel B, from Figs. (40 and 41)

The theoretical analysis supported by the experimental findings in this study showed that cracks when nucleated do not develop immediately, but multiply by nucleating fresh cracks, then they link together to form large cracks of definite initial volumes before they start to grow. In other words, the crack nucleation process begins at low strains and continues for part of the life-time of deformation, during which the increase in the volume of voids is due to more nucleation and not due to the growth of few nucleated cracks. The nucleation process continues and not until high strain (60% strain in steels A and B) does the effective void growth begin.

The theoretical analysis may not quite agree with experimental results measured on steels of non-uniform microstructure. In this case the assumptions made for the theoretical analysis are not valid for the following reasons:

(1) The disturbances in the stresses produced by one particle affect the matrix around the neighbouring particles. This changes the stress concentrations.

(2) Void nucleation depends on the shapes, sizes and the distributions of inclusions and second-phases.

(3) The nucleation process also changes for irregular shapes of rigid particles, where cracks form by the cracking or shearing of these particles. This differs from void nucleation by decohesion

because voids form by decohesion when soft matrix is unable to flow around the rigid particle whilst maintaining contact at the same time. This happens when the strength of the particle-matrix interface is insufficient to withstand the high local stress concentrations. But cracking of particles is expected earlier than that.

(4) When particles crack, the fragmented parts must become separated by a considerable distance before any steel from the matrix can flow around the fragmented parts. Therefore, there is instantaneous growth of voids immediately following their nucleation. This also increases the rate of growth, hence, decreases the total failure strain.

So in the case of steels with non-uniform structures, both the strain at the beginning of void growth and the total failure strain are lower compared with steels of uniform structures, at the same level of volume fractions of the second-phases, and inclusions.

3.2 Void Growth in steels A and B

The voids were found to begin to grow at strains $\bar{\varepsilon}_o = 0.50 - 0.60$ approximately for steels A and B as calculated from the above experimental results. These voids continue to grow into large critical sizes which cause fracture.

Theories of void growth (40, 44, 57) showed that at the early stage of the process of growth, the strain concentration factor is large, and that its value controls the process. It was also found to decrease to unity with the void growth, therefore, at an advanced state of void growth, the volume of voids increases exponentially with the increase in strain. To get a good

description of the process of void growth the variations in the strain concentration factor were calculated. The relationship between the strain concentration factor and strain in Figs. (48 & 49) showed that this factor dropped very sharply to unity.

Figs. (40 and 41) showed the general picture of the growth of voids with the increase in the strain. They showed critical values of the ratios of the volume fractions of voids to the volume fractions of carbides $(fv/fc)_{cri}$ at fracture.

This critical ratio was $(fv/fc)_{cri} = 1.90$ for steel A, and $(fv/fc)_{cri} = 2.00$ for steel B. This critical ratio, $(fv/fc)_{cri}$, at fracture seems to be dependent on the volume fractions of the carbides fc. Both steels gave a ratio of (fv/fc) = 1.0 at about 100% strain.

3.3 Voids Formation and Growth in steel C

Less voids were observed in this steel compared to steels A and B. This was due to the lack of nucleation sites, because there were not enough carbides or inclusions. However, the volume fractions of voids in this steel increased rapidly close to fracture strain, Fig. (50) and this increase in volume of voids is believed to have caused dilatation.

4.0 The Effect of MnS inclusions on the Fracture Behaviour of steels D

These steels were found to contain varying amounts of Type I manganese sulphide inclusions. ~~[Type I is harder than Type III, due to the presence of oxygen, while the matrix surrounding Type I is softer than the matrix surrounding Type III due to less alloying elements (61), thus]~~ Type I Mn -inclusions are of low relative plasticity compared with the matrix surrounding them, hence cracks and voids are expected to nucleate in the vicinity

of such inclusions during deformation of the notched specimens of steels D, Figs. (84) Eventually these voids link together with the progress of deformation.

It was observed that the ratio ($^{Mn\%}/_{S\%}$) in these steels affected the joining-up of nucleated cracks. In alloys of low sulphur content, D10, D20, the voids were linked by cusps of fractured matrix, Fig.(84a). In alloys of high sulphur content, D12, D22, there were several small voids, nucleated around very small inclusions as a result of the very high local strains required to separate the intervening matrix, Fig. (84_b)

Alloys of high Mn content, D30, D31, D32 contained large numbers of sulphide inclusions. In these alloys, the features of the fracture surface appeared to be different; the extent of the voids around the inclusions decreased, also the number of secondary voids decreased. The fracture surface of most of the specimens of alloy D30 appeared to become flatter, and cleavage fracture was detected.Fig.(84c) In steel D31, D32 the fracture surface was almost wholly covered by sulphide inclusions which were delineated by fine cusps of the deformed matrix, Fig. (84_d); this decreased the amount of steel which was to be ruptured to achieve void coalescence, hence decreased the strain necessary to produce fracture.

For the alloys of low sulphur content D10, D20, the load at fracture was less than the maximum load, where the load decreased gradually from the maximum to a lower load at fracture. For the alloys D12, D22, of high S-content (= 0.2%) the load at fracture was approximately equal to the maximum i.e. no 'load drop'.

5.0 The Effect of Notches on Fracture :

Tables (19 - 29) show data obtained from the deformed notch tensile tests, for specimens of steels A, B and D, with notches of varying root radii and depths.

To analyse the effect of notches on fracture, it is interesting to examine its effects on the notched specimens of steel A and B and then compare them with the results of the tensile test. The direct effect of the introduction of notches, is the change in the state of stress, where the notch increases the resistance to flow and decreases the ratio of the shear stress to the tensile stress. (27) Thus the volume fraction of voids at the beginning of the process of growth is less than the value given by equation (18) section 5.I, Chapter II, in the case of notched specimens compared with unnotched specimens. This means that the introduction of notches, affects the process of cracks/voids nucleation, it advances the occurrence of nucleation, speeds the process, and shortens its duration. The multiplication of cracks is checked, and their growth and linking are speeded. This effect is optimised when it causes a crack to start at the root of the notch and propagate inwards, but this depends on the sharpness of the notch, its root radius.

To further investigate this effect, it is necessary to estimate the sharpness and the root radius of the notches that can propagate such cracks in the steels A and B and also in steels D. The examination of the feature of the fracture surfaces of these steels helped in this investigation.

All the specimens of steels A, B and D showed that the fracture is ductile except for partial cleavage in some of the

specimens of steels A, B, D30, D31 and D32 (examples are specimens A5, A7, B4, D306, D307, D313, D316, D327, D328 and D329) an example of the ductile fracture surface is in Fig.(83)

The fracture, in general, was a cup and cone type. For the specimens of the notch root radii, Γ= 100 mm. and Γ= 0.26mm. The fracture was a combination of normal rupture and shear, while the specimens with the notch root radii, Γ = 0.18 mm. and Γ = 0.16 mm., generally showed normal rupture.

This showed that the notches of Γ = 0.18 and Γ = 0.16 mm. produced high elastic stress concentration factors of about K_t = 4.0 and had high local strain concentrations at the roots. And for most specimens these strain concentrations were high enough to accelerate the nucleation and growth of cracks and start a large crack at the root of the notch, which propagates inwards.

The data in tables (19 - 29) were presented in Figs.(51 - 61) to relate (NSR) to the elastic stress concentration factors and notches roots radii. In these figures the slope A (Γ) varied for the different steels (i.e. different steels with different microstructure). This variation was more clear for the small notch root radii of Γ = 0.18 mm. and Γ = 0.16 mm. Therefore the function A (Γ) - believed to be a polynomial of the third degree in r - is dependent on the notch root radius and the microstructure of the steel. This dependency was examined from the relationships in Figs. (62, 63 and 64)

In these figures(62, 63 and 64) the polynomial A (Γ) was related to the ratio ($^{Mn\%}/_{S\%}$) for steels D, for different notch root radii. As expected the polynomial A (Γ) showed more variation with the variation of the ratio ($^{Mn\%}/_{S\%}$) in the case of the small notch root radius, Γ= 0.16 mm. as in Fig.(64).

The coefficients of the polynomial A (r) were evaluated from the experimental values in Figs. (51 - 61). These coefficients are given in table (30) for the steels A, B and D; they are different for the different steels. The influence of these different steels on the polynomial A (r) and its coefficients is easily studied in the case of notches of small root radii; thus the theory of sharp notches can be applied to verify this influence.

In this theory, the elastic stress concentration factors of sharp notches (i.e. of root radii $r \geq 0$), were determined by Neuber's model from equations based on continuum mechanics, provided the actual root radius of the notch, r, is replaced by, r'. This was given by the equation:(71, 105)

$$r' = r + [(2\pi - w)/(\pi - w)]\,\eta$$

where w = included angle of the notch

η = assumed to be the material constant

Therefore, according to the above equation, the polynomial A (r) gives values for the material constant only at root radius, $r = o$. This is calculated from the coefficients of the polynomial as :

$$A(r) = a_o + a_1 r + a_2 r^2 + a_3 r^3$$

and for $r = o$, $A(o) = a_o$: this gives the material constant.

The values of a_o for different steels are given in table (30.) These values of a_o vary for the different steels; hence show that there is a dependency of the polynomial A (r) on the metallurgical properties of the steels. But the values of A_o are very small compared to a_2, thus the dependency of A (r) on the square of the notch root radius overwhelms its dependency on the properties of the material.

Figs. (65 - 75) related the notch strength ratios to the notch depths. These figures showed little variation of the notch strength ratio, NSR, with varying notch depths. This may be due to the fact that the differences in the notch geometries did not produce wide variations in the notch depth, or it can be that triaxiality had less influence on fracture compared with high local stress and strain concentrations.

In conclusion, it can be said that sharp notches of root radii $r \leq 0.18$ mm. in general, showed brittle behaviour for steels A, B and D, where it is believed that cracks propagated from the notch root. For notches of root radii $r \geq 0.26$ mm. the fractured specimens of steels A, B and D showed shear ductile fracture.

6.0 The Compression Test

The cone angles showed little improvement in the barrelling of the compressed specimens. Also when compressing specimens with diameter-height ratios $(^{Do}/Ho) \leq 0.3$, more buckling occurred with cone angles compared to the flat ends.

This was believed to occur because impurities or discontinuities on the inclined surface produced more variations in friction and non-uniform plastic flow than the flat horizontal surfaces. This affected the state of the stress.

On the other hand, the use of lubricant improved the compression. It minimised barreling and very much reduced buckling, even with specimens of $(^{Do}/Ho) \leq 0.3$ and inclined end surfaces. This was because the lubricant reduced the coefficients of friction μ ; and when $\mu \leq \tan\phi$ (ϕ = cone angle), the resultant stress in the surface of the two cones was to be parallel to the direction of compression.

This was to produce a pure axial compressive stress in the specimen.

Voids first appeared at higher nucleation strains compared to the tensile test, $\bar{\varepsilon}_o = 0.65$ —— 0.70; and continued to increase with strain but at a lower rate than in the case of the tensile tests : as seen by figs. (79 and 80) In general, the more the barreling, the more the volume fractions of voids.

CHAPTER VI

Conclusions

Some of the proposed theories of ductile failure were reviewed; it was found that during deformation, cracks nucleate, and that the growth of these cracks and their linking together produces failure. The growth of these cracks was investigated and it was found to be dependent on the microstructure, i.e. second-phase, inclusions, etc., and the state of stresses and strains during deformation. Examining the dependency of the crack/void growth process on the microstructure was the main objective of this study. The relationship between microstructure, growth of voids and the strain was studied, formulated, then applied to experimental results from different low carbon steels.

A theoretical analysis of the critical stage at which growth begins was attempted, to bridge the gap between nucleation and growth processes. This helped in estimating the average values of the strain at which voids nucleated around rigid particles begin to grow. The estimated values agreed with those obtained from experiments. They were considerable and higher than the values obtained or estimated earlier.

The early stage of growth of voids was also examined; the voids/cracks were believed to undergo major changes in their shapes before they increase much in volume. This caused a dilatational growth in the vicinity of the expanding cracks/voids, and was accounted for by a strain concentration factor. This factor was found to be large at the early stage of growth but decreased with the progress of growth. The rate of decrease of this factor with respect to the increasing strain was obtained

by applying the equations of growth to the experimental results. This gave a measure of how fast the shape of voids changes during their growth.

To complete the process of ductile fracture, experimental values for the failure strain were obtained for three different steels A, B and C.

The observations on the strain distributions within fractured specimens were extended to explain dilatation. Dilatation occurs close to fracture, and since fracture is a localised phenomenon, the manner of growth of voids in the small region of the fractured edge is important, and it is the growth of voids in this region which causes dilatation.

Dilatation means that Poisson's ratio is less than 0.5, so an attempt was made to relate dilatation; hence Poisson's ratio to the transverse circumferential strain at necking. This was also a relation of Poisson's ratio to the strain-hardening index.

High local stress concentration due to rigid particles and barriers caused the nucleation of cracks in the tensile tests; these stress concentrations were affected by the introduction of notches, hence affected the nucleation and growth of cracks and voids. The extent of this effect of the stress concentrations and triaxiality on the propagation of cracks and on fracture was investigated by using notches of varying depths and root radii.

In the case of sharp notches of small root radii, $\rho = 0.18$ mm. and $\rho = 0.16$ mm. there were very high strain gradients at the roots of the notches; the strains at points a little below the roots of the notches were much smaller than the surface strains. And fracture, in these notches, began at the high local strains at

the roots of the notches; whereas in specimens with notches of large root radii, Γ = 1.0 mm. and Γ = 0.26 mm., the ductile fracture was by shearing of the edges. The small strain concentrations that prevailed at the root of these notches were not high enough to propagate cracks at the roots of notches for such ductile steels.

The results of the notch tensile tests were governed by two phenomena :

(1) The nucleation of cracks around inclusions and their linking together to form a large crack.

(2) The propagation of this large crack to separate the specimen; this propagation was greatly affected by the notch root radius and slightly affected by the metallurgical properties of the steels, where there were partial cleavage areas shown on most of the specimens of steels A, B, D30, D31 and D32, of the relatively high inclusion concentrations. Strain distributions different from those in the tensile test were obtained within the compressed specimens. This resulted in slightly different ratios of the principal strains for different states of barreling.

CHAPTER VII

Recommendations for Further Work

(1) Voids growth limits the ductility of the steel, and it would be helpful to further explore the processes of crack/void nucleation and growth. The proposed theoretical analysis for the beginning growth can be extended into a more general treatment considering the effects of all regular and irregular shapes of particles of non-uniform distributions and of varying hardness. This is to be verified on a wider range of steels with more variation in their chemical compositions, including dirty steels of high concentrations of non-metallic inclusions. Such steels can provide a wide range of values for the volume fractions of second-phases, inclusions, which enables a relationship to be established between the critical ratios of volume fraction of voids to volume fractions of the second-phases $(fv/fc)_{cri}$, and the volume fractions of second-phases (fc). Such a relationship established can be used to evaluate the volume fractions of voids at fracture, provided the microstructure is known.

(2) To have a more detailed interpretation of the physical significance of the polynomial A (Γ) and its dependence on the metallurgical properties of the steels, notches of smaller root radii, i.e. of $\Gamma = 0.1$ mm. or even less are to be used if possible; because for such small values of Γ, the terms containing Γ in the polynomial are minimised, and the contribution of the term dependent on the characteristics of the material is magnified.

(3) The axial compression test is to be carried out on a machine of a capacity larger than 50 tons for these types of steels.

This would enable the specimens to be compressed to fracture.

Also the sizes of the specimens used can be changed. Round bars of larger diameters allow for the design of specimens of greater height within the ratio of height to diameter (Ho/Do), that prevents buckling. This allows for more deformation, which gives chance for the formation of more voids due to the large plastic flow of the material.

Chapter VIII

8.0. Figures and Tables

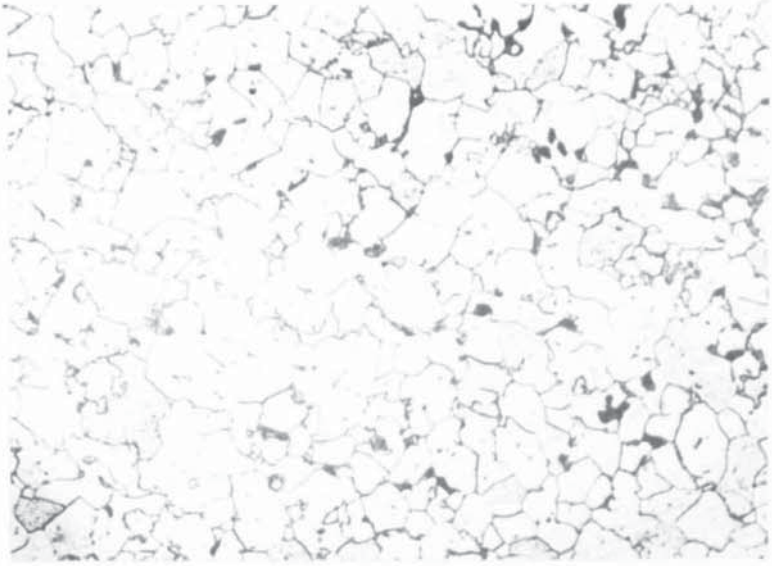

FIG.21.a. Steel B, etched in 2% Nital, Magnification 200X

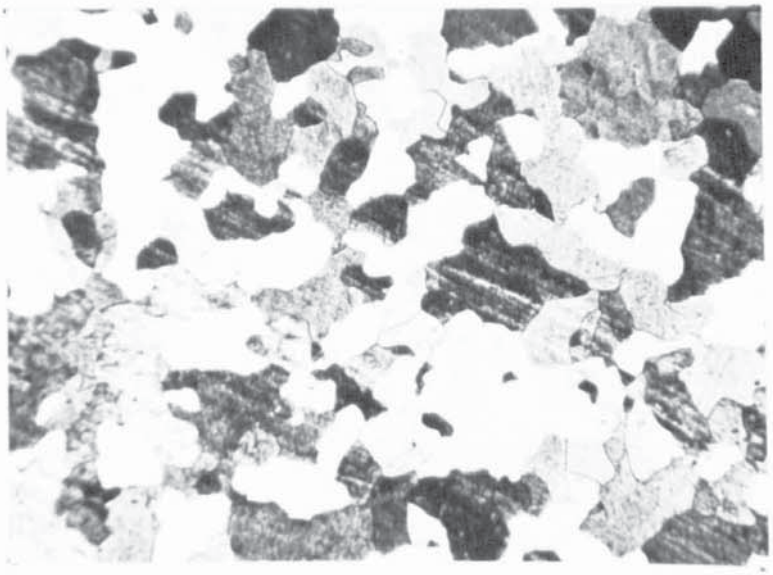

FIG.21.b. Steel C, etched in 2% Nital, Magnification 50X

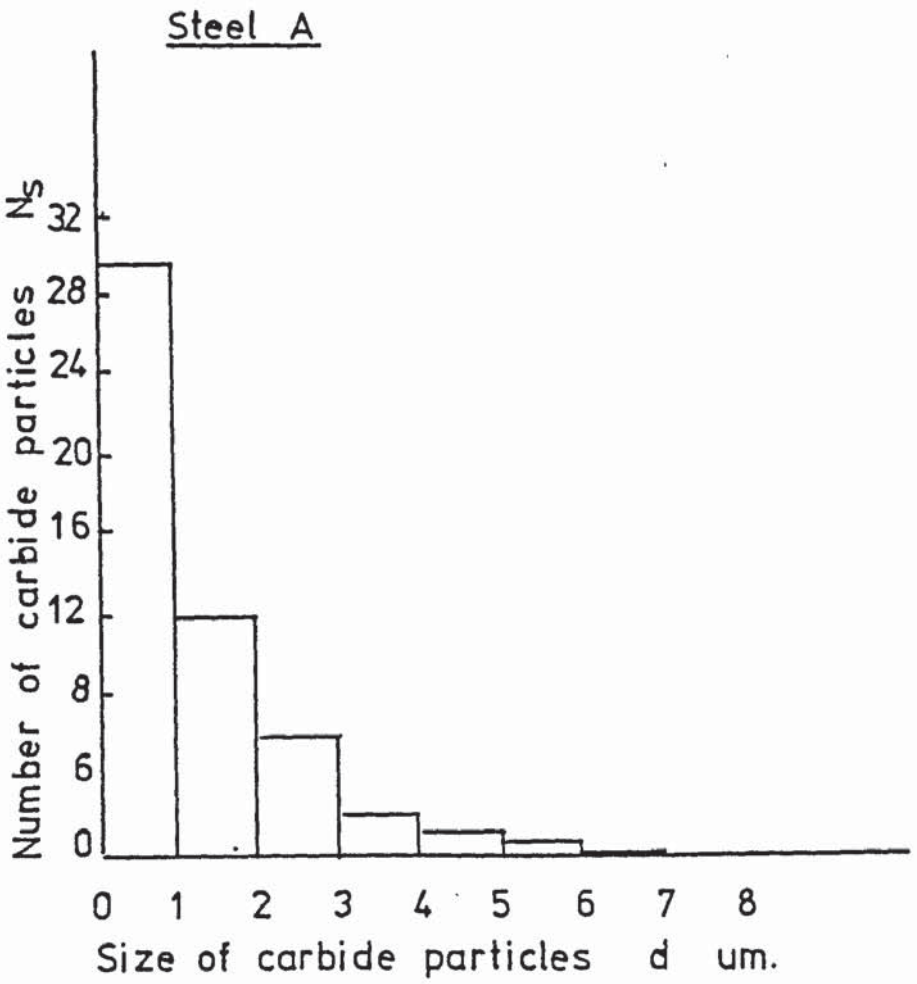

FIG·22·a·

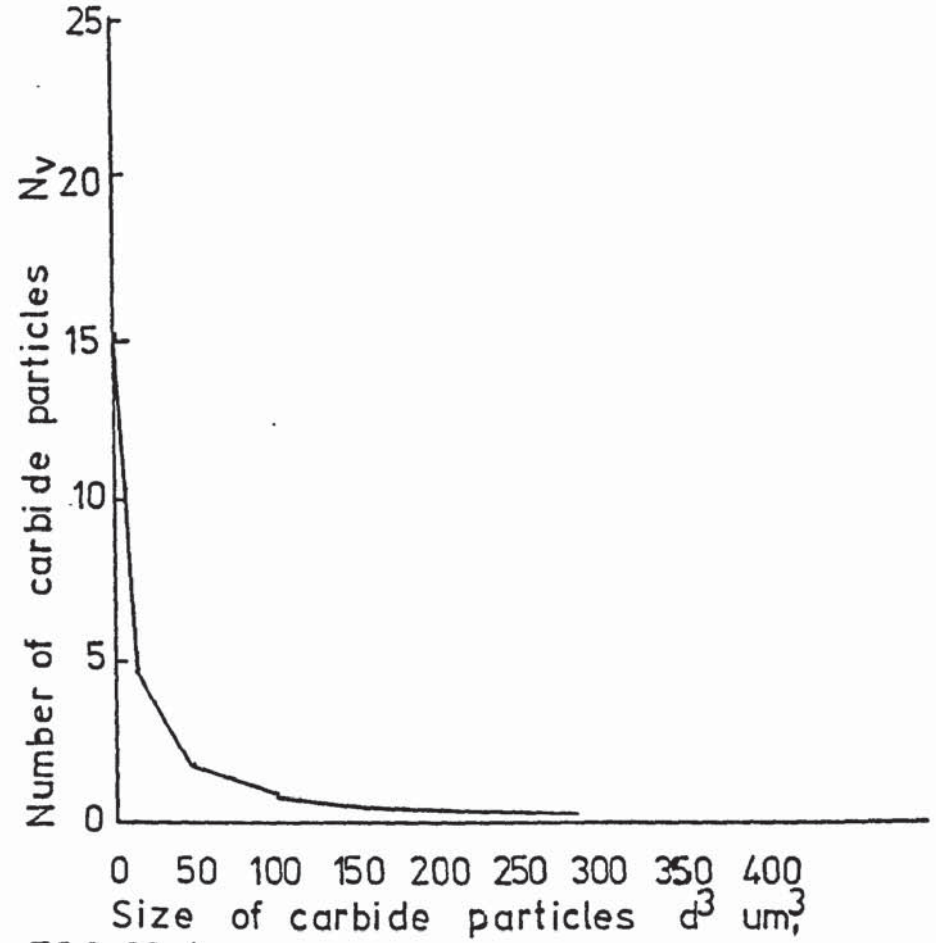

FIG·22·b·

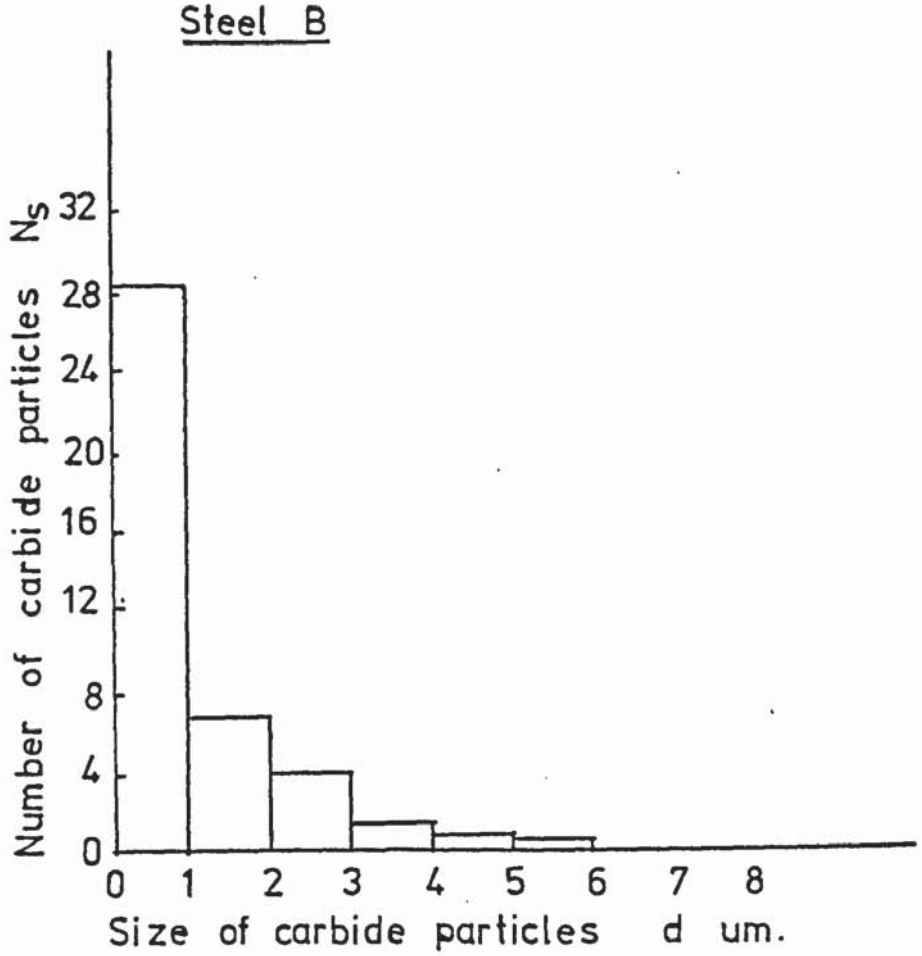

FIG. 23.a.

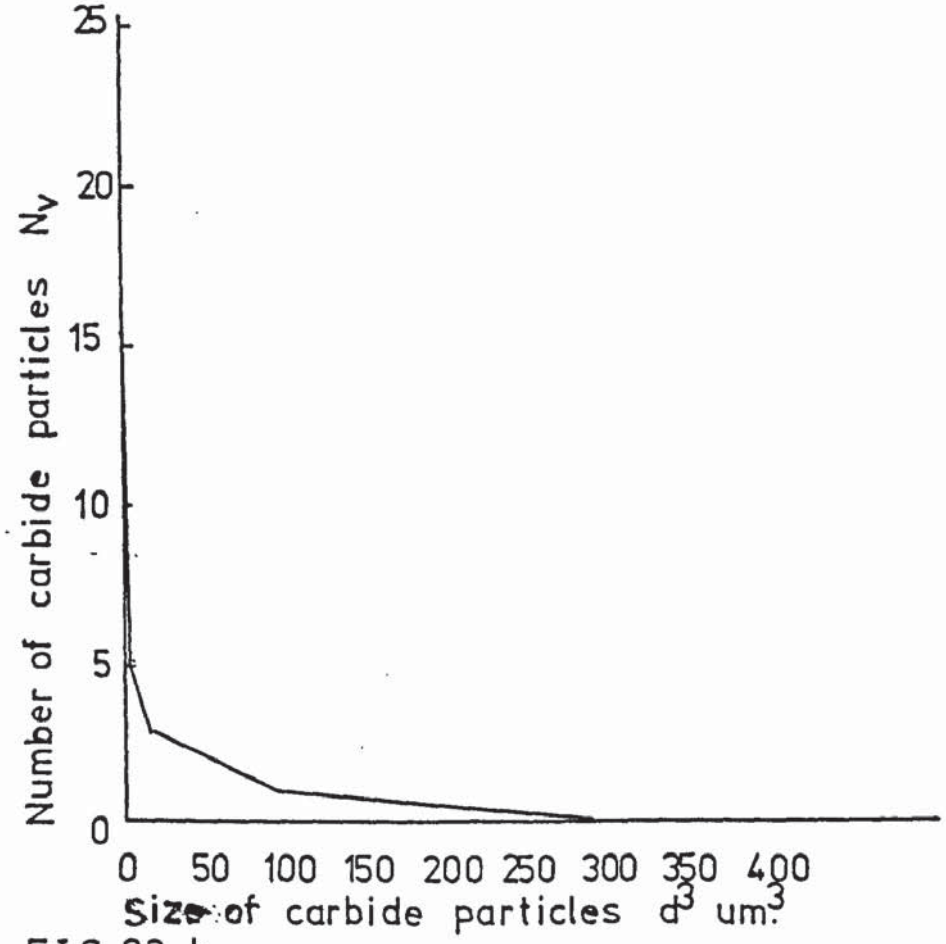

FIG. 23.b.

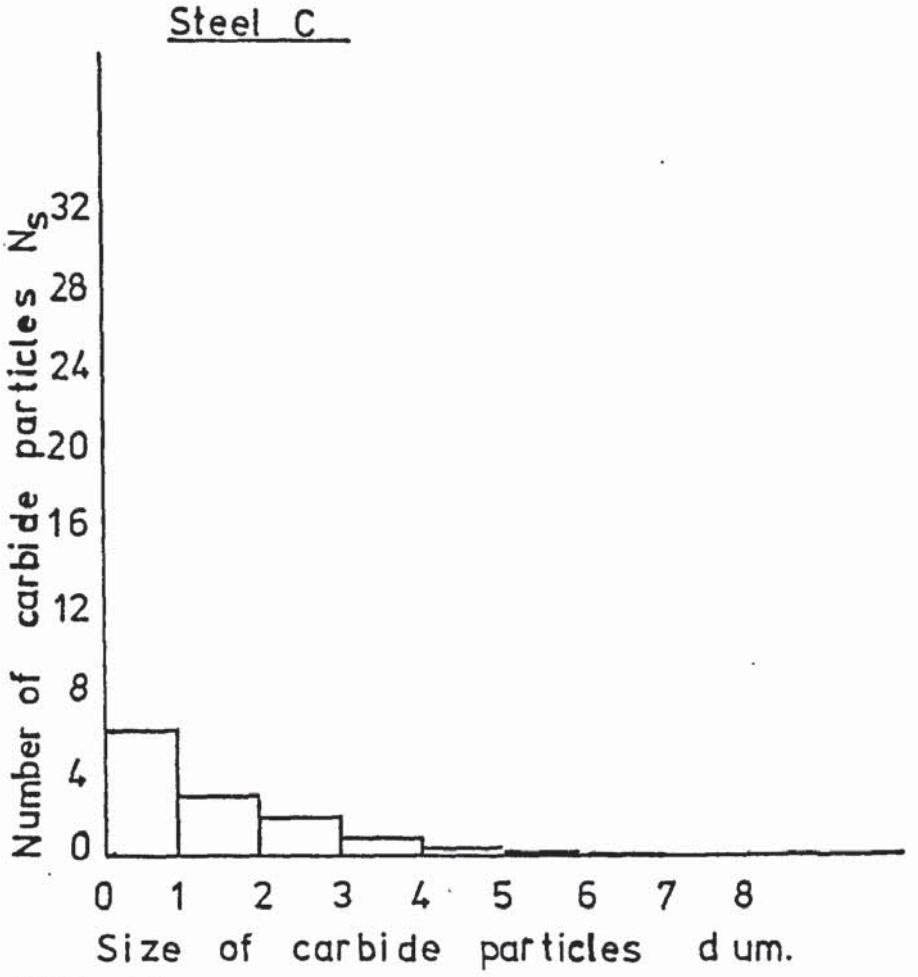

FIG. 24.a.

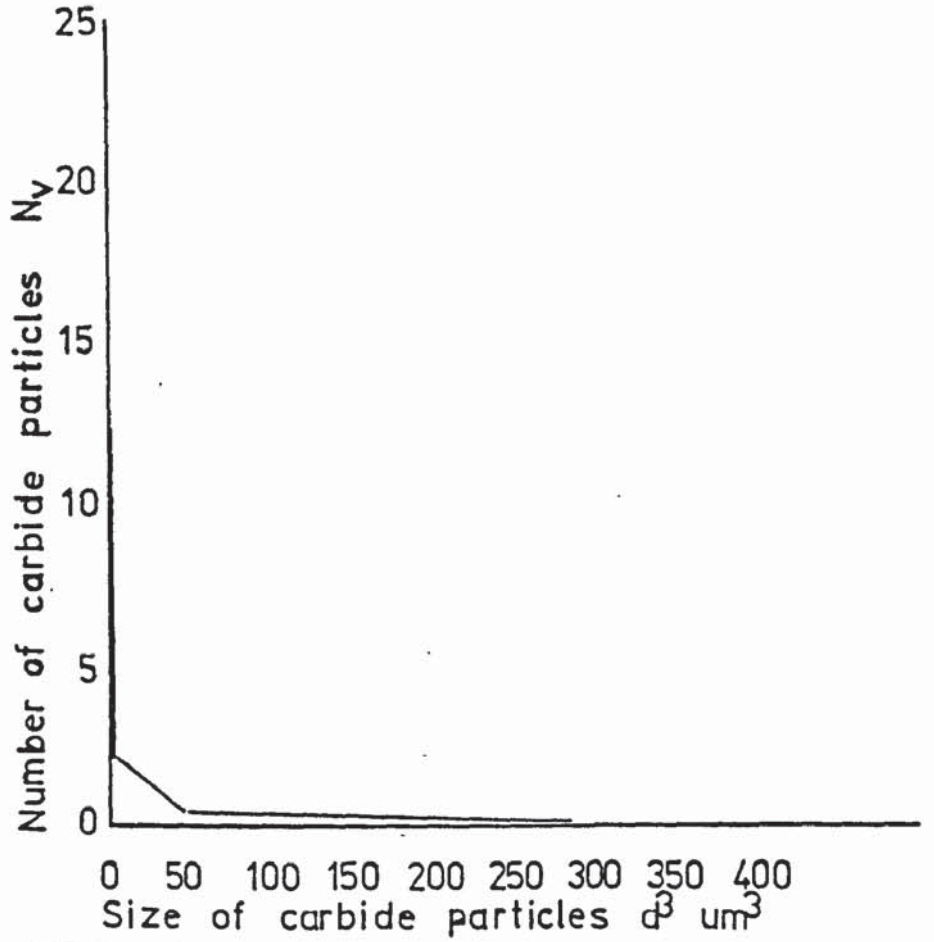

FIG. 24.b.

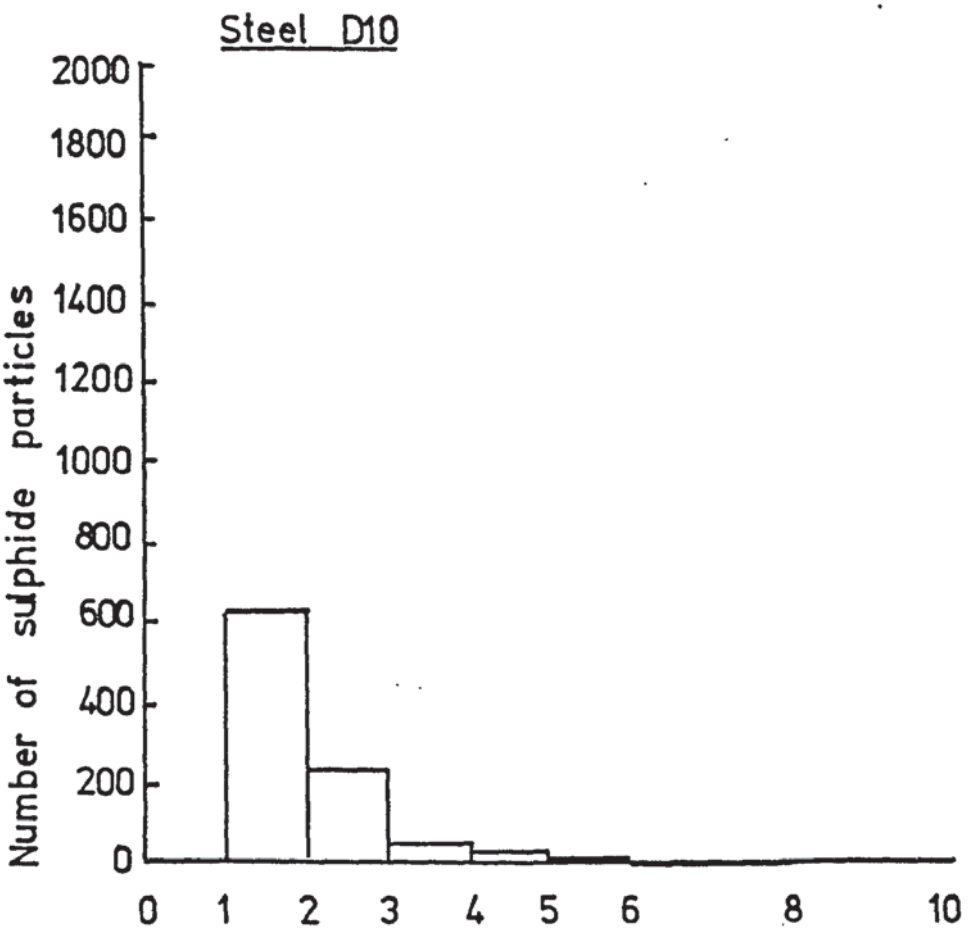

FIG·25·a.

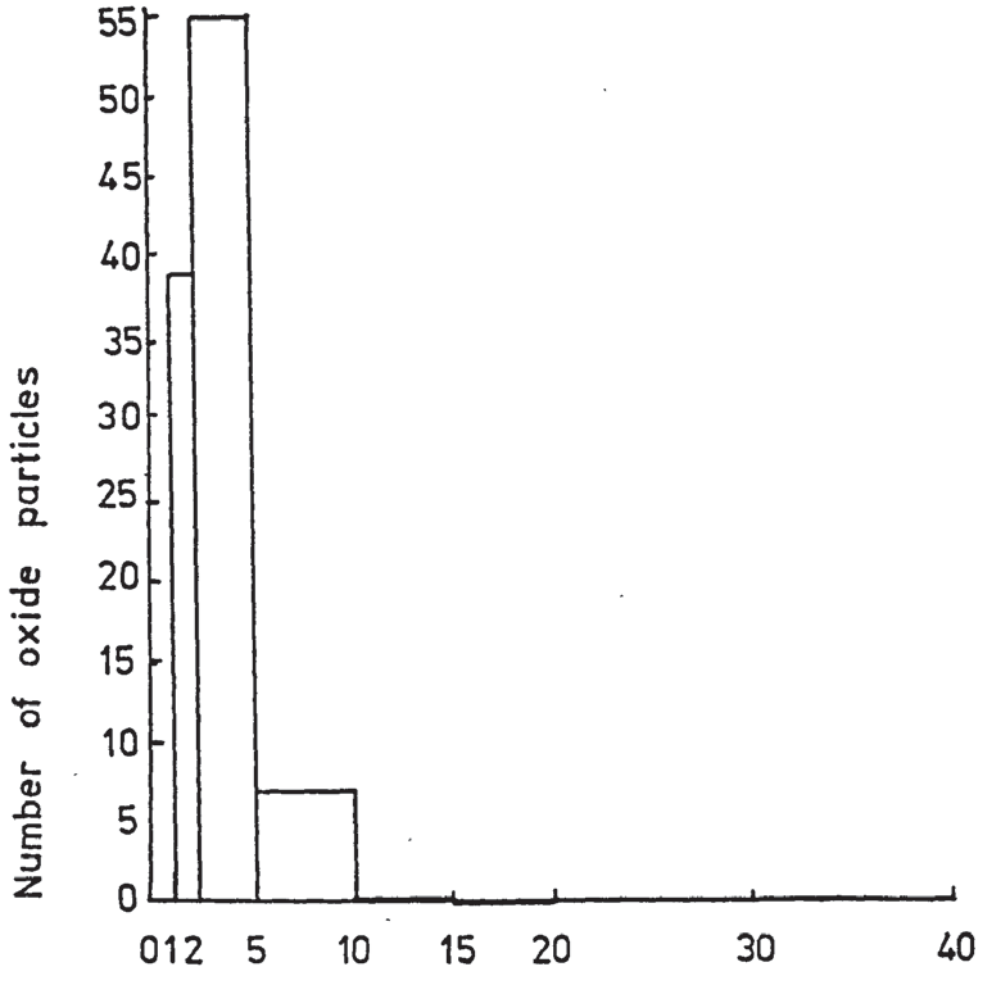

FIG·25·b.

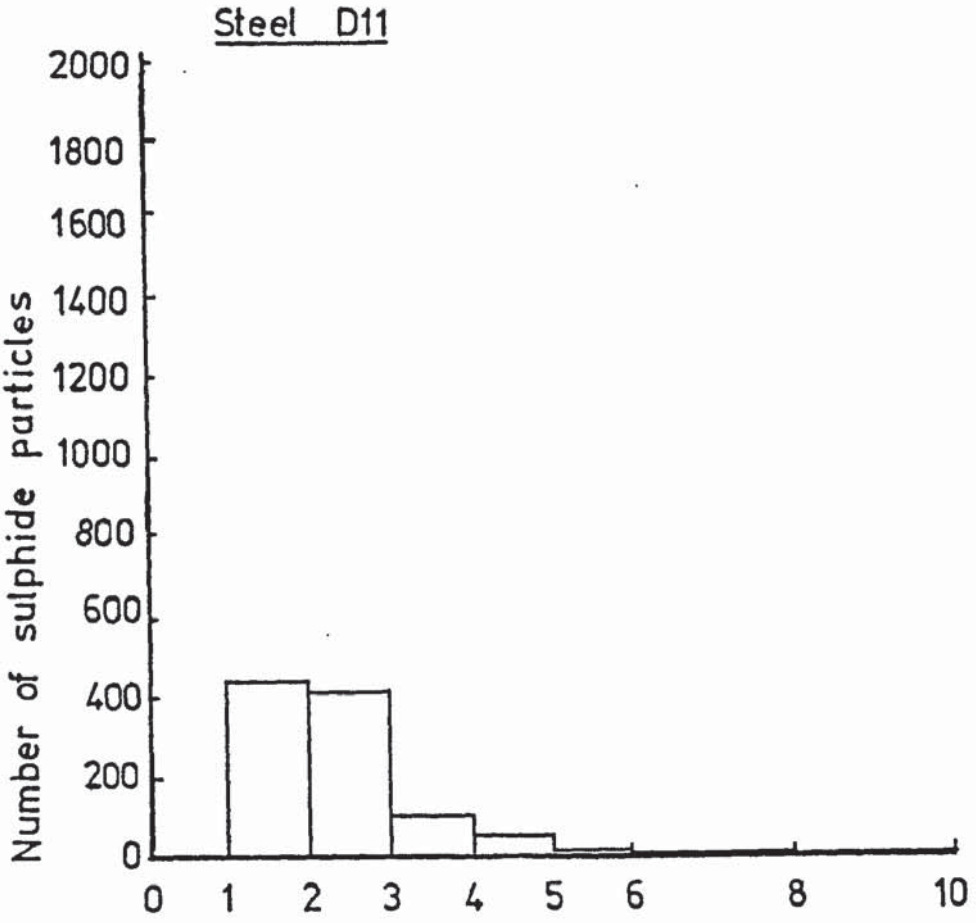

FIG.26.a.

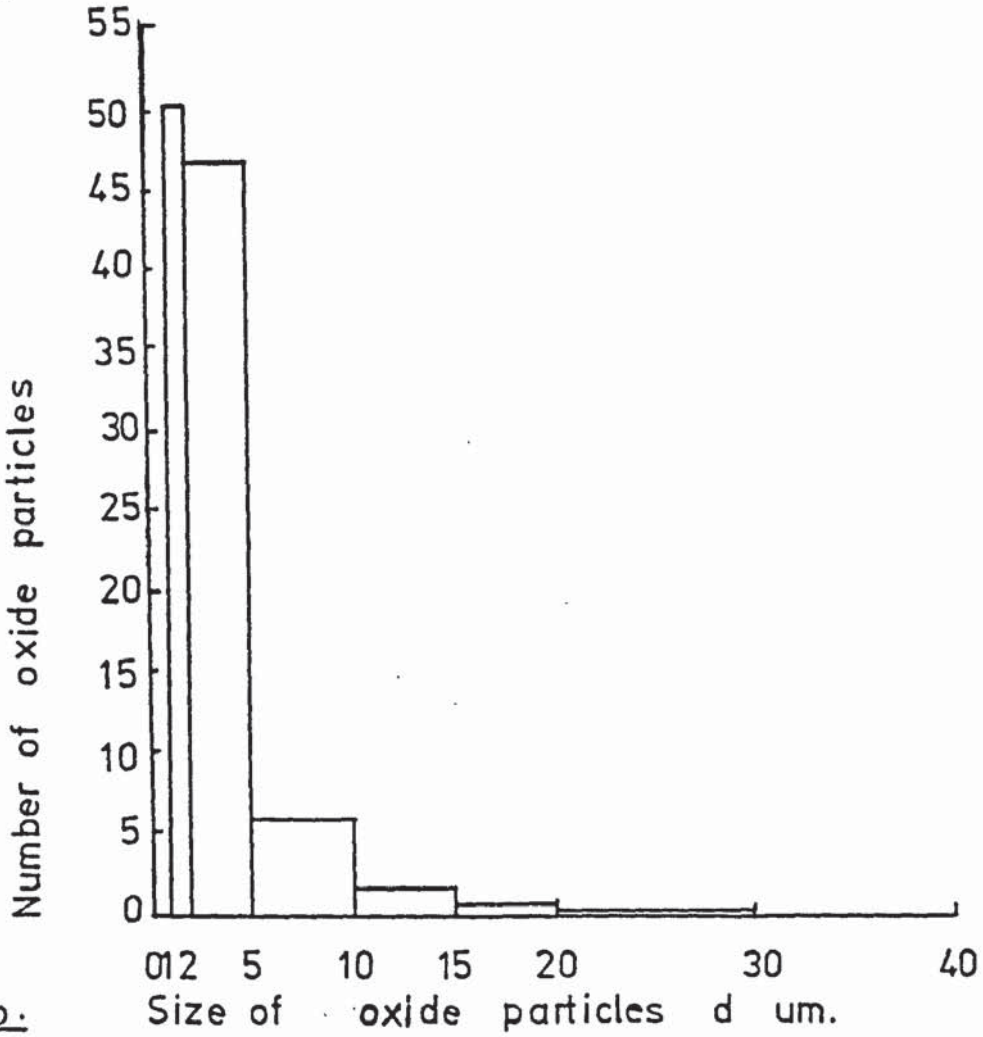

FIG.26.b.

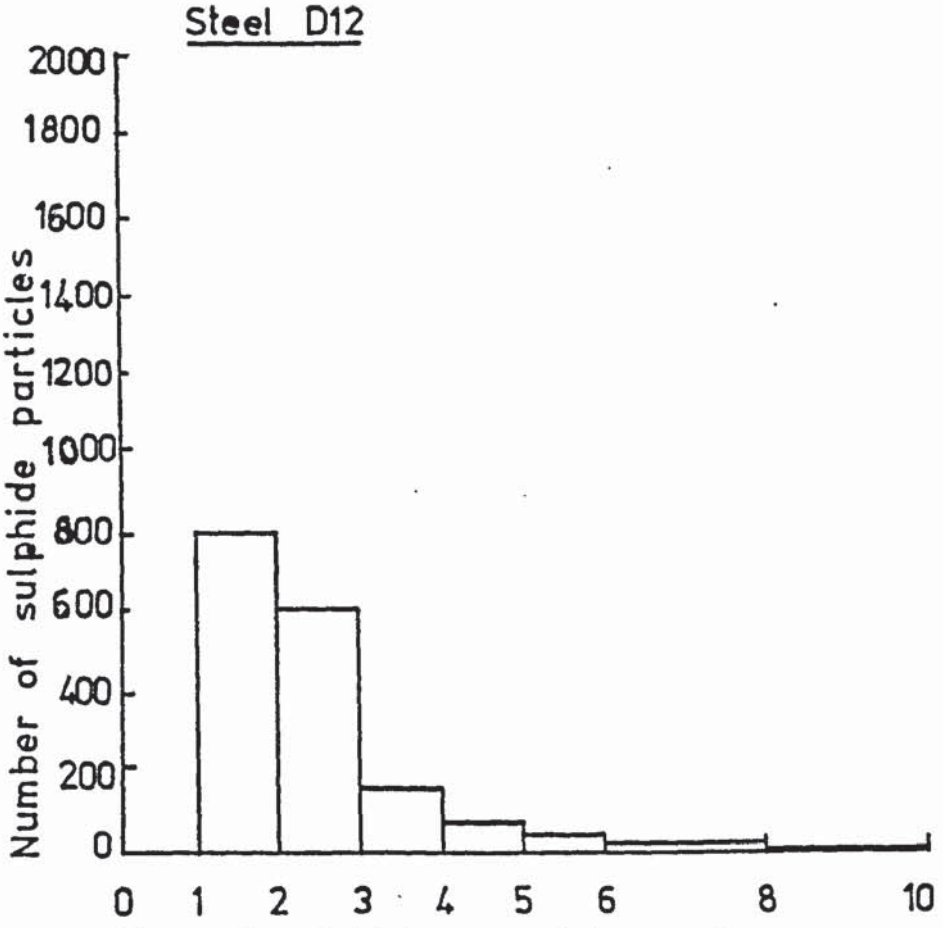

FIG.27.a.

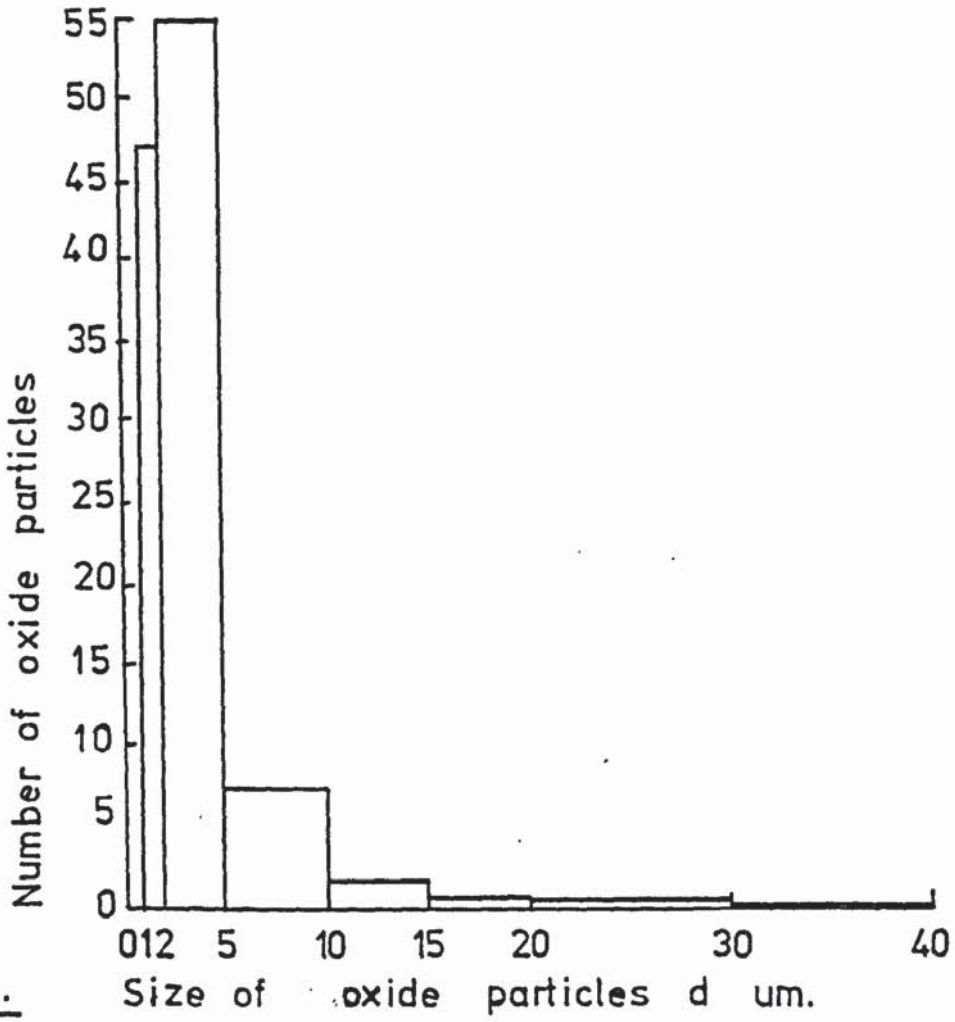

FIG.27.b.

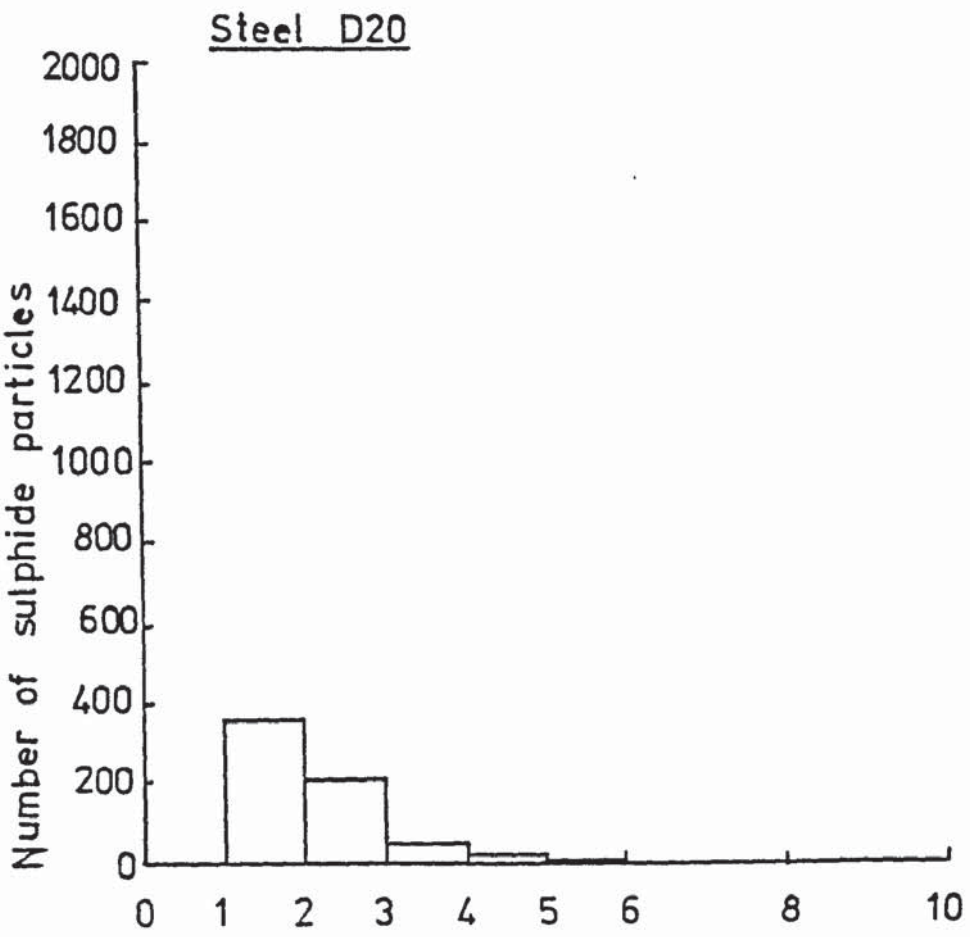

FIG.28.a.

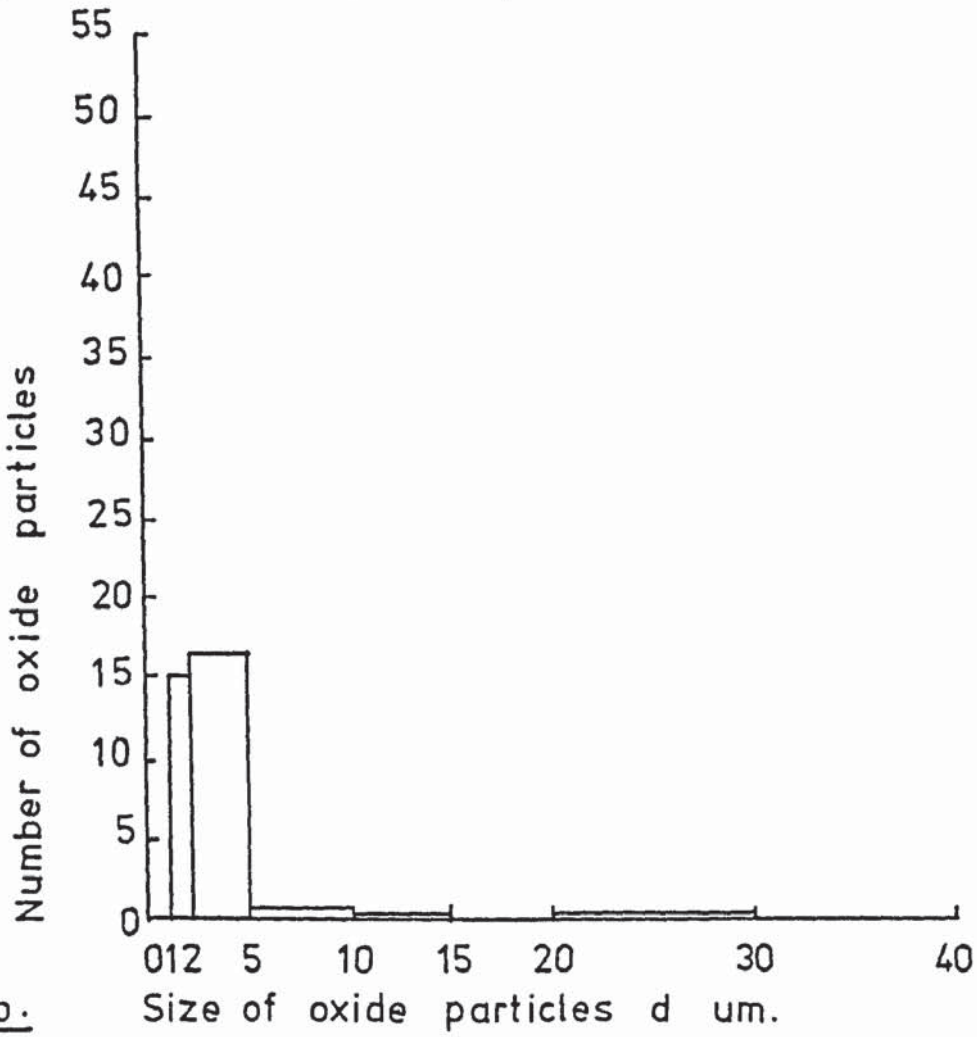

FIG.28.b.

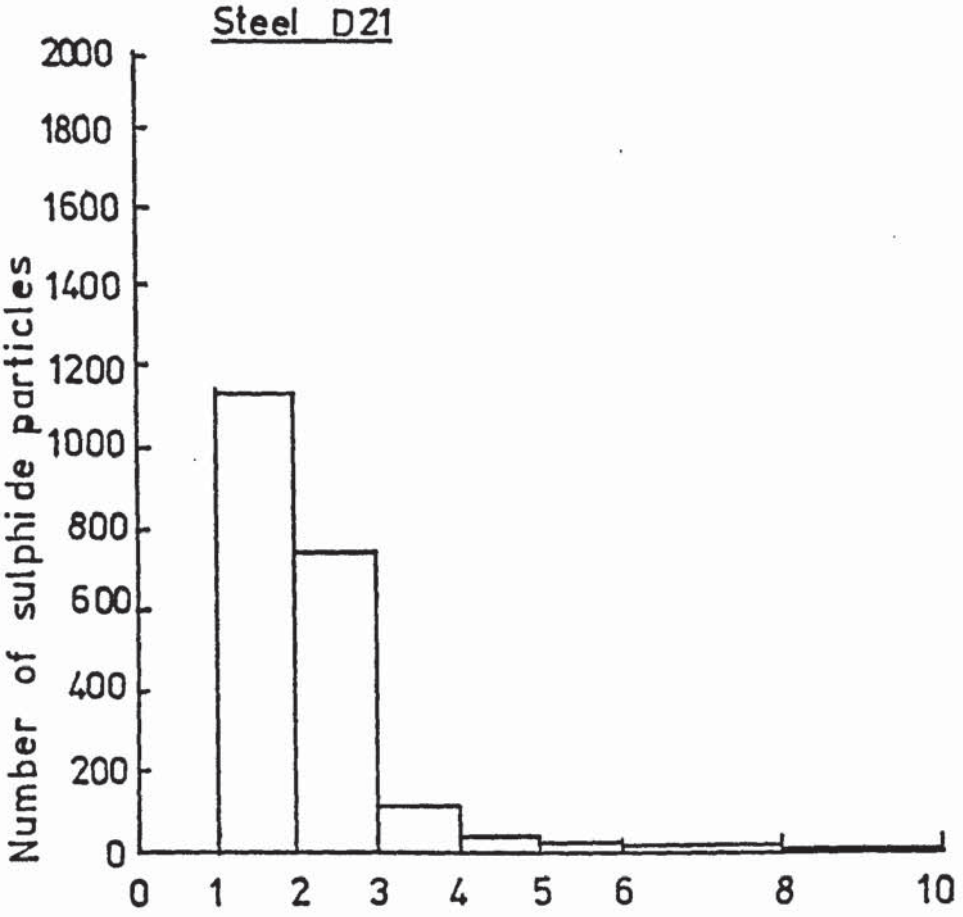

FIG.29.a.

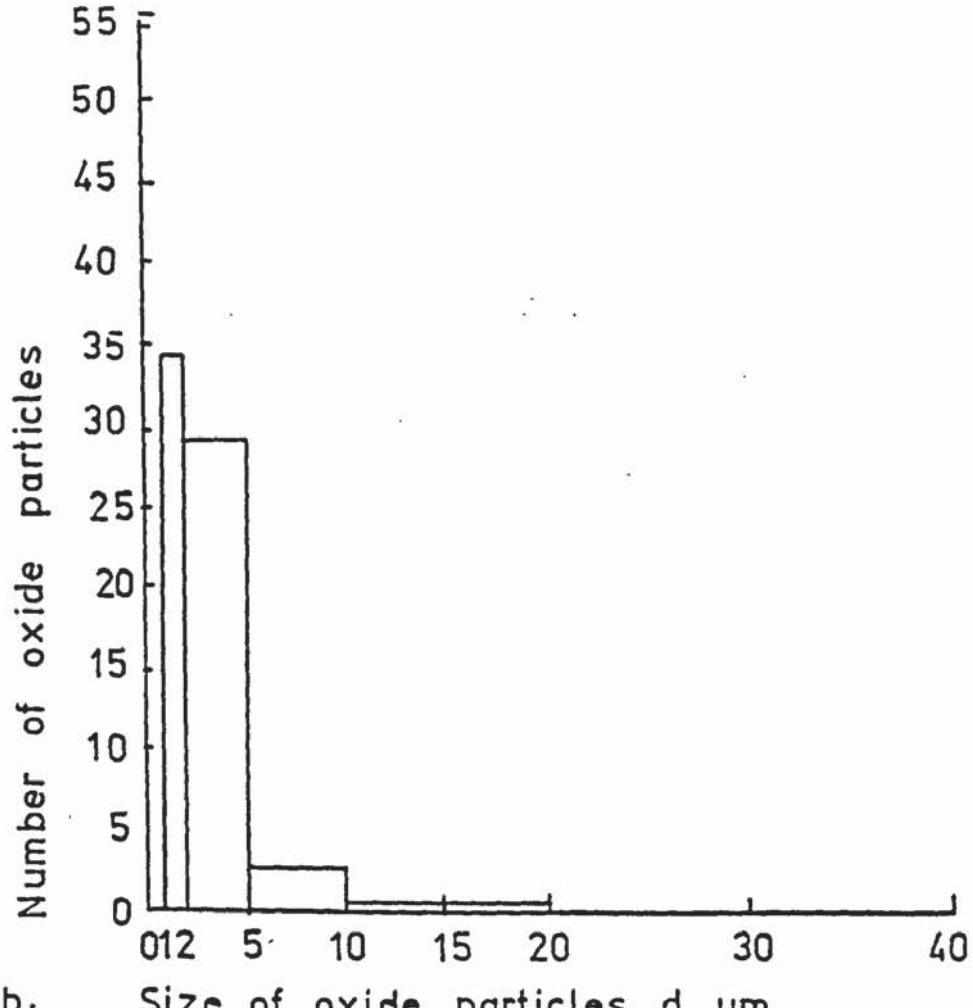

FIG.29.b.

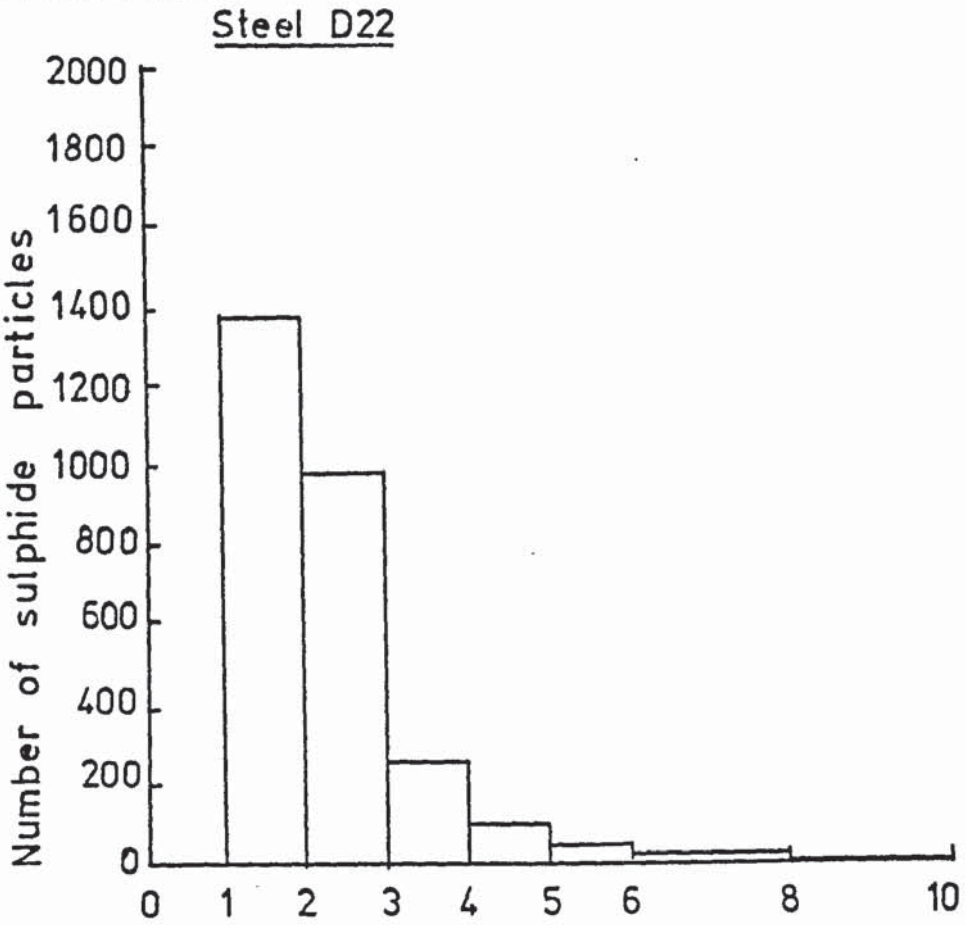

FIG.30.a.

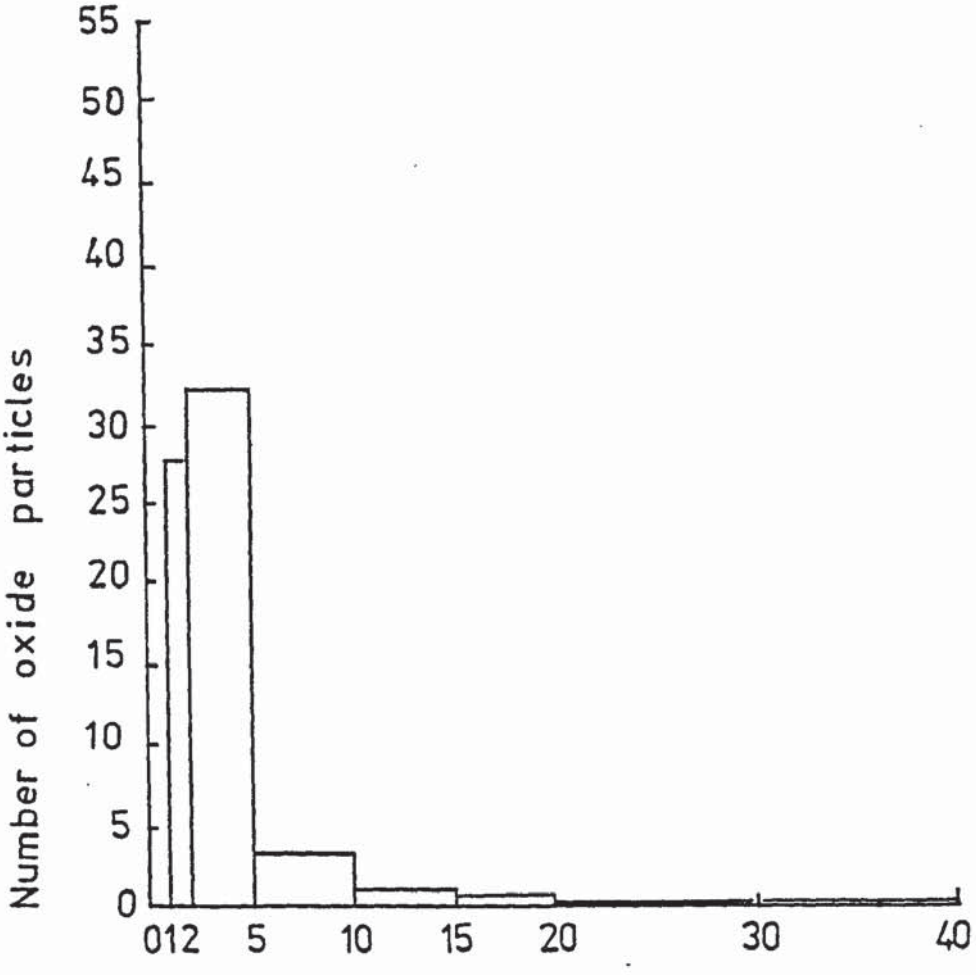

FIG.30.b.

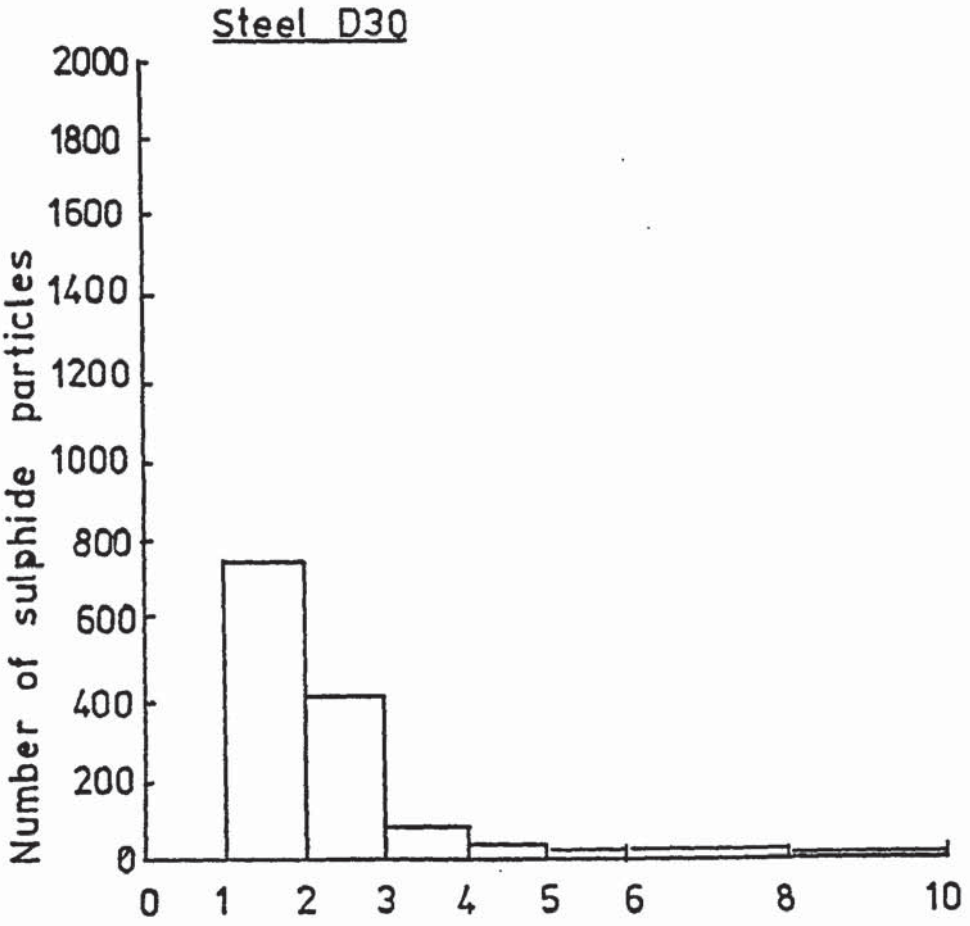

FIG.31.a.

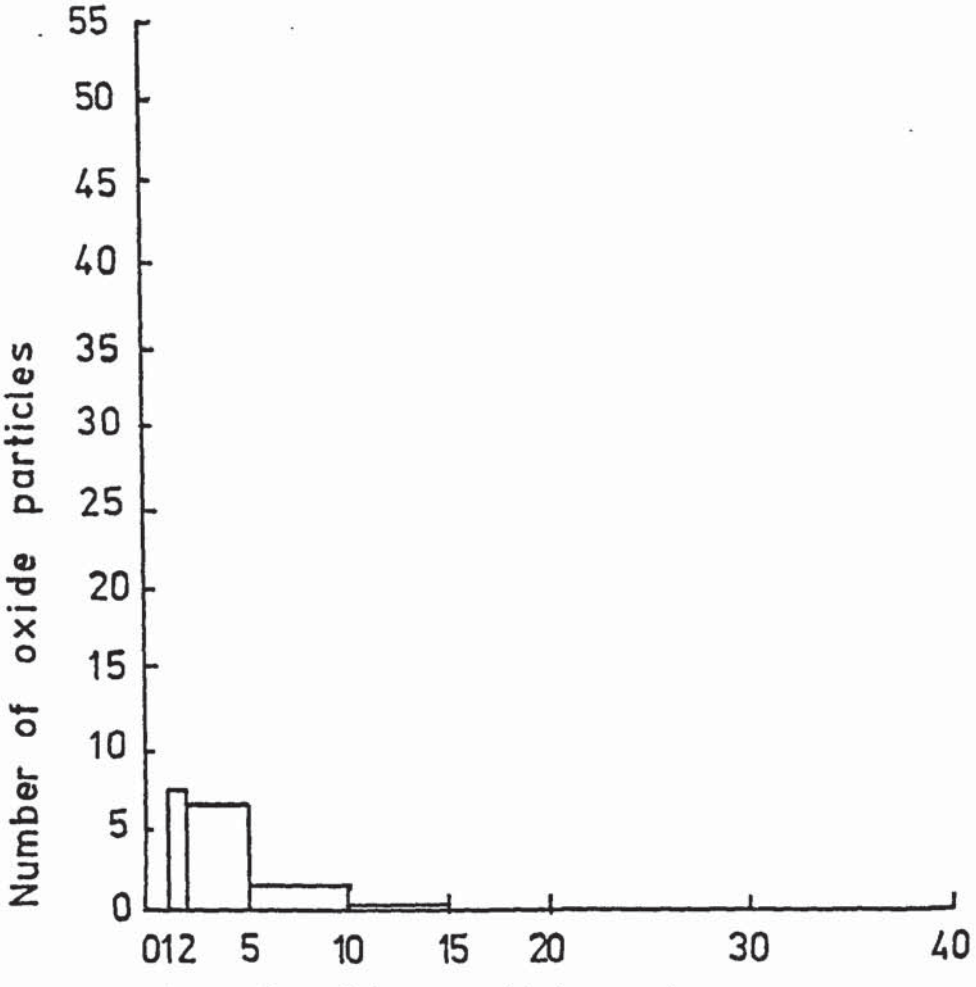

FIG.31.b.

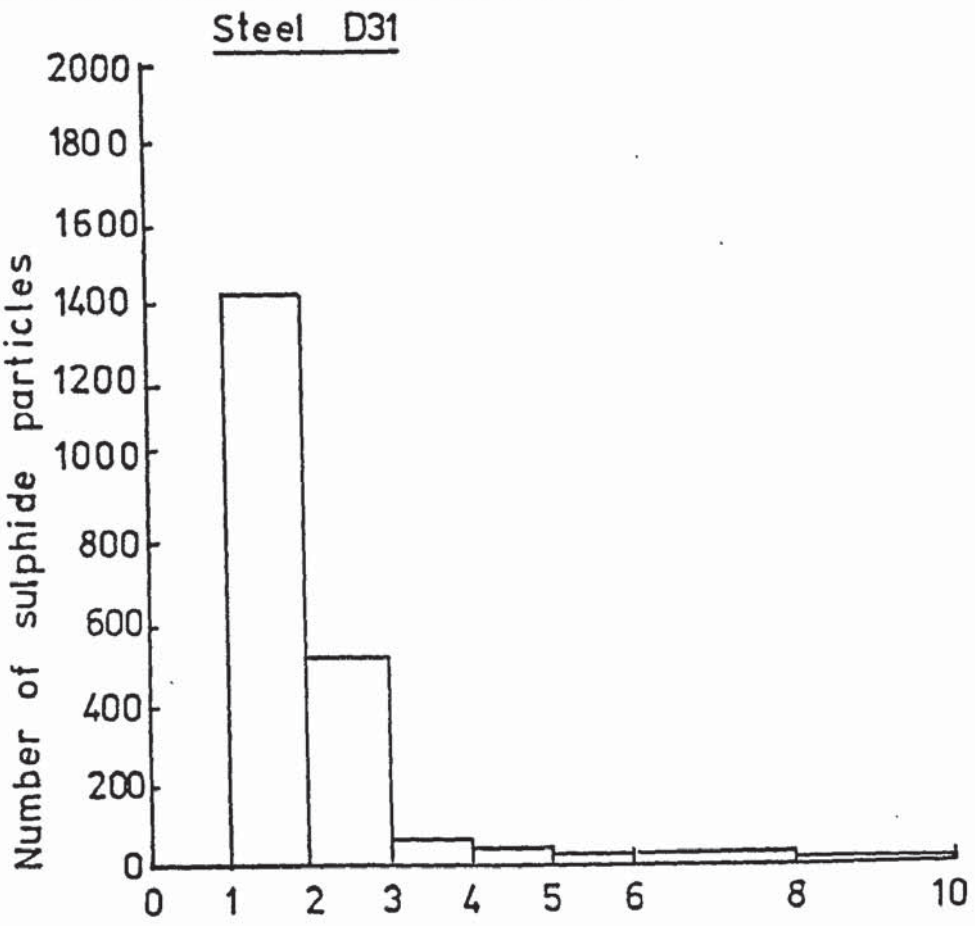

FIG.32.a.

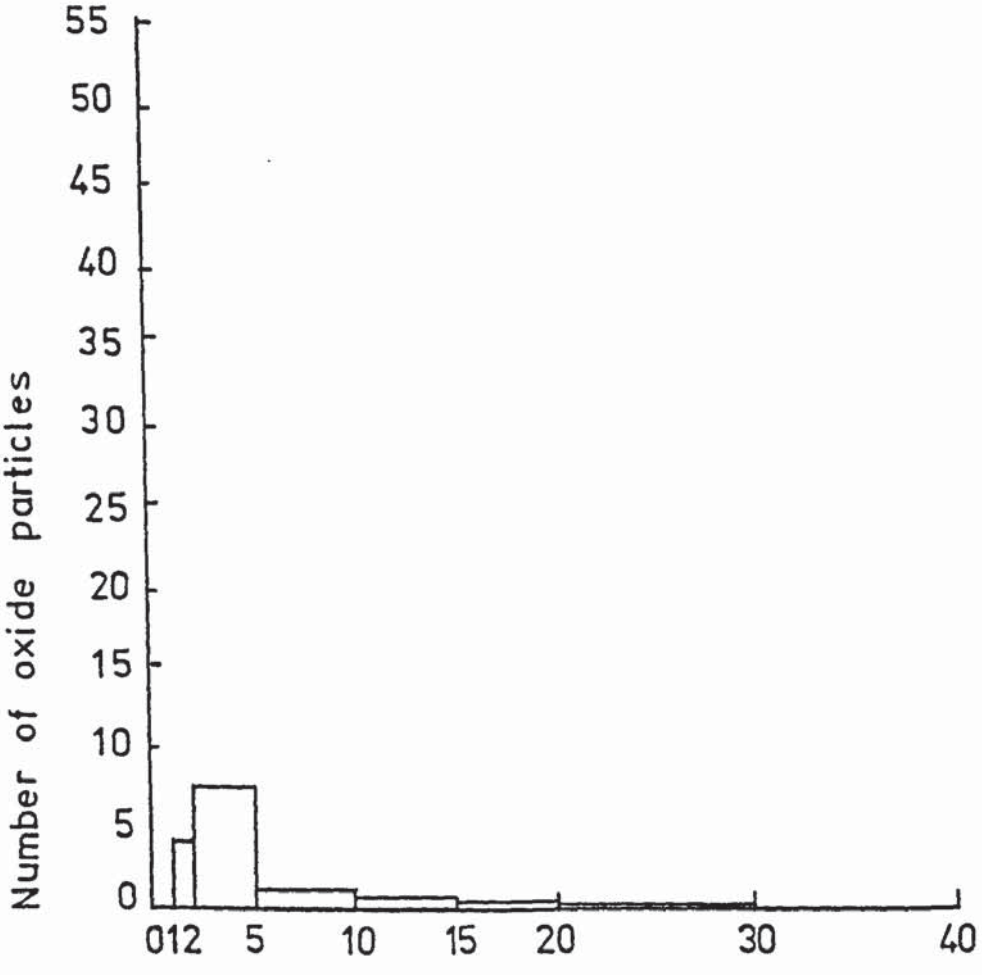

FIG.32.b.

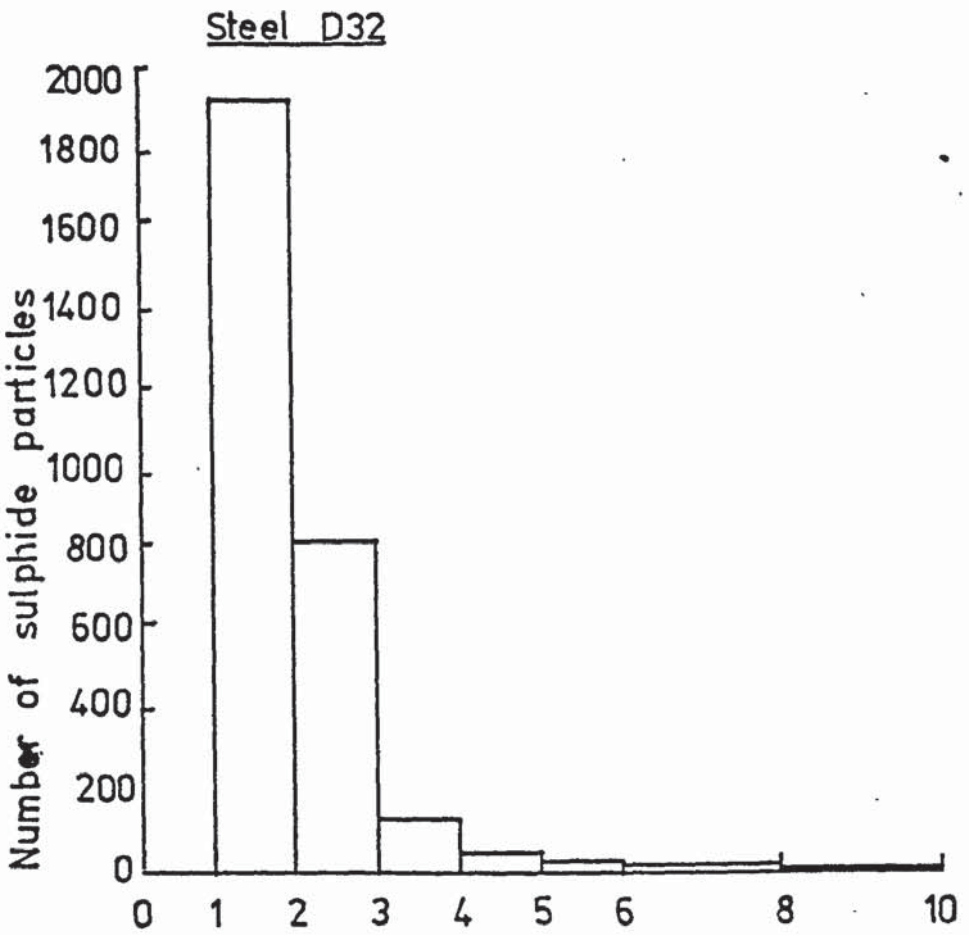

FIG. 33.a.

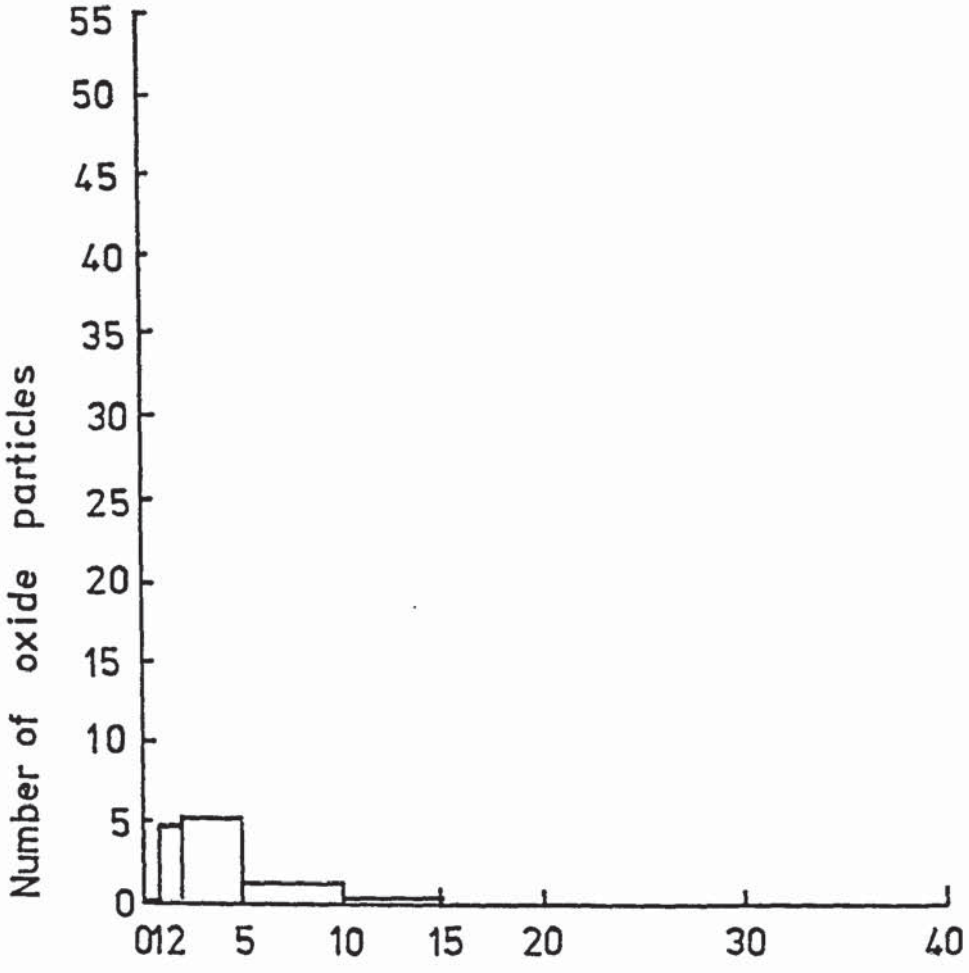

FIG. 33.b.

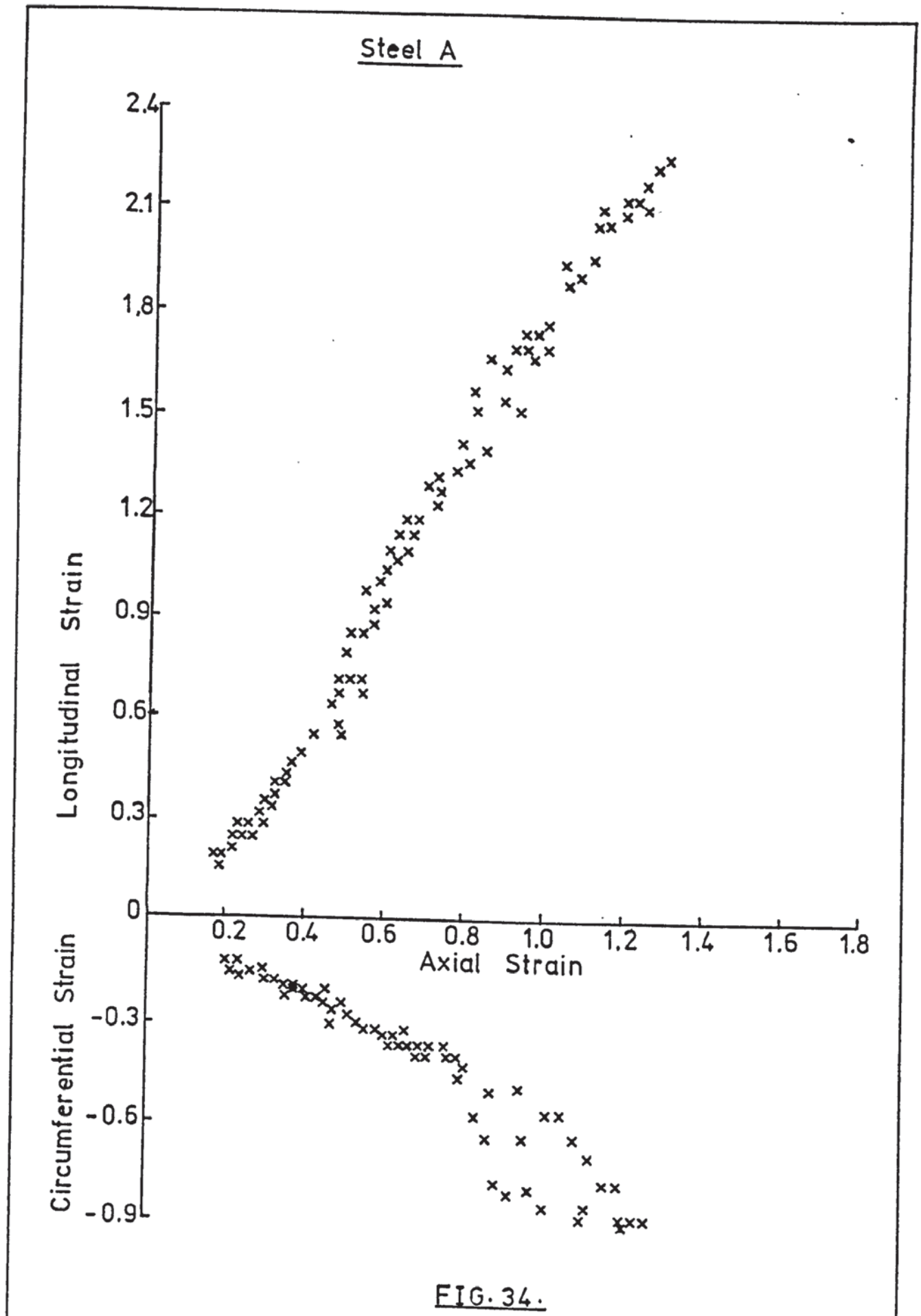
Steel A
2.4
2.1
1.8
1.5
1.2
0.9
0.6
0.3
0
-0.3
-0.6
-0.9
Longitudinal Strain
Circumferential Strain
0.2
0.4
0.6
0.8
1.0
1.2
1.4
1.6
1.8
Axial Strain

FIG. 34.

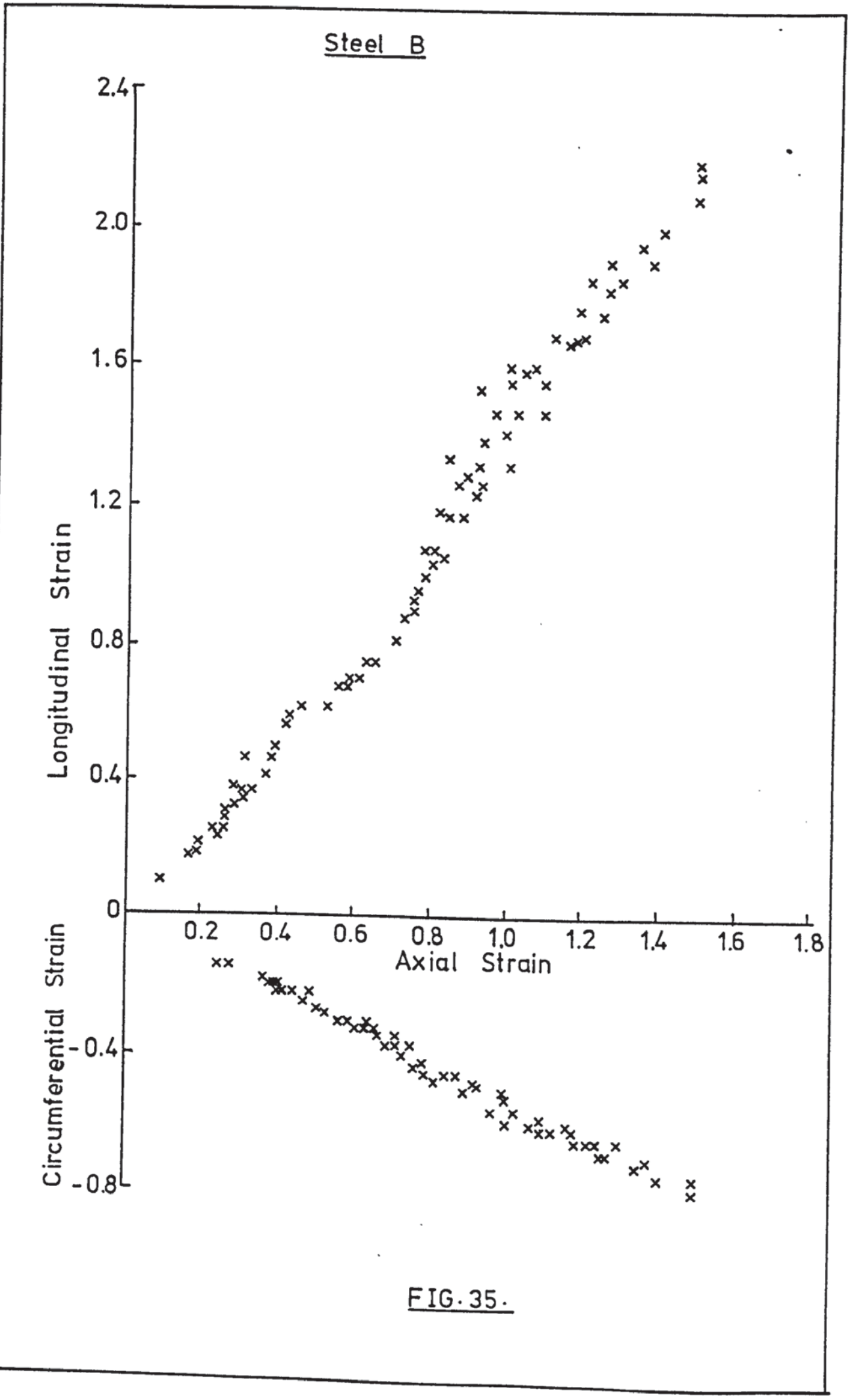
Steel B
2.4
2.0
1.6
1.2
0.8
0.4
0
-0.4
-0.8
Longitudinal Strain
Circumferential Strain
0.2
0.4
0.6
0.8
1.0
1.2
1.4
1.6
1.8
Axial Strain

FIG. 35.

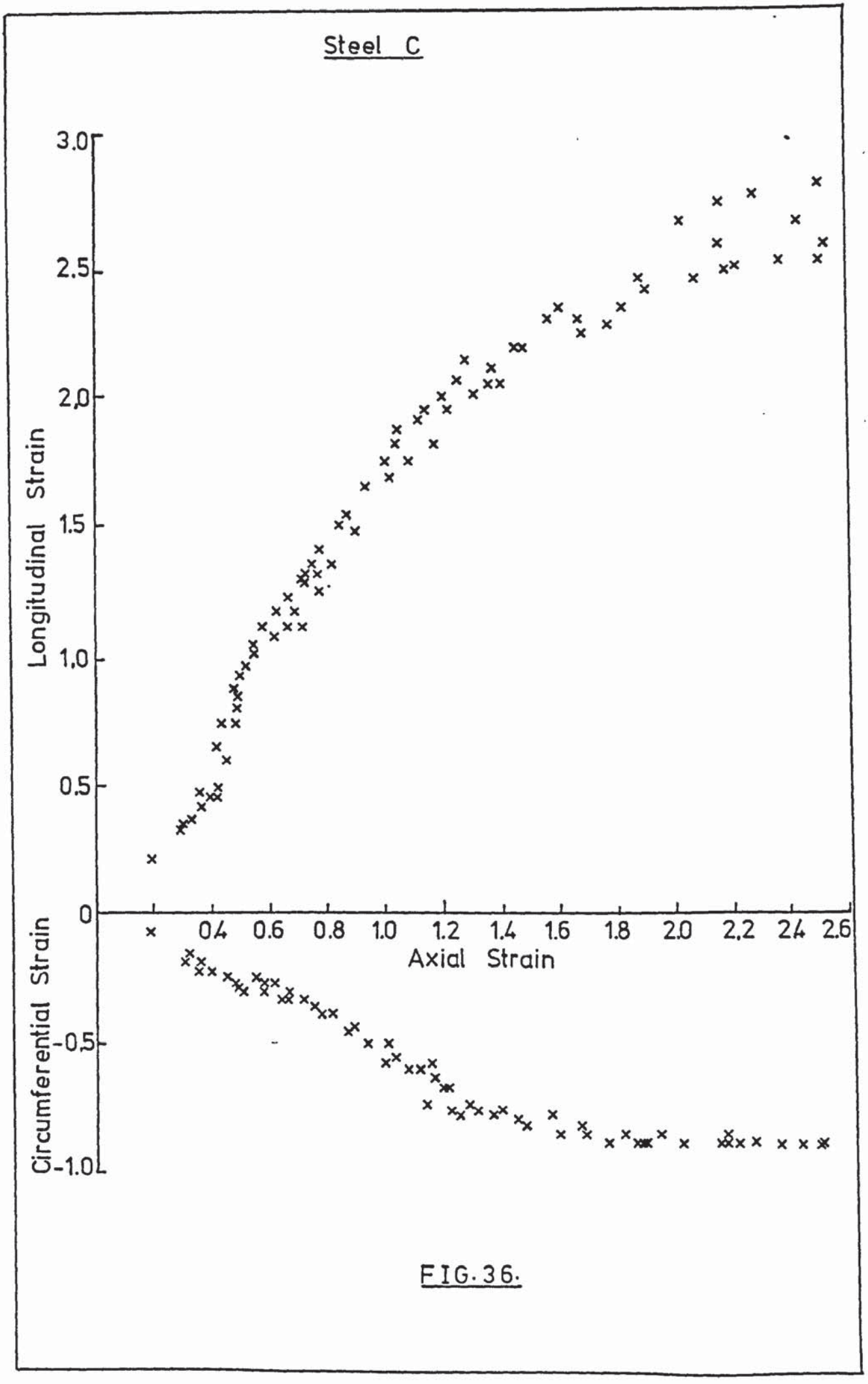
Steel C
3.0
2.5
2.0
1.5
1.0
0.5
0
-0.5
-1.0
Longitudinal Strain
Circumferential Strain
0.4
0.6
0.8
1.0
1.2
1.4
1.6
1.8
2.0
2.2
2.4
2.6
Axial Strain

FIG. 36.

Steel A

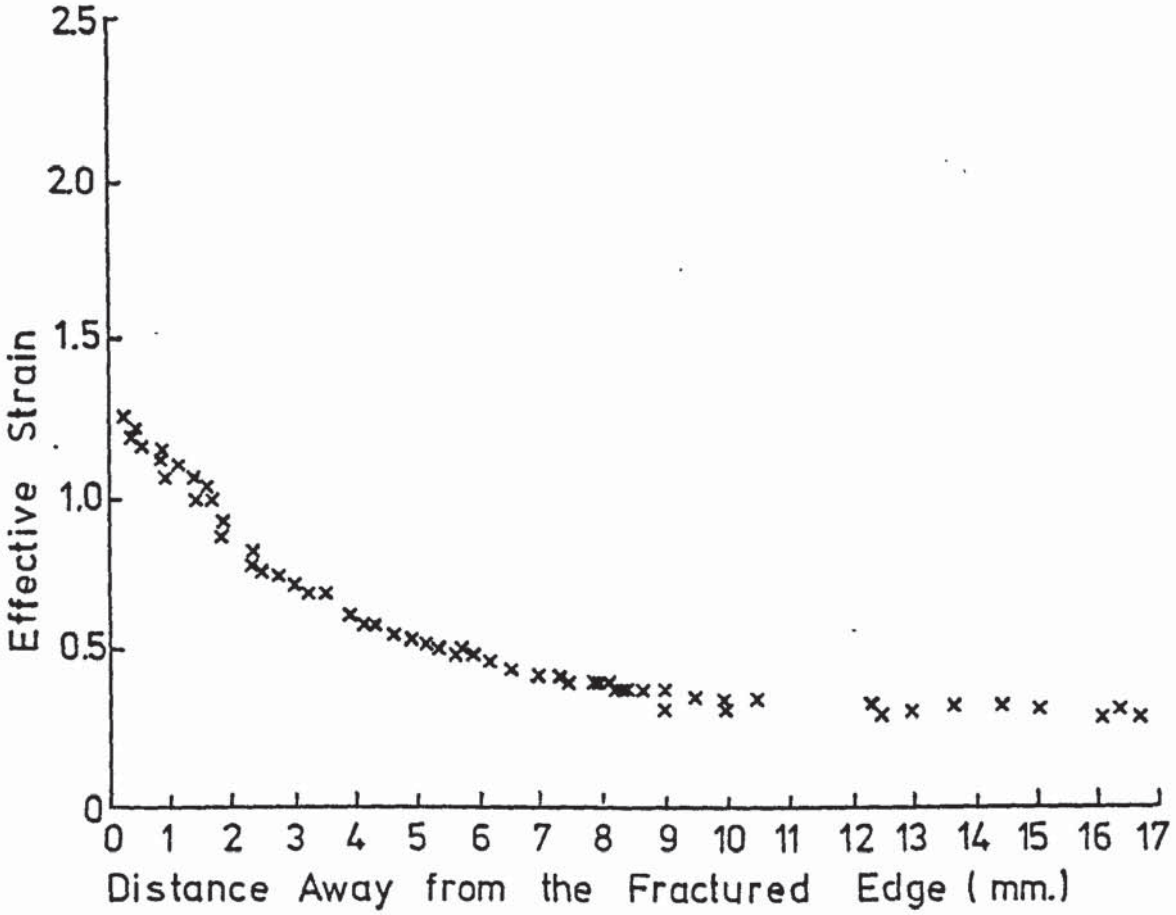

FIG·37·

Steel B

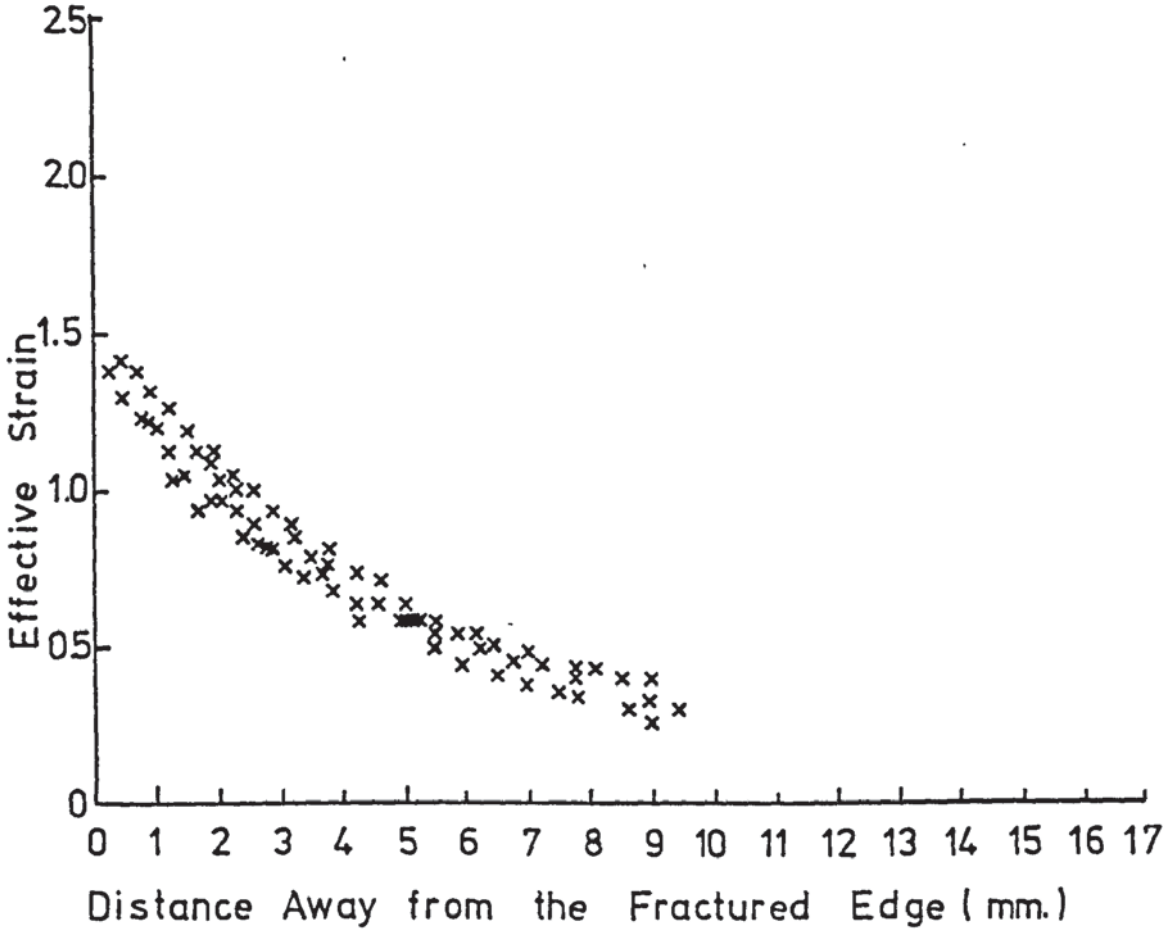

FIG.38.

Steel C

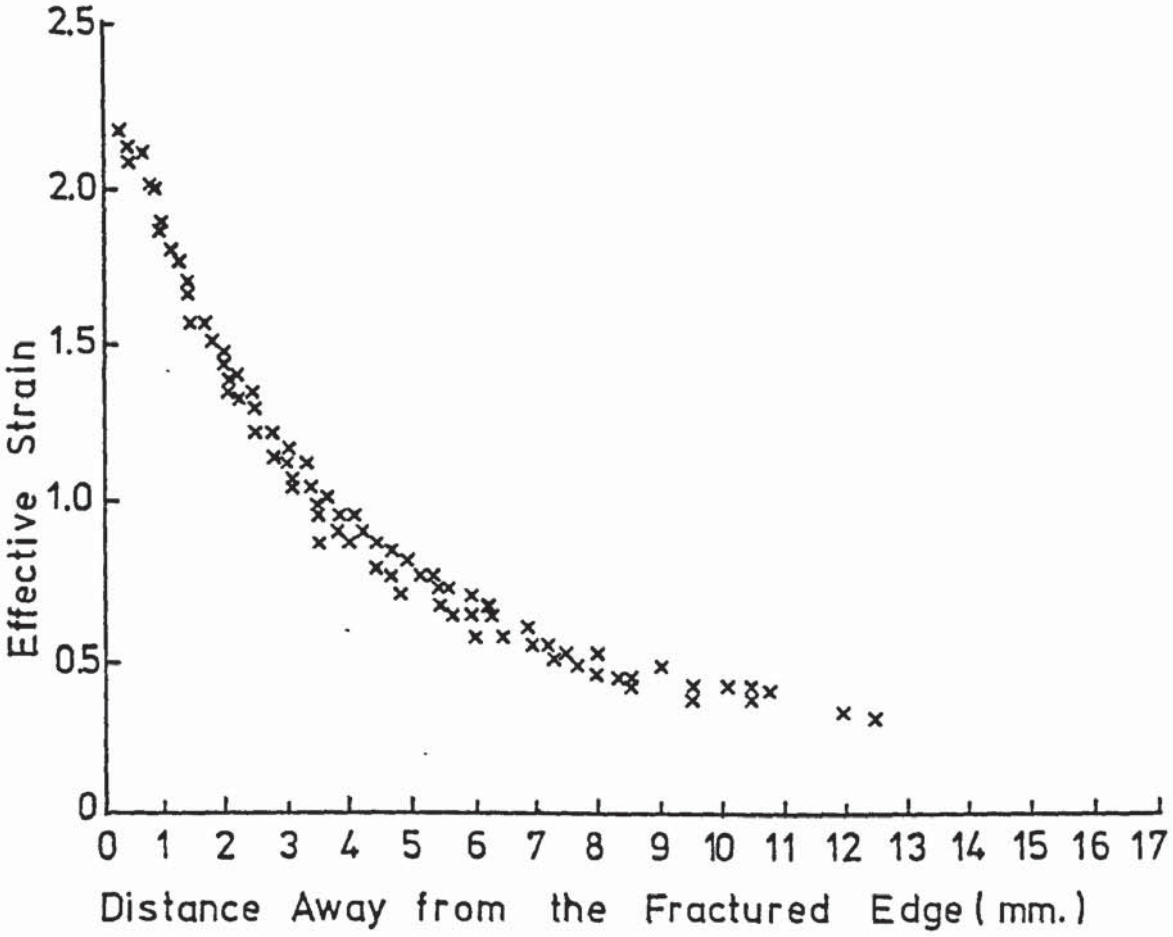

FIG. 39.

Steel A

— — — — The broken lines are the values of the Theoretical Equation [18].

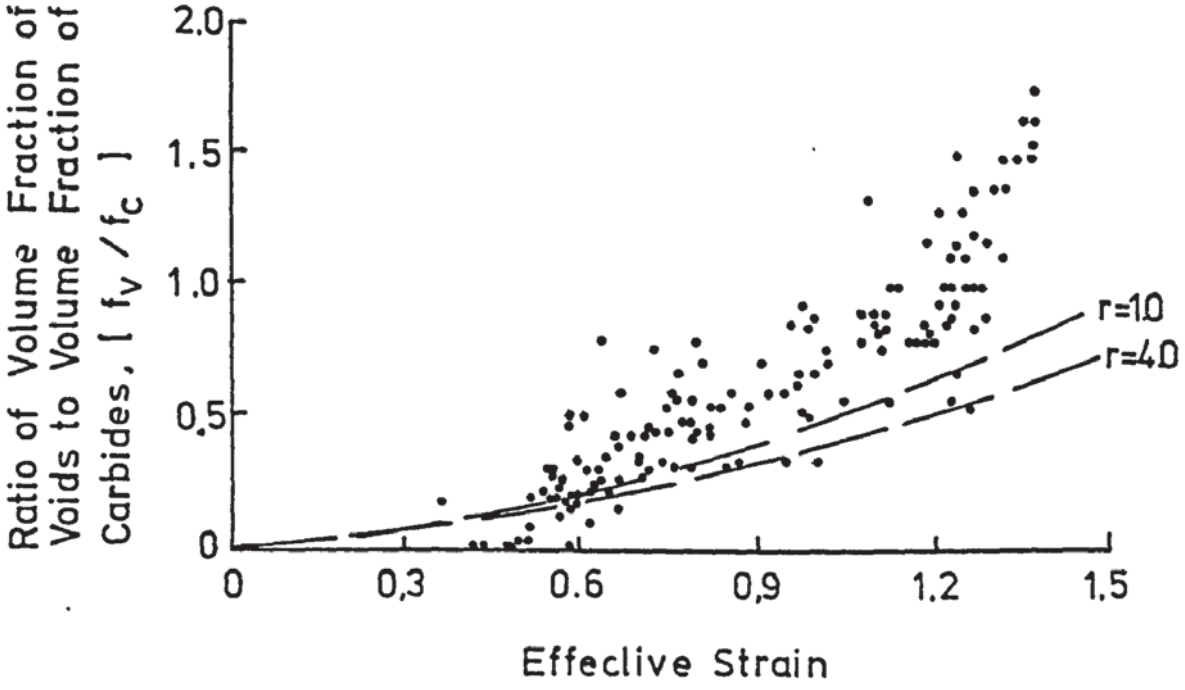

FIG·40·

Steel B

— — — — — The broken lines are the values of the Theoretical Equation [18].

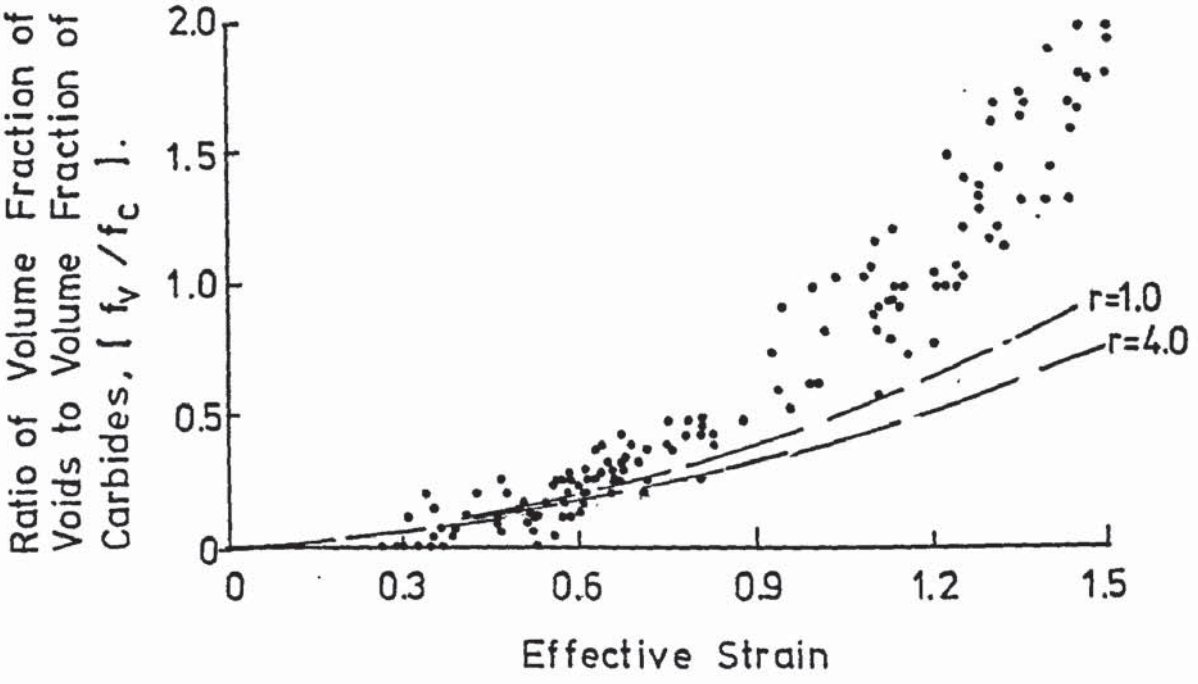

FIG. 41.

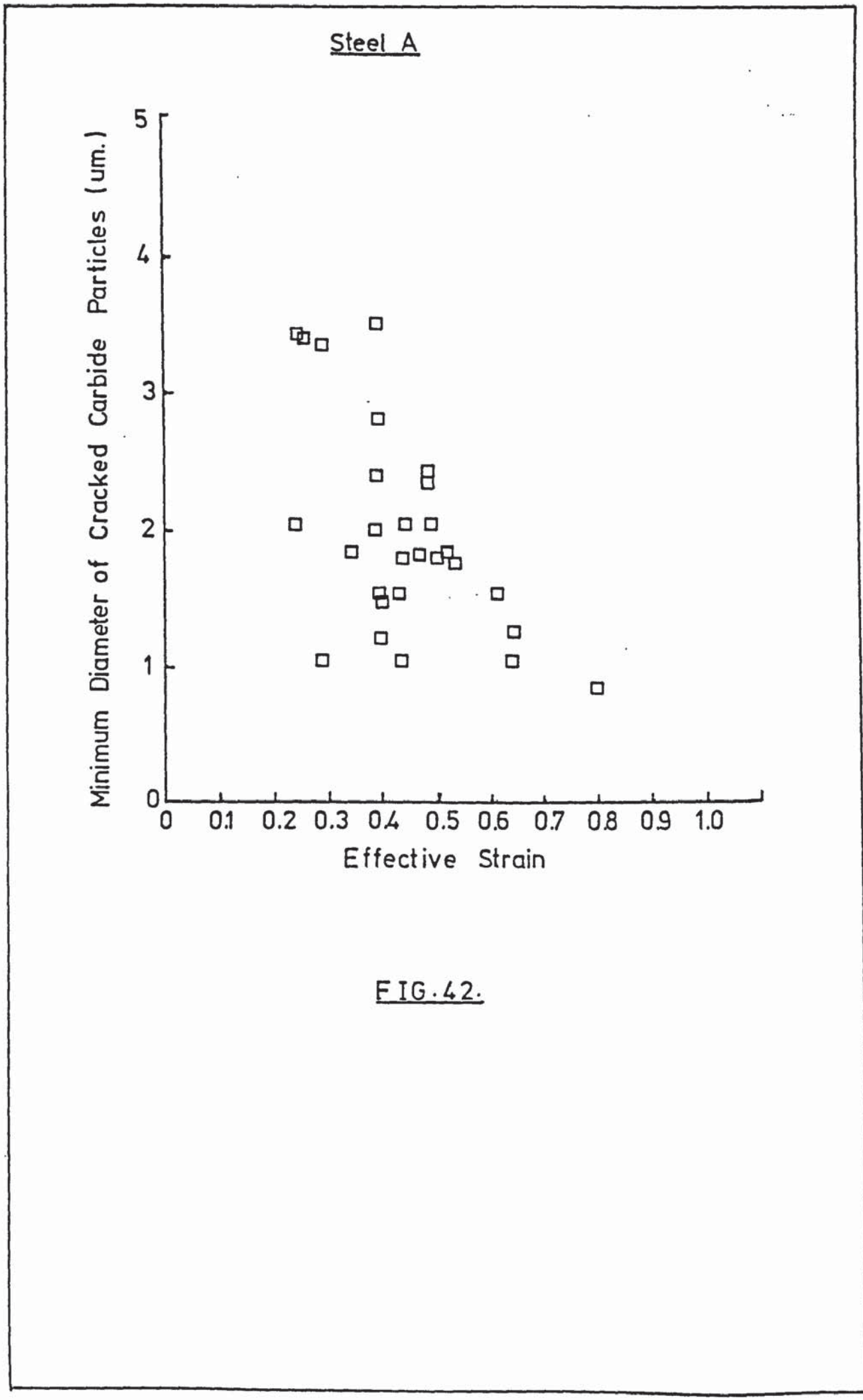
Steel A
Minimum Diameter of Cracked Carbide Particles (um.)
5
4
3
2
1
0
0
0.1
0.2
0.3
0.4
0.5
0.6
0.7
0.8
0.9
1.0
Effective Strain

FIG.42.

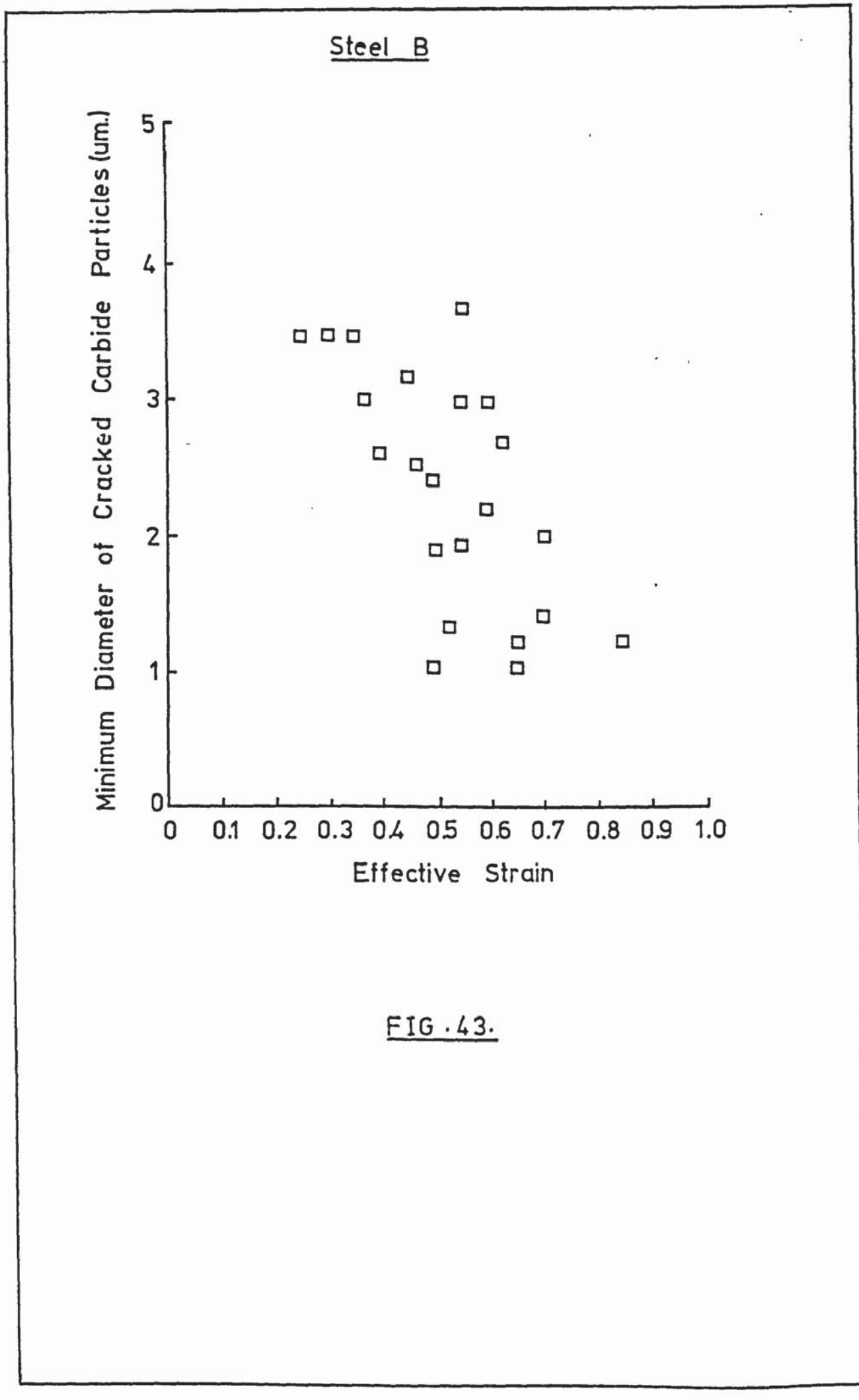
Steel B
Minimum Diameter of Cracked Carbide Particles (um.)
0
1
2
3
4
5
0
0.1
0.2
0.3
0.4
0.5
0.6
0.7
0.8
0.9
1.0
Effective Strain

FIG .43.

Steel A

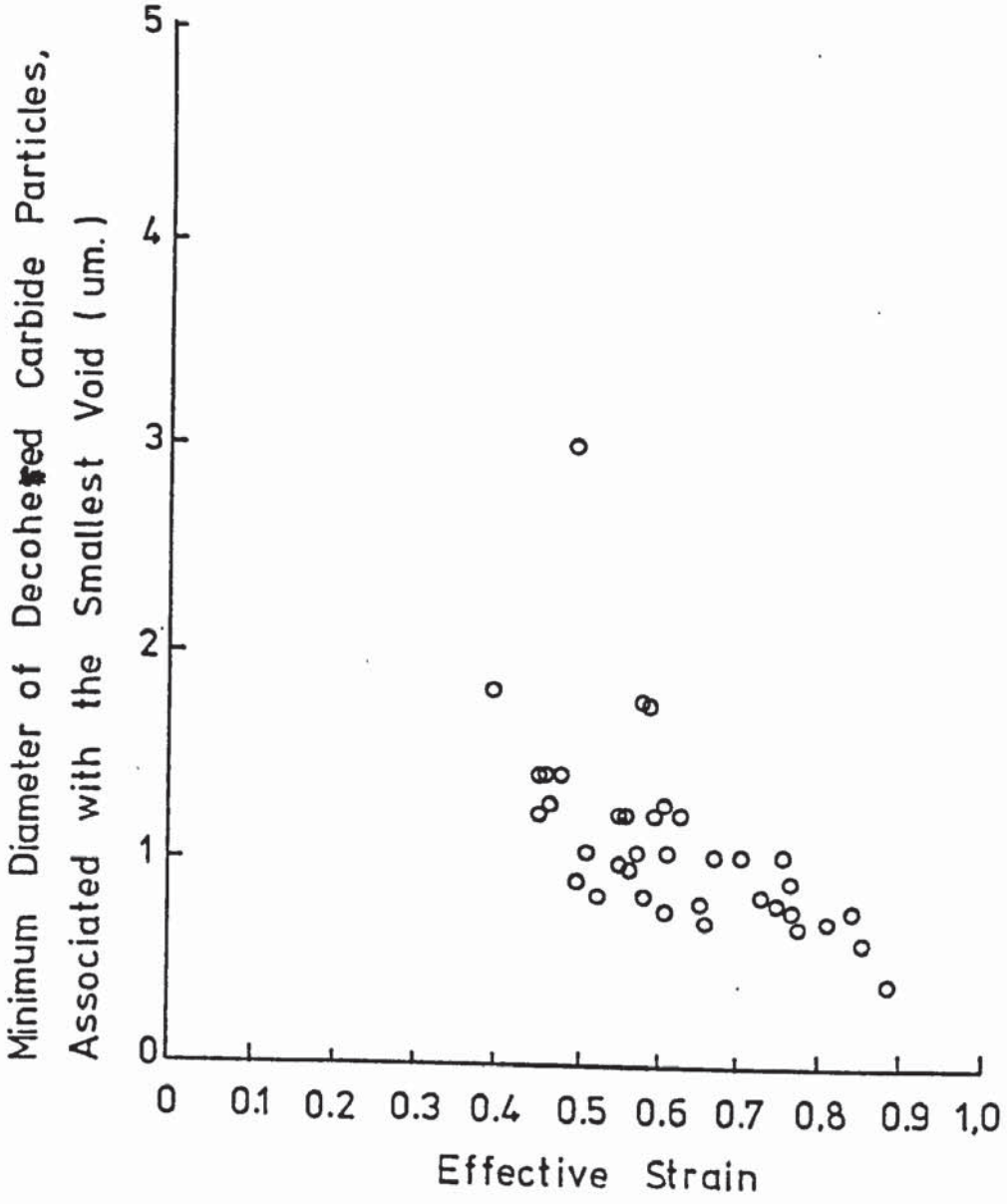

FIG. 44.

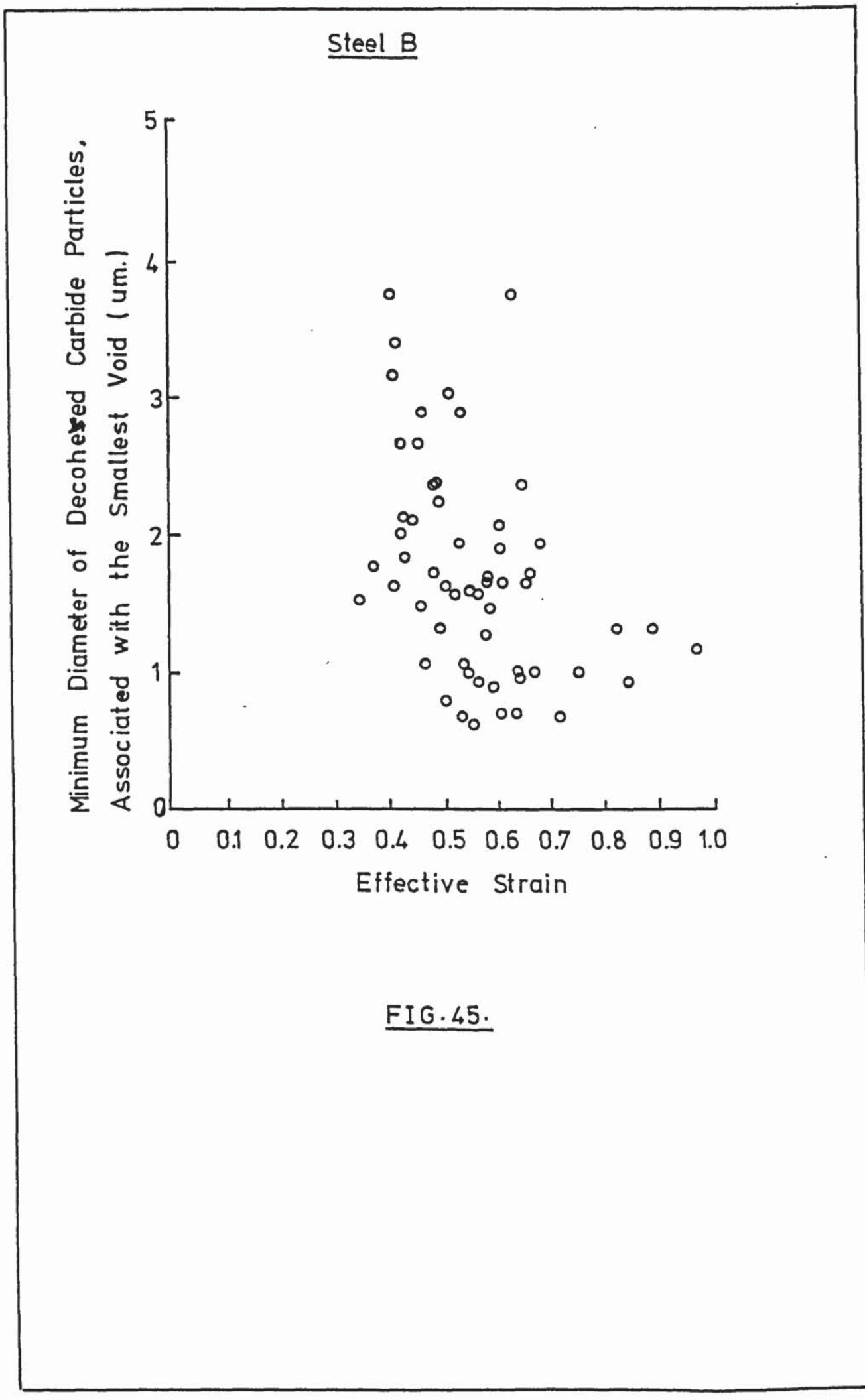
Steel B
Minimum Diameter of Decohered Carbide Particles, Associated with the Smallest Void (um.)
0
1
2
3
4
5
0
0.1
0.2
0.3
0.4
0.5
0.6
0.7
0.8
0.9
1.0
Effective Strain

FIG.45.

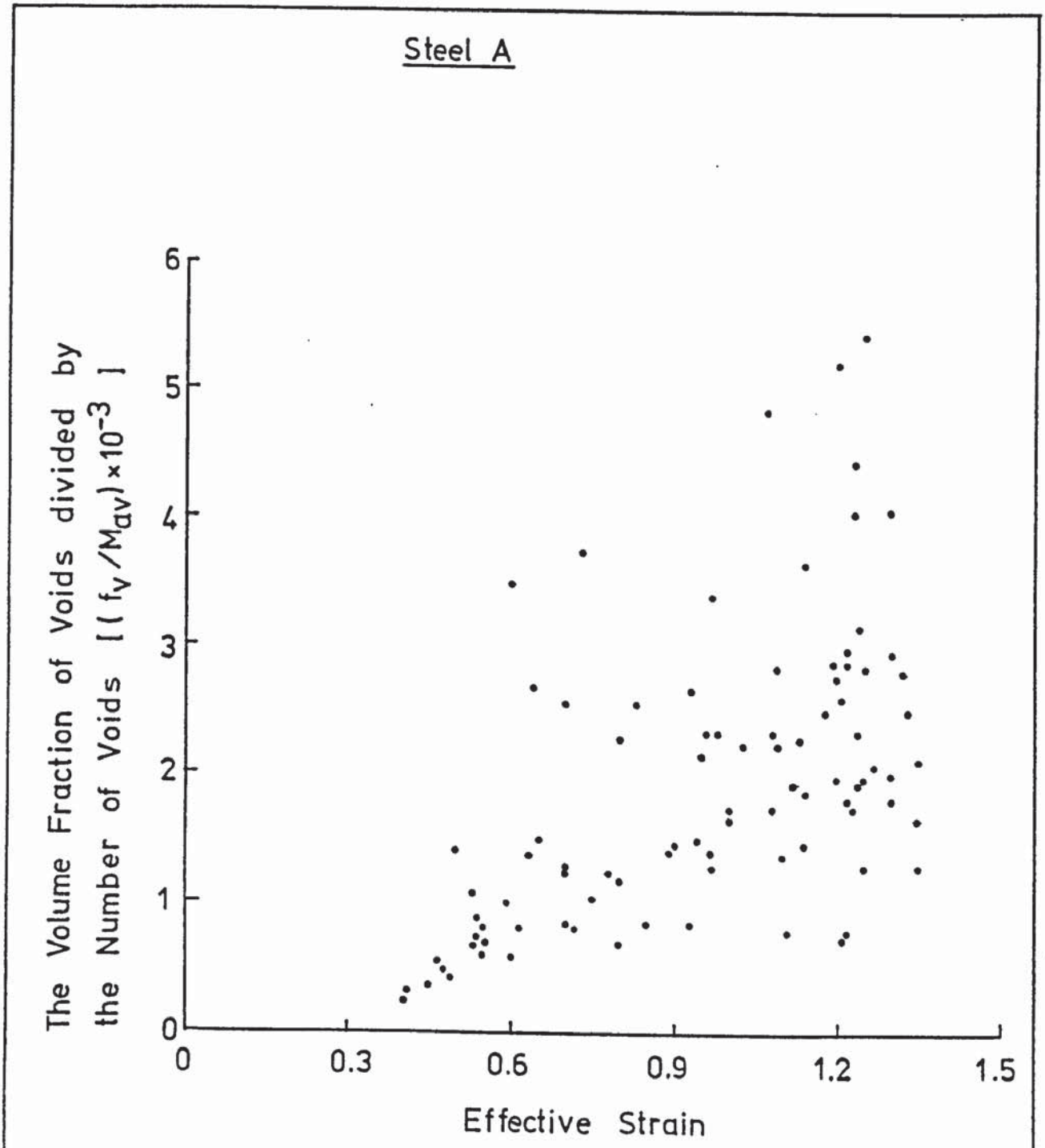
Steel A
The Volume Fraction of Voids divided by the Number of Voids [(f_V / M_{av}) $\times 10^{-3}$]
0
1
2
3
4
5
6
0
0.3
0.6
0.9
1.2
1.5
Effective Strain

FIG. 46.

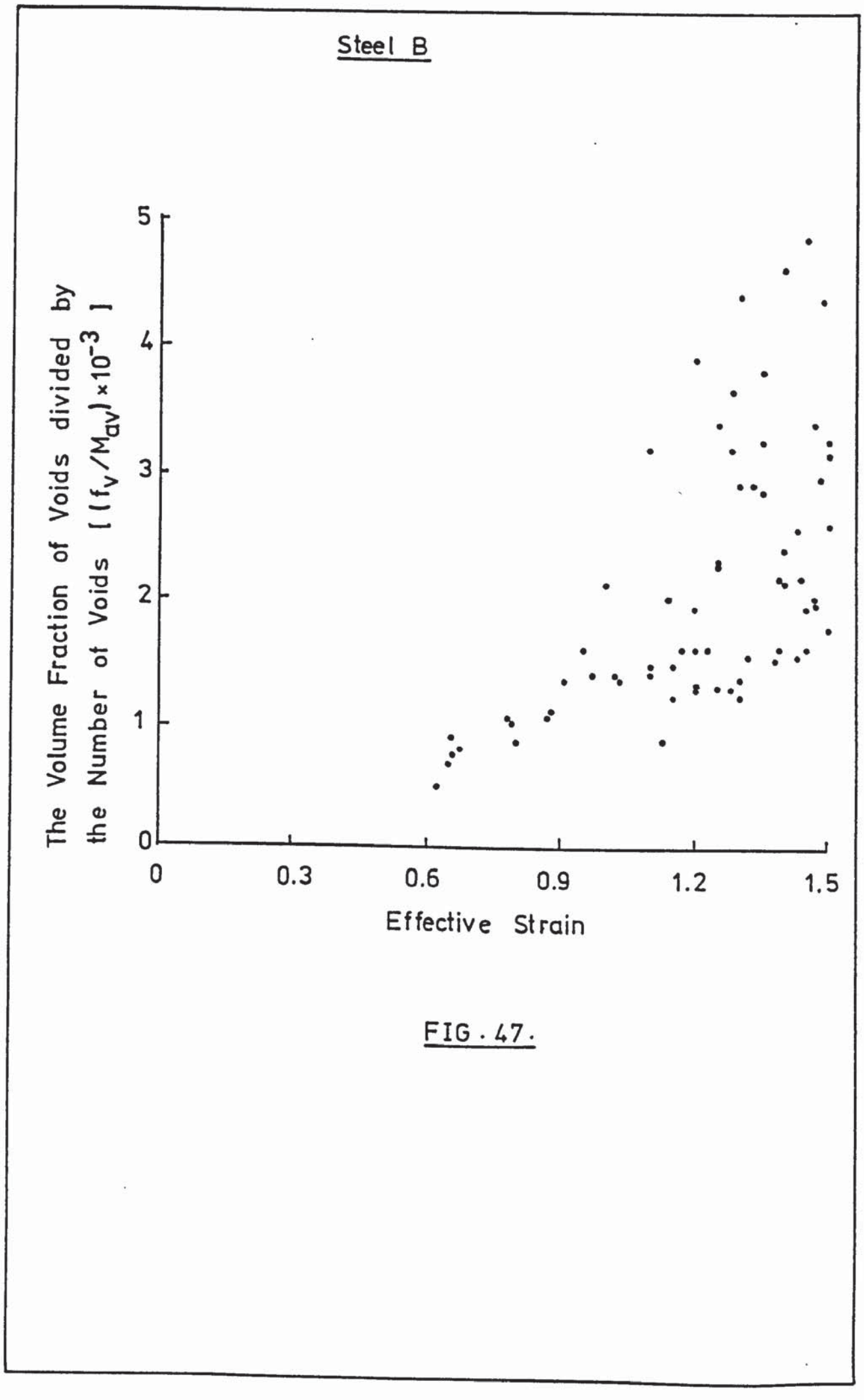
Steel B
The Volume Fraction of Voids divided by the Number of Voids [(f_V / M_{AV}) $\times 10^{-3}$]
0
1
2
3
4
5
0
0.3
0.6
0.9
1.2
1.5
Effective Strain

FIG . 47.

Steel A

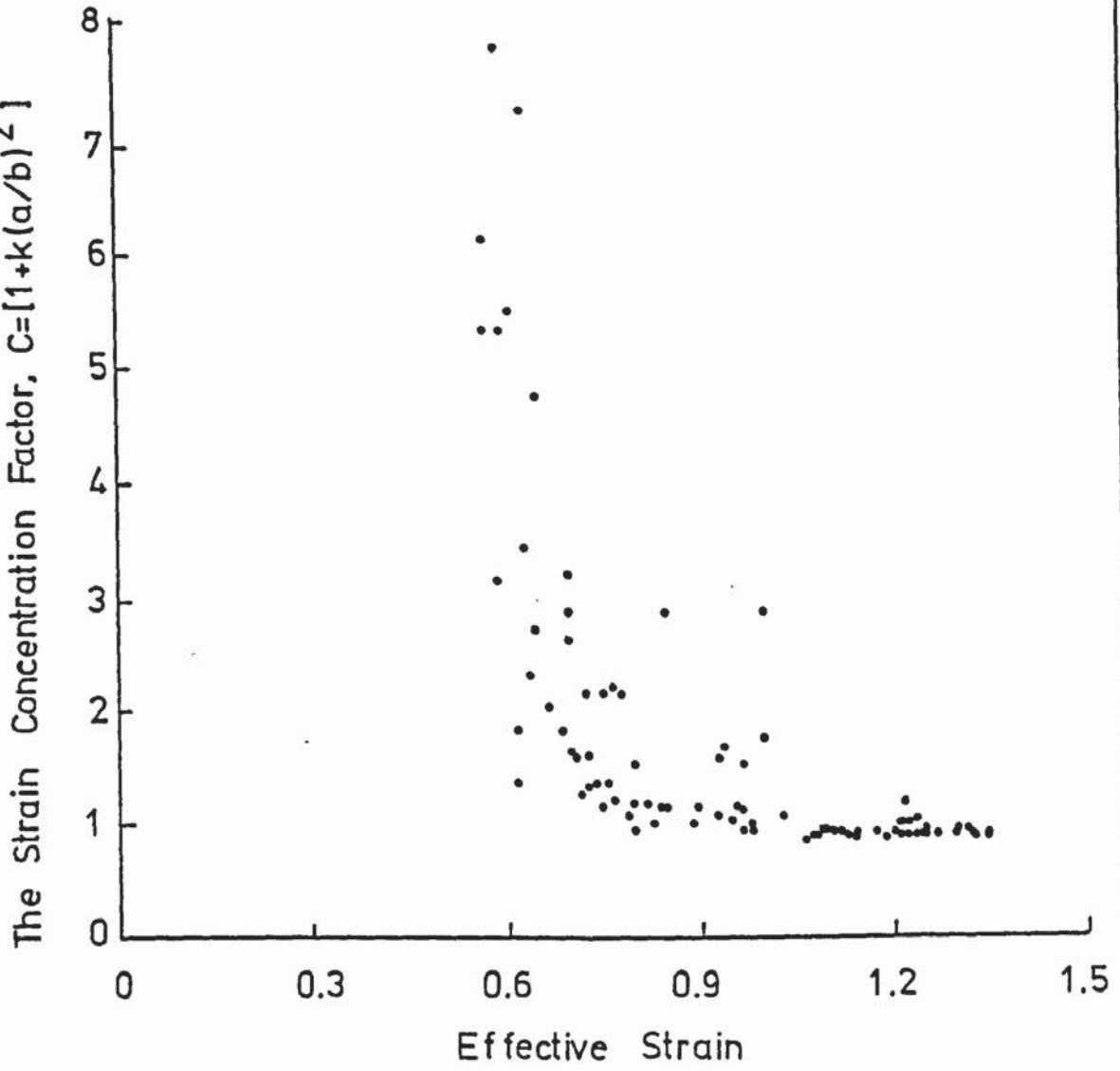

FIG. 48.

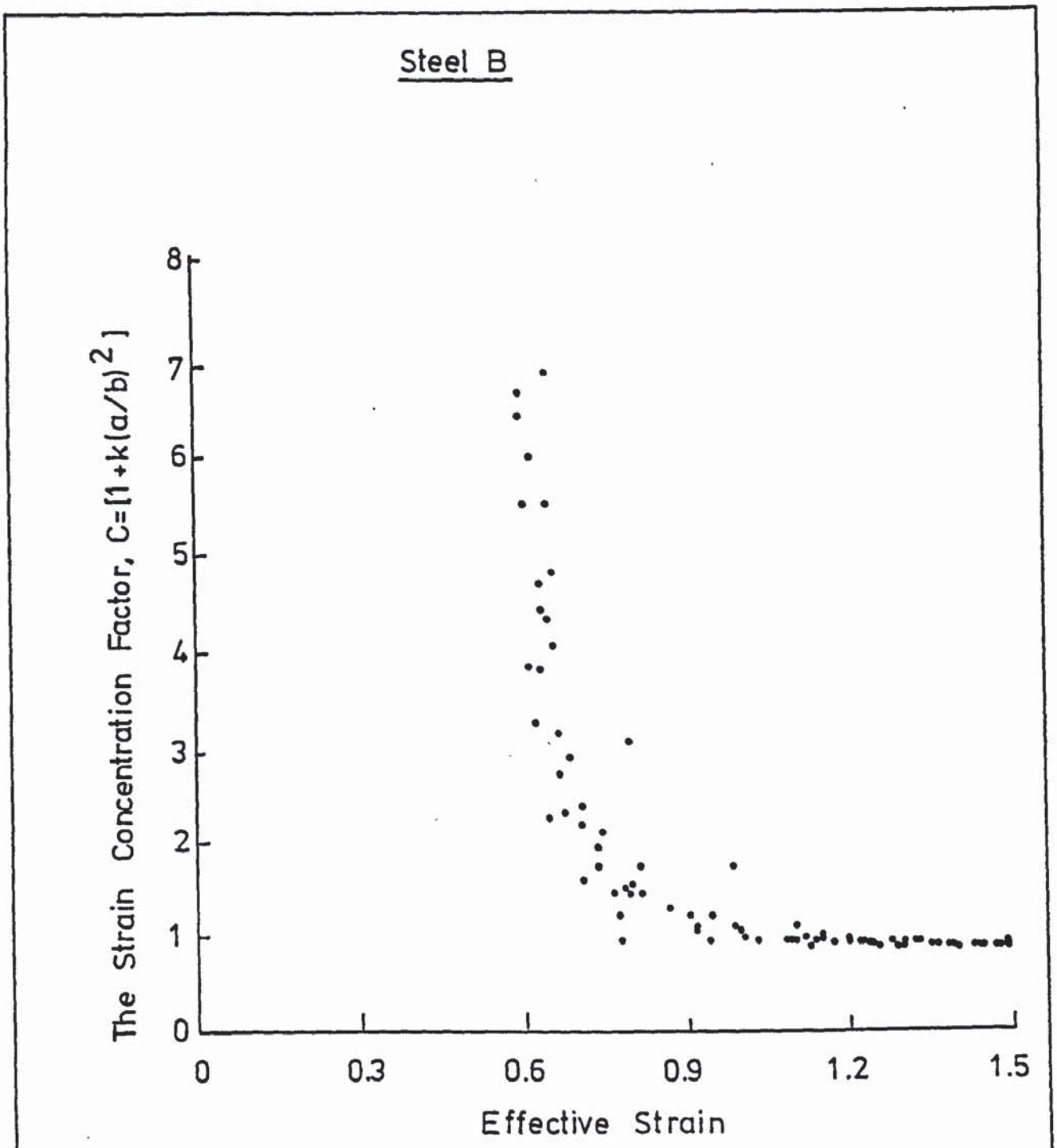
Steel B
The Strain Concentration Factor, C=[1+k(a/b)^2]
0
1
2
3
4
5
6
7
8
0
0.3
0.6
0.9
1.2
1.5
Effective Strain

FIG.49.

Steel C

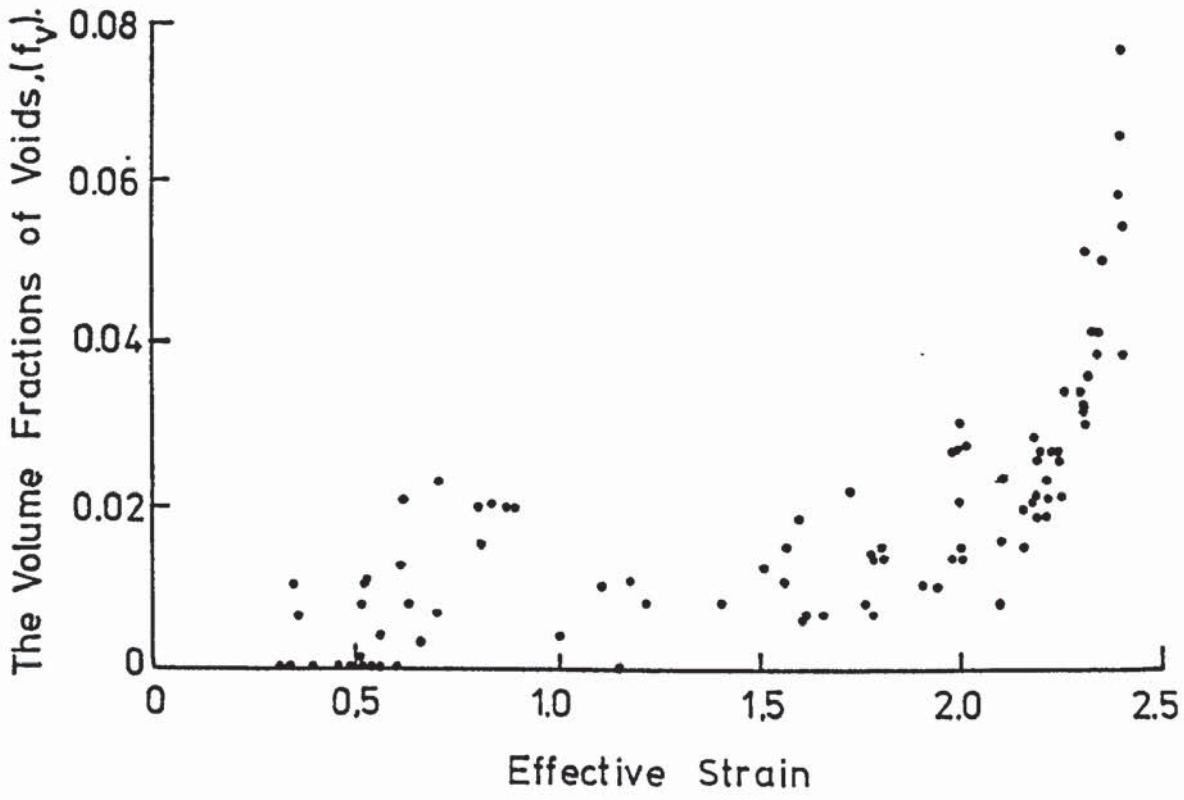

FIG.50.

Steel A

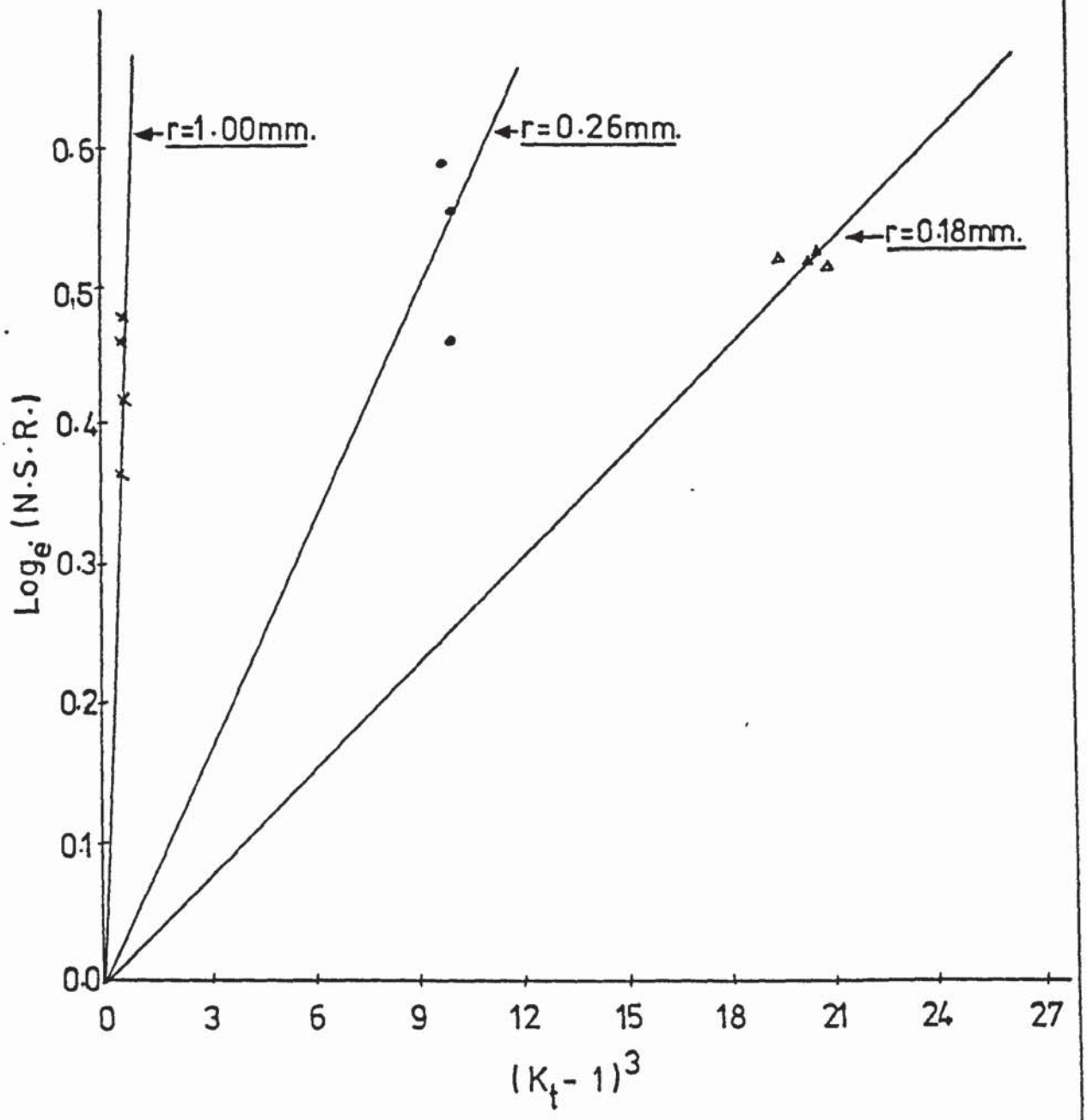

FIG.51.

Steel B

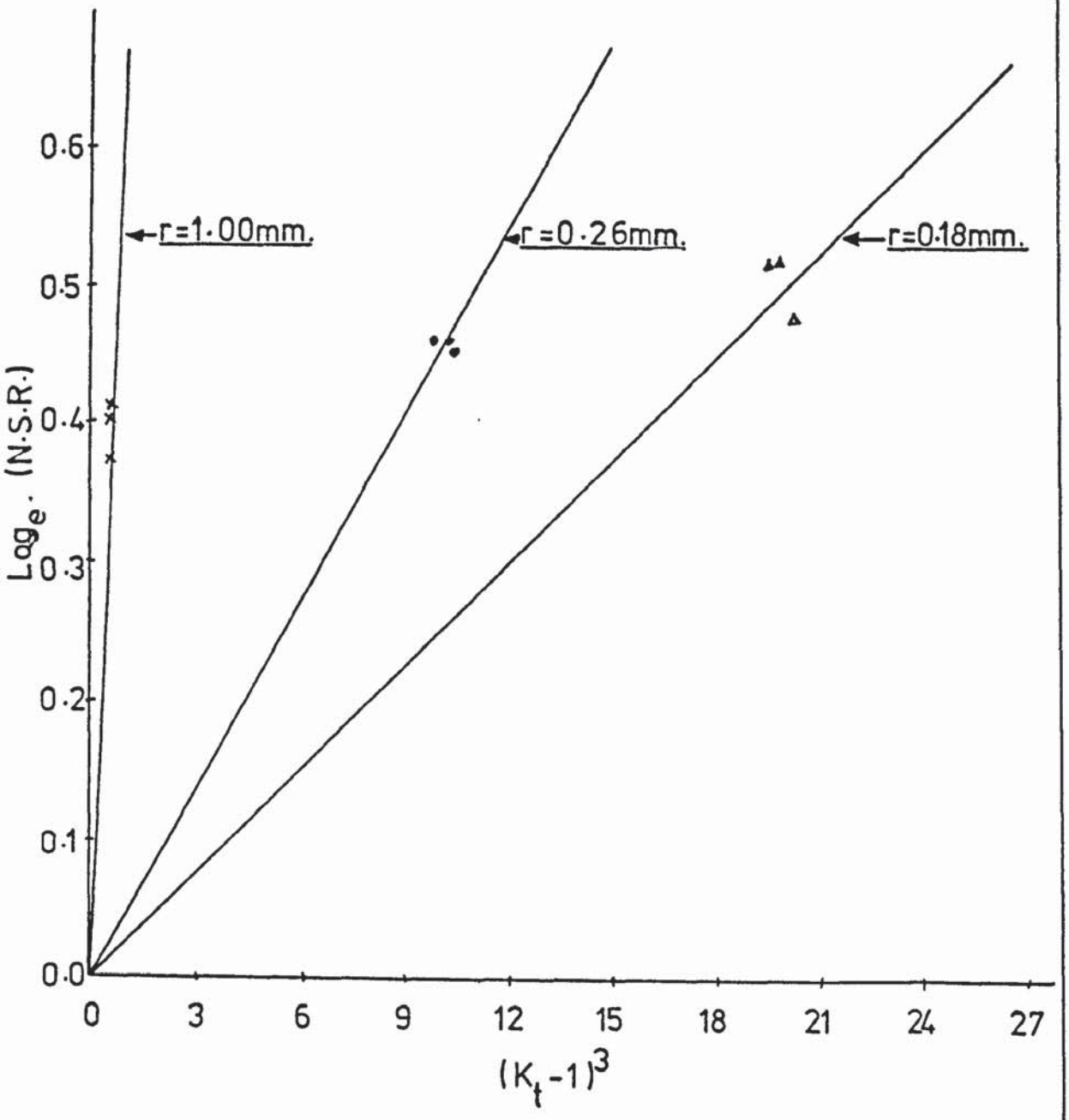

FIG·52.

Steel D10

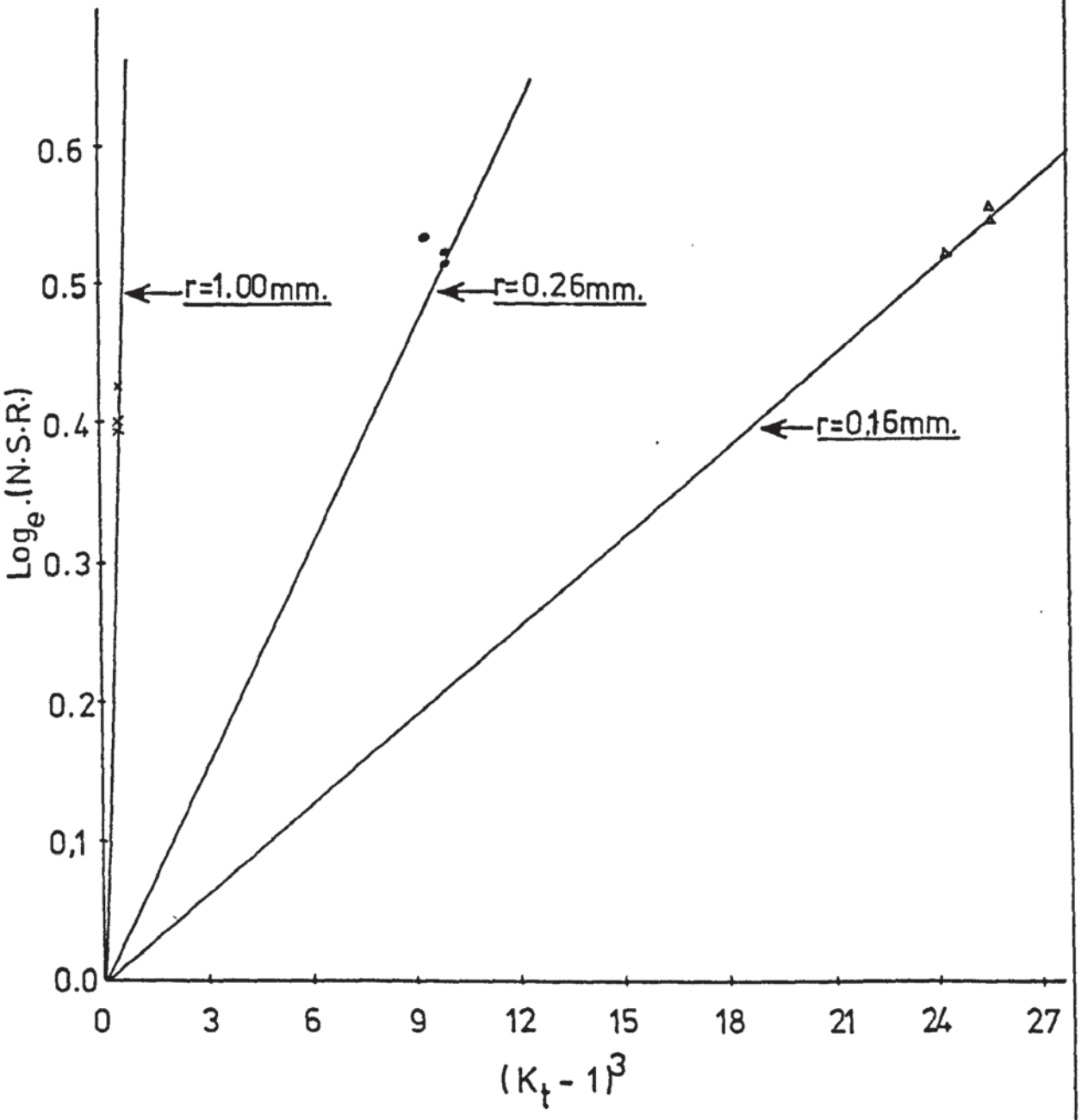

FIG.53.

Steel D11

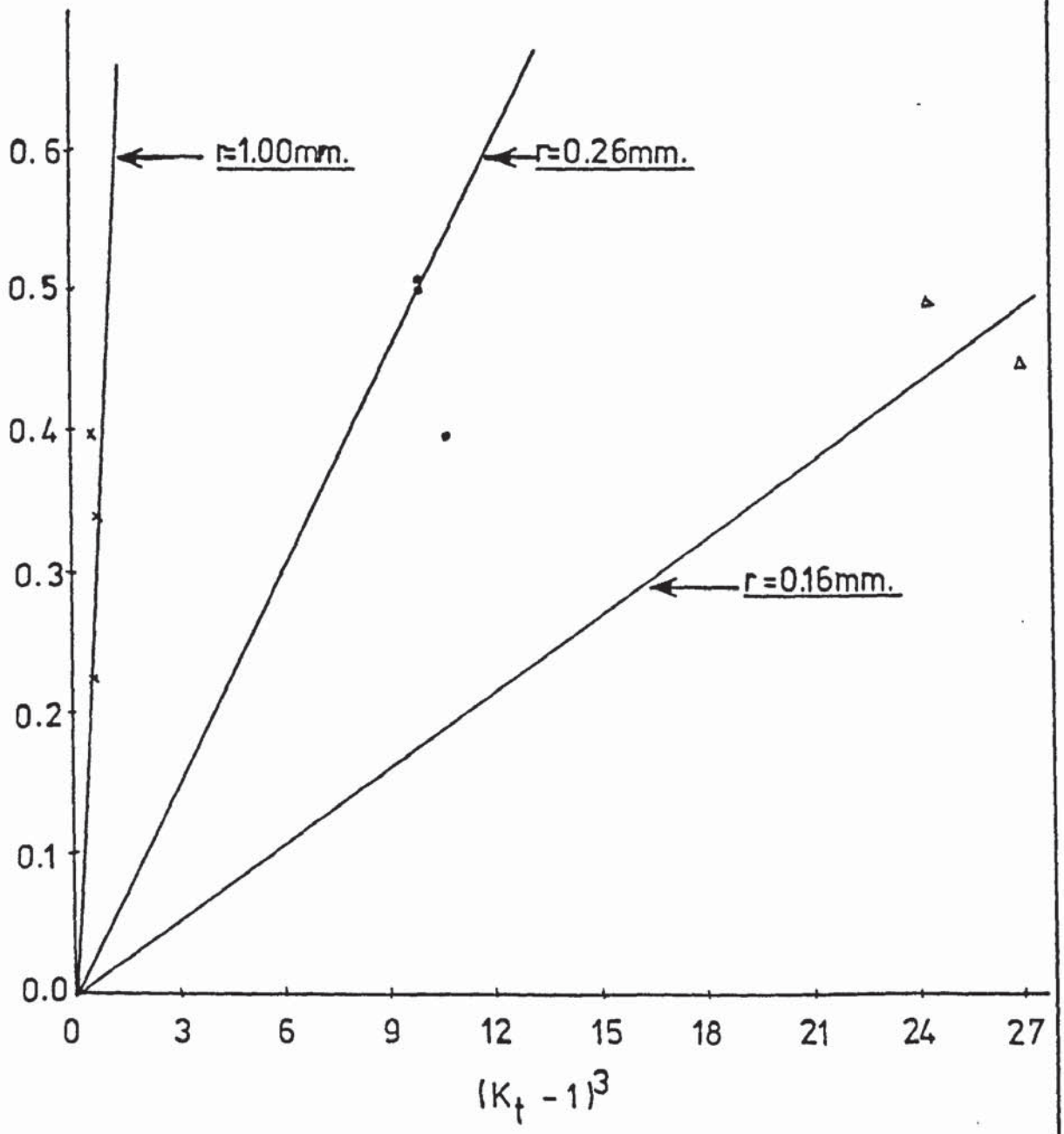

FIG.54.

Steel D12

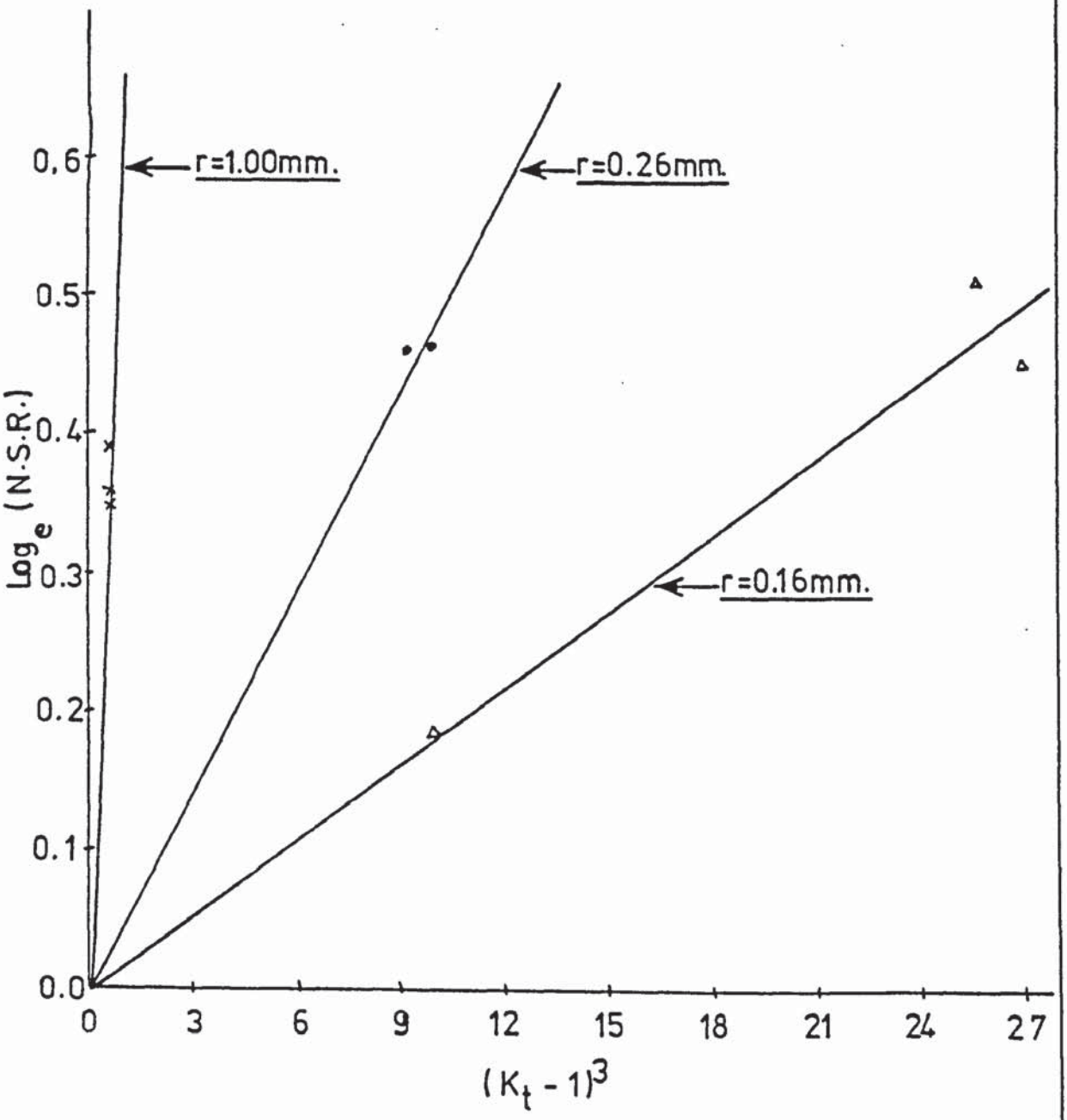

FIG.55.

Steel D20

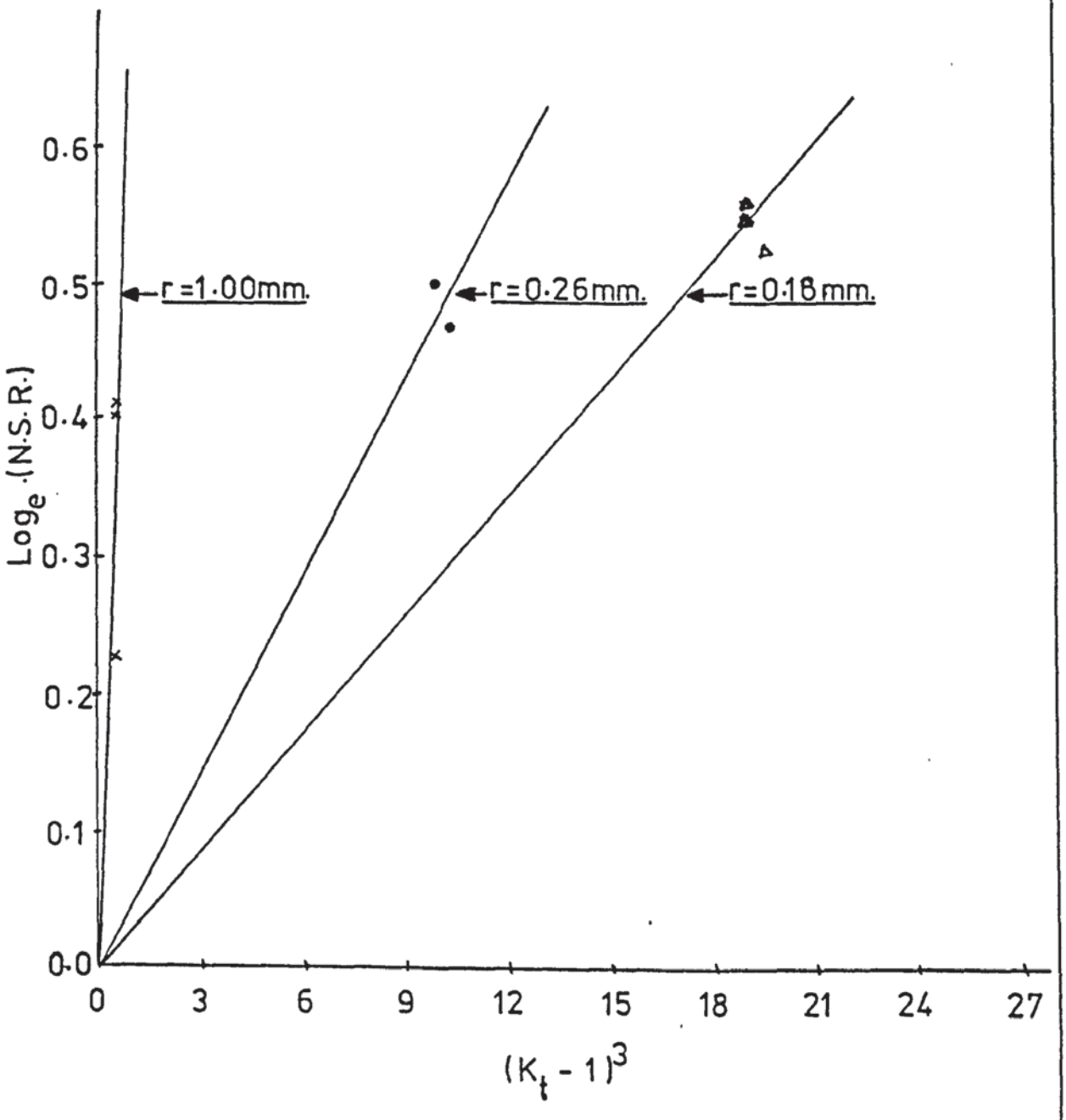

FIG.56.

Steel D21

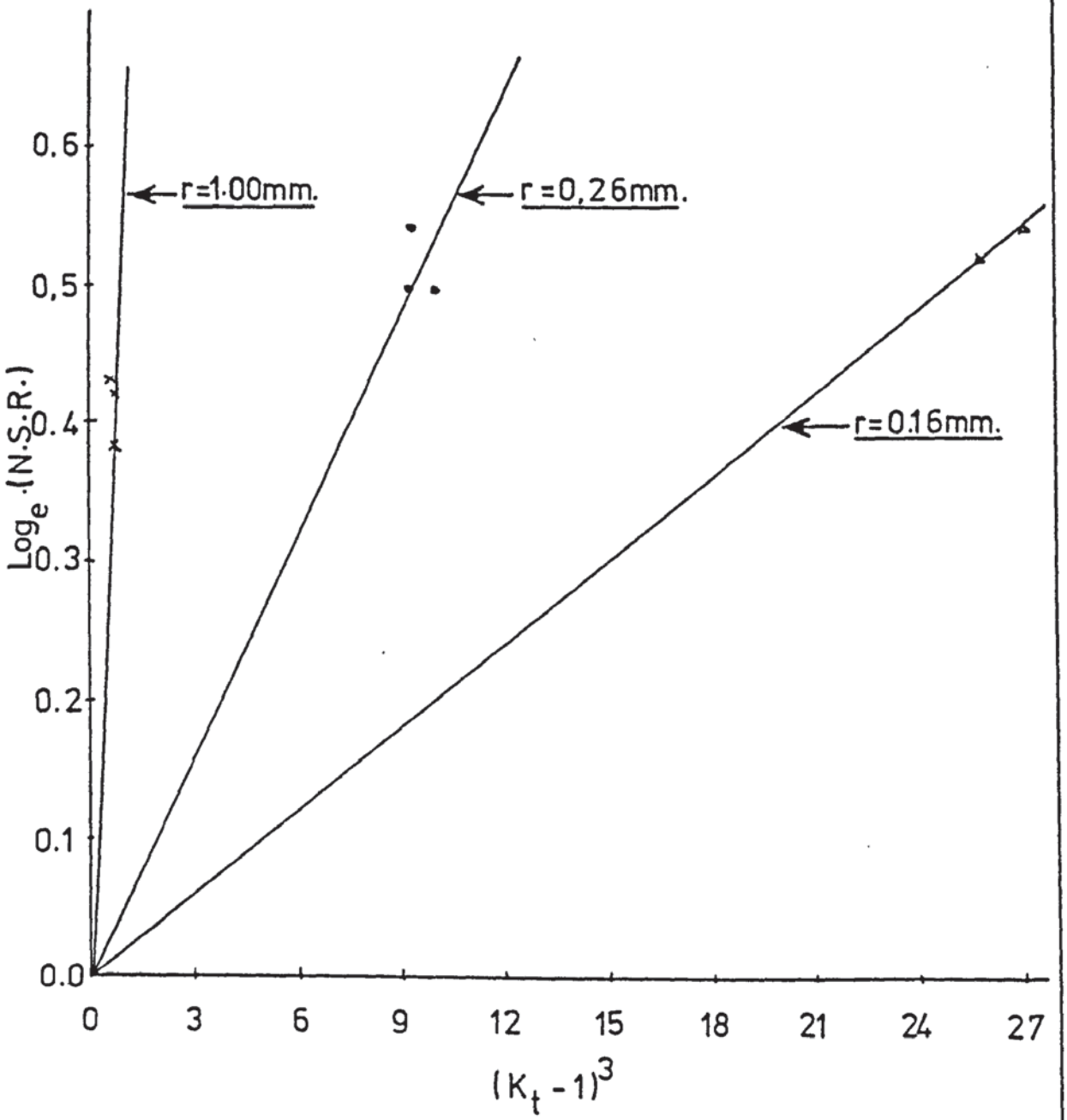

FIG·57.

Steel D 22

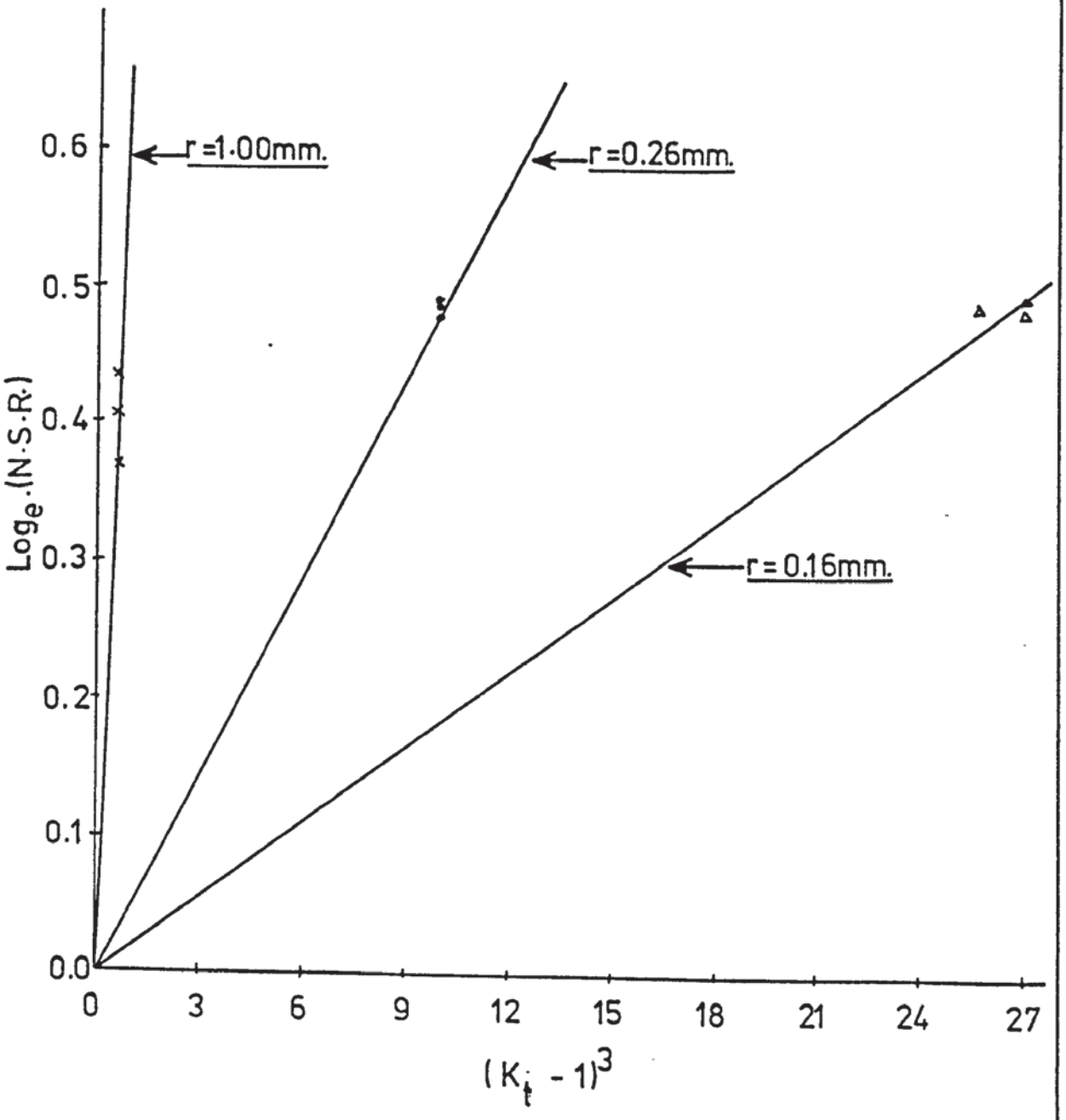

FIG·58.

Steel D30

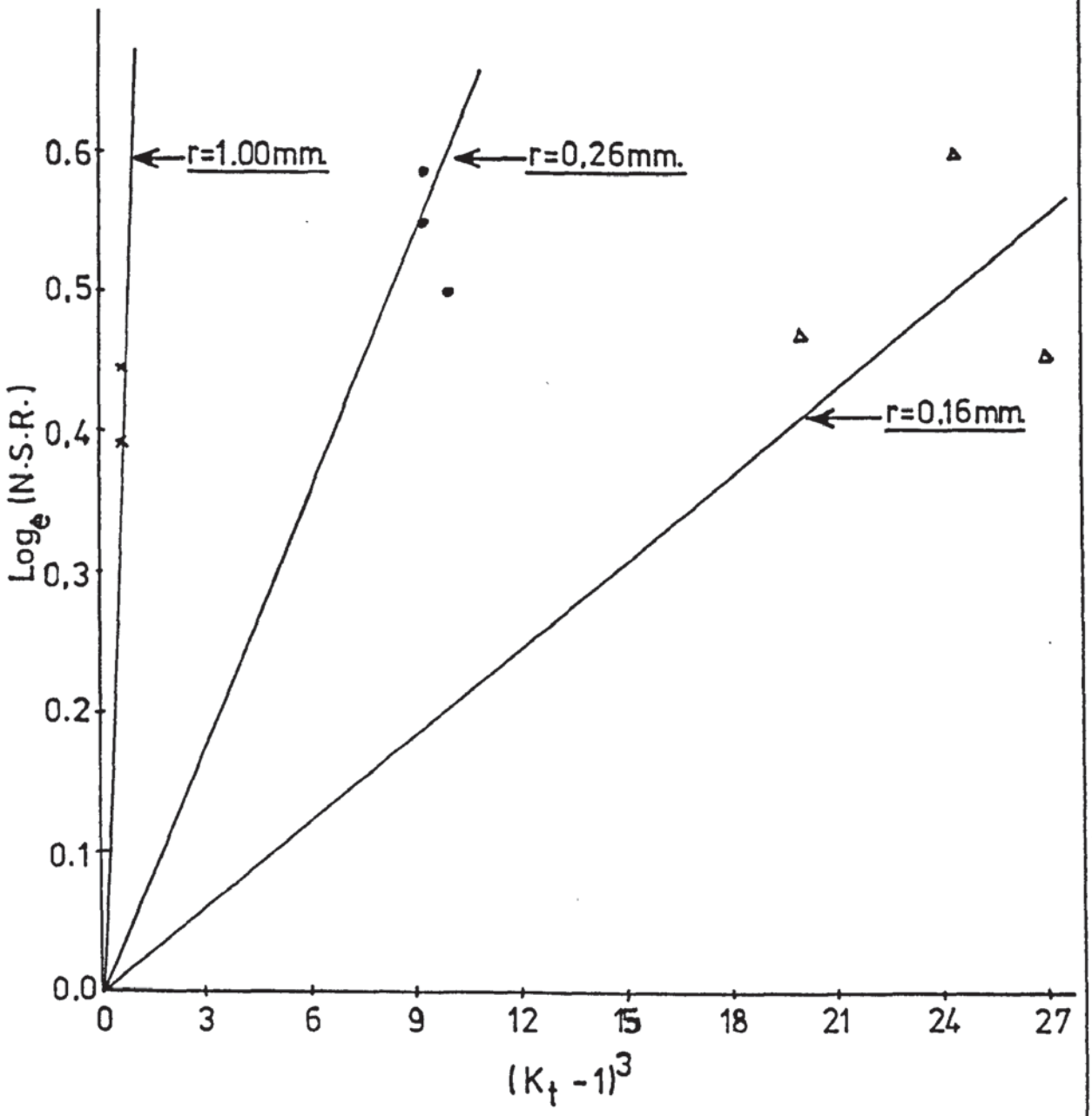

FIG.59.

Steel D31

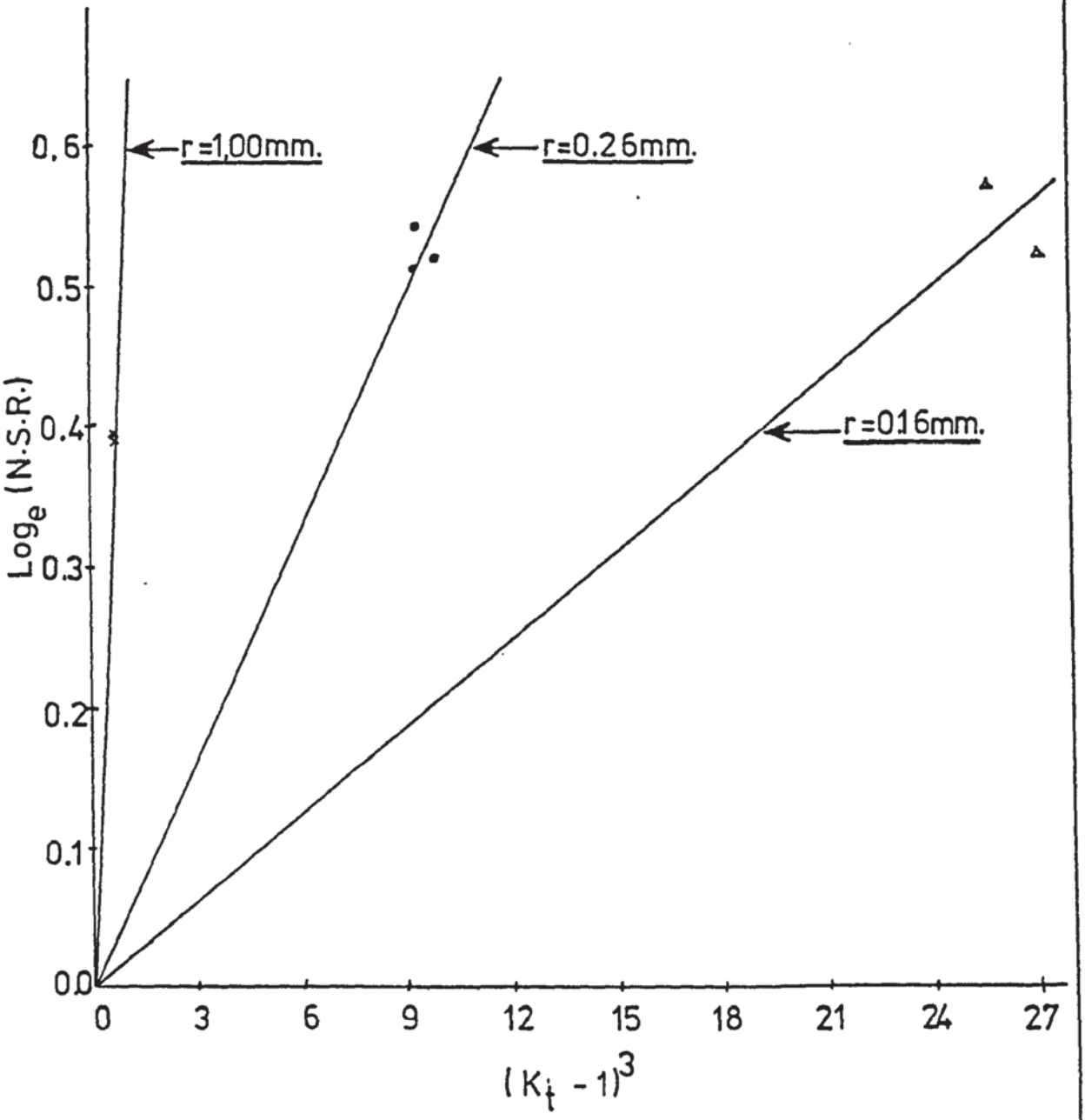

FIG. 60.

Steel D32

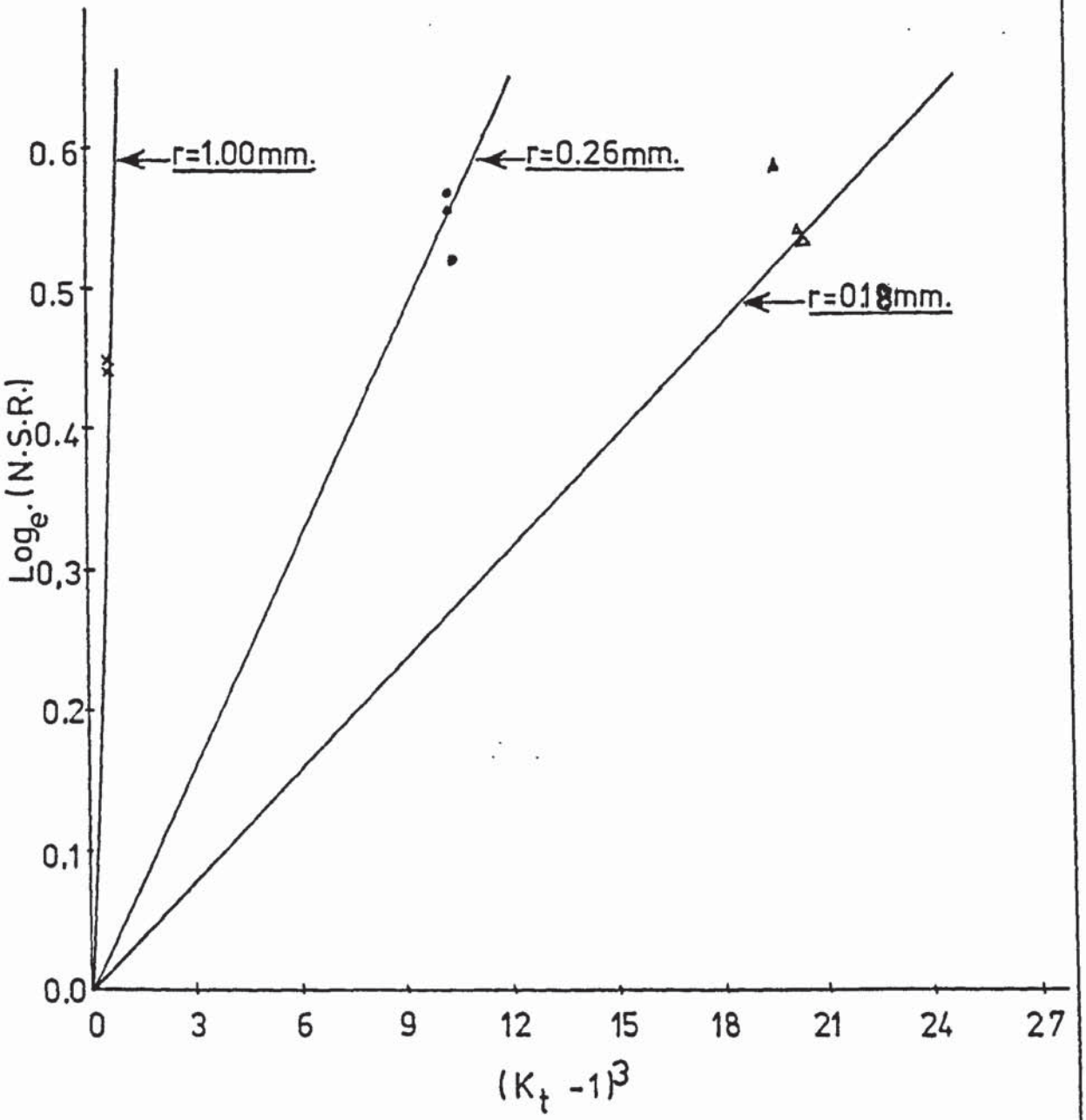

FIG. 61.

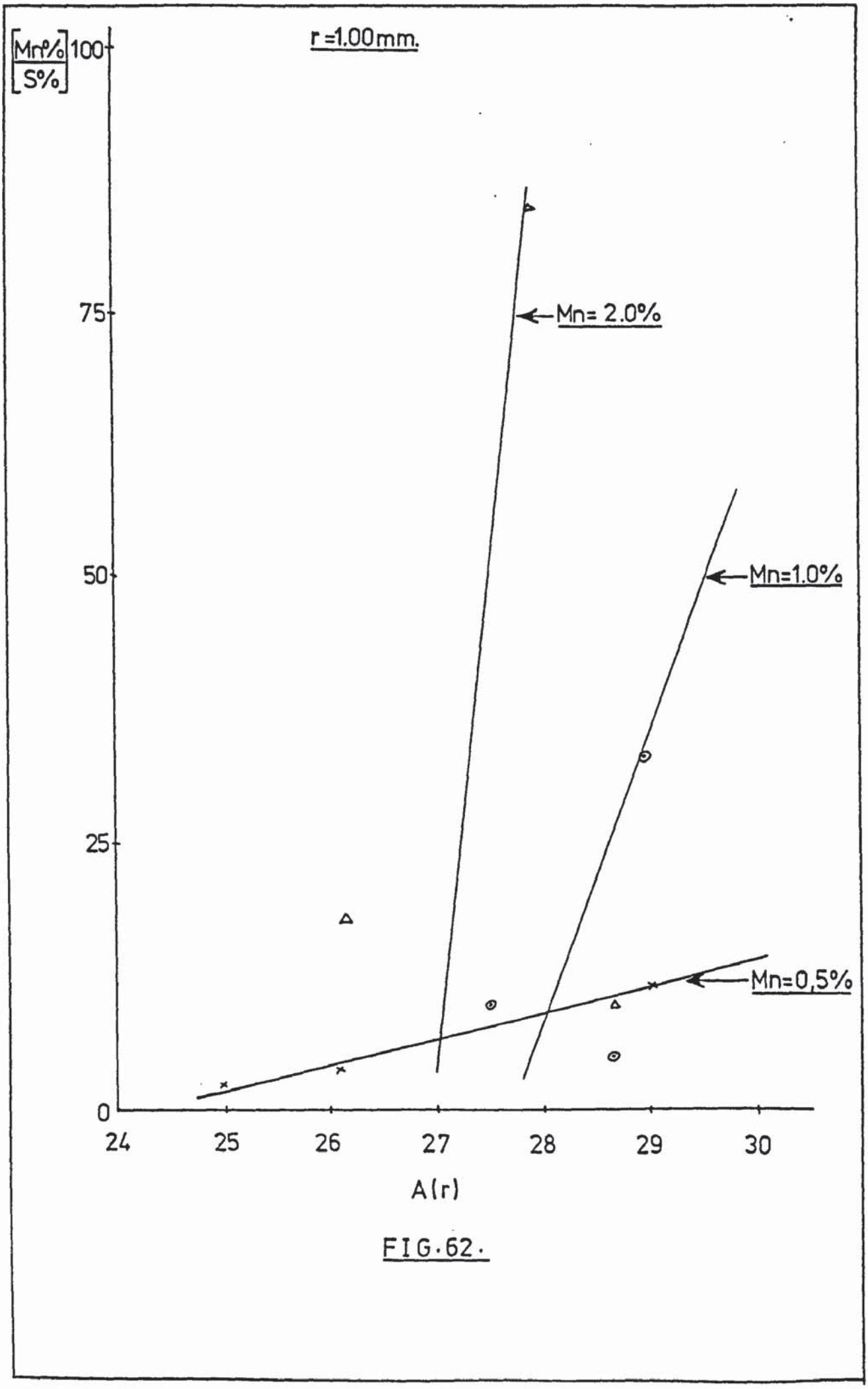

FIG.62.

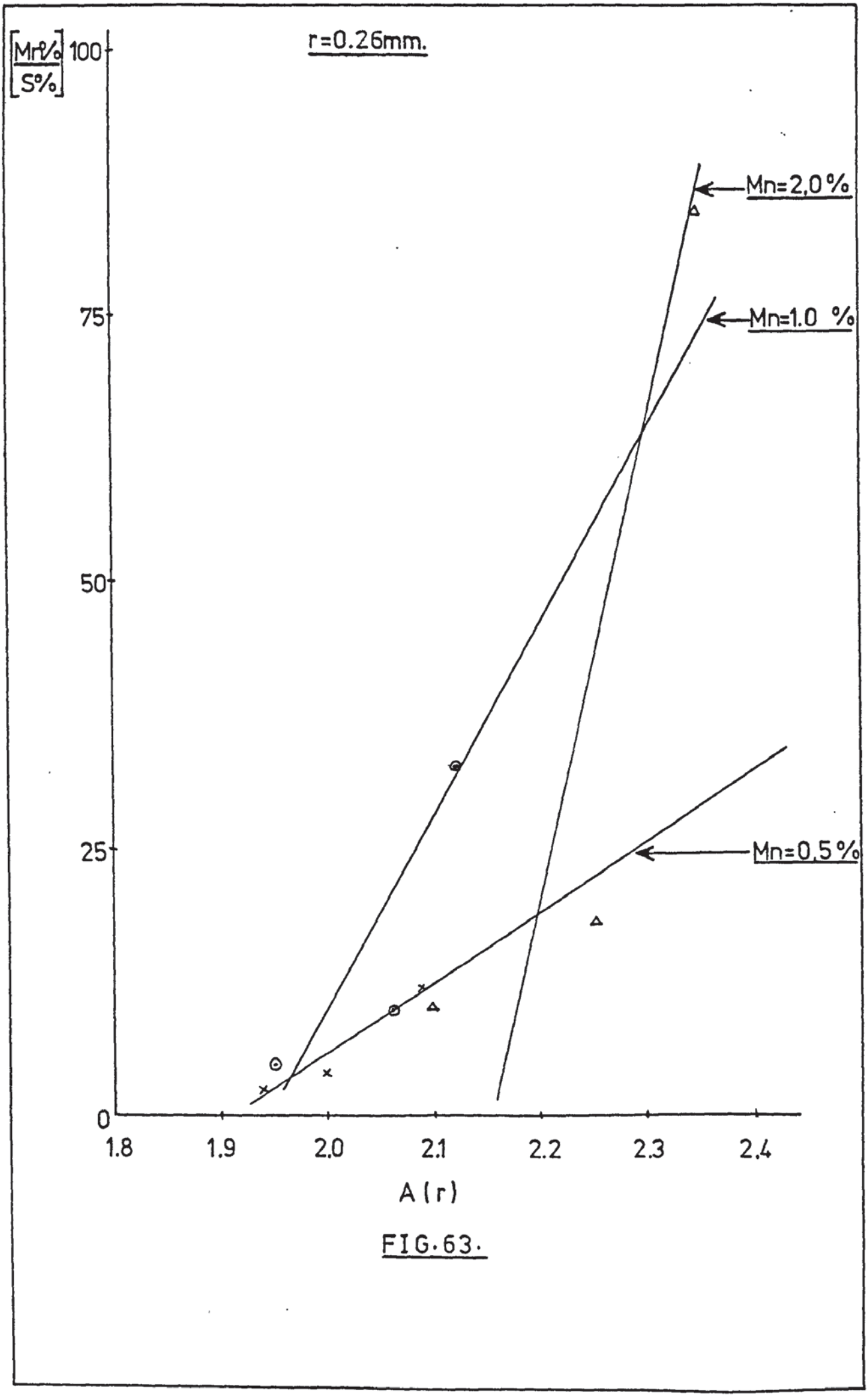

FIG.63.

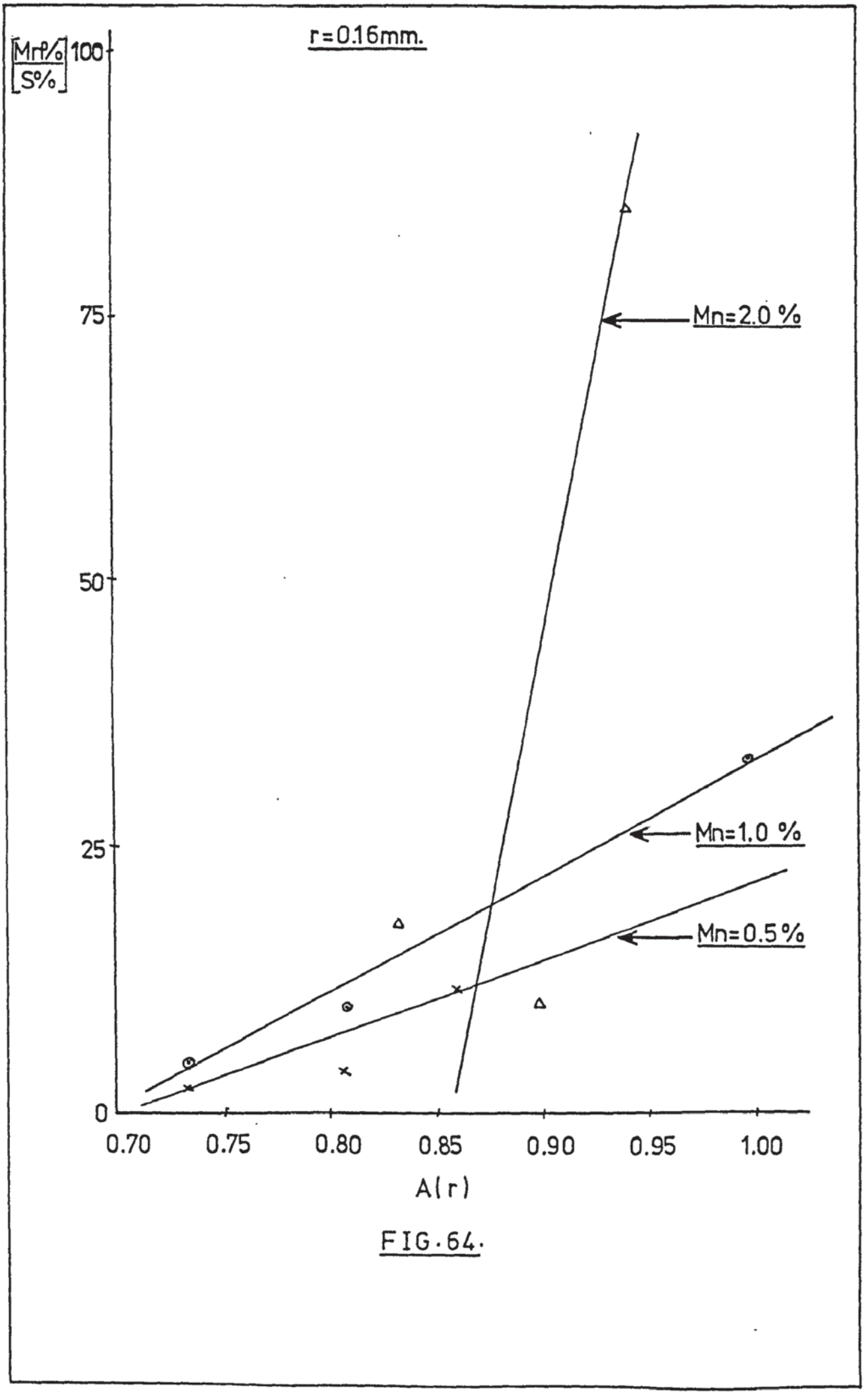
r=0.16mm.
[Mn%/S%]
100
75
50
25
0
0.70
0.75
0.80
0.85
0.90
0.95
1.00
A(r)
Mn=2.0 %
Mn=1.0 %
Mn=0.5 %

FIG.64.

Steel A

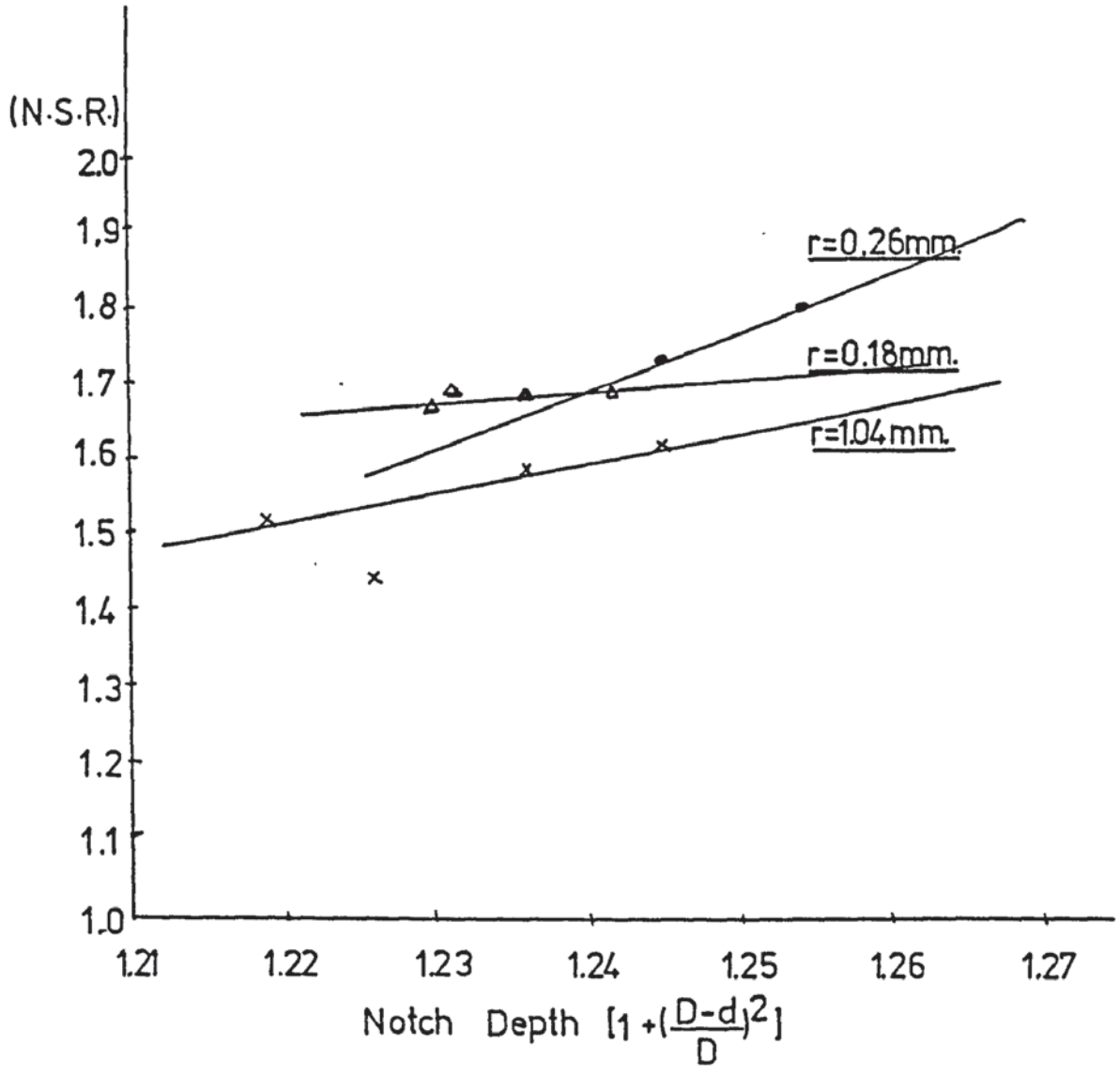

FIG.65.

Steel B

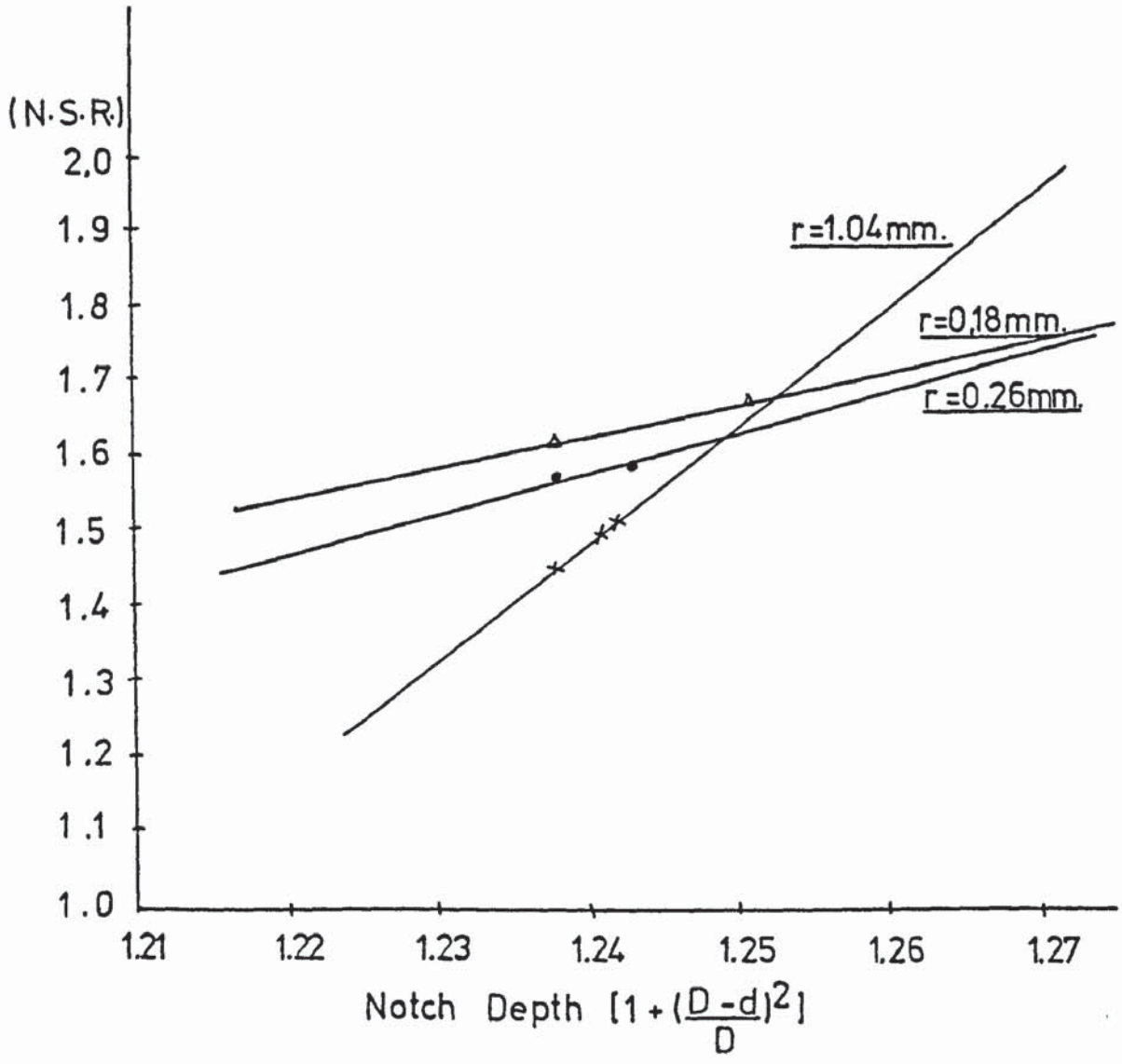

FIG. 66.

Steel D10

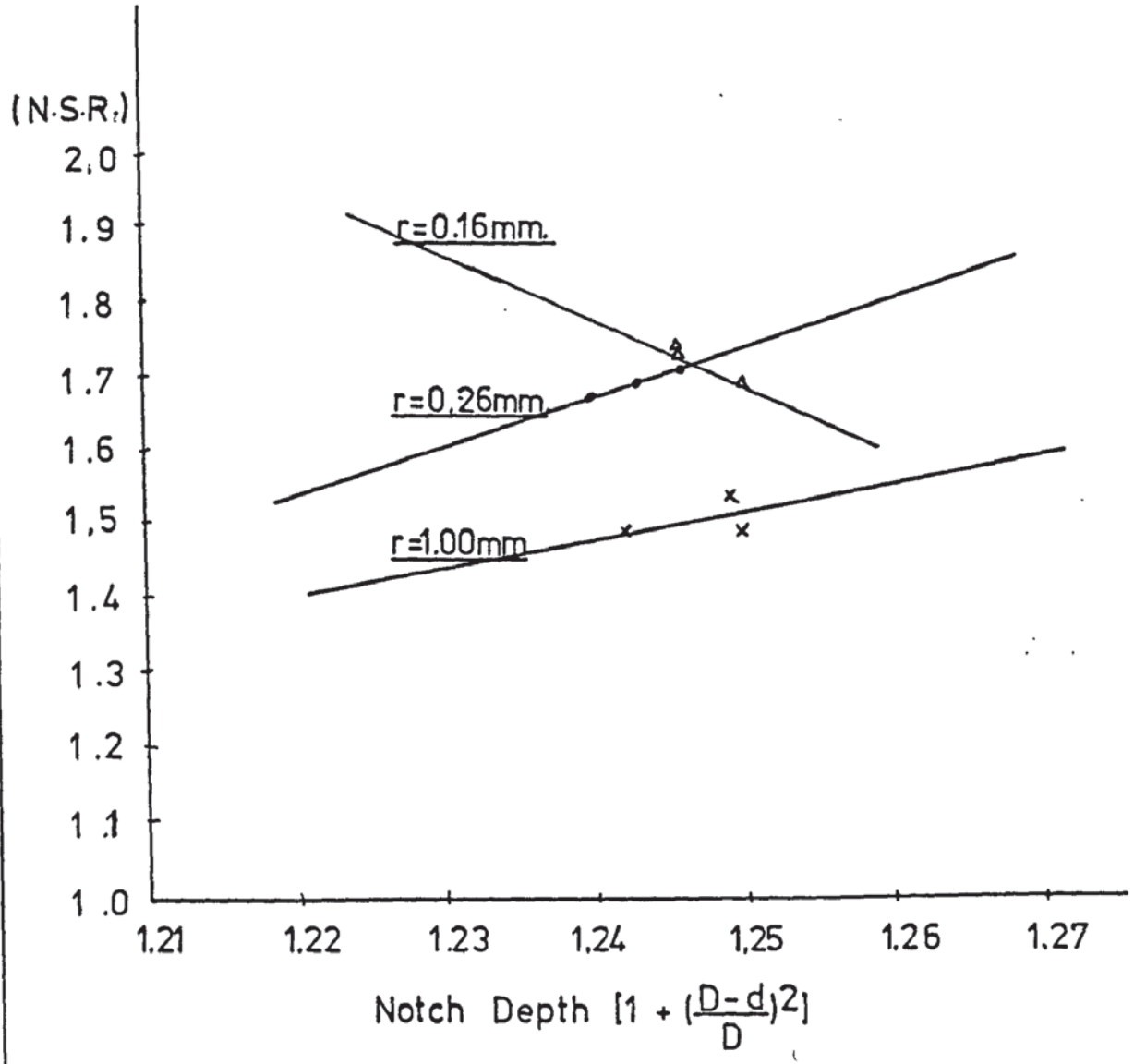

FIG.67.

Steel D11

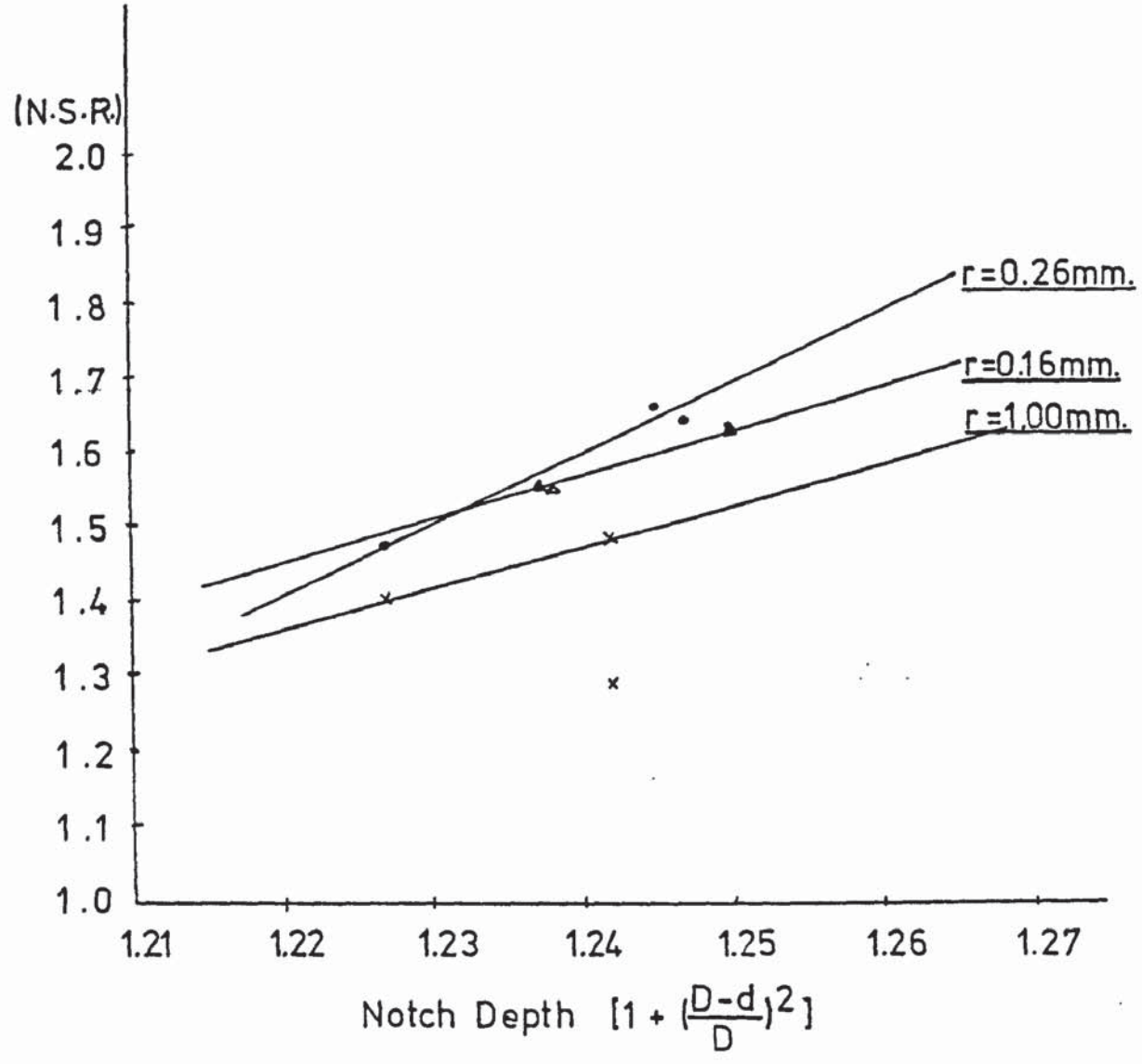

FIG. 68.

Steel D12

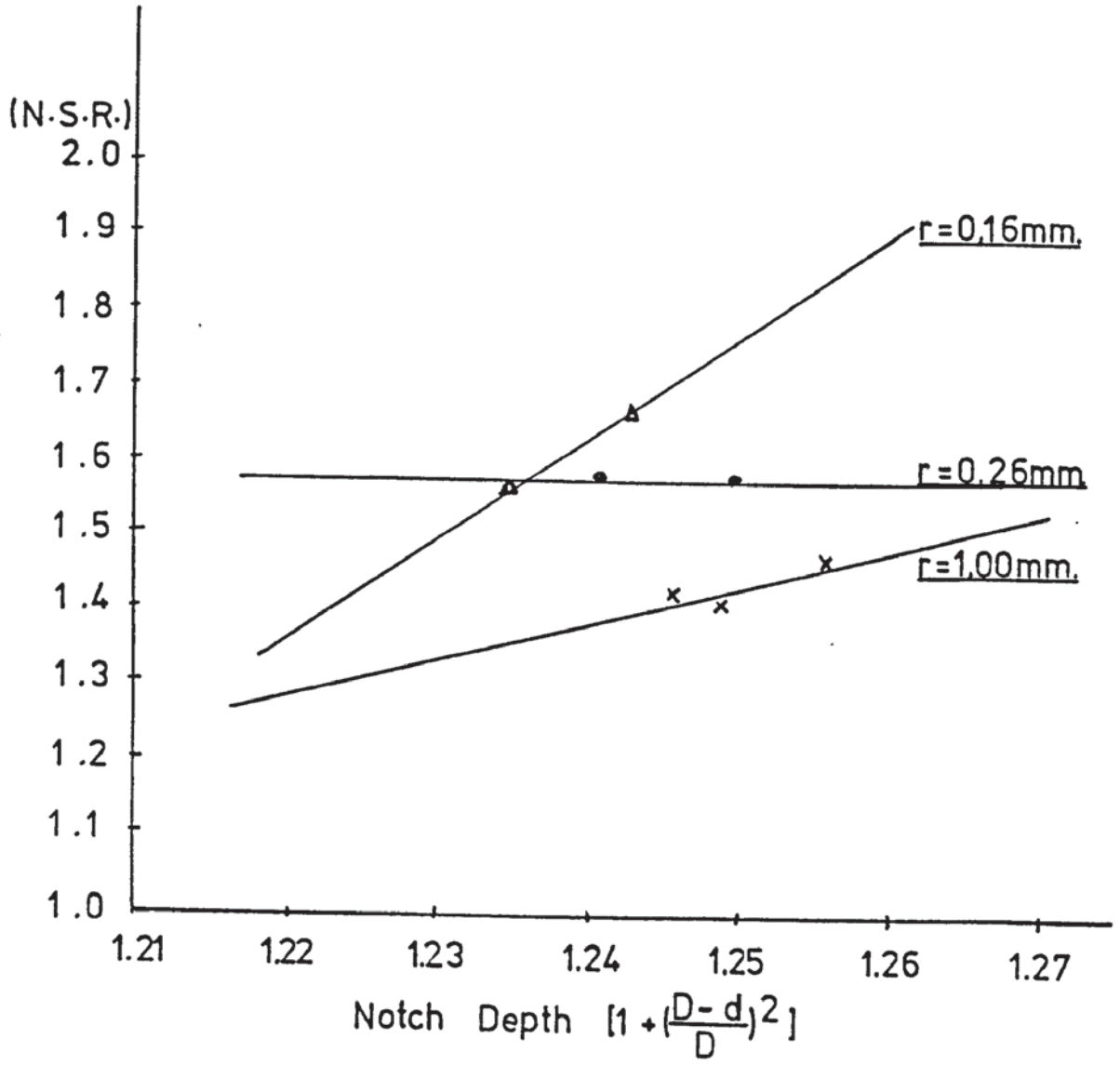

FIG.69.

Steel D20

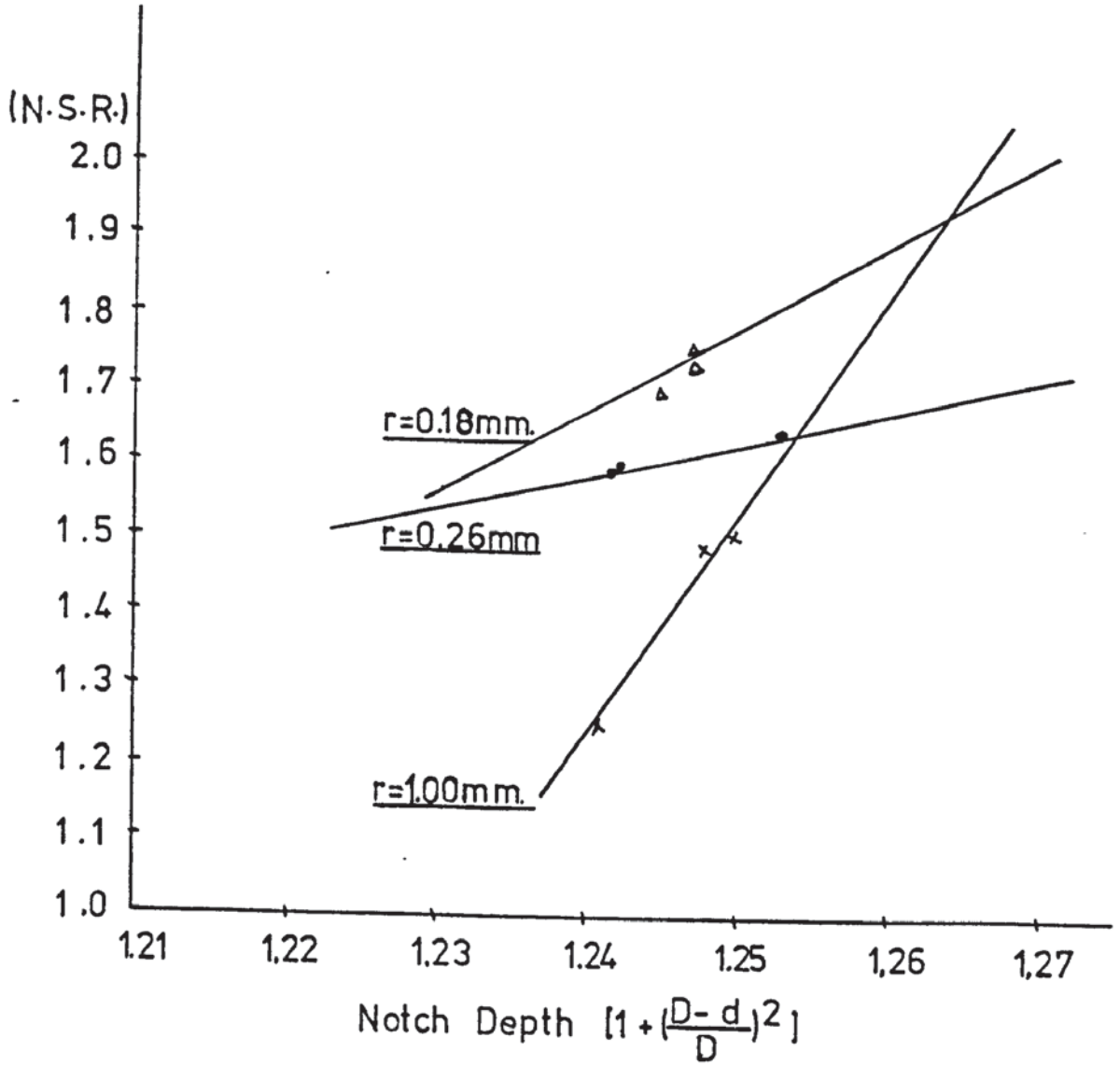

FIG·70.

Steel D21

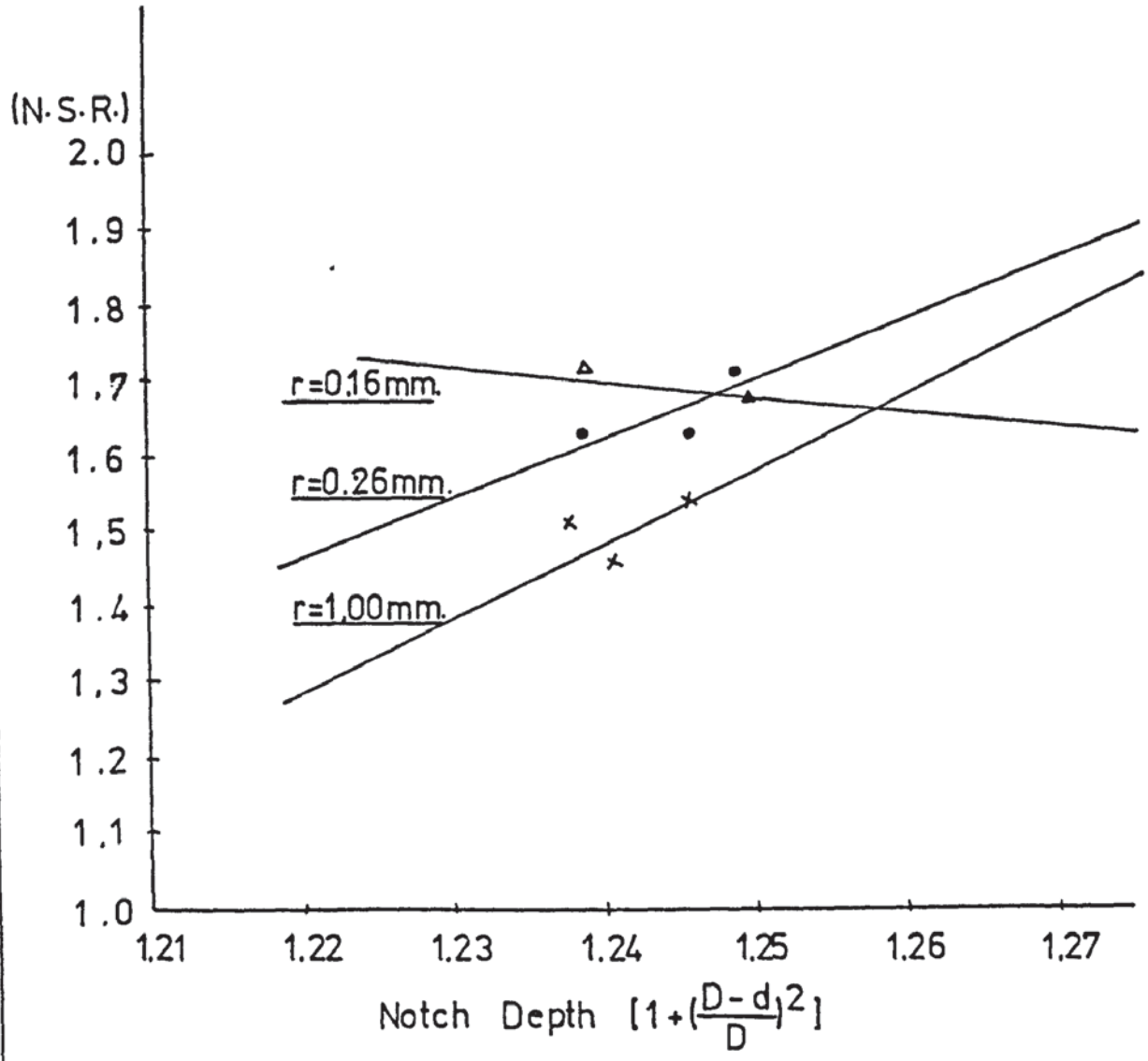

FIG.71.

Steel D22

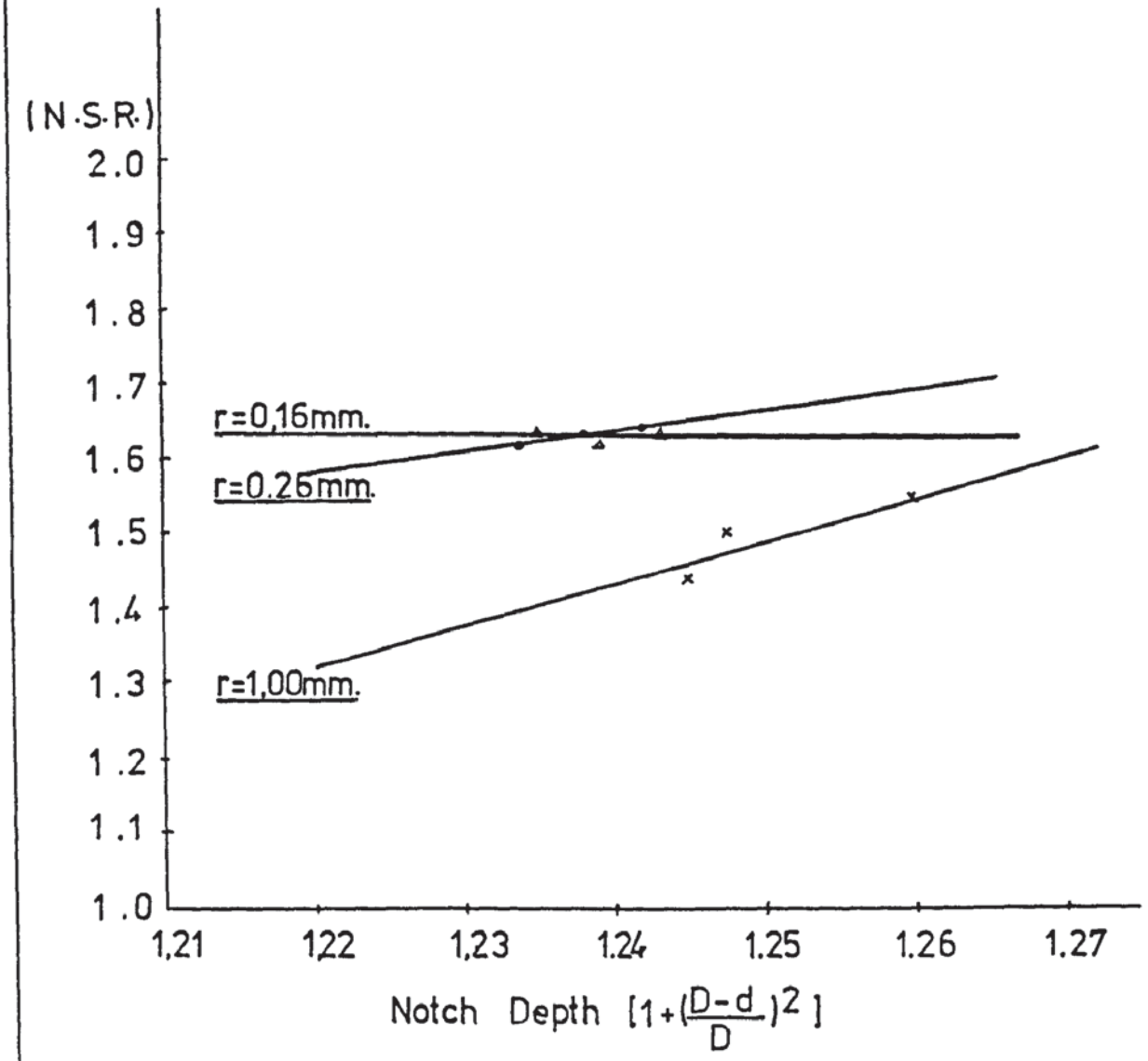

FIG. 72.

Steel D30

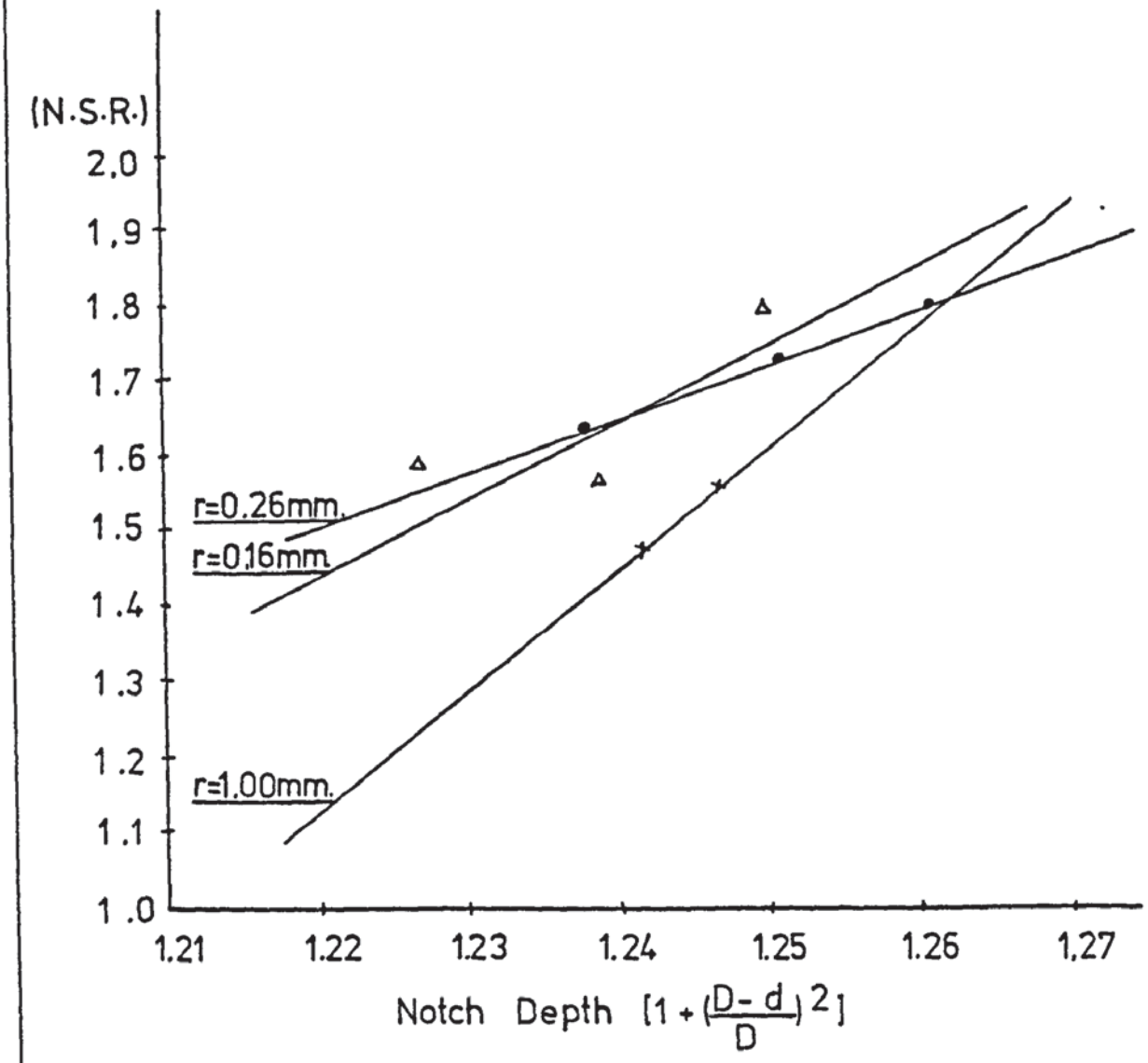

FIG.73.

Steel D31

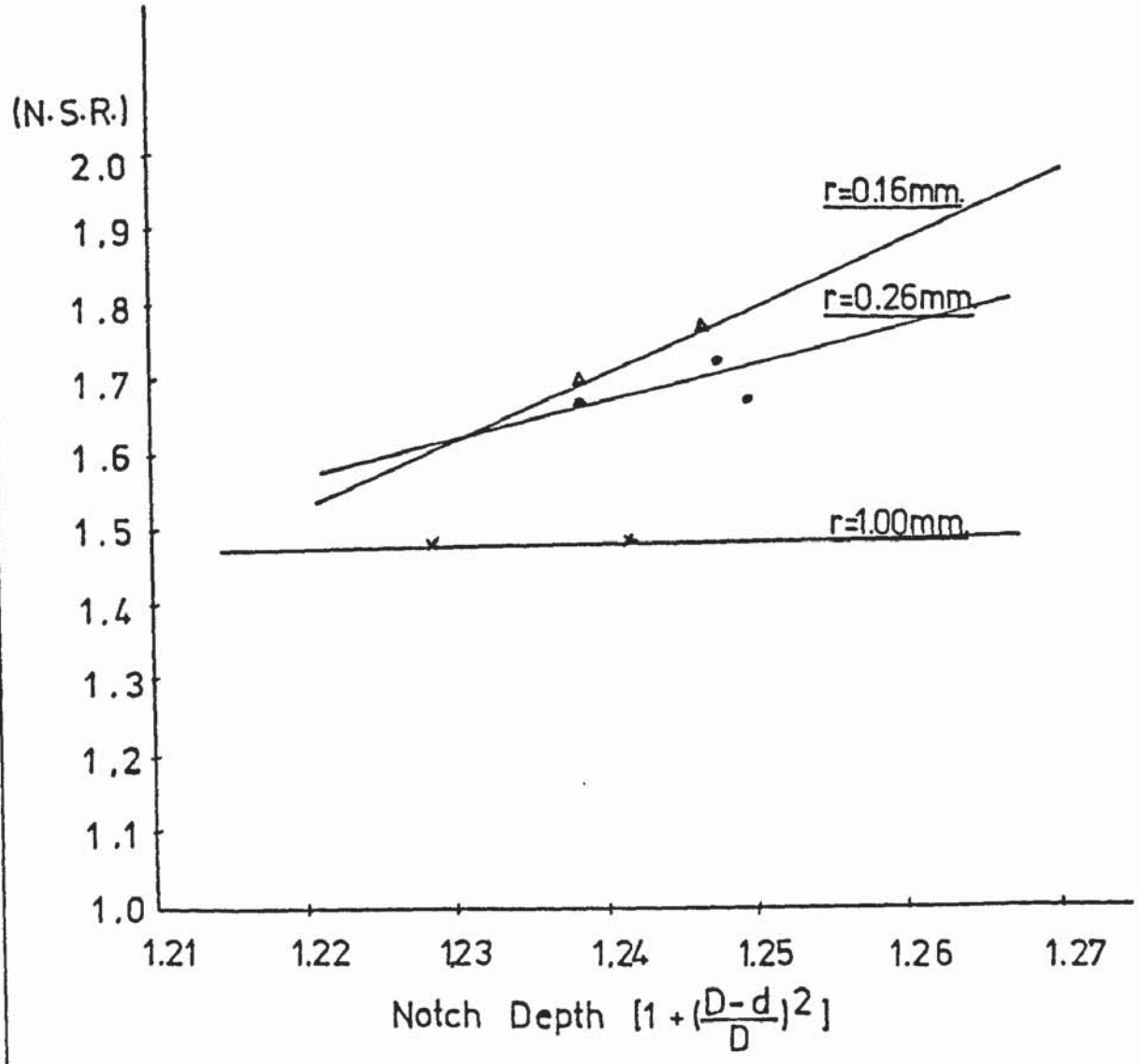

FIG. 74.

Steel D 32

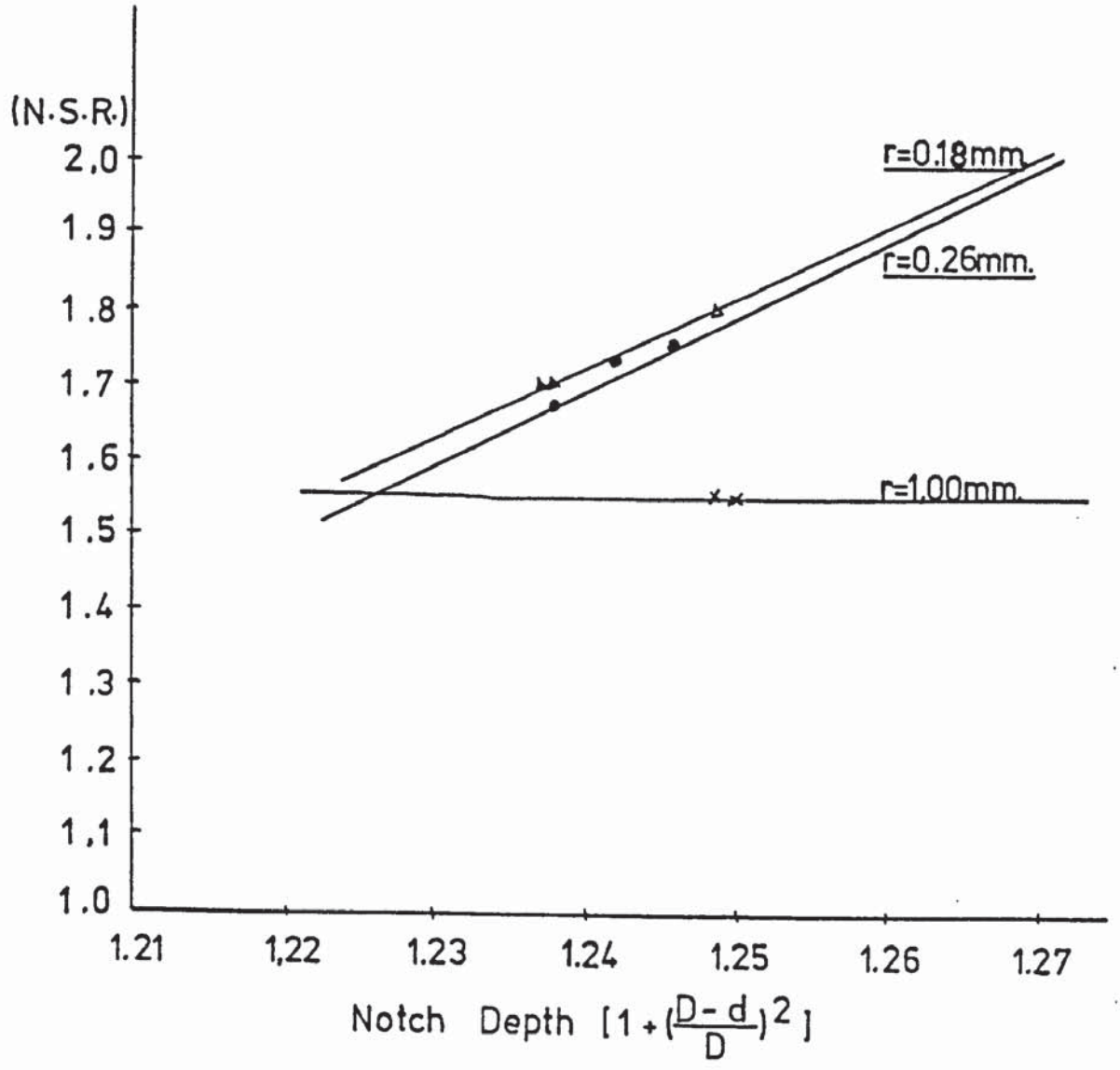

FIG. 75.

Steel A

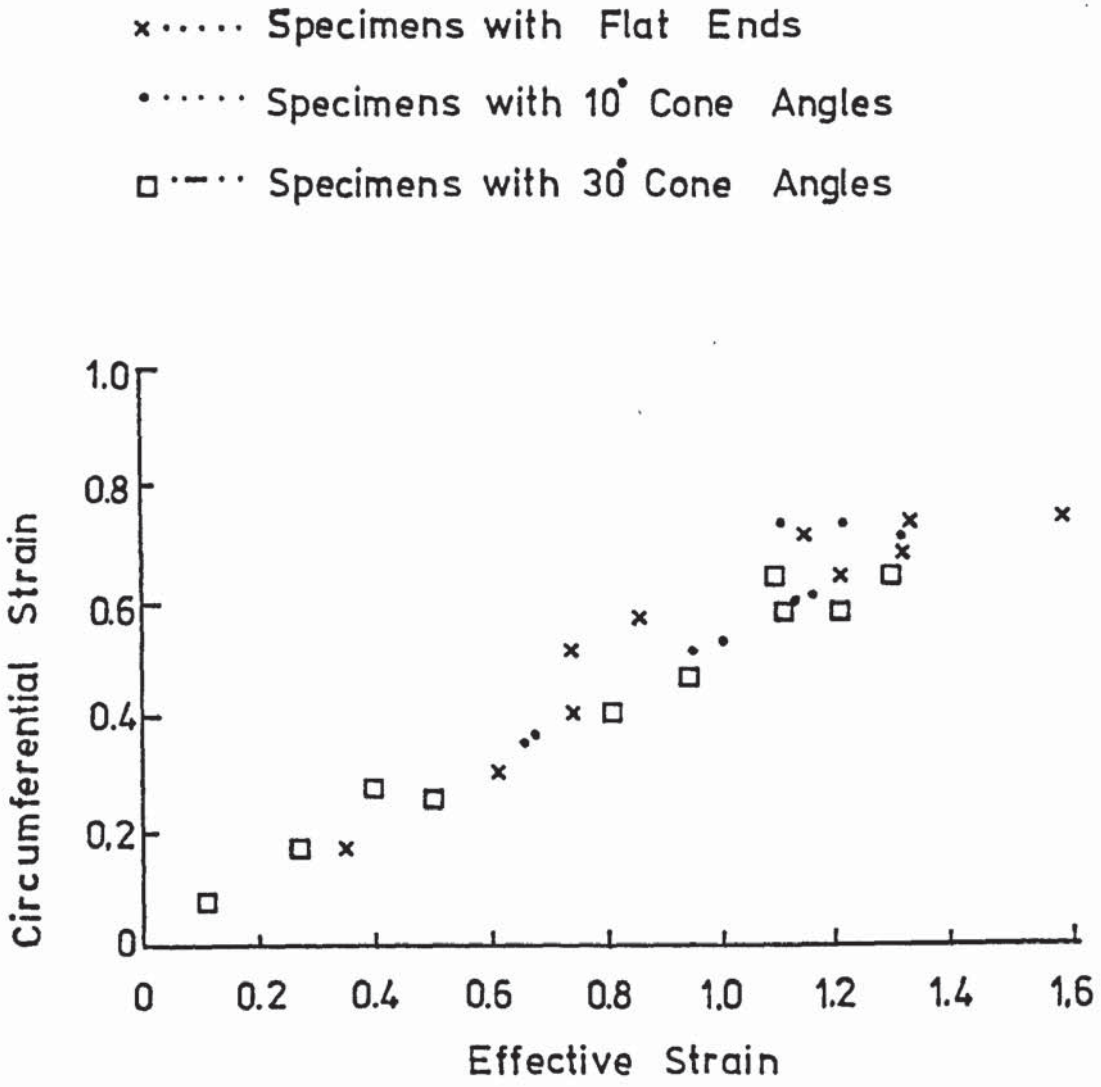

FIG.76.

Steel B

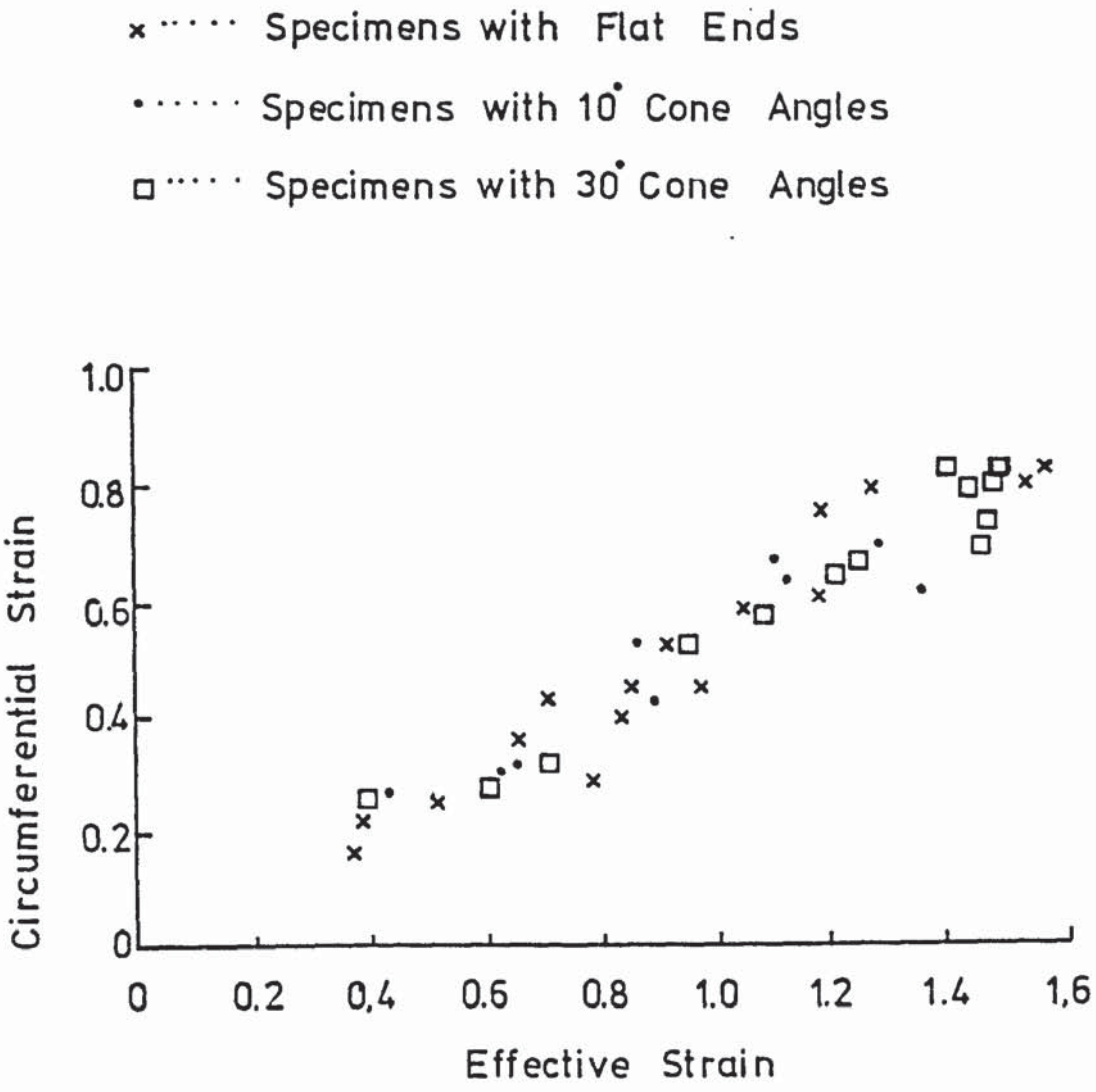

FIG. 77.

Steel C

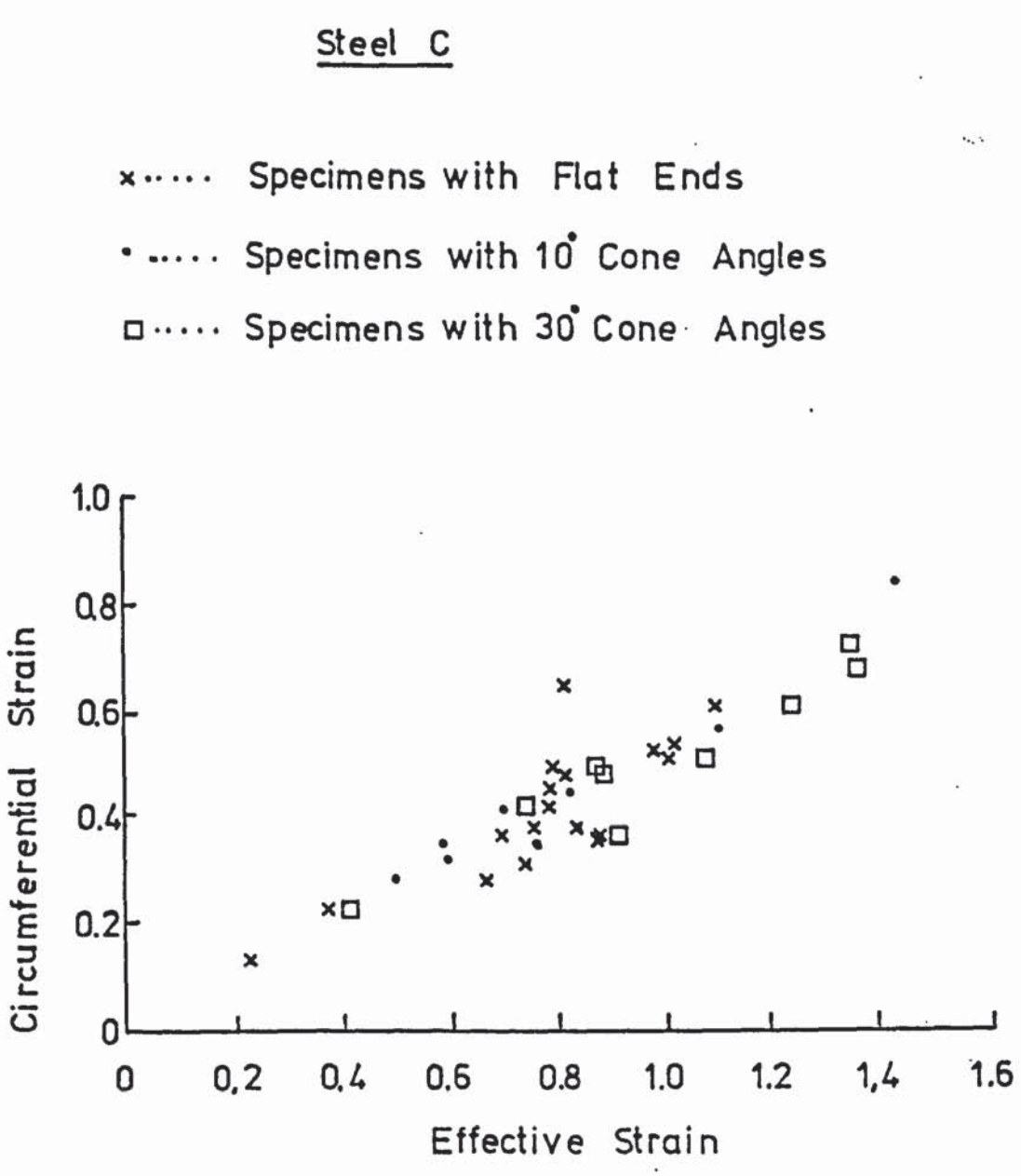

FIG. 78.

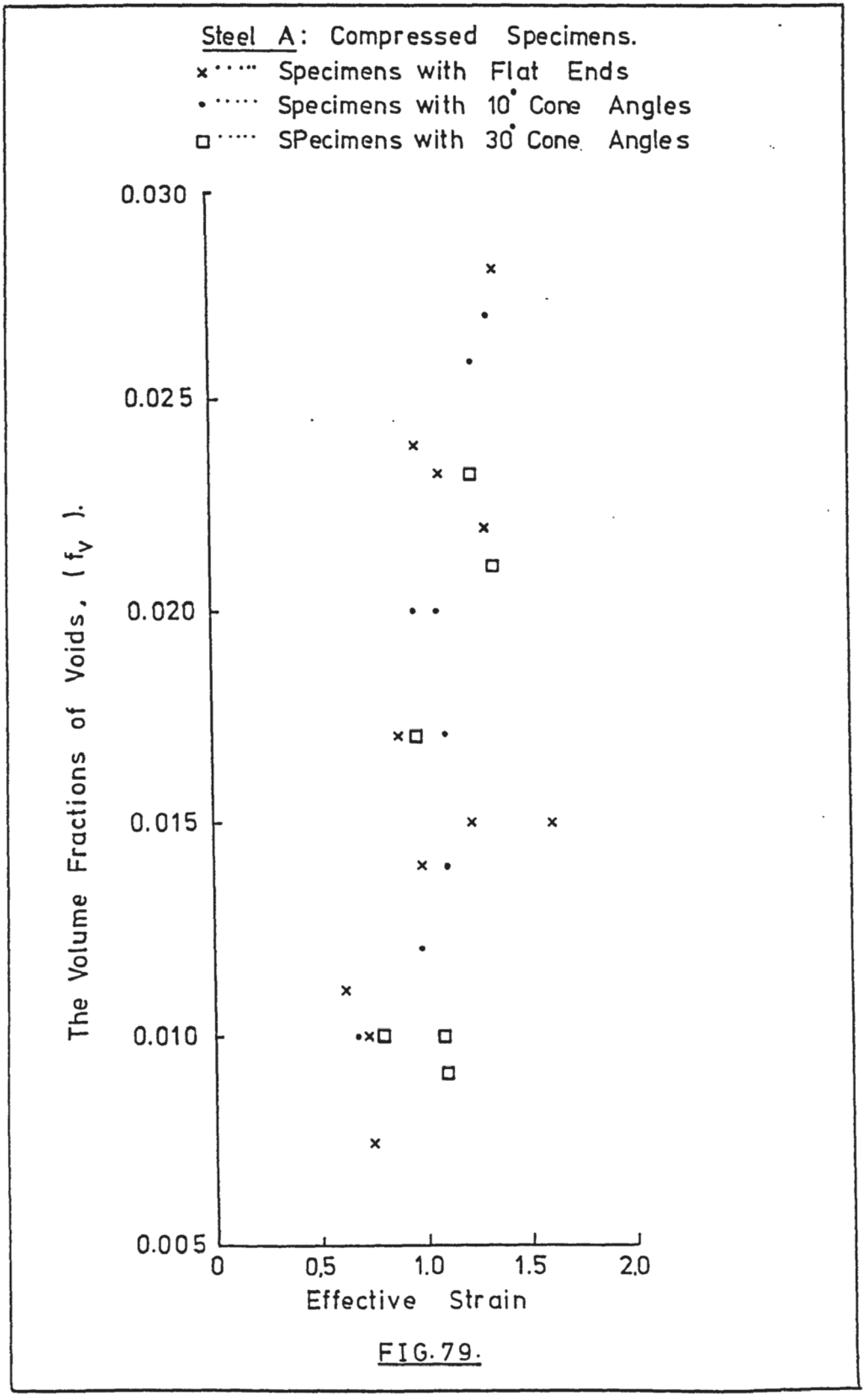
Steel A: Compressed Specimens.
× ···· Specimens with Flat Ends
• ····· Specimens with 10° Cone Angles
□ ····· SPecimens with 30° Cone Angles
0.030
0.025
0.020
0.015
0.010
0.005
The Volume Fractions of Voids, (f_V).
0
0,5
1.0
1.5
2.0
Effective Strain

FIG. 79.

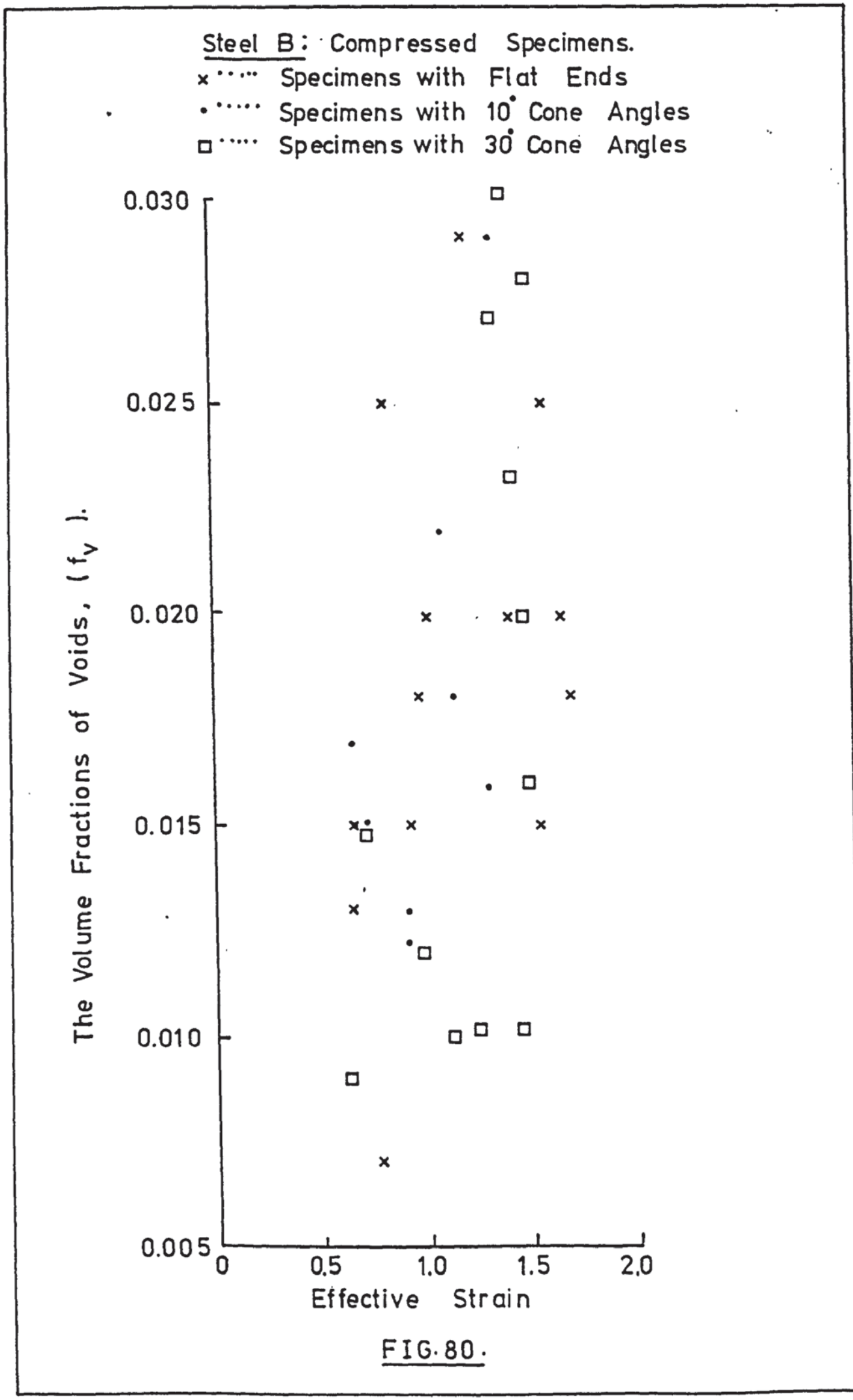
Steel B: Compressed Specimens.
Specimens with Flat Ends
Specimens with 10° Cone Angles
Specimens with 30° Cone Angles
0.030
0.025
0.020
0.015
0.010
0.005
The Volume Fractions of Voids, (f_v).
0
0.5
1.0
1.5
2.0
Effective Strain

FIG. 80.

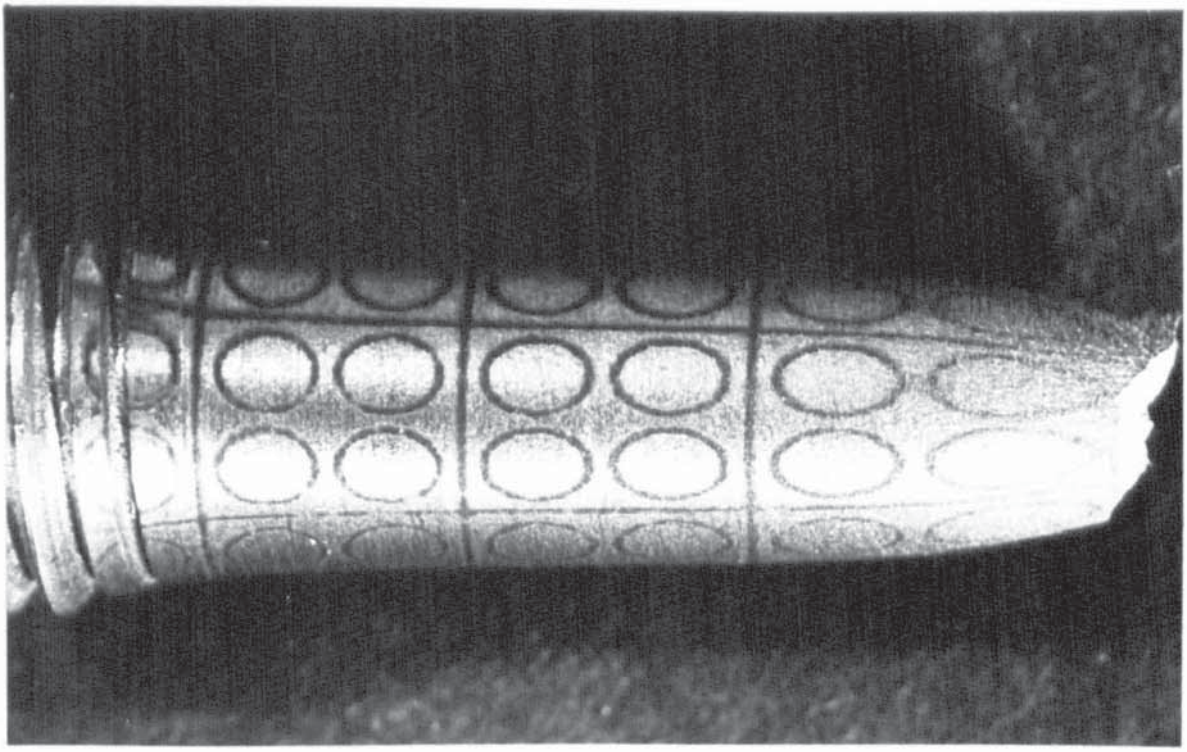

(a) Steel A.

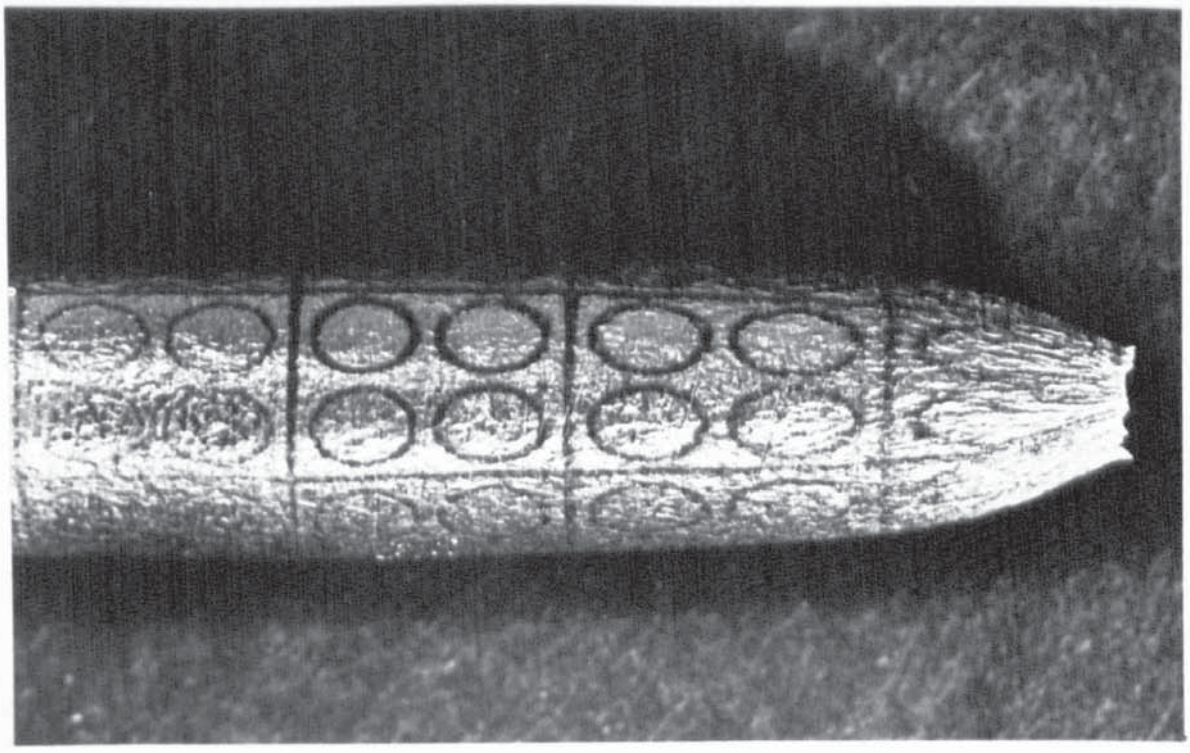

(b) Steel C.

FIG. 81. Gridmarks on the surface of a fractured tensile specimens.

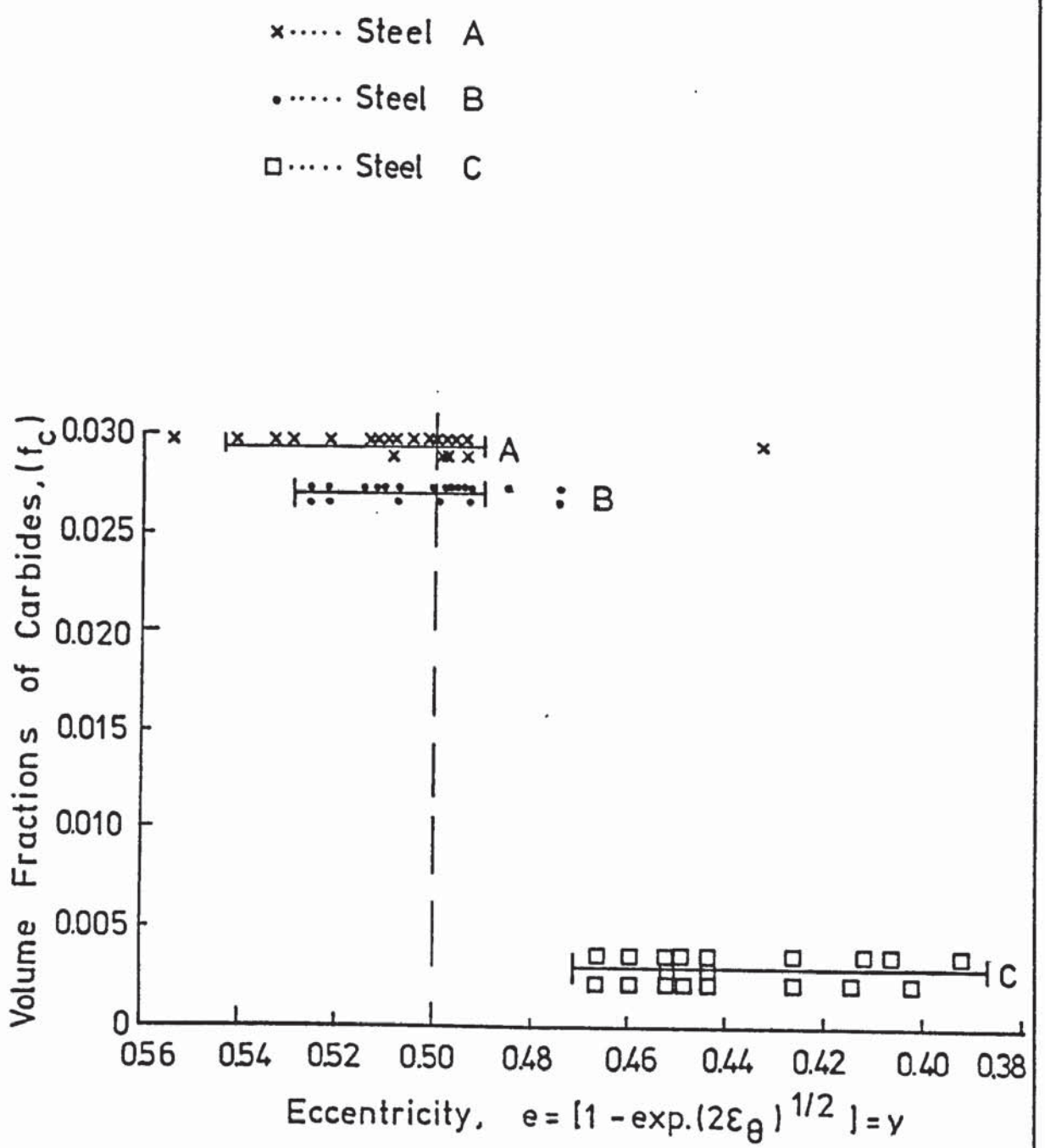
× ····· Steel A
• ····· Steel B
□ ····· Steel C
Volume Fractions of Carbides, (f_c)
0.030
0.025
0.020
0.015
0.010
0.005
0
A
B
C
0.56
0.54
0.52
0.50
0.48
0.46
0.44
0.42
0.40
0.38
Eccentricity, $e = [1 - \exp.(2\varepsilon_\theta)^{1/2}] = y$

FIG. 81.c.

FIG.82.a. Cracking of carbides, Steel B, 6K.

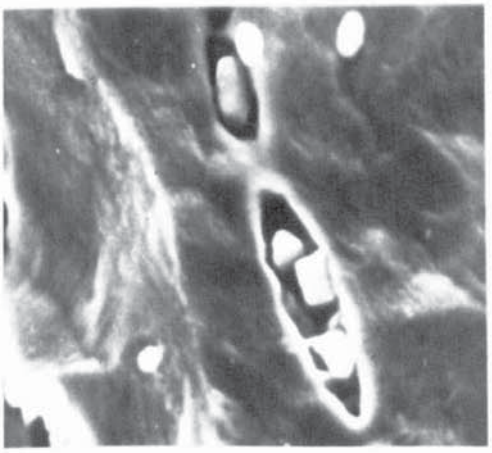

FIG.82.b. Decohesion of particle-matrix interface, Steel B, Magnification 5K.

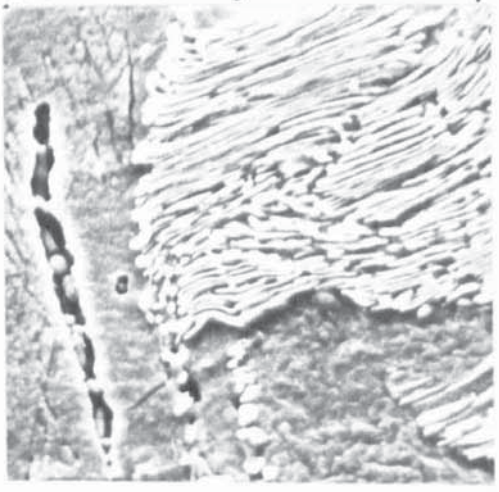

FIG.82.c. a long void formed by decohesion & cracking of particles, Steel A, Magnification 3K.

FIG. 83. A fractured notched tensile specimen.

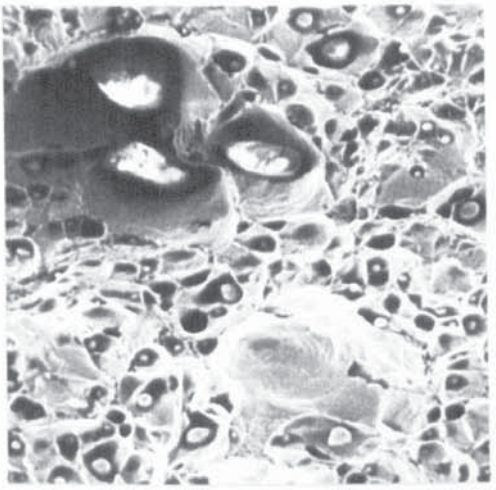

FIG. 84.a. Ductile fracture surface, Steel D10, 500X.

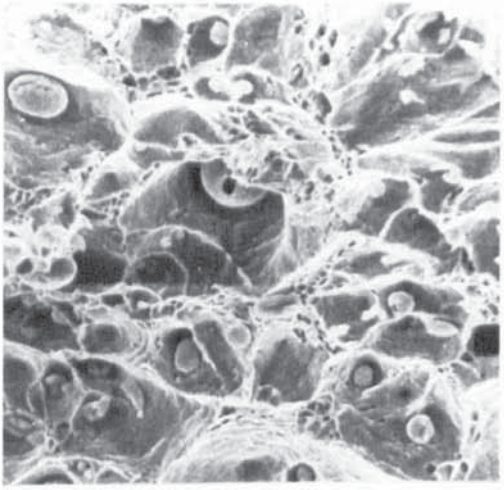

FIG. 84.b. Ductile fracture surface, Steel D12, 1.1K.

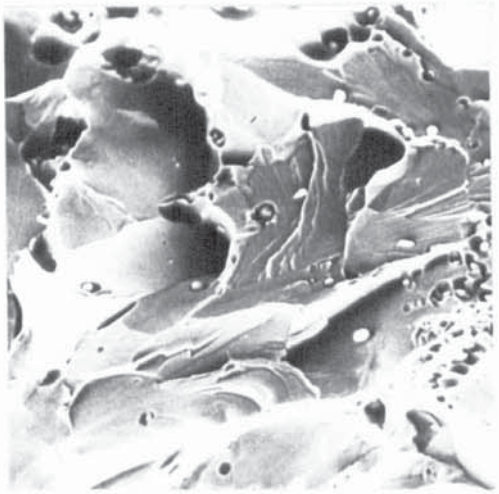

FIG. 84.c. Cleavage fracture Steel D30, specimen 307, 750X.

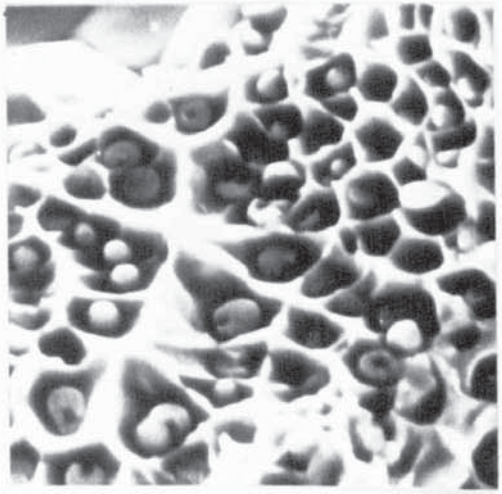

FIG. 84.d. Ductile fracture showing sulphide particles associated with cusps, Steel D32, Magnification 5K.

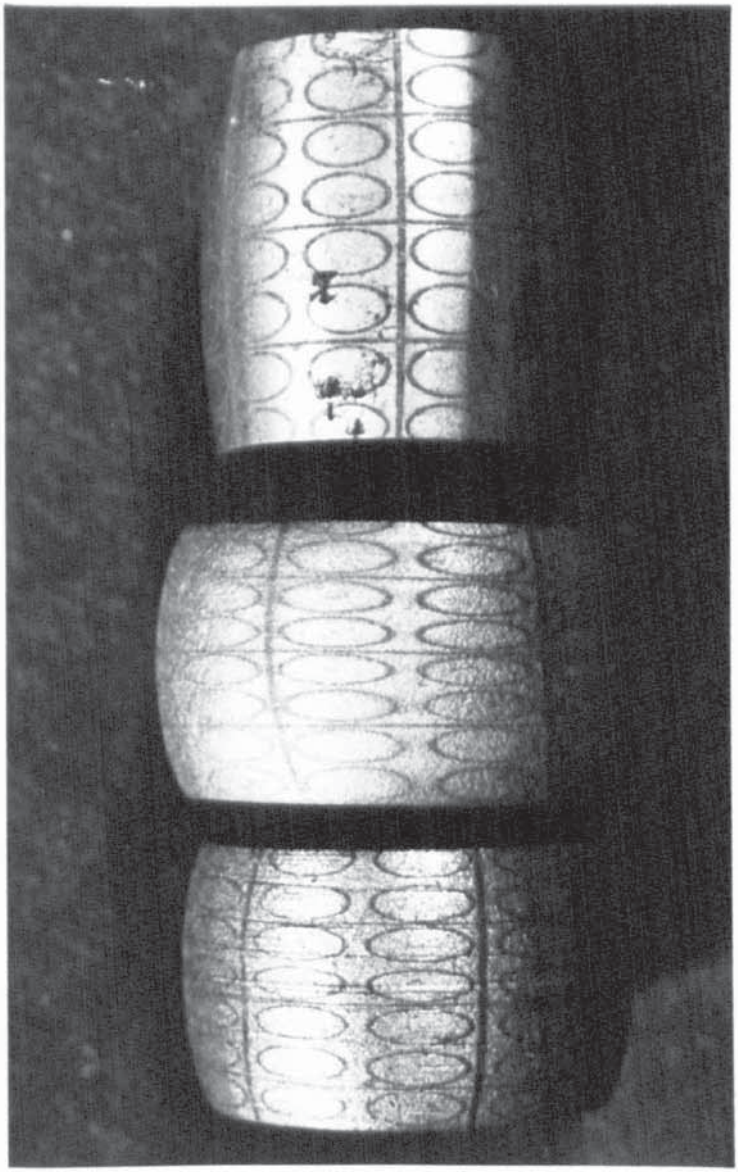

FIG. 85. Gridmarks on the surface of compressed specimens.

Table I.a THE CHEMICAL COMPOSITIONS OF THE STEELS

Types of Steels Used	Chemical Composition								
	% C	% Mn	%Si	% S	% P	% AL	%Cu	%Cr	% Ni
A	0.19	0.70	0.30	0.039	0.014	-	0.020	0.020	0.020
B	0.17	1.69	0.022	0.029	0.013	-	-	-	-
C	0.019	-	-	0.005	0.008	-	-	-	-
Steels.									
D 10	0.01	0.44	0.26	0.037	-	0.010			
D.11	0.03	0.41	0.22	0.10	-	0.005			
D.12	0.06	0.47	0.44	0.19	-	0.009			
D.20	0.01	0.98	0.38	0.03	-	0.010			
D.21	0.03	0.99	0.33	0.10	-	0.048			
D.22	0.07	0.97	0.26	0.19	-	0.008			
D.30	0.02	1.80	0.32	0.022	-	0.005			
D.31	0.03	1.65	0.44	0.089	-	0.005			
D.32	0.06	1.79	0.43	0.170	-	0.007			

Table I.b THE OXYGEN CONTENTS DURING MELTING AND CASTING OF STEELS D.

Steels Type D	$\%O_2$ before the addition of Fe_2O_3	$\%O_2$ after the addition of Fe_2O_3	$\%O_2$ after addition of deoxidation alloy	O_2/S
D.10	0.023	0.101	0.055	1.50
D.11	0.071	0.141	0.098	1.00
D.12	0.068	0.138	0.082	0.40
D.20	0.072	0.152	0.031	1.00
D.21	0.077	0.141	0.058	0.60
D.22	0.075	0.113	0.054	0.28
D.30	0.062	0.128	0.038	1.50
D.31	0.070	0.121	0.055	0.60
D.32	0.068	0.123	0.043	0.25

Table (2)
STEEL A.
Q.T.M. (

Objective : X 20
Eye piece : X 10
Turret scale : X 1.0
Screen Size : 25 cm. * 25cm.

Scale on Screen : 14.0 cm. 0.1 mm.

Heat treatment (1)		Heat treatment (2)		Heat treatment (3)		Heat treatment (4)	
Area % pearlite %	Boundary projection Intercept	Area % pearlite %	Boundary projection Intercept	Area % pearlite %	Boundary projection Intercept	Area % pearlite %	Boundary projection Intercept
13.0	5.0	24.0	7.0	14.0	7.0	20.0	6.0
18.0	8.0	17.0	7.0	20.0	8.0	25.0	9.0
21.0	8.0	22.0	7.0	14.0	6.0	25.0	6.0
17.0	8.0	15.0	6.0	22.0	8.0	19.0	9.0
22.0	5.0	22.0	8.0	24.0	6.0	14.0	7.0
18.0	8.0	14.0	7.0	21.0	9.0	19.0	9.0
17.0	5.0	19.0	7.0	25.0	8.0	16.0	7.0
13.0	8.0	13.0	8.0	21.0	8.0	20.0	6.0
20.0	5.0	19.0	7.0	20.0	7.0	14.0	6.0
15.0	8.0	14.0	6.0	26.0	7.0	20.0	10.0
16.0	7.0	21.0	8.0	15.0	7.0	25.0	6.0
23.0	9.0	22.0	5.0	22.0	8.0	20.0	8.0
20.0	7.0	20.0	8.0	15.0	6.0	16.0	7.0
25.0	8.0	18.0	6.0	22.0	9.0	22.0	10.0
22.0	7.0	24.0	10.0	17.0	7.0	24.0	6.0
18.0	7.0	15.0	6.0	25.0	9.0	20.0	9.0
22.0	8.0	22.0	9.0	16.0	6.0	24.0	7.0
18.0	8.0	21.0	7.0	24.0	8.0	20.0	10.0
17.0	4.9	17.0	7.0	23.0	7.0	15.0	7.0
13.0	7.0	15.0	7.0	20.0	8.0	22.0	8.0
20.0	4.8	22.0	8.0	16.0	6.0	16.0	7.0
25.0	7.0	18.0	7.0	22.0	8.0	22.0	9.0
16.0	6.0	14.0	7.0	25.0	6.0	14.0	6.0
22.0	8.0	24.0	5.0	22.0	8.0	20.0	10.0
22.0	6.0	21.0	8.0	18.0	8.0	17.0	7.0

Table (2) : continued
STEEL A.

Heat treatment (1)		Heat treatment (2)		Heat treatment (3)		Heat treatment (4)	
Area % pearlite %	Boundary projection Intercept	Area % pearlite %	Boundary projection Intercept	Area % pearlite %	Boundary projection Intercept	Area % pearlite %	Boundary projection Intercept
20.0	9.0	19.0	6.0	24.0	8.0	22.0	9.0
22.0	6.0	23.0	8.0	13.0	6.0	18.0	5.0
18.0	8.0	20.0	5.0	18.0	9.0	25.0	9.0
18.0	7.0	24.0	8.0	12.0	6.0	22.0	6.0
34.0	10.0	17.0	7.0	16.0	10.0	17.0	9.0
20.0	6.0	22.0	10.0	21.0	6.0	25.0	7.0
26.0	10.0	18.0	7.0	16.0	9.0	20.0	7.0
12.0	6.0	23.0	9.0	14.0	6.0	27.0	8.0
19.0	9.0	21.0	8.0	20.0	10.0	15.0	9.0
18.0	5.0	29.0	10.0	20.0	8.0	21.0	6.0
21.0	8.0	19.0	10.0	14.0	8.0	18.0	9.0
14.0	5.0	24.0	7.0	20.0	5.0	23.0	7.0
20.0	8.0	20.0	7.0	25.0	9.0	21.0	10.0
20.0	8.0	27.0	9.0	21.0	6.0	20.0	8.0
17.0	8.0	12.0	6.0	18.0	9.0	17.0	8.0
20.0	5.0	18.0	8.0	22.0	7.0	21.0	8.0
17.0	9.0	15.0	6.0	28.0	10.0	20.0	9.0
14.0	6.0	21.0	8.0	26.0	7.0	22.0	6.0
20.0	9.0	14.0	6.0	22.0	10.0	20.0	10.0
26.0	9.0	20.0	9.0	20.0	7.0	22.0	6.0
17.0	6.0	15.0	6.0	24.0	10.0	18.0	8.0
16.0	6.0	20.0	8.0	16.0	7.0	20.0	8.0
24.0	6.0	22.0	8.0	22.0	6.0	17.0	9.0
15.0	6.0	16.0	6.0	22.0	6.0	22.0	6.0
20.0	9.0	18.0	7.0	20.0	8.0	20.0	10.0

Table (2) : continued
STEEL A

Percentage Pearlite	Heat treatment No.1	Heat treatment No.2	Heat treatment No.3	Heat treatment No.4
Pearlite % (Mean)	19.2	± 19.2	± 20.10	± 20.0
Standard Error of Mean	± 0.6	± 0.5	± 0.60	± 0.50
Number of Observations	50	50	50	50
Standard Deviation	4.0	3.5	3.90	3.20
Variance	16.4	12.2	15.40	10.30
Average Percentage of Pearlite : 19.6 ± 0.55 20%				

Ferrite Grain size dia. (μm)	Heat treatment No.1	Heat treatment No.2	Heat treatment No.3	Heat treatment No.4
Intercept (Mean)	± 7.1	± 7.3	± 7.6	± 7.8
Standard Error of Mean	± 0.2	± 0.2	± 0.2	± 0.2
Number of Observations	50	50	50	50
Standard Deviation	1.5	1.3	1.3	1.5
Variance	2.2	1.7	1.8	2.1
Ferrite Grain Size	20.3 ± 0.5	19.8 ± 0.5	18.8 ± 0.5	18.3 ± 0.5
Average Ferrite Grain Diameter : 19.3 ± 0.5 19.5 μm				

Ferrite Grain Size : Mean Ferrite Grain Diameter : ± 17.9
From Photograph : Standard Error of Mean : ± 0.4
Measurements : Number of Measurements : 31 Standard Deviation : 2.3 Variance: 5.4
Average Grain Diameter (d) 18 μm

Interparticle Spacing λ μm

Interparticle Spacing (Mean)	: 11.12
Standard Error of Mean	: 1.26
Number of Observations	: 24
Standard Deviation	: 6.16
Variance	: 37.98

Average Spacing 12 μm

Table (3)
STEEL B
Q.T.M. (

Objective : X 20
Eye piece : X 10
Turret scale : X 1.5
Screen Size : 25 cm. *25 cm.

Scale on Screen : 15 cm 0.1 mm

Heat treatment (1)		Heat treatment (2)		Heat treatment (3)		Heat treatment (4)	
Area % pearlite %	Boundary projection Intercept	Area % pearlite %	Boundary projection Intercept	Area % pearlite %	Boundary projection Intercept	Area % pearlite %	Boundary projection Intercept
13.0	7.0	24.6	7.5	22.0	7.5	18.2	6.0
19.0	7.0	23.8	6.0	20.0	8.0	21.2	6.9
11.5	7.0	16.1	8.0	12.0	7.5	20.3	7.1
10.0	8.0	16.6	10.0	19.0	6.5	22.5	7.0
16.0	6.5	15.2	9.0	17.0	5.0	14.5	7.5
17.0	6.5	17.2	10.5	10.0	7.0	18.1	7.3
19.0	5.5	21.0	8.0	17.0	6.5	19.0	6.9
21.2	9.0	16.0	7.5	16.0	5.5	15.3	6.2
18.3	8.0	16.7	8.0	18.5	6.0	18.3	6.0
19.0	8.5	9.5	8.0	16.5	5.0	17.9	6.1
18.2	7.5	15.9	7.5	24.5	5.5	20.7	6.2
23.8	5.0	14.0	9.0	16.5	5.0	19.5	7.2
18.1	8.0	23.0	9.0	15.0	5.0	19.1	7.0
23.2	7.0	24.7	9.5	17.0	6.0	16.8	6.6
20.2	7.0	25.3	6.0	18.0	6.5	20.4	7.3
21.2	7.5	17.2	6.0	20.0	8.0	19.3	6.0
17.9	7.0	24.2	7.0	21.0	7.0	19.7	7.0
15.0	6.5	20.7	10.5	19.0	8.0	20.0	7.2
19.5	6.5	26.2	10.5	20.0	6.5	20.4	6.7
20.9	8.5	15.4	7.0	18.0	7.5	19.0	6.6
19.9	7.0	24.7	8.1	15.2	4.8	18.0	4.1
20.7	6.7	15.0	5.2	21.5	7.5	26.0	6.7
18.6	7.7	26.5	4.6	35.3	8.4	28.5	6.1
19.0	7.2	27.0	9.0	38.0	5.4	29.0	6.0
20.7	7.3	28.0	4.4	19.6	5.4	26.5	5.9

Table (3) : Continued
STEEL B

Heat treatment (1)		Heat treatment (2)		Heat treatment (3)		Heat treatment (4)	
Area % pearlite %	Boundary projection Intercept	Area % pearlite %	Boundary projection Intercept	Area % pearlite %	Boundary projection Intercept	Area % pearlite %	Boundary projection Intercept
27.4	7.0	16.0	6.8	17.6	8.0	31.0	5.0
19.8	7.7	18.6	8.0	27.2	8.0	36.0	5.9
17.4	6.5	21.0	8.0	18.4	7.0	23.0	5.3
16.0	6.9	18.0	7.0	14.8	5.6	33.0	5.7
16.0	6.5	22.0	7.0	20.8	5.3	25.0	5.1
14.9	6.5	18.0	7.0	18.0	7.0	22.0	8.0
17.2	6.2	22.0	7.0	22.0	10.0	13.0	6.0
23.2	6.7	17.0	7.0	17.0	7.0	18.2	6.7
17.4	7.6	22.0	7.0	22.0	10.0	24.6	9.0
15.5	7.2	19.0	7.0	14.0	6.0	20.0	9.0
17.3	6.2	24.0	7.0	18.0	9.0	19.0	8.0
14.3	5.7	19.0	9.0	18.0	7.0	22.5	7.0
13.7	4.9	15.0	9.0	23.0	10.0	23.0	7.0
17.0	5.3	18.0	7.0	20.0	7.0	22.0	7.0
18.2	5.8	23.0	7.0	25.0	10.0	17.0	10.0
17.0	5.5	22.0	8.0	14.0	6.0	12.0	7.0
22.0	6.6	18.0	8.0	19.0	9.0	17.9	7.0
12.7	6.6	25.0	7.0	21.0	8.0	19.5	9.0
18.0	7.0	21.0	7.0	27.0	10.0	19.0	9.0
22.0	9.0	19.0	8.0	14.0	6.0	24.0	9.0
18.0	7.0	24.0	8.0	19.0	10.0	25.0	7.0
24.0	9.0	24.0	8.0	16.0	7.0	20.4	8.0
22.0	8.0	20.0	8.0	21.0	9.0	19.0	7.0
18.0	10.0	18.0	7.0	15.0	7.0	26.0	7.0
17.0	7.0	22.0	9.0	20.0	9.0	18.0	7.0

Table (3) : continued
STEEL B

Percentage Pearlite	Heat treatment No.1	Heat treatment No.2	Heat treatment No.3	Heat treatment No.4
Pearlite (Mean)	$\pm$ 18.3	$\pm$ 20.2	$\pm$ 19.4	$\pm$ 21.2
Standard Error of Mean	$\pm$ 0.5	$\pm$ 0.6	$\pm$ 0.7	$\pm$ 0.7
Number of Observations	50	50	50	50
Standard Deviation	3.4	4.1	5.0	4.7
Variance	11.2	16.5	24.7	22.3
Average Percentage of Pearlite : 19.8 $\pm$ 0.6				
20%				

Ferrite Grain Size dia. (μm)	Heat treatment No.2	Heat treatment No.2	Heat treatment No.3	Heat treatment No.4
Intercept (Mean)	$\pm$ 7.0	$\pm$ 7.7	$\pm$ 7.2	$\pm$ 6.9
Standard Error of Mean	$\pm$ 0.1	$\pm$ 0.2	$\pm$ 0.2	$\pm$ 0.2
Number of Observations	50	50	50	50
Standard Deviation	1.0	1.3	1.6	1.1
Variance	1.1	1.8	2.4	1.3
Ferrite Grain Size d. (μm)	19.5 $\pm$ 0.2	17.3 $\pm$ 0.5	18.7 $\pm$ 0.4	19.0 $\pm$ 0.4
Average Ferrite Grain Diameter : 18.6 $\pm$ 0.3 d = 19μm				

Ferrite Grain Size From Photograph Measurements	: Mean Ferrite Grain Diameter (μm)	: $\pm$ 17.6	
	: Standard Error of Mean	: $\pm$ 0.6	
	: Number of Measurements	: 28	Standard Deviation : 3.0
Average Grain Diameter		18.0 μm	

Interparticle Spacing		Maximum	Minimum
Interparticle Spacing (Mean)		$\pm$ 14.97	$\pm$ 8.20
Standard Error of Mean		$\pm$ 1.07	$\pm$ 0.46
Number of Observations		51	31
Standard Deviation		7.63	2.56
Variance		58.20	6.55
Average Spacing	12 μm	15.0	8.0

Table (4)
STEEL C
Q.T.M. (

Objective : X 20
Eye piece : X 10
Turret scale : X 1.0
Screen size : 25 cm.* 25 cm.

Scale on Screen : 14.0 cm. 0.1 mm

Heat treatment (1)		Heat treatment (2)		Heat treatment (3)		Heat treatment (4)	
Area % pearlite %	Boundary projection Intercept	Area % pearlite %	Boundary projection Intercept	Area % pearlite %	Boundary projection Intercept	Area % pearlite %	Boundary projection Intercept
3.0	1.0	2.9	1.4	4.0	2.1	3.0	2.0
0.4	0.3	10.9	2.7	1.6	1.0	4.5	2.0
1.4	1.4	11.0	3.4	3.4	2.2	2.5	2.0
1.6	0.7	1.7	0.5	2.6	1.8	3.7	2.1
1.4	1.2	5.3	1.8	5.2	3.0	5.8	3.0
1.6	1.5	4.0	1.0	2.5	1.0	11.5	4.2
0.3	0.4	0.6	0.3	5.5	4.0	1.7	1.0
0.9	1.0	2.8	1.1	3.8	2.7	5.0	3.0
0.5	0.6	2.3	1.0	1.4	1.20	3.0	1.8
0.4	0.2	5.0	1.6	1.0	0.8	3.0	2.0
4.0	3.0	1.3	0.4	1.4	0.9	1.6	1.0
1.3	0.9	1.7	0.8	2.4	1.5	1.6	1.0
0.7	0.9	0.4	0.3	1.7	1.1	0.7	0.5
0.9	0.9	1.2	0.6	0.7	0.8	2.6	2.0
1.0	0.8	8.0	3.0	2.0	1.4	1.3	1.0
1.2	0.8	1.0	0.5	1.8	1.1	3.3	2.2
0.6	0.4	0.7	0.4	5.5	2.8	2.7	2.0
2.7	0.4	2.3	0.6	6.0	4.0	2.3	2.0
2.2	2.0	11.0	2.5	7.0	2.8	3.1	3.0
0.8	0.4	0.7	0.2	4.0	2.0	6.0	3.5
3.2	0.7	3.1	1.1	0.5	-	-	-
0.9	0.3	0.7	0.4	0.3	-	3.1	-
1.7	0.6	3.0	1.0	0.7	-		
1.4	0.7	2.8	1.0	0.7	-		
2.8	0.2	0.9	0.4	4.7	-		
6.5	1.8	0.9	0.5	7.0	-		
2.4	0.8	2.5	0.7	2.3	-		

Table (4) : continued
STEEL C

Percentage Pearlite	Average for all four Annealing treatments
Percentage Perlite (Mean)	2.81
Standard Error of Mean	0.24
Number of Observations	102.00
Standard Deviation	2.41
Variance	5.82
Average percentage of pearlite = 2.81 ± 0.24 2.80 %	
Ferrite Grain Size	Average for all four Annealing treatments
Intercept (Mean)	1.41
Standard Error of Mean	0.10
Number of Observations	94.0
Standard Deviation	0.99
Variance	0.97
Average Ferrite grain diameter = 125 μm	
Ferrite Grain Size from Photograph Measurements = 122 μm ⟶ 132 μm	

TABLE 5. Steel A. Annealing Procedure (1)

Size - Distribution of Carbide Particles

Number of all particles	Number of particles						
	0-1.0 µm	1.0-2.0 µm	2.0-3.0 µm	3.0-4.0 µm	4.0-5.0 µm	5.0-6.0 µm	6.0-7.0 µm
39	32	4	2	0	0	0	1
50	41	3	3	1	2	0	0
50	35	7	4	1	1	1	1
41	30	4	3	2	1	1	0
51	37	12	1	1	0	0	0
44	30	7	4	1	1	1	0
42	34	5	2	1	0	0	0
55	43	7	2	1	1	1	0
40	29	6	3	1	1	0	0
60	45	7	3	2	2	1	0
51	35	9	6	1	0	0	0
65	15	21	15	7	3	3	1
50	31	10	6	2	1	0	0
59	42	6	4	2	3	2	0
41	33	6	1	0	1	0	0
79	51	14	9	4	0	0	1
35	16	14	3	2	0	0	0
49	30	14	3	2	0	0	0
50	25	14	8	2	1	0	0
85	45	23	12	3	1	1	0
54	33	12	7	1	0	1	0
56	31	11	8	2	2	2	0
55	38	9	5	3	0	0	0
49	24	11	8	2	4	0	0
38	23	5	3	2	2	0	3

TABLE 5. Steel A. Annealing Procedure (1)

Size - Distribution of Carbide Particles

Number of all particles	Number of particles						
	0-1.0 µm	1.0-2.0 µm	2.0-3.0 µm	3.0-4.0 µm	4.0-5.0 µm	5.0-6.0 µm	6.0-7.0 µm
32	12	9	7	3	1	0	0
65	35	20	4	3	3	0	0
38	13	15	5	3	1	1	0
45	24	14	6	1	0	0	0
65	27	24	9	3	1	1	0
85	45	25	11	3	0	1	0
47	22	11	9	2	2	1	0
45	23	10	4	3	2	2	1
22	14	5	1	0	1	1	0
70	30	25	11	3	1	0	0
34	21	8	2	1	1	1	0
80	50	21	6	3	0	0	0
29	23	5	1	0	0	0	0
76	49	15	5	3	3	1	0
60	38	6	6	5	2	2	1
32	14	9	5	2	1	1	0
70	48	20	2	0	0	0	0
60	36	21	2	1	0	0	0
32	14	10	4	3	1	0	0
68	42	19	3	1	1	2	0
30	16	10	3	1	0	0	0
38	20	11	4	2	1	0	0
60	31	16	6	2	1	2	2
46	27	12	1	1	4	1	0
50	23	17	7	1	1	1	0

TABLE 5. Steel A. Annealing Procedure (2)

Size - Distribution of Carbide Particles

Number of all particles	Number of particles						
	0- 1.0 µm	1.0-2.0 µm	2.0-3.0 µm	3.0-4.0 µm	4.0-5.0 µm	5.0-6.0 µm	6.0-7.0 µm
42	18	4	9	5	3	3	0
15	7	4	1	3	0	0	0
45	22	8	7	3	3	2	0
70	30	15	10	5	5	3	2
40	16	12	4	4	4	0	0
32	8	14	6	2	1	1	0
30	7	9	4	2	1	3	1
71	33	13	13	9	2	1	0
10	2	2	2	3	1	0	0
48	12	16	14	4	2	0	0
26	11	8	4	2	1	0	0
32	5	13	8	2	2	2	0
49	22	9	13	3	1	1	0
64	42	10	7	4	1	0	0
34	25	4	2	1	1	1	0
37	16	8	4	2	6	0	1
68	38	15	10	2	2	1	0
99	44	29	18	4	2	2	0
35	25	4	3	3	0	0	0
75	38	20	12	3	1	1	0
58	46	4	2	2	2	1	1
53	33	11	4	3	1	1	0
47	38	6	2	1	0	0	0
36	28	5	2	1	0	0	0
41	29	5	4	1	1	1	0

TABLE 5. Steel A. (Contd.) Annealing Procedure (2)

Size - Distribution of Carbide Particles

Number of all particles	Number of particles						
	0-1.0 µm	1.0-2.0 µm	2.0-3.0 µm	3.0-4.0 µm	4.0-5.0 µm	5.0-6.0 µm	6.0-7.0 µm
30	23	4	2	0	1	0	0
17	9	4	2	2	0	0	0
55	37	10	5	1	1	1	0
36	28	6	2	0	0	0	0
37	23	6	4	2	1	1	0
53	34	9	5	1	2	1	1
56	31	14	9	1	1	0	0
43	34	5	3	1	0	0	0
55	36	10	6	1	1	1	0
81	43	19	11	5	3	0	0
41	22	11	4	2	1	1	0
62	45	9	5	1	2	0	0
61	38	12	8	1	1	1	0
43	18	14	3	4	1	2	1
40	35	3	3	1	3	3	1
25	15	3	6	1	1	0	0
43	33	4	2	2	2	0	0
45	27	11	5	1	0	1	0
53	24	22	5	1	1	0	0
41	18	17	3	2	1	0	0
55	42	8	2	2	1	0	0
60	34	13	5	2	4	1	0
40	29	7	3	0	1	0	0
52	34	11	5	2	0	0	0
62	47	3	8	4	0	0	0

TABLE 5. STEEL A. Annealing Procedure (3)

Size - Distribution of Carbide Particles

Number of all particles	Number of Particles						
	0-1.0 µm	1.0-2.0 µm	2.0-3.0 µm	3.0-4.0 µm	4.0-5.0 µm	5.0-6.0 µm	6.0-7.0 µm
34	20	4	3	4	2	1	0
32	21	9	2	0	0	0	0
44	23	14	5	2	0	0	0
80	44	24	6	4	1	1	0
50	41	5	3	1	0	0	0
60	38	16	4	1	0	0	1
60	34	18	4	3	1	0	0
76	46	21	5	1	1	0	1
85	48	27	7	3	0	0	0
85	50	28	5	2	0	0	0
60	36	14	6	4	0	0	0
105	45	46	11	3	0	0	0
80	44	18	10	4	2	1	1
28	14	6	2	2	1	3	0
34	17	10	5	1	1	0	0
32	10	16	2	1	1	1	1
57	27	24	4	2	0	0	0
55	25	18	7	4	1	0	0
64	40	15	6	3	0	0	0
43	17	22	4	1	1	1	1
40	30	7	1	2	0	0	0
14	7	3	4	0	0	0	0
30	20	6	3	1	0	0	0
43	28	10	4	1	0	0	0
41	28	10	1	0	2	0	0

TABLE 5. Steel A. Annealing Procedure (3)

Size - Distribution of Carbide Particles

Number of all particles	Number of Particles						
	0.-1.0 µm	1.0-2.0 µm	2.0-3.0 µm	3.0-4.0 µm	4.0-5.0 µm	5.0-6.0 µm	6.0-7.0 µm
38	26	4	3	2	1	0	2
37	25	7	4	1	0	0	0
47	34	5	2	2	2	1	1
33	22	5	4	1	1	0	0
74	48	14	7	2	2	1	0
42	27	8	3	1	2	1	0
53	45	5	3	0	0	0	0
47	25	12	7	1	1	1	0
28	14	5	3	4	2	0	0
27	13	8	5	1	0	0	0
38	26	4	2	2	2	2	0
61	35	11	7	3	2	1	2
56	34	14	5	1	1	1	0
78	39	17	12	6	2	1	1
70	42	14	10	2	1	1	0
58	33	13	7	4	1	0	0
64	42	10	7	2	2	1	0
51	25	13	9	2	1	1	0
52	37	9	4	1	1	0	0
47	31	10	3	1	2	0	0
45	23	11	8	3	0	0	0
80	48	16	10	4	1	1	0
72	44	13	9	3	2	1	0
68	36	17	12	1	1	1	0
45	28	7	4	4	2	0	0

TABLE 5. Steel A.

Annealing Procedure (4)

Size - Distribution of Carbide Particles

Number of all particles	Number of Particles						
	0 - 1.0 µm	1.0-2.0 µm	2.0-3.0 µm	3.0-4.0 µm	4.0-5.0 µm	5.0-6.0 µm	6.0-7.0 µm
60	20	15	10	3	1	1	0
68	43	18	5	1	1	0	0
90	36	24	16	7	3	2	2
50	36	10	4	0	0	0	0
46	13	16	11	4	1	1	0
30	8	12	4	3	1	1	1
80	32	27	15	3	2	1	0
110	61	24	14	3	3	3	2
49	21	13	7	4	3	1	0
24	13	5	3	1	1	1	0
50	31	10	7	2	0	0	0
30	14	7	4	1	2	1	1
52	32	12	8	0	0	0	0
35	20	7	5	1	1	1	0
53	28	14	10	1	0	0	0
51	32	9	6	2	2	0	0
60	24	18	12	3	1	2	0
68	38	18	12	0	0	0	0
77	45	20	10	2	0	0	0
44	24	12	8	0	0	0	0
94	56	20	14	1	2	1	0
84	44	23	16	1	0	0	0
73	33	22	18	0	0	0	0
52	26	15	10	1	0	0	0
53	36	10	5	2	0	0	0

TABLE 5. Steel A.

Annealing Procedure (4)

Size - Distribution of Carbide Particles

Number of all particles	Number of Particles						
	0-1.0 µm	1.0-2.0 µm	2.0-3.0 µm	3.0-4.0 µm	4.0-5.0 µm	5.0-6.0 µm	6.0-7.0 µm
98	59	16	12	4	3	2	2
48	31	10	7	0	0	0	0
78	45	15	10	4	3	1	0
53	27	15	9	2	0	0	0
65	28	20	11	2	2	2	0
56	24	17	12	1	1	1	0
30	8	12	4	3	1	1	1
9	2	3	0	2	1	1	0
72	30	20	11	6	3	2	0
45	17	19	8	0	1	0	0
80	35	20	15	7	2	1	0
37	22	11	3	1	0	0	0
44	23	5	11	3	2	0	0
80	50	24	5	1	0	0	0
47	27	8	9	1	1	1	0
31	13	14	3	0	1	0	0
65	45	12	7	0	0	0	0
37	28	5	4	0	0	0	0
58	34	10	8	3	1	1	1
50	34	13	2	0	1	0	0
30	24	5	1	0	0	0	0
36	18	11	5	2	0	0	0
45	20	7	9	3	3	2	1
45	27	9	5	2	1	1	0
54	20	19	7	3	1	0	0

TABLE 6. Steel B.

Annealing Procedure (1)

Size - Distribution of Carbide Particles

Number of all particles	Number of Particles						
	0-1.0 µm	1.0-2.0 µm	2.0-3.0 µm	3.0-4.0 µm	4.0-5.0 µm	5.0-6.0 µm	6.0-7.0 µm
43	27	8	5	2	1	0	0
53	39	4	3	3	2	2	0
65	52	5	3	3	1	1	0
50	43	2	2	2	1	0	0
52	27	13	8	3	1	0	0
38	23	5	3	2	2	3	0
78	49	13	9	3	1	0	0
53	37	8	3	3	1	1	0
40	24	5	3	4	2	1	1
33	26	3	1	1	1	1	0
25	22	1	0	2	0	0	0
49	34	8	4	1	2	0	0
43	33	5	3	2	0	0	0
40	39	0	0	1	0	0	0
44	34	6	4	0	0	0	0
50	38	7	5	0	0	0	0
38	16	8	4	2	6	1	1
62	49	4	2	2	2	2	1
57	36	11	5	3	1	1	0
51	33	12	4	0	0	2	0
48	32	8	4	2	1	1	0
45	29	10	3	3	0	0	0
52	44	3	1	1	1	1	1
24	19	3	2	0	0	0	0
34	26	4	2	2	0	0	0

TABLE 6. Steel B.

Annealing Procedure (1)

Size - Distribution of Carbide Particles

Number of all particles	Number of Particles						
	0-1.0 µm	1.0-2.0 µm	2.0-3.0 µm	3.0-4.0 µm	4.0-5.0 µm	5.0-6.0 µm	6.0-7.0 µm
44	30	8	2	3	1	0	0
40	20	15	0	4	1	0	0
39	11	4	8	8	6	1	1
37	12	8	9	7	1	0	0
27	11	4	6	3	2	1	0
21	10	3	1	6	0	1	0
29	14	6	3	6	0	0	0
35	15	12	1	1	1	1	1
45	23	7	6	6	3	0	0
41	24	10	3	1	1	1	1
44	30	3	3	3	4	1	0
28	21	3	4	0	0	0	0
58	50	3	3	1	1	0	0
55	36	2	5	7	3	2	0
37	23	7	4	2	1	0	0
58	49	2	4	3	0	0	0
74	49	14	8	2	1	0	0
37	16	10	4	4	2	1	0
85	45	18	11	4	2	2	3
38	14	10	5	5	3	1	0
79	48	9	8	6	4	2	2
59	36	11	3	6	3	0	0
27	14	5	2	5	1	0	0
56	42	8	2	2	2	0	0
25	16	2	2	2	2	1	0

TABLE 6. Steel B.

Annealing Procedure (2)

Size - Distribution of Carbide Particles

Number of all particles	Number of Particles						
	0-1.0 µm	1.0-2.0 µm	2.0-3.0 µm	3.0-4.0 µm	4.0-5.0 µm	5.0-6.0 µm	6.0-7.0 µm
50	25	9	7	7	2	0	0
42	30	5	4	1	1	1	0
18	10	3	3	1	1	0	0
24	17	2	2	0	3	0	0
49	21	10	10	8	0	0	0
42	20	9	7	2	2	2	0
34	24	4	4	0	1	1	0
48	28	9	6	5	0	0	0
30	25	5	2	2	0	1	1
41	25	6	3	5	2	0	0
41	34	2	1	1	3	0	0
40	19	10	7	1	4	0	0
29	12	7	6	1	1	1	1
52	38	7	5	2	0	0	0
43	30	6	3	3	1	0	0
52	41	4	2	2	1	1	1
50	35	5	3	3	2	1	1
44	32	4	3	3	1	1	0
26	19	3	2	1	1	0	0
42	36	2	2	1	1	0	0
40	16	7	4	4	4	4	1
29	22	3	2	1	1	0	0
25	19	2	1	1	1	1	0
32	21	5	1	3	1	1	0
34	26	4	2	1	1	0	0

TABLE 6. Steel B.

Annealing Procedure (2)

Size - Distribution of Carbide Particles

Number of all particles	Number of Particles						
	0-1.0 µm	1.0-2.0 µm	2.0-3.0 µm	3.0-4.0 µm	4.0-5.0 µm	5.0-6.0 µm	6.0-7.0 µm
28	22	3	1	2	0	0	0
31	22	3	3	1	1	1	0
39	25	5	2	3	1	2	1
46	33	6	3	3	0	1	0
15	7	3	2	1	1	1	0
51	22	10	7	4	3	3	1
35	24	4	2	2	1	1	1
42	26	5	4	2	2	1	2
26	16	4	2	1	1	1	1
40	25	6	5	2	1	1	0
42	26	6	3	3	1	2	1
30	19	5	3	1	1	1	0
40	29	7	3	1	0	0	0
51	22	13	4	6	3	2	1
37	30	3	2	0	2	0	0
24	16	2	2	2	1	1	0
23	18	1	1	3	0	0	0
13	7	4	2	0	0	0	0
35	22	3	4	4	1	0	1
31	21	4	2	2	1	1	0
39	25	7	3	4	0	0	0
40	29	1	5	3	0	1	1
50	39	1	4	3	2	1	0
52	43	2	1	2	2	1	1
25	17	2	1	3	0	0	2

TABLE 6. Steel B.

Annealing Procedure (3)

Size - Distribution of Carbide Particles

Number of all particles	Number of Particles						
	0-1.0 µm	1.0-2.0 µm	2.0-3.0 µm	3.0-4.0 µm	4.0-5.0 µm	5.0-6.0 µm	6.0-7.0 µm
51	33	5	5	3	2	2	1
36	28	3	2	3	0	0	0
38	25	5	4	3	1	0	0
52	29	14	4	4	1	0	0
42	10	17	7	5	2	1	0
37	23	5	5	3	1	0	0
37	15	14	5	3	0	0	0
49	30	10	3	1	1	4	0
68	44	6	8	7	2	1	0
34	20	4	8	2	0	0	0
39	20	9	5	4	0	0	0
46	32	7	3	2	2	0	0
41	30	7	2	2	0	0	0
47	30	3	7	6	0	1	0
47	35	4	7	0	1	0	0
46	33	2	9	1	0	1	0
64	54	4	2	1	2	0	1
60	46	5	2	3	1	2	1
66	43	10	5	5	0	1	2
56	45	3	4	2	1	1	0
40	30	4	3	2	1	0	0
65	30	10	10	5	5	3	2
25	11	4	4	5	1	0	0
27	20	3	1	3	0	0	0
33	25	3	2	2	1	0	0

TABLE 6. Steel B.

Annealing Procedure (3)

Size - Distribution of Carbide Particles

Number of all particles	Number of Particles						
	0-1.0 µm	1.0-2.0 µm	2.0-3.0 µm	3.0-4.0 µm	4.0-5.0 µm	5.0-6.0 µm	6.0-7.0 µm
54	37	4	5	3	2	2	1
53	35	4	4	4	1	3	2
38	27	4	2	2	1	1	1
40	28	6	4	2	0	0	0
44	34	4	2	2	1	1	0
38	26	5	1	2	2	2	0
45	30	5	3	2	3	1	1
37	23	4	2	4	2	1	1
37	28	3	4	1	1	0	0
41	33	5	1	2	0	0	0
35	26	3	3	1	1	1	0
29	25	2	0	2	0	0	0
30	28	1	1	0	0	0	0
50	37	5	3	2	1	1	1
53	44	3	2	1	1	1	1
39	21	5	4	2	2	2	3
57	37	7	4	4	2	2	1
56	33	9	4	6	3	1	0
43	26	8	4	3	1	1	0
96	49	10	10	14	9	2	2
84	43	10	9	17	3	1	1
36	23	6	3	3	1	0	0
45	24	9	4	5	1	2	0
34	26	4	1	2	1	0	0
37	26	3	4	1	1	1	1

TABLE 6. Steel B.

Annealing Procedure (4)

Size - Distribution of Carbide Particles

Number of all particles	Number of Particles						
	0-1.0 Um	1.0-2.0 Um	2.0-3.0 Um	3.0-4.0 Um	4.0-5.0 Um	5.0-6.0 Um	6.0-7.0 Um
48	37	6	4	1	0	0	0
59	27	16	7	4	2	2	1
29	15	6	5	1	1	1	0
50	30	10	9	1	0	0	0
58	29	12	6	3	4	3	1
45	28	6	3	6	1	1	0
50	19	6	7	4	9	3	2
44	26	5	5	5	2	1	0
40	29	4	2	2	1	1	1
43	25	6	7	3	1	1	0
40	20	13	2	4	0	1	0
55	33	9	3	3	3	3	1
43	15	11	7	7	2	1	0
72	44	11	7	5	4	1	0
70	39	12	3	1	2	1	2
64	29	11	12	6	2	2	1
47	28	5	4	8	0	1	1
50	30	8	5	4	3	0	0
46	27	7	6	3	1	1	1
41	17	7	6	5	2	4	0
35	12	12	6	2	3	0	0
30	14	12	3	1	0	0	0
45	24	14	3	3	1	0	0
62	47	10	1	4	0	0	0
25	28	11	3	1	1	1	0

TABLE 6. Steel B.

Annealing Procedure (4)

Size - Distribution of Carbide Particles

Number of all Particles	Number of Particles						
	0-1.0 µm	1.0-2.0 µm	2.0-3.0 µm	3.0-4.0 µm	4.0-5.0 µm	5.0-6.0 µm	6.0-7.0 µm
40	19	10	7	2	1	1	0
39	24	8	3	1	1	1	1
66	42	7	5	8	3	1	0
70	33	8	12	4	8	3	1
37	20	10	2	4	1	0	0
55	30	8	8	4	3	0	2
54	33	12	4	2	2	1	0
33	20	6	4	1	2	0	0
48	35	12	0	0	1	0	0
46	30	0	4	1	1	0	0
39	21	8	4	2	1	1	0
27	18	5	2	1	1	0	0
27	22	3	2	0	0	0	0
19	11	4	2	1	1	0	0
63	35	13	6	3	2	2	2
36	22	6	5	2	0	0	0
45	30	10	2	1	1	1	0
63	40	12	7	2	1	1	0
74	47	14	6	5	0	2	0
75	45	20	7	3	0	0	0
55	38	7	5	2	1	2	0
28	19	3	2	1	1	1	1
56	34	8	6	1	1	0	0
51	30	8	7	3	2	1	0
47	19	12	10	4	2	0	0

TABLE 7. Steel C.

Annealing Procedure (1)

Size - Distribution of Carbide Particles

Number of all particles	Number of Particles						
	0-1.0 µm	1.0-2.0 µm	2.0-3.0 µm	3.0-4.0 µm	4.0-5.0 µm	5.0-6.0 µm	6.0-7.0 µm
17	6	4	4	1	2	0	0
7	3	2	2	0	0	0	0
10	4	3	1	0	1	1	0
12	8	2	2	0	0	0	0
30	15	11	2	1	1	0	0
6	5	1	0	0	0	0	0
15	5	5	2	1	1	1	0
9	2	2	2	0	0	0	0
14	12	2	0	0	0	0	0
7	4	2	1	0	0	0	0
4	2	2	0	0	0	0	0
9	8	0	1	0	0	0	0
16	13	3	0	0	0	0	0
33	15	10	4	2	0	1	1
7	3	2	1	0	1	0	0
7	4	0	2	0	1	0	0
3	2	1	0	0	0	0	0
6	4	2	0	0	0	0	0
6	3	1	1	0	1	0	0
6	1	2	2	0	1	0	0
4	3	1	0	0	0	0	0
19	3	6	5	2	0	2	1
14	8	1	1	0	4	0	0
12	8	1	3	0	0	0	0
7	5	2	0	0	0	0	0

TABLE 7. Steel C.

Annealing Procedure (1)

Size - Distribution of Carbide Particles

Number of all particles	Number of Particles						
	0-1.0 µm	1.0-2.0 µm	2.0-3.0 µm	3.0-4.0 µm	4.0-5.0 µm	5.0-6.0 µm	6.0-7.0 µm
7	4	1	1	0	0	1	0
3	1	1	0	0	0	1	0
7	6	1	0	0	0	0	0
2	2	0	0	0	0	0	0
3	3	0	0	0	0	0	0
11	7	0	0	0	4	0	0
1	1	0	0	0	0	0	0
13	4	1	2	3	2	1	0
12	8	3	0	0	0	1	0
37	15	12	8	1	0	1	0
7	4	1	1	1	0	0	0
23	8	2	9	3	1	0	0
4	3	1	0	0	0	0	0
7	6	0	0	0	1	0	0
9	3	4	0	1	1	0	0
2	1	0	0	0	1	0	0
4	1	3	0	0	0	0	0
14	7	2	5	0	0	0	0
12	5	4	1	1	0	1	0
7	4	2	0	0	0	1	0
3	2	0	0	0	1	0	0
4	3	0	0	0	0	1	0
4	3	1	0	0	0	0	0
8	5	3	0	0	0	0	0
5	4	1	0	0	0	0	0

TABLE 7. Steel C.

Annealing Procedure (2)

Size - Distribution of Carbide Particles

Number of all particles	Number of Particles						
	0-1.0 Um	1.0-2.0 Um	2.0-3.0 Um	3.0-4.0 Um	4.0-5.0 Um	5.0-6.0 Um	6.0-7.0 Um
37	24	6	6	1	0	0	0
61	11	5	25	14	3	3	0
72	25	9	22	9	5	2	0
9	4	0	2	2	1	0	0
32	9	8	11	3	1	0	0
23	17	5	2	0	0	0	0
8	7	1	0	0	0	0	0
18	12	4	1	1	0	0	0
13	7	3	2	1	0	0	0
24	12	3	7	2	0	0	0
6	4	1	0	1	0	0	0
11	9	2	0	0	0	0	0
13	1	0	0	0	0	0	0
15	10	3	2	0	0	0	0
8	5	3	0	0	0	0	0
4	4	0	0	0	0	0	0
7	6	1	0	0	0	0	0
9	4	1	2	1	0	1	0
26	7	4	3	6	5	1	0
3	2	1	0	0	0	0	0
22	15	2	5	0	0	0	0
5	4	0	1	0	0	0	0
13	8	2	3	0	0	0	0
11	3	2	5	1	0	0	0
3	3	0	0	0	0	0	0

TABLE 7. Steel C.

Annealing Procedure (2)

Size - Distribution of Carbide Particles

Number of all particles	Number of Particles						
	0-1.0 μm	1.0-2.0 μm	2.0-3.0 μm	3.0-4.0 μm	4.0-5.0 μm	5.0-6.0 μm	6.0-7.0 μm
3	3	0	0	0	0	0	0
17	10	5	1	0	0	1	0
8	4	1	2	0	0	1	0
9	7	1	1	0	0	0	0
19	10	4	3	2	0	0	0
18	10	1	4	1	2	0	0
9	7	2	0	0	0	0	0
4	4	0	0	0	0	0	0
12	4	7	0	0	1	0	0
8	8	0	0	0	0	0	0
27	15	9	1	1	0	1	0
10	5	0	2	2	1	0	0
28	12	9	4	2	0	0	1
19	9	3	3	2	1	1	0
4	3	1	0	0	0	0	0
5	2	0	1	1	0	1	0
9	5	1	2	1	0	0	0
13	8	3	0	0	2	0	0
5	3	1	1	0	0	0	0
9	9	0	0	0	0	0	0
11	7	2	1	1	0	0	0
17	6	3	2	2	1	3	0
12	5	2	0	1	2	2	0
5	4	1	0	0	0	0	0
12	6	1	3	2	0	0	0

TABLE 7. Steel C.

Annealing Procedure (3)

Size - Distribution of Carbide Particles

Number of all particles	Number of Particles						
	0-1.0 µm	1.0-2.0 µm	2.0-3.0 µm	3.0-4.0 µm	4.0-5.0 µm	5.0-6.0 µm	6.0-7.0 µm
28	8	8	6	2	2	1	1
4	2	1	0	0	0	0	1
16	9	2	3	1	0	0	1
20	4	11	4	1	0	0	0
25	10	7	5	2	1	0	0
9	2	1	3	1	0	0	2
18	13	2	3	0	0	0	0
19	10	3	1	1	4	0	0
24	14	6	1	2	1	0	0
8	6	0	2	0	0	0	0
8	1	2	4	0	0	1	0
5	3	1	1	0	0	0	0
14	8	4	2	0	0	0	0
10	0	3	6	0	1	0	0
6	3	3	0	0	0	0	0
17	8	7	1	0	1	0	0
18	8	8	1	0	0	1	0
19	4	5	6	1	2	1	0
22	6	7	5	0	1	2	1
15	9	2	2	1	1	0	0
10	8	1	0	1	0	0	0
30	14	4	5	1	3	2	1
14	3	9	1	1	0	0	0
10	6	2	0	2	0	0	0
21	12	4	2	2	1	0	0

TABLE 7. Steel C.

Annealing Procedure (3)

Size - Distribution of Carbide Particles

Number of all particles	Number of Particles						
	0-1.0 Um	1.0-2.0 Um	2.0-3.0 Um	3.0-4.0 Um	4.0-5.0 Um	5.0-6.0 Um	6.0-7.0 Um
14	5	5	3	1	0	0	0
16	4	3	4	1	2	1	1
11	8	2	0	0	0	0	1
21	14	5	1	0	0	0	1
16	4	6	4	2	0	0	0
9	5	2	1	0	1	0	0
12	6	2	1	1	0	0	2
16	8	4	3	1	0	0	0
10	1	5	0	0	4	0	0
17	7	7	2	0	1	0	0
14	7	5	2	0	0	0	0
8	3	1	4	0	0	0	0
10	2	4	1	2	0	1	0
17	9	0	4	4	0	0	0
13	6	5	1	0	1	0	0
14	8	5	1	0	0	0	0
17	11	4	2	0	0	0	0
12	3	4	4	1	0	0	0
10	6	0	3	0	0	1	0
7	3	0	0	1	2	1	0
10	5	2	1	0	0	1	1
15	12	2	1	0	0	0	0
10	6	3	1	0	0	0	0
6	3	3	0	0	0	0	0
9	4	1	2	2	0	0	0

TABLE 7. Steel C.

Annealing Procedure (4)

Size - Distribution of Carbide Particles

Number of all particles	Number of Particles						
	0-1.0 µm	1.0-2.0 µm	2.0-3.0 µm	3.0-4.0 µm	4.0-5.0 µm	5.0-6.0 µm	6.0-7.0 µm
12	3	5	4	0	0	0	0
26	11	7	2	1	3	0	2
6	3	0	2	0	1	0	0
6	3	1	1	0	0	0	1
11	1	2	1	4	1	0	2
14	4	2	2	2	3	0	1
10	5	2	1	1	0	0	1
21	6	3	6	1	2	0	3
19	15	1	0	0	1	0	2
21	7	8	4	1	1	0	0
22	12	4	2	1	1	2	0
8	2	1	2	1	1	1	0
9	1	5	2	1	0	0	0
6	3	1	2	0	0	0	0
9	2	5	1	0	1	0	0
10	8	2	0	0	0	0	0
18	15	0	2	0	1	0	0
19	13	4	2	0	0	0	0
9	3	4	2	0	0	0	0
16	7	6	3	0	0	0	0
3	2	1	0	0	0	0	0
28	14	6	3	3	1	1	0
11	5	3	1	1	0	0	1
9	6	0	2	1	0	0	0
12	6	5	1	0	0	0	0

TABLE 7. Steel C.

Annealing Procedure (4)

Size - Distribution of Carbide Particles

Number of all particles	Number of Particles						
	0-1.0 Um	1.0-2.0 Um	2.0-3.0 Um	3.0-4.0 Um	4.0-5.0 Um	5.0-6.0 Um	6.0-7.0 Um
4	1	3	0	0	0	0	0
12	9	0	2	0	1	0	0
15	12	2	1	0	0	0	0
12	8	0	0	2	2	0	0
13	2	3	6	1	0	1	0
10	4	3	0	1	0	1	1
13	5	3	2	1	1	1	0
17	10	5	1	0	1	0	0
26	10	6	6	1	2	1	0
7	3	3	0	1	0	0	0
25	18	5	1	0	1	0	0
9	2	1	4	0	0	1	1
7	3	0	1	1	1	1	0
12	6	3	0	2	1	0	0
10	5	4	0	0	1	0	0
18	9	6	2	1	0	0	0
15	7	3	1	2	2	0	0
15	11	1	1	2	0	0	0
16	11	2	1	2	0	0	0
30	24	4	1	0	0	1	0
12	9	2	1	0	0	0	0
9	4	1	3	1	0	0	0
16	8	8	0	0	0	0	0
11	9	1	0	0	1	0	0
5	3	0	1	1	0	0	0

TABLE 8a. Steels D.

Size - Distribution of Sulphides

Number of Fields: 120

Area scanned: 2.508 mms

Steels D	Number of Sulphides							Area %
	1 - 2 Um	2 - 3 Um	3 - 4 Um	4 - 5 Um	5 - 6 Um	6 - 8 Um	8 - 10 Um	
D 10	635	225	44	24	4.4	4.4	0.8	0.283
D 11	440	412	99	50	15	11.8	2.0	0.503
D 12	795	593	151	63	24	14.8	7.2	0.73
D 20	352	202	40	17	3	1.2	1.0	0.226
D 21	1143	744	102	33	13	10.8	2.4	0.70
D 22	1367	970	238	95	32	20	6.4	0.993
D 30	763	394	77	26	5	8	3.0	0.375
D 31	1422	495	58	20	4	4	2.0	0.557
D 32	1902	792	118	35	10	6	3.0	0.814

TABLE 8b. Steels D.

Size - Distribution of Oxides

Number of Fields: 120

Area scanned: 2.508 mms

Steels D	Number of Oxides							Area %
	1 - 2 Um	2 - 5 Um	5 - 10 Um	10-15 Um	15-20 Um	20-30 Um	30-40 Um	
D 10	39	168	35.5	4.0	0.40	0.40	-	0.197
D 11	50	138	30.0	8.0	2.50	0.50	-	0.236
D 12	47	167.8	36.0	7.5	3.0	0.80	0.80	0.339
D 20	15.1	49.5	7.5	0.80	-	0.80	-	0.054
D 21	34.4	88.0	11.0	0.80	0.75	-	-	0.114
D 22	27.8	96.6	17.5	4.5	0.75	1.0	0.40	0.180
D 30	7.1	20.5	6.5	0.5	-	-	-	0.029
D 31	4.3	21.9	5.0	3.0	0.50	0.50	-	0.048
D 32	4.8	15.0	6.0	1.0	-	-	-	0.036

TABLE 9. Average Strain Values at the Point of Necking

Steel A.

Extension at the point of necking ΔL mm.	Average longitudinal strain at necking $\text{Log}_e\left(\frac{L_o+\Delta L}{L_o}\right)$	Average circumferential strain at the point of necking $\varepsilon_\theta = \log_e(b/r)$	The eccentricity of the grid ellipse at the point of necking $e = [1-\exp.(2\varepsilon_\theta)]^{1/2}$
11.7	0.210	0.168	0.534
11.6	0.209	0.143	0.499
11.4	0.205	0.151	0.511
9.6	0.176	0.140	0.494
12.3	0.220	0.141	0.496
11.8	0.212	0.143	0.499
14.3	0.252	0.149	0.508
14.3	0.252	0.184	0.555
7.6	0.141	0.140	0.494
10.10	0.184	0.150	0.509
14.4	0.253	0.144	0.500
10.5	0.191	0.104	0.433
11.3	0.204	0.165	0.530
11.7	0.210	0.146	0.503
11.3	0.204	0.154	0.515
11.0	0.199	0.147	0.505
12.3	0.220	0.159	0.522
11.2	0.202	0.143	0.499
11.0	0.199	0.174	0.542
12.9	0.230	0.150	0.509

TABLE 10. Average Strain Values at the Point of Necking Steel B.

Extension of the specimen at the point of necking ΔL mm.	Average longitudinal strain at necking $\text{Log}_e\left(\frac{L_o+\Delta L}{L_o}\right)$	Average circumferential strain at the point of necking $\varepsilon_\theta = \log_e(b/r)$	The eccentricity of the grid mark ellipse at the point of necking $e=[1-(\exp.2\varepsilon_\theta)]^{1/2}$
12.2	0.218	0.160	0.523
10.7	0.193	0.153	0.513
12.2	0.218	0.155	0.516
11.8	0.212	0.145	0.504
12.0	0.215	0.143	0.499
10.0	0.182	0.140	0.594
13.0	0.231	0.144	0.500
12.6	0.225	0.142	0.497
9.7	0.177	0.163	0.527
12.0	0.215	0.149	0.508
11.8	0.212	0.135	0.486
11.3	0.204	0.149	0.508
13.6	0.240	0.160	0.523
11.0	0.199	0.128	0.475
11.2	0.202	0.151	0.511
11.0	0.182	0.128	0.475
11.4	0.205	0.163	0.527
11.2	0.202	0.141	0.496
11.2	0.202	0.140	0.494
11.5	0.207	0.145	0.502

TABLE 11. Average Strain Values at the Point of Necking

Steel C.

Extension of the specimen at the point of necking ΔL mm.	Average longitudinal strain at necking $\log_e\left(\frac{L_o+\Delta L}{L_o}\right)$	Average circumferential strain at the point of necking $\varepsilon_\theta = \log_e (b/r)$	The eccentricity of the grid mark ellipse at the point of necking $e=[1-\exp.(2\varepsilon_\theta)]^{1/2}$
13.5	0.237	0.114	0.452
13.2	0.234	0.100	0.426
12.0	0.214	0.090	0.406
13.0	0.231	0.119	0.460
13.0	0.231	0.110	0.444
14.8	0.259	0.114	0.452
14.2	0.249	0.100	0.426
10.0	0.182	0.088	0.402
11.5	0.207	0.113	0.450
12.0	0.215	0.113	0.450
12.0	0.215	0.113	0.450
15.0	0.262	0.123	0.467
12.3	0.220	0.094	0.414
10.0	0.182	0.083	0.391
12.0	0.215	0.110	0.444
13.1	0.233	0.119	0.460
13.0	0.231	0.123	0.467
10.5	0.191	0.093	0.412
11.5	0.207	0.114	0.452
13.0	0.231	0.137	0.490

TABLE 12. Strain Distribution for Steel (A)

Distance away from the neck along the tensile axis of specimen mm	Longitudinal strains		Negative transverse strain		
	Along the tensile axis of the specimen ε_x	On the outer surface of the specimen ε_L	Radial strain ε_r	Circum-ferential ε_θ	Effective Strain $\bar{\varepsilon}$
24.50	0.20	0.18	0.10	0.14	0.24
23.80	0.21	0.17	0.10	0.14	0.25
20.90	0.23	0.17	0.10	0.15	0.24
20.60	0.24	0.17	0.12	0.14	0.25
16.70	0.26	0.18	0.13	0.16	0.27
16.40	0.27	0.18	0.13	0.18	0.29
16.10	0.25	0.20	0.12	0.15	0.26
15.10	0.27	0.22	0.14	0.18	0.29
13.70	0.30	0.21	0.15	0.20	0.31
13.00	0.29	0.22	0.15	0.16	0.30
12.50	0.30	0.26	0.15	0.18	0.32
10.50	0.32	0.27	0.16	0.20	0.33
10.00	0.30	0.24	0.15	0.19	0.32
0.50	0.33	0.24	0.16	0.20	0.34
9.00	0.33	0.25	0.16	0.20	0.34
8.50	0.35	0.30	0.18	0.20	0.36
8.30	0.36	0.30	0.18	0.20	0.38
7.90	0.38	0.32	0.19	0.21	0.39
7.50	0.40	0.33	0.20	0.22	0.40
7.30	0.41	0.36	0.21	0.22	0.42
7.00	0.41	0.36	0.21	0.23	0.42
6.70	0.44	0.40	0.22	0.23	0.44
6.60	0.43	0.38	0.21	0.24	0.43
6.50	0.42	0.40	0.21	0.23	0.43
6.20	0.45	0.43	0.23	0.24	0.45
6.00	0.45	0.44	0.23	0.23	0.46
5.75	0.47	0.55	0.23	0.26	0.48
5.50	0.48	0.53	0.24	0.26	0.49
5.45	0.50	0.61	0.25	0.27	0.50
5.20	0.49	0.68	0.25	0.29	0.50

TABLE 12 (Contd.) Strain Distribution for Steel (A)

Distance away from the neck along the tensile axis of specimen mm	Longitudinal strains		Negative Transverse strains		
	Along the tensile axis of the specimen ε_x	On the outer surface of the specimen ε_L	Radial strain ε_r	Circum-ferential ε_θ	Effective strain $\bar{\varepsilon}$
5.00	0.54	0.70	0.27	0.30	0.55
4.90	0.52	0.81	0.26	0.31	0.54
4.75	0.56	0.90	0.28	0.31	0.57
4.65	0.54	0.91	0.27	0.33	0.56
4.40	0.59	0.96	0.30	0.32	0.60
4.30	0.57	0.97	0.29	0.33	0.58
4.10	0.62	1.08	0.31	0.32	0.62
4.00	0.60	1.07	0.30	0.35	0.61
3.90	0.60	1.12	0.30	0.34	0.61
3.65	0.64	1.15	0.32	0.36	0.66
3.50	0.64	1.15	0.32	0.35	0.65
3.30	0.69	1.22	0.34	0.36	0.69
3.15	0.69	1.29	0.35	0.38	0.70
3.00	0.71	1.32	0.36	0.40	0.72
2.95	0.74	1.31	0.37	0.37	0.74
2.60	0.77	1.41	0.39	0.39	0.77
2.45	0.83	1.40	0.42	0.39	0.82
2.40	0.79	1.37	0.40	0.39	0.78
2.25	0.80	1.54	0.40	0.45	0.82
2.00	0.84	1.66	0.42	0.57	0.89
1.90	0.92	1.53	0.46	0.42	0.91
1.85	0.88	1.63	0.44	0.50	0.90
1.80	0.88	1.62	0.44	0.53	0.91
1.65	0.90	1.70	0.45	0.78	1.03
1.60	0.92	1.69	0.46	0.67	0.99
1.50	0.95	1.71	0.47	0.58	1.00
1.40	0.96	1.75	0.48	0.64	1.01
1.25	0.98	1.77	0.49	0.78	1.09
1.10	1.06	1.93	0.53	0.56	1.07
1.00	1.03	1.92	0.51	0.69	1.11
0.70	1.11	2.01	0.56	0.64	1.14
0.50	1.13	2.09	0.56	0.76	1.21
0.35	1.18	2.15	0.59	0.78	1.25
0.00	1.24	2.21	0.62	0.88	1.34

TABLE 13. Strain Distributions for Steel (B)

Distance away from the neck along the tensile axis of specimen mm	Longitudinal strains		Negative Transverse Strains		Effective strain
	Along the tensile axis of the specimen $-\varepsilon_x$	On the outer surface of the specimen ε_L	Radial strain ε_r	Circum-ferential ε_θ	$\bar{\varepsilon}$
21.50	0.21	0.20	0.13	0.13	0.22
20.00	0.20	0.20	0.10	0.13	0.21
16.80	0.20	0.20	0.10	0.14	0.22
16.50	0.22	0.20	0.11	0.15	0.24
16.00	0.22	0.20	0.11	0.14	0.23
13.00	0.25	0.20	0.12	0.14	0.26
12.50	0.24	0.22	0.12	0.16	0.25
12.00	0.25	0.20	0.13	0.12	0.25
11.50	0.25	0.23	0.13	0.14	0.26
11.00	0.25	0.23	0.13	0.16	0.26
10.50	0.28	0.25	0.14	0.15	0.28
10.00	0.25	0.25	0.13	0.15	0.26
9.50	0.28	0.27	0.14	0.18	0.30
9.00	0.30	0.27	0.15	0.18	0.32
8.65	0.28	0.28	0.14	0.16	0.30
8.50	0.35	0.28	0.17	0.19	0.36
8.00	0.42	0.30	0.21	0.20	0.42
7.80	0.36	0.30	0.18	0.20	0.37
7.60	0.38	0.30	0.19	0.20	0.39
7.50	0.38	0.33	0.19	0.20	0.39
7.20	0.38	0.35	0.19	0.19	0.38
7.00	0.37	0.38	0.19	0.21	0.39
6.80	0.43	0.40	0.21	0.22	0.43
6.70	0.41	0.39	0.20	0.22	0.42
6.50	0.45	0.39	0.22	0.23	0.45
6.20	0.48	0.30	0.24	0.25	0.48
6.00	0.44	0.39	0.22	0.23	0.44
5.50	0.52	0.46	0.26	0.30	0.54
5.30	0.57	0.42	0.29	0.30	0.58

TABLE 13. (Contd.) Strain Distributions for Steel (B)

Distance away from the neck along the tensile axis of specimen mm	Longitudinal strains		Negative Transverse Strains		Effective strain $\bar{\varepsilon}$
	Along the tensile axis of the specimen ε_x	On the outer surface of the specimen ε_L	Radial strain ε_r	Circum-ferential ε_θ	
5.20	0.55	0.49	0.27	0.31	0.57
5.10	0.57	0.50	0.29	0.26	0.56
4.90	0.59	0.47	0.29	0.32	0.59
4.80	0.56	0.55	0.28	0.24	0.55
5.60	0.61	0.58	0.30	0.32	0.62
4.30	0.60	0.60	0.30	0.31	0.60
4.20	0.66	0.64	0.33	0.35	0.67
4.00	0.66	0.68	0.33	0.33	0.66
3.75	0.72	0.73	0.36	0.37	0.72
3.30	0.77	0.81	0.39	0.42	0.78
3.15	0.82	1.00	0.41	0.42	0.82
2.90	0.85	1.15	0.42	0.45	0.86
2.80	0.85	1.17	0.43	0.47	0.86
2.65	0.90	1.21	0.45	0.47	0.92
2.50	0.90	1.33	0.45	0.56	0.93
2.30	0.92	1.04	0.46	0.53	0.96
2.10	0.95	1.35	0.48	0.52	0.97
2.00	1.01	1.53	0.50	0.60	1.05
1.85	0.98	1.40	0.49	0.55	1.00
1.70	1.00	1.41	0.50	0.55	1.02
1.50	1.10	1.45	0.55	0.58	1.11
1.20	1.18	1.60	0.59	0.63	1.19
1.00	1.15	1.72	0.58	0.63	1.17
1.25	1.25	1.77	0.62	0.67	1.26
0.80	1.22	1.85	0.61	0.67	1.24
0.50	1.31	1.93	0.66	0.69	1.33
0.45	1.40	2.00	0.70	0.71	1.41
0.25	1.38	1.90	0.69	0.70	1.39
0.00	1.50	2.15	0.75	0.77	1.50

TABLE 14. Strain Distributions for Steel (C)

Distance a way from the neck along the tensile axis of specimen mm	Longitudinal strains		Negative Transverse strains		
	Along the tensile axis of the specimen ε_x	On the outer surface of the specimen ε_L	Radial strain ε_r	Circum-ferential ε_θ	Effective strain $\bar{\varepsilon}$
50.00	0.20	0.20	0.10	0.08	0.19
30.50	0.22	0.20	0.11	0.10	0.22
30.00	0.20	0.20	0.10	0.10	0.20
29.50	0.22	0.20	0.11	0.09	0.21
29.00	0.21	0.21	0.10	0.10	0.21
28.20	0.23	0.23	0.11	0.10	0.22
20.20	0.22	0.24	0.11	0.10	0.22
16.70	0.23	0.25	0.11	0.10	0.22
13.50	0.25	0.29	0.13	0.08	0.23
13.00	0.27	0.30	0.13	0.10	0.25
12.50	0.29	0.30	0.15	0.13	0.30
12.40	0.30	0.35	0.15	0.15	0.30
12.00	0.31	0.36	0.15	0.20	0.33
10.80	0.37	0.32	0.19	0.21	0.38
10.50	0.35	0.39	0.19	0.23	0.39
10.10	0.40	0.45	0.20	0.23	0.42
9.50	0.38	0.39	0.19	0.22	0.39
9.00	0.45	0.49	0.23	0.28	0.47
8.50	0.40	0.45	0.20	0.23	0.42
8.35	0.42	0.65	0.21	0.25	0.43
8.00	0.45	0.68	0.23	0.27	0.47
7.70	0.46	0.80	0.23	0.26	0.48
7.50	0.49	0.83	0.25	0.27	0.50
7.20	0.51	0.95	0.25	0.27	0.52
7.00	0.55	0.88	0.27	0.31	0.56
6.50	0.55	1.00	0.28	0.31	0.56
6.30	0.65	1.01	0.33	0.33	0.65
6.00	0.62	1.12	0.31	0.33	0.63
5.80	0.67	0.98	0.34	0.34	0.67
5.65	0.66	1.20	0.33	0.35	0.67
5.50	0.70	1.25	0.35	0.37	0.71
5.20	0.77	1.27	0.39	0.41	0.78

TABLE 14. (Contd.) Strain Distribution for Steel (C)

Distance away from the neck along the tensile axis of specimen mm	Longitudinal strains		Negative Transverse strains		
	Along the tensile axis of the specimen ε_x	On the outer surface of the specimen ε_L	Radial strain ε_r	Circum-ferential strains ε_θ	Effective strain $\bar{\varepsilon}$
5.00	0.72	1.22	0.36	0.40	0.74
4.80	0.76	1.32	0.38	0.39	0.77
4.70	0.77	1.42	0.39	0.41	0.78
4.50	0.80	1.40	0.40	0.42	0.81
4.20	0.91	1.51	0.45	0.50	0.92
4.00	0.85	1.51	0.43	0.45	0.86
3.90	0.90	1.57	0.45	0.48	0.92
3.65	0.94	1.63	0.47	0.50	0.95
3.50	0.92	1.52	0.46	0.47	0.92
3.40	1.05	1.74	0.52	0.58	1.07
3.10	1.04	1.82	0.52	0.60	1.07
3.00	1.10	1.82	0.55	0.63	1.12
2.80	1.13	1.93	0.57	0.68	1.17
2.70	1.20	1.89	0.60	0.65	1.21
2.50	1.23	1.96	0.61	0.72	1.27
2.20	1.32	2.03	0.66	0.76	1.37
2.10	1.30	2.06	0.65	0.76	1.35
2.00	1.38	2.13	0.69	0.82	1.40
1.85	1.48	2.20	0.74	0.83	1.51
1.70	1.56	2.30	0.78	0.82	1.57
1.50	1.58	2.24	0.79	0.84	1.60
1.40	1.68	2.38	0.84	0.84	1.68
1.25	1.77	2.29	0.89	0.88	1.77
1.15	1.82	2.35	0.91	0.85	1.80
1.00	1.88	2.48	0.94	0.88	1.86
0.70	2.10	2.60	1.05	0.89	2.05
0.50	2.18	2.58	1.09	0.86	2.12
0.30	2.27	2.80	1.14	0.88	2.19
0.10	2.36	2.55	1.18	0.88	2.27
0.00	2.50	2.68	1.25	0.88	2.39

TABLE 15. Steel A. Total number of grid intersections falling on the Photograph = 400

True effective strain	Voids				Carbide Particles						
	$\bar{a}$	M_{av}	N_{pv}	f_v	$\bar{a}$	M_{ac}	N_{pc}	f_c	(f_v/f_c)	(f_v/M_a)	$C = [1+k(a/b)^2]$
1.22	21.5	38	46	0.115	2.6	32	40	0.100	1.15	3.03	1.045
1.35	7.0	40	23	0.058	6.9	24	15	0.038	1.53	1.45	1.024
1.20	22.7	21	45	0.113	3.7	32	53	0.133	0.85	5.38	1.084
1.19	11.8	19	23	0.058	5.3	31	18	0.045	1.29	3.05	1.037
1.14	34.2	18	28	0.070	20.8	18	30	0.076	0.93	3.83	1.073
1.14	20.7	19	15	0.038	11.5	26	19	0.048	0.79	2.00	1.102
1.14	46.8	36	23	0.058	39.4	8	28	0.070	0.83	1.61	1.092
1.25	69.7	30	36	0.090	6.5	25	30	0.075	1.20	3.00	1.041
1.09	33.6	33	40	0.100	13.4	22	54	0.135	0.74	3.00	1.122
0.96	30.0	20	20	0.050	17.5	13	13	0.033	0.52	2.50	1.291
0.85	58.8	33	13	0.033	2.2	69	60	0.150	0.22	1.00	3.015
1.03	18.4	18	17	0.043	20.0	27	30	0.075	0.57	2.39	1.219
1.08	17.3	12	12	0.030	14.3	12	14	0.035	0.86	2.50	1.091
1.07	30.1	16	32	0.080	3.8	44	24	0.060	1.33	5.00	1.038
1.09	10.0	38	36	0.090	1.9	38	43	0.108	0.83	2.37	1.097
1.08	23.8	60	46	0.115	30.7	18	52	0.130	0.89	1.91	1.085
1.00	11.6	23	17	0.043	30.5	27	23	0.058	0.74	1.87	1.135
0.98	11.7	17	10	0.025	27.0	16	18	0.045	0.29	1.42	1.907
0.98	107.2	66	40	0.100	21.8	40	45	0.113	0.89	1.50	1.096
0.63	0.9	65	10	0.025	2.3	102	47	0.118	0.21	0.38	7.438
0.73	4.6	18	28	0.070	1.4	39	63	0.158	0.44	3.89	1.752
0.62	220.9	70	26	0.065	63.7	41	43	0.108	0.60	0.92	1.936
0.63	21	45	27	0.068	56.8	33	79	0.198	0.34	1.51	3.564
0.93	87	39	15	0.038	5.2	64	25	0.063	0.60	0.97	1.230
0.97	15.5	15	9	0.023	7.1	56	32	0.080	0.31	1.53	1.806
0.94	4.7	15	10	0.025	28.7	51	23	0.080	0.86	1.67	1.110
0.97	5.9	17	24	0.060	23.9	58	28	0.070	0.86	3.53	1.105
0.95	30.9	84	42	0.105	77.7	21	46	0.115	0.92	1.07	1.094

TABLE 15. Steel A. Total number of grid intersections falling on the photograph = 210

True effective strain	Voids				Carbide Particles						C=
	$\bar{a}$	M_{aV}	N_{pv}	f_v	$\bar{a}$	M_{aC}	N_{pc}	f_c	(f_v/f_c)	(f_v/M_{aV})	$1+k(a/b)^2$
0.80	5.0	41	10	0.055	0.7	24	18	0.099	0.56	1.34	1.357
1.32	4.0	26	14	0.077	2.6	29	16	0.088	0.88	2.96	1.072
1.27	4.9	22	9	0.049	2.2	18	6	0.033	1.49	2.23	1.026
0.97	5.3	14	15	0.082	1.8	45	29	0.159	0.52	5.86	1.286
0.95	2.5	22	9	0.049	1.8	24	14	0.077	0.64	2.23	1.195
1.25	16.0	12	14	0.067	8.9	8	15	0.072	0.93	5.58	1.068
1.25	34.6	40	20	0.095	9.9	35	20	0.095	1.00	2.23	1.058
1.24	18.9	25	13	0.062	16.8	7	9	0.043	1.44	2.48	1.028
1.24	30.7	42	22	0.105	3.7	18	26	0.124	0.85	2.50	1.081
1.24	17.6	25	11	0.052	7.0	15	11	0.052	1.04	2.08	1.059
1.35	8.8	20	9	0.043	15.4	6	6	0.029	1.41	2.15	1.025
1.21	3.7	12	7	0.033	12.0	10	7	0.033	1.05	2.75	1.060
1.10	13.3	44	14	0.067	15.0	18	17	0.081	0.83	1.52	1.096
0.70	4.2	39	8	0.038	7.9	40	26	0.124	0.31	0.97	2.767
1.20	3.2	18	8	0.038	11.7	10	8	0.038	1.00	2.11	1.060
0.89	3.4	24	10	0.037	3.4	40	14	0.052	0.71	1.54	1.177
0.70	4.6	20	6	0.029	17.8	32	21	0.100	0.29	1.45	3.019
1.00	8.9	16	6	0.029	8.7	9	8	0.038	0.76	1.81	1.128
0.90	2.1	18	6	0.024	4.5	9	10	0.048	0.60	1.61	1.290
0.75	5.3	16	4	0.019	10.0	16	7	0.033	0.58	1.19	1.397
0.72	2.1	26	5	0.024	8.4	25	15	0.071	0.39	0.92	2.321
0.78	9.25	19	7	0.026	5.8	15	9	0.033	0.81	1.37	1.196
0.41	6.3	32	3	0.014	8.4	18	19	0.090	0.18	0.44	
0.48	26.6	49	7	0.033	14.7	30	17	0.081	0.47	0.67	
0.47	15.2	26	4	0.019	23.1	20	17	0.081	0.30	0.73	
0.55	4.9	29	5	0.024	8.2	25	18	0.086	0.33	0.83	
0.35	1.4	42	7	0.033	4.6	60	40	0.190	0.19	0.79	

TABLE 15. (Contd.) Steel A. Total Number of Grid Intersections Falling on the Photograph = 238

True effective strain	Voids				Carbide Particles						
	$\bar{a}$	M_{av}	N_{pv}	f_v	$\bar{a}$	M_{ac}	N_{pc}	f_c	(f_v/f_c)	(f_v/M_{av})	$C=[1+k(a/b)^2]$
1.33	16.6	8	5	0.021	12	7	3	0.013	1.62	2.63	1.021
1.30	8.4	16	12	0.050	16.9	15	8	0.034	1.47	3.13	1.026
0.65	3.6	13	5	0.021	13.9	23	20	0.084	0.25	1.62	4.884
0.80	10.6	12	7	0.029	9.1	15	16	0.067	0.43	2.42	1.605
1.30	8.4	13	13	0.055	10.7	11	12	0.050	1.10	4.23	1.047
1.35	5.0	15	8	0.034	5.5	10	5	0.021	1.62	2.27	1.021
1.25	5.6	18	9	0.038	11.3	23	11	0.046	0.83	2.11	1.085
0.64	10.0	12	8	0.034	7.0	39	19	0.080	0.43	2.83	2.445
0.98	8.4	10	6	0.025	12.2	15	9	0.038	0.66	2.50	1.175
1.23	16.0	14	14	0.059	0.7	23	14	0.059	1.00	4.21	1.059
0.93	5.9	15	10	0.042	10.1	51	29	0.122	0.38	2.80	1.715
1.24	9.8	15	12	0.050	6.3	40	22	0.092	0.51	3.33	1.202
0.70	36.0	17	11	0.046	9.0	17	23	0.097	0.47	3.70	1.769
0.60	13.7	8	7	0.029	16.8	18	22	0.092	0.34	3.63	5.515
1.18	5.2	19	12	0.050	1.5	21	15	0.063	0.79	2.63	1.098
1.20	10.3	13	9	0.038	14.8	11	9	0.038	1.02	2.92	1.060
1.23	17.6	10	11	0.046	14.7	14	10	0.042	1.10	4.60	1.049
0.83	3.2	14	9	0.038	5.6	32	30	0.126	0.30	2.71	1.140
0.92	4.2	9	3	0.013	11.7	9	6	0.025	0.52	1.44	1.286
0.70	3.2	28	9	0.038	6.2	69	34	0.143	0.27	1.35	3.329
0.98	13.7	24	9	0.038	6.8	28	27	0.113	0.34	1.58	1.660
1.22	3.8	16	12	0.050	2.9	38	18	0.076	0.66	3.13	1.137
1.21	4.4	16	14	0.059	1.7	33	25	0.105	0.56	3.69	1.191
0.54	26.2	33	8	0.034	6.1	26	25	0.105	0.36	1.03	
0.53	8.8	24	7	0.029	28.6	7	22	0.092	0.32	1.21	
0.60	4.8	22	6	0.025	3.3	80	52	0.218	0.14	1.13	
0.60	26.7	20	3	0.013	18.9	15	28	0.118	0.17	0.65	
0.55	5.6	18	3	0.013	14.2	16	13	0.055	0.28	0.72	
0.50	11.1	16	6	0.025	3.9	36	29	0.122	0.22	1.56	
0.49	2.4	7	1	0.004	8.9	37	20	0.084	0.08	0.57	

TABLE 15. (Contd.) Steel A. Total number of grid intersections falling on the photograph = 224

True effective strain	Voids				Carbide Particles				(f_v/f_c)	(f_v/M_{av})	$C = 1+k(a/b)^2$
	$\bar{a}$	M_{av}	N_{pv}	f_v	$\bar{a}$	M_{ac}	N_{pc}	f_c			
1.22	3.6	35	7	0.031	4.2	20	12	0.054	0.57	0.89	1.183
1.27	0.9	28	7	0.031	0.9	40	6	0.026	1.17	1.11	1.042
1.28	2.5	28	11	0.049	1.6	26	8	0.036	1.36	1.75	1.031
1.23	3.2	31	13	0.058	1.2	52	10	0.045	1.29	1.87	1.036
1.30	5.2	25	11	0.049	1.8	62	8	0.036	1.36	1.96	1.031
1.35	4.6	30	12	0.054	1.0	30	7	0.031	1.74	1.80	1.018
1.22	1.9	26	9	0.040	0.6	30	6	0.027	1.50	1.54	1.026
1.25	0.6	32	10	0.045	1.1	32	8	0.036	1.35	1.41	1.032
1.17	1.6	25	8	0.036	1.5	55	7	0.031	1.16	1.44	1.046
1.12	4.3	20	7	0.031	1.1	42	7	0.031	1.00	1.55	1.065
1.22	0.8	15	7	0.031	1.5	33	6	0.027	1.15	2.07	1.045
1.22	2.0	23	10	0.045	2.3	35	9	0.040	1.13	1.96	1.047
1.22	0.7	15	6	0.027	0.4	60	7	0.031	0.87	1.80	1.079
0.73	0.8	42	5	0.022	0.9	59	9	0.040	0.55	0.52	1.481
1.13	0.6	20	11	0.049	3.5	19	11	0.049	1.00	2.45	1.064
1.11	0.9	24	5	0.022	4.1	19	6	0.027	0.82	0.92	1.097
1.12	1.3	31	8	0.036	4.3	26	8	0.036	1.00	1.16	1.065
1.21	0.8	36	7	0.031	2.3	27	12	0.054	0.57	0.86	1.185
1.21	3.0	24	9	0.040	1.0	50	8	0.036	1.11	1.67	1.049
1.10	5.0	21	8	0.036	3.3	31	9	0.040	0.90	1.71	1.081
0.80	0.7	26	5	0.022	1.2	43	11	0.049	0.47	0.85	1.552
0.74			6	0.028			10	0.045	0.60		1.387
0.68			5	0.021			14	0.060	0.36		2.483
0.71			5	0.021			7	0.030	0.70		1.328
0.61			4	0.020			16	0.079	0.25		7.225
0.58			2	0.010			11	0.051	0.18		
0.50			0	0.00			19	0.080	0.00		
0.47			0	0.00			6	0.025	0.00		

TABLE 15. (Contd.) Steel A. Total number of grid intersections falling on the photograph = 270

True effective strain	Voids		Carbide Particles			(f_v / f_c)	$C = [1+k(a/b)^2]$
	N_{pv}	f_v		N_{pc}	f_c		
0.95	15	0.056		26	0.096	0.58	1.290
0.82	12	0.044		22	0.081	0.55	1.349
0.77	5	0.099		9	0.033	0.56	1.394
0.84	3	0.011		5	0.019	0.60	1.278
0.58	1	0.004		3	0.011	0.33	7.938
0.69	4	0.015		9	0.033	0.44	1.931
0.62	4	0.015		5	0.019	0.80	1.526
0.67	5	0.019		12	0.044	0.42	2.169
0.61	2	0.007		7	0.026	0.29	5.627
0.57	3	0.011		6	0.022	0.50	5.489
0.75	2	0.007		3	0.011	0.67	1.297
0.71	6	0.022		13	0.048	0.46	1.759
0.65	5	0.019		14	0.052	0.36	2.873
0.79	5	0.019		7	0.026	0.71	1.229
0.57	5	0.019		11	0.041	0.46	6.303
0.59	3	0.011		6	0.022	0.50	3.289
0.77	7	0.030		23	0.100	0.30	2.373
0.75	4	0.020		8	0.040	0.50	1.534
0.74	3	0.015		10	0.045	0.33	2.278
0.73	6	0.030		10	0.049	0.60	1.404
0.76	3	0.015		6	0.030	0.50	1.513
0.47	0	0.00		7	0.026	0.00	
0.57	1	0.003		5	0.019	0.20	
0.55	2	0.007		11	0.041	0.18	
0.52	3	0.011		13	0.048	0.23	
0.54	3	0.011		14	0.052	0.21	

TABLE 16. Steel B. Total number of grid intersections falling on the Photograph - 270

True effective strain	Voids				Carbide Particles						
	$\bar{a}$	M_{av}	N_{pv}	f_v	$\bar{a}$	M_{ac}	N_{pc}	f_c	(f_v/f_c)	(f_v/M_{av})	$C=[1+k(a/b)^2]$
1.45	7.0	29	16	0.059	1.7	30	9	0.033	2.03	1.03	1.020
1.45	2.0	17	11	0.041	0.6	61	11	0.041	1.03	1.41	1.066
1.20	1.8	22	10	0.037	0.8	41	13	0.048	0.77	1.68	1.123
1.15	5.4	25	9	0.033	3.0	42	12	0.044	0.75	1.32	1.135
1.10	2.5	21	9	0.033	2.2	52	16	0.059	0.56	1.57	1.253
1.47	8.1	44	25	0.093	6.6	17	14	0.052	1.79	2.11	1.020
1.44	7.5	31	19	0.070	4.2	26	12	0.044	1.59	2.26	1.025
1.43	2.4	38	17	0.063	6.0	63	13	0.048	1.31	1.66	1.037
1.13	2.2	31	8	0.030	3.6	33	8	0.030	1.00	0.97	1.077
1.39	1.4	28	17	0.063	1.5	37	13	0.048	1.31	2.25	1.038
1.35	7.9	25	20	0.074	3.9	35	15	0,056	1.32	2.96	1.038
1.24	7.8	12	13	0.048	2.6	36	12	0.044	1.09	4.00	1.060
1.14	5.1	23	13	0.048	8.2	19	14	0.053	0.91	2.09	1.092
1.00	10.1	15	9	0.033	1.4	78	14	0.052	0.64	2.20	1.218
1.33	13.2	27	22	0.081	5.8	17	19	0.070	1.16	3.00	1.050
1.30	130.3	32	26	0.096	4.0	39	21	0.078	1.24	3.00	1.044
1.28	41.5	17	15	0.056	4.2	14	13	0.048	1.15	3.29	1.052
1.39	41.0	24	11	0.041	2.1	24	8	0.030	1.38	1.71	1.034
1.20	2.4	40	15	0.056	0.9	30	14	0.052	1.07	1.40	1.064
1.17	18.2	44	20	0.074	1.4	28	17	0.063	1.18	1.68	1.054
0.79	1.3	17	5	0.019	2.2	26	17	0.063	0.29	1.12	1.653
1.50	5.3	16	14	0.052	0.7	22	7	0.026	2.00	3.25	1.016
1.35	23.7	20	21	0.078	0.5	24	12	0.045	1.73	3.90	1.022
1.40	3.8	31	21	0.078	0.6	40	11	0.041	1.90	2.52	1.018
1.30	3.0	18	22	0.081	1.1	55	15	0.056	1.45	4.50	1.032
1.49	1.3	38	46	0.170	2.1	68	23	0.085	2.00	4.47	1.016
1.15	0.6	19	8	0.030	1.3	41	8	0.030	1.00	1.58	1.076
1.50	0.7	40	20	0.074	0.05	50	11	0.041	1.95	1.85	1.016

TABLE 16. (Contd.) Steel B. Total number of grid intersections falling on the photograph = 255

True effective strain	Voids				Carbide Particles				(f_v/f_c)	(f_v/M_{av})	$C = [1+k(a/b)^2]$
	$\bar{a}$	M_{av}	N_{pv}	f_v	$\bar{a}$	M_{ac}	N_{pc}	f_c			
1.50	12.4	30	22	0.081	3.8	38	12	0.045	1.80	2.70	1.019
1.45	4.0	33	15	0.056	2.3	34	9	0.033	1.70	1.70	1.022
1.10	8.9	20	8	0.030	3.6	32	9	0.033	0.91	1.50	1.096
1.32	9.9	36	16	0.059	1.1	85	14	0.052	1.14	1.64	1.052
1.30	3.7	40	14	0.052	4.2	44	12	0.044	1.18	1.30	1.049
1.43	11.1	16	9	0.033	2.9	26	6	0.022	1.50	2.06	1.028
0.91	23.7	50	21	0.078	0.5	74	40	0.157	0.53	1.46	1.368
1.28	1.9	29	9	0.040	0.9	27	6	0.020	1.52	1.38	1.031
1.25	8.7	32	12	0.044	1.6	26	9	0.033	1.33	1.38	1.040
1.23	3.8	16	6	0.027	0.6	25	5	0.022	1.20	1.69	1.050
0.78	2.8	16	4	0.018	1.0	43	12	0.054	0.33	1.13	1.320
1.31	4.2	25	10	0.037	0.8	40	8	0.030	1.23	1.48	1.045
1.28	6.3	8	8	0.030	0.3	35	6	0.022	1.36	3.75	1.037
1.25	4.1	40	10	0.037	0.6	58	8	0.030	1.29	0.93	1.046
1.47	9.8	18	14	0.063	3.4	17	7	0.031	2.00	3.50	1.016
1.10	6.7	12	9	0.040	3.1	15	10	0.045	0.90	3.33	1.098
1.50	4.2	27	27	0.100	0.5	33	12	0.044	2.27	3.70	1.012
1.35	2.2	33	33	0.122	2.3	32	20	0.074	1.65	3.70	1.024
1.40	8.4	16	17	0.076	4.6	18	9	0.040	1.90	4.75	1.018
1.45	10.7	16	18	0.080	2.6	28	9	0.040	2.00	5.00	1.016
1.20	4.3	24	11	0.049	2.1	41	11	0.049	1.03	2.04	1.073
1.25	17.3	32	17	0.076	2.4	26	12	0.054	1.41	1.38	1.035
1.48	28.5	46	38	0.141	3.7	15	28	0.070	2.01	3.07	1.016
1.38	6.0	39	25	0.063	1.9	49	17	0.043	1.47	1.62	1.030
1.40	7.7	38	23	0.085	2.2	39	16	0.059	1.44	2.24	1.031
1.43	10.6	36	26	0.096	1.7	60	15	0.056	1.71	2.67	1.022
1.20	11.9	29	16	0.059	3.9	38	15	0.056	1.05	1.03	1.066

TABLE 16. (Contd.) Steel B. Total number of grid intersections falling falling on the photograph = 195

True effective strain	Voids				Carbide Particles				(f_v/f_c)	(f_v/M_{av})	$C = [1+k(a/b)^2]$
	$\bar{a}$	M_{av}	N_{pv}	f_v	$\bar{a}$	M_{ac}	N_{pc}	f_c			
0.95	0.80	18	6	0.30	1.0	24	11	0.056	0.54	1.67	1.339
0.80	2.1	33	6	0.030	1.1	24	12	0.062	0.48	0.91	1.585
0.87	3.5	39	9	0.045	1.6	45	18	0.092	0.52	1.15	1.467
0.67	4.7	45	8	0.041	2.8	30	22	0.113	0.35	0.91	2.814
0.65	1.8	19	3	0.015	1.1	30	10	0.051	0.29	0.79	4.477
0.65	0.5	15	3	0.015	1.1	30	13	0.067	0.22	1.00	7.041
0.62	2.8	17	2	0.010	2.9	18	7	0.036	0.28	0.59	6.175
0.66			3	0.015			10	0.051	0.19		4.191
0.65			9	0.045			36	0.182	0.25		5.678
0.69			1	0.005			3	0.015	0.33		2.993
0.71			3	0.015			8	0.040	0.38		2.340
0.75			10	0.051			28	0.131	0.36		2.240
0.66			7	0.031			26	26	0.25		4.970
0.64			15	0.067			51	51	0.29		4.826
0.64			3	0.013			10	10	0.030		4.575
0.74			6	0.027			15	15	0.40		2.048
0.63			8	0.035			20	20	0.39		3.357
0.82			8	0.035			18	18	0.44		1.656
0.71			16	0.071			45	45	0.36		2.493
0.80			16	0.071			39	39	0.44		1.696
0.57			7	0.031			24	0.107	0.29		17.072
0.67			7	0.031			21	0.093	0.33		3.281
0.59			5	0.022			22	0.098	0.22		
0.47			2	0.009			10	0.044	0.21		
0.46			7	0.031			25	0.111	0.28		

TABLE 16. (Contd.) Steel B. Total number of grid intersections falling on the photograph = 400

True effective strain	Voids		Carbide Particles			(f_v / f_c)	$C=[1+k(a/b)^2]^{-1}$
	N_{pv}	f_v	N_{pc}	f_c			
1.30	13	0.033	8	0.020		1.63	1.026
1.10	14	0.035	12	0.030		1.17	1.058
1.03	13	0.032	12	0.030		1.03	1.081
1.01	10	0.025	12	0.30		0.83	1.128
0.92	9	0.023	12	0.030		0.75	1.180
1.36	12	0.030	7	0.018		1.71	1.023
1.28	26	0.065	20	0.050		1.30	1.041
1.24	27	0.068	27	0.068		1.00	1.071
1.12	18	0.045	19	0.048		0.95	1.086
1.09	19	0.047	18	0.045		1.06	1.071
1.08	27	0.067	26	0.065		1.04	1.075
0.94	12	0.030	13	0.033		0.92	1.116
0.78	6	0.015	12	0.030		0.50	1.575
0.77	5	0.013	12	0.030		0.42	1.844
0.74	15	0.038	22	0.055		0.48	1.728
0.71	2	0.005	8	0.020		0.25	4.097
0.66	7	0.018	16	0.040		0.44	2.386
0.65	4	0.010	16	0.040		9.25	5.678
0.61	4	0.010	14	0.035		0.29	6.578
0.60	4	0.010	15	0.038		0.27	8.640
1.30	12	0.030	7	0.018		1.71	1.023
1.15	10	0.025	10	0.025		1.00	1.076
1.12	8	0.020	10	0.025		0.80	1.122
1.13	12	0.030	10	0.025		1.20	1.054
1.10	20	0.050	24	0.060		0.83	1.115
0.99	5	0.013	8	0.020		0.63	1.228
1.23	15	0.038	10	0.025		1.50	1.072
0.99	6	0.015	6	0.015		1.00	1.880
0.36	0	0.000	8	0.020		0.00	
0.32	3	0.008	20	0.050		0.002	

TABLE 16. (Contd.) Steel B. Total number of grid intersections falling on the Photograph = 288

True Effective strain	Voids		Carbide Particles			(f_v / f_c)	$C = [1+k(a/b)^2]$
	N_{pv}	f_v		N_{pc}	f_c		
0.80	3	0.010		12	0.042	0.25	3.144
0.92	3	0.010		5	0.017	0.60	1.282
0.68	4	0.014		10	0.035	0.40	2.447
0.64	3	0.010		9	0.031	0.33	3.954
0.62	3	0.010		8	0.028	0.37	3.963
0.60	4	0.014		13	0.045	0.31	6.795
1.22	5	0.017		5	0.017	1.00	1.072
0.82	9	0.031		24	0.083	0.38	1.880
0.57	3	0.010		15	0.052	0.20	
0.56	2	0.007		15	0.052	0.13	
0.55	5	0.017		20	0.069	0.25	
0.55	2	0.007		35	0.122	0.06	
0.52	2	0.007		17	0.059	0.12	
0.50	4	0.014		25	0.087	0.16	
0.42	4	0.014		18	0.063	0.22	
0.30	0	0.00		17	0.059	0.00	
0.38	1	0.003		20	0.069	0.05	
0.36	1	0.003		60	0.200	0.02	
0.34	0	0.00		20	0.069	0.00	
0.49	3	0.010		20	0.069	0.15	
0.41	2	0.007		10	0.035	0.20	
0.33	9	0.031		44	0.153	0.20	
0.30	3	0.010		17	0.059	0.18	

TABLE 17. Steel C.

Total No. of grid intersections falling on Photo N = 255			Total No. of grid intersections falling on Photo N = 270			Total No. of grid intersections falling on Photo N = 288		
True effective strain	Intersections falling on voids N_{pv}	Volume fraction of voids f_v	True effective strain	Intersections falling on voids N_{pv}	Volume fraction of voids f_v	True effective strain	Intersections falling on voids N_{pv}	Volume fraction of voids f_v
2.40	20	0.078	2.25	7	0.026	2.20	9	0.031
2.40	10	0.039	2.20	7	0.026	2.15	3	0.010
2.35	13	0.051	2.18	8	0.029	2.10	7	0.024
2.32	10	0.039	1.80	4	0.015	2.00	8	0.028
2.30	8	0.031	1.00	1	0.004	0.70	7	0.024
2.22	6	0.024	0.45	0	0.000	0.68	0	0.000
1.40	2	0.008	0.52	3	0.011	0.65	1	0.003
0.63	2	0.008	0.55	0	0.00	0.40	0	0.000
2.40	14	0.055	2.40	18	0.067	0.35	3	0.010
2.25	7	0.027	2.32	10	0.037	0.30	0	0.000
2.18	7	0.027	2.30	9	0.033	0.50	2	0.007
2.10	2	0.008	2.20	5	0.019	0.60	6	0.021
0.50	0	0.000	2.15	4	0.015	2.35	15	0.052
0.60	0	0.000	0.55	0	0.000	2.22	6	0.021

TABLE 17 (Contd.) Steel C.

Total No. of grid intersections falling on Photo N = 255			Total No. of grid intersections falling on Photo N = 270			Total No. of grid intersections falling on Photo N = 288		
True effective strain	Intersections falling on voids N_{pv}	Volume fraction of voids f_v	True effective strain	Intersections falling on voids N_{pv}	Volume fraction of voids f_v	True effective strain	Intersections falling on voids N_{pv}	Volume fraction of voids f_v
2.30	9	0.035	2.18	6	0.022	2.00	6	0.021
2.22	5	0.020	0.35	2	0.007	0.70	2	0.007
2.15	5	0.020	0.55	1	0.004	0.35	0	0.000
2.10	4	0.016	1.90	3	0.011	2.40	17	0.059
0.50	0	0.000	1.71	6	0.022	2.35	12	0.042
0.60	3	0.012	1.65	2	0.007	2.32	12	0.042
1.75	2	0.008	1.60	5	0.019	2.25	6	0.021
1.50	3	0.012	1.55	4	0.015	2.20	8	0.028
1.20	2	0.008	1.80	4	0.015	2.00	4	0.014
1.15	0	0.000	1.77	2	0.007	1.10	3	0.010
0.88	5	0.020	1.60	2	0.007	1.80	4	0.014
0.85	5	0.020	1.55	3	0.011	2.25	10	0.035
0.80	4	0.016	1.17	3	0.011	2.00	4	0.014

TABLE 18. Tensile Tests on Unnotched Specimens from the Alloys of Steel D, using the Hounsfield Tensile Machine

with (1) No. 12 specimens
(2) 1 ton load bar
(3) Gear ratio (magnification) x 4

Specimen	Elongation %	Reduction %	UTS N/mm^2	UTS $Kgf./mm^2$
D10 (a)	45	76	355.218	36.222
(b)	45	75	364.484	37.167
D11 (a)	44	70	321.241	32.757
(b)	45	70	319.696	32.600
D12 (a)	42	65	342.862	34.962
D20	46	80	362.940	37.010
D21 (a)	42	68	367.573	37.482
(b)	45	70	362.940	37.010
D22	42	68	344.407	35.120
D30 (a)	38	65	418.539	42.679
(b)	40	66	420.084	42.837
D31 (a)	42	68	413.906	43.207
(b)	34	66	424.717	43.309
D32	45	75	409.273	41.734

TABLE 19. Notch Tensile Test. Steel (A)

Specimen	Dia.of specimen mms	Dia.of notch section mms	Notch root radius mms	Notch Width mms	Stress concentration factor K_t	$(K_t - 1)/3$	Notch depth	Max: load Kgf	Notch strength Kg/mm^2	Notch strength ratio NSR	Log_e (NSR)	Load at fracture Kgf	Total extension mms	Total time to fracture mins	Features of Fracture surface
A1	0.77	5.13	1.04	2.08	1.84	0.59	1.236	1315	63.62	1.59	0.46	1238	-	7.00	Normal & shear
A2	10.0	5.33	1.04	2.08	1.85	0.61	1.220	1360	60.95	1.52	0.42	1263	-	8.00	Shear & normal rupt:
A3	10.02	5.26	1.12	2.34	1.81	0.53	1.236	1255	57.75	1.44	0.37	1050	0.60	9.11	Shear & normal
A4	10.02	5.06	1.02	2.06	1.84	0.59	1.245	1325	64.77	1.62	0.48	-	-	-	Normal & shear
A5	10.01	4.97	0.26	3.36	3.15	9.94	1.254	1400	72.17	1.80	0.59	-	-	-	Normal & partial cleavage
A6	10.03	5.07	0.26	3.32	3.20	10.65	1.245	1400	69.35	1.73	0.56	1250	0.60	-	Normal & shear
A7	10.03	5.07	0.26	3.30	3.20	10.65	1.245	1283	63.53	1.58	0.46	975	0.65	9.53	Normal & cleavage
A8	9.97	5.01	0.26	3.30	3.18	10.36	1.247	358	18.14	-	-	325	0.60	6.90	Defect with hole
A9	10.00	5.20	0.18	3.10	3.76	21.03	1.230	1425	67.099	1.68	0.52	1350	0.60	6.70	Normal & cleavage
A10	9.98	5.18	0.18	3.08	3.75	20.80	1.231	1430	67.856	1.70	0.53	1375	0.60	7.00	Normal & cleavage
A11	9.99	5.07	0.18	3.14	3.70	19.68	1.243	1368	67.74	1.69	0.53	-	-	-	Normal
A12	9.96	5.12	0.18	3.10	3.74	20.57	1.236	1385	67.27	1.68	0.52	1275	0.70	6.67	Normal & cleavage

TABLE 20. Notch Tensile Test. Steel (B)

Specimen	Dia.of specimen mms	Dia.of notch section mms	Notch root radius mms	Notch width mms	Stress concentration factor K_t	$(K_t - 1)/3$	Notch depth	Max: load Kgf	Notch strength Kg/mm^2	Notch strength ratio NSR	$\log_e$(NSR)	Load at fracture Kgf	Total extension mms	Total time to fracture mins	Features of fracture surface
B1	10.01	5.09	1.04	2.08	1.83	0.53	1.242	1200	58.97	1.51	0.41	925	1.10	-	Normal & shear
B2	10.01	5.13	1.04	2.08	1.84	0.59	1.238	1170	56.61	1.45	0.37	925	0.80	8.80	Normal & shear
B3	10.02	5.10	1.04	2.08	1.83	0.57	1.241	1193	58.38	1.50	0.40	900	1.25	8.80	Normal & shear
B4	9.93	4.97	0.26	3.40	3.15	9.94	1.249	2088	107.60	2.76	1.02	-	-	-	More cleavage
B5	9.99	5.07	0.26	3.32	3.18	10.36	1.243	1245	61.67	1.58	0.46	900	-	9.17	Normal & cleavage
B6	10.00	5.22	0.26	3.30	3.19	10.50	1.238	1251	61.32	1.57	0.45	915	0.60	9.03	Normal & cleavage
B7	9.98	4.98	0.18	3.16	3.70	19.68	1.251	1275	65.46	1.68	0.52	860	-	9.10	Normal & cleavage
B8	10.01	5.13	0.18	3.24	3.73	20.35	1.238	1305	63.14	1.62	0.48	888	0.40	8.90	Normal & cleavage

TABLE 21. Notch Tensile Test. Steel (D10)

Specimen	Dia. of specimen mms	Dia. of notch section mms	Notch root radius mms	Notch Width mms	Stress concentration factor K_t	$(K_t - 1)/3$	Notch depth	Max: load Kgf	Notch strength Kg/mm^2	Notch strength ratio NSR	Log_e(NSR)	Load at fracture Kgf	Total extension mms	Total time to fracture mins	Features of fracture surface
D101	9.98	5.00	1.02	2.12	1.835	0.58	1.249	1095	55.77	1.532	0.427	875	1.23	8.50	Normal & shear
D102	10.00	5.00	1.02	2.18	1.835	0.58	1.250	1065	54.24	1.490	0.399	825	1.30	8.17	Normal & shear
D103	9.99	5.08	1.02	2.18	1.840	0.59	1.242	1098	54.15	1.488	0.397	850	1.22	8.23	Normal & shear
D104	10.03	5.12	0.26	3.30	3.150	9.94	1.240	1253	60.83	1.671	0.514	1100	1.25	8.17	Normal & shear
D105	10.01	5.08	0.26	3.30	3.150	9.94	1.243	1245	61.43	1.688	0.523	1000	1.30	9.00	Normal & shear
D106		5.04	0.16	3.32	3.100	9.26	1.246	1240	62.15	1.708	0.535	1100	1.15	8.10	-
D107	9.99	5.04	0.16	3.16	3.950	25.67	1.246	1258	63.03	1.732	0.549	1000	1.26	8.80	Normal
D108	9.99	5.04	0.16	3.18	3.950	25.67	1.246	1260	63.16	1.732	0.551	1050	1.26	8.17	Normal & shear
D109	10.00	5.00	0.16	3.20	3.900	24.39	1.250	1205	61.37	1.686	0.522	1013	1.28	8.87	Normal & shear

TABLE 22. Notch Tensile Test. Steel (D11)

Specimen	Dia.of specimen mms	Dia.of notch section mms	Notch root radius mms	Notch Width mms	Stress concentration factor K_t	$(K_t - 1)\sqrt{3}$	Notch depth	Max: load Kgf	Notch strength Kg/mm^2	Notch Strength ratio NSR	Log_e(NSR)	Load at fracture Kgf	Total extension mms	Total time to fracture mins	Features of fracture surface
D111	10.0	5.24	1.00	1.96	1.87	0.65	1.227	993	46.02	1.41	0.34	900	1.26	8.00	Normal rupture/ shear
D112	10.00	5.08	1.00	1.96	1.85	0.60	1.242	855	42.18	1.29	0.25	250	1.20	5.83	Defects & holes/ cleavage
D113	10.00	5.08	1.00	1.96	1.85	0.60	1.242	988	48.72	1.49	0.40	925	1.00	7.03	Normal/ shear
D114	10.00	5.04	0.26	3.34	3.15	9.94	1.247	1075	53.88	1.65	0.50	1075	0.90	7.10	Normal & shear
D115	9.98	5.04	0.26	3.34	3.15	9.94	1.245	1083	54.26	1.66	0.51	1000	1.10	7.80	Normal & cleavage
D116	10.00	5.24	0.27	3.26	3.20	10.65	1.227	1045	48.46	1.48	0.39	950	0.90	6.67	Normal & shear
D117	10.01	5.08	0.16	3.14	3.95	25.67	1.243	1360	67.10	1.05	0.72	1350	0.65	6.40	Normal/ shear/ cleavage
D118	9.99	5.12	0.16	3.14	4.00	27.00	1.238	1045	50.76	1.55	0.44	1000	1.15	7.73	Normal rupture
D119	10.01	5.00	0.16	3.20	3.90	24.39	1.250	1048	53.35	1.63	0.49	975	1.15	7.77	Normal rupture

TABLE 23. Notch Tensile Test. Steel (D12)

Specimen	Dia.of specimen mms	Dia.of notch section mms	Notch root radius mms	Notch width mms	Stress Concentration factor K_t	$(K_t-1)/3$	Notch depth	Max: load Kgf	Notch strength Kg/mm^2	Notch strength ratio NSR	$Log_e(NSR)$	Load at fracture Kgf	Total extension mms	Total time to fracture mins	Features of fracture surface
D121	10.00	5.04	1.00	1.98	1.840	0.593	1.246	998	50.00	1.430	0.358	998	0.90	6.80	Shear at edges
D122	9.98	5.00	1.00	1.98	1.840	0.593	1.249	973	49.53	1.417	0.348	963	0.47	4.73	Shear at ends
D123	10.04	4.94	1.00	1.98	1.835	0.582	1.256	998	51.63	1.477	0.390	998	0.90	6.67	Shear at ends
D124	10.00	5.00	0.26	3.32	3.10	9.261	1.250	1088	55.39	1.584	0.460	1088	0.61	5.33	Normal shear
D125	9.98	5.04	0.26	3.32	3.25	9.938	1.245	838	41.98	1.201	0.183	800	0.60	3.93	-
D126	9.98	5.08	0.26	3.28	3.15	9,939	1.241	1125	55.51	1.588	0.462	1125	0.60	5.73	Normal & shear
D127	10.02	5.08	0.16	3.16	3.95	25.672	1.243	1178	58.34	1.669	0.512	1175	0.73	6.17	Normal & shear
D128	10.02	5.16	0.16	3.10	4.00	17.000	1.235	1145	54.75	1.566	0.449	1138	0.90	6.27	Normal rupture

TABLE 24. Notch Tensile Test. Steel (D20)

Specimen	Dia.of specimen mms	Dia.of notch section mms	Notch root radius mms	Notch width mms	Stress concentration factor K_t	$(K_t - 1)\omega$	Notch depth	Max: load Kgf	Notch strength Kg/mm^2	Notch Strength ratio NSR	$\log_e$(NSR)	Load at fracture Kgf	Total extension mms	Total time to fracture mins	Features of fracture Surface
D201	9.96	5.00	1.02	2.06	1.835	0.582	1.248	1083	55.13	1.490	0.399	775	1.40	8.73	Shear at edges
D202	9.95	5.07	1.02	2.06	1.840	0.593	1.241	935	46.31	1.251	0.224	750	1.45	-	-
D203	10.00	5.00	1.02	2.06	1.835	0.582	1.250	1095	55.77	1.507	0.410	775	1.37	8.28	Shear at edges
D204	10.02	4.98	0.26	3.38	3.150	9.938	1.253	1188	60.97	1.647	0.499	950	1.25	8.80	Normal & partial cleavage
D205	9.96	4.96	0.26	3.32	3.150	9.938	1.252	-	-	-	-	-	-	-	Normal & cleavage
D206	10.00	5.08	0.26	3.30	3.180	10.360	1.242	1198	59.08	1.596	0.468	925	1.50	9.10	Shear at edges
D207	9.97	5.01	0.18	3.16	3.67	19.034	1.247	1265	64.17	1.734	0.550	963	1.50	9.23	Shear at edges
D208	9.97	5.01	0.18	3.16	3.67	19.034	1.247	1280	64.93	1.754	0.562	950	1.50	9.83	Normal & Shear
D209	10.02	5.06	0.18	3.16	3.69	19.465	1.245	1263	62.78	1.696	0.528	1100	1.40	9.33	

TABLE 25. Notch Tensile Test. Steel (D21)

Specimen	Dia.of specimen mms	Dia.of notch section mms	Notch root radius mms	Notch width mms	Stress concentration factor K_t	$(K_t - 1)^3$	Notch depth	Max. load Kgf	Notch strength Kg/mm^2	Notch strength ratio NSR	$\log_e$(NSR)	Load at fracture Kgf	Total extension mms	Total time to fracture mins	Features of fracture surface
D211	10.00	5.12	1.00	1.98	1.850	0.614	1.238	1165	56.58	1.519	0.418	1050	1.10	7.92	Shear at ends
D212	9.97	5.08	1.00	1.96	1.850	0.614	1.241	1108	54.64	1.467	0.383	1025	1.07	7.80	Shear at ends
D213	10.00	5.04	1.00	2.00	1.845	0.603	1.246	1145	57.39	1.541	0.432	1025	1.00	7.90	Shear at edges
D214	9.99	5.00	0.26	3.32	3.100	9.261	1.249	1258	64.04	1.719	0.542	1200	0.91	7.23	Normal & shear
D215	10.01	5.12	0.26	3.28	3.150	9.938	1.239	1255	60.96	1.637	0.493	1225	0.93	7.37	Shear/ defect cleavage
D216	9.99	5.04	0.26	3.32	3.100	9.261	1.246	1215	60.90	1.635	0.492	1076	0.92	7.87	Normal & shear
D217	9.94	5.08	0.16	3.36	4.000	27.000	1.239	1295	63.89	1.715	0.540	1275	0.71	6.47	Normal & shear cleavage
D218	10.00	5.00	0.16	3.16	3.950	25.672	1.250	1228	62.52	1.678	0.518	1175	0.90	7.43	Normal

TABLE 26. Notch Tensile Test. Steel (D22)

Specimen	Dia.of specimen mms	Dia.of notch section mms	Notch root radius mms	Notch width mms	Stress concentration factor K_t	$(K_t-1)^3$	Notch depth	Max: load Kgf	Notch strength Kg/mm^2	Notch strength ratio NSR	$\log_e$(NSR)	Load at fracture Kgf	Total extension mms	Total time to fracture mins	Features of fracture surface
D221	10.03	4.92	1.00	1.98	1.830	0.57	1.260	1033	54.31	1.546	0.436	1000	0.92	7.13	Shear
D222	9.97	5.04	1.00	1.98	1.840	0.59	1.245	1010	50.63	1.442	0.366	975	1.08	7.13	Normal & shear
D223	10.02	5.04	1.00	1.98	1.840	0.59	1.247	1050	52.63	1.499	0.405	1000	1.05	6.90	Shear
D224	10.00	5.16	0.26	3.24	3.150	9.94	1.234	1195	56.67	1.614	0.479	1175	1.00	7.37	Normal & shear
D225	10.00	5.12	0.26	3.26	3.150	9.94	1.238	1175	57.07	1.625	0.486	1175	1.00	7.10	Normal & shear
D226	10.00	5.08	0.26	3.30	3.150	9.94	1.242	1163	57.36	1.633	0.490	1163	1.00	7.37	-
D227	10.01	5.08	0.16	3.16	3.950	25.67	1.243	1160	57.23	1.630	0.489	1150	0.96	7.40	Defects/ normal
D228	10.02	5.12	0.16	3.12	4.000	27.00	1.239	1170	56.83	1.618	0.481	1150	0.96	6.83	Normal
D229	10.01	5.16	0.16	3.10	4.000	27.00	1.235	1200	57.38	1.634	0.490	1200	0.88	6.43	Normal

TABLE 27. Notch Tensile Test. Steel (D30)

Specimen	Dia.of specimen mms	Dia.of notch section mms	Notch root radius mms	Notch width mms	Stress concentration factor K_t	$(K_t - 1)^3$	Notch depth	Max: load Kgf	Notch strength Kg/mm^2	Notch strength ratio NSR	$\log_e$(NSR)	Load at fracture Kgf	Total extension mms	Total time to fracture mins	Features of fracture surface
D301	0.04	5.00	1.00	1.96	1.840	0.593	1.247	1310	66.72	1.561	0.445	1310	0.714	7.50	Shear
D302	10.00	5.08	1.00	1.96	1.850	0.614	1.242	1280	63.15	1.477	0.390	1275	0.630	6.67	Shear
D303	10.03	5.00	0.26	3.32	3.100	9.261	1.251	1453	73.98	1.730	0.548	1450	0.60	6.30	Normal & cleavage
D304	9.99	5.12	0.26	3.26	3.150	9.938	1.238	1445	70.18	1.642	0.416	1438	0.60	6.67	Normal & shear
D305	10.05	4.92	0.26	3.38	3.100	0.261	1.261	1463	76.93	1.799	0.587	not broken	0.50	-	-
D306	10.01	5.00	0.16	3.20	3.900	24.389	1.250	1525	77.67	1.817	0.597	1525	0.55	6.63	Partial cleavage
D307	10.00	5.24	0.18	3.08	3.750	20.797	1.227	1473	68.28	1.597	0.468	1463	0.67	6.60	Partial cleavage
D308	10.01	5.12	0.16	3.10	4.000	17.000	1.239	1383	67.29	1.576	0.455	1338	0.50	5.60	Normal rupture

TABLE 28. Notch Tensile Test. Steel: D31.

Specimen	Dia, of specimen mms	Dia, of notch section mms	Notch root radius mms	Notch width mms	Stress concentration factor K_t	$(K_t - 1)^3$	Notch depth	Max: load Kgf	Notch strength Kg/mm^2	Notch strength ratio NSR	$\log_e$(NSR)	Load at fracture Kgf	Total extension mms	Total time to fracture mins	Features of fracture surface
D311	9.96	5.20	1.00	1.96	1.860	0.636	1.228	1358	63.92	1.479	0.391	1275	0.93	7.33	Shear
D312	9.98	5.08	1.00	1.98	1.850	0.614	1.241	1298	64.02	1.482	0.393	1275	1.05	7.73	Shear
D313	9.99	5.00	0.26	3.32	3.10	9.261	1.249	1418	72.19	1.671	0.613	1278	1.04	7.63	More cleavage
D314	10.01	5.04	0.26	3.30	3.10	9.261	1.247	1485	74.44	1.723	0.544	1463	0.84	7.13	Normal/ cleavage
D315	9.99	5.12	0.26	3.24	3.15	9.938	1.238	1493	72.49	1.678	0.518	1475	0.93	6.83	Normal& shear
D316	10.00	5.04	0.16	3.16	3.95	25.672	1.246	1525	76.44	1.769	0.570	1525	0.84	6.80	Partial cleavage
D317	9.99	5.12	0.16	3.12	4.00	27.000	1.238	1505	73.10	1.692	0.526	1500	0.80	6.78	Normal & cleavage

TABLE 29. Notch Tensile Test. Steel D32.

Specimen	Dia.of specimen mms	Dia.of notch section mms	Notch root radius mms	Notch width mms	Stress concentration factor K_t	$(K_t - 1)^3$	Notch depth	Max: load Kgf	Notch strength Kg/mm^2	Notch strength ratio NSR	$Log_e(NSR)$	Load at fracture Kgf	Total extension mms	Total time to fracture mins	Features of fracture surface
D321	10.02	5.02	1.02	2.10	1.835	0.582	1.249	1290	65.18	1.562	0.446	975	1.46	9.07	Shear at edges
D332	10.00	5.04	1.02	2.08	1.838	0.588	1.246	-	-	-	-	-	-	-	-
D323	10.01	5.01	1.02	2.08	1.835	0.582	1.250	1280	64.93	1.556	0.442	975	1.50	9.00	Normal & shear
D324	10.00	5.08	0.26	3.28	3.18	10.360	1.242	1475	72.77	1.744	0.556	1188	1.46	9,47	Normal & shear cleavage
D325	10.01	5.13	0.26	3.28	3.19	10.503	1.238	1448	70.03	1.678	0.518	1200	1.46	9.10	Normal & shear
D326	10.00	5.04	0.26	3.30	3.18	10.360	1.246	1468	73.56	1.763	0.567	1150	1.50	9.27	Normal & shear cleavage
D327	10;02	5.02	0.18	3.18	3.70	19.683	1.249	1485	75.03	1.798	0.587	1150	1.65	9.27	Normal cleavage
D328	9.92	5.08	0.18	3.10	3.73	20.346	1.238	1443	71.17	1.705	0.538	1150	1.46	9.27	Normal cleavage
D329	10.03	5.15	0.18	3.12	3.73	20.346	1.237	1485	71.29	1.708	0.535	1175	1.46	9.33	Normal cleavage

TABLE 30. Verification of the polynomial A(r)

Steel	Polynomials A(r) for notch root radii				Coefficients of the polynomial A(r) $A(r) = a_0 + a_1 r_1 + a_2 r_2^2 + a_3 r_3^3$			
	r = 1.00 mm	r = 0.26 mm	r = 0.18 mm	r = 0.16 mm	a_0	a_1	a_2	a_3
A	28.50	2.00	1.00	-	- 0.073	1.175	26.568	- 1.669
B	28.64	1.84	-	-	- 0.093	1.439	26.283	- 2.288
D10	20.99	2.10	-	0.86	- 0.024	0.967	28.552	- 2.403
D11	26.05	2.00	-	0.81	- 0.240	3.317	20.964	1.445
D12	25.00	1.94	-	0.73	0.260	- 2.188	32.901	6.845
D20	29.00	2.00	1.15	-	- 0.022	1.056	28.967	- 3.467
D21	27.50	2.16	-	0.81	- 0.300	3.642	21.399	2.718
D22	28.64	1.95	-	0.74	- 0.132	1.349	24.864	2.856
D30	27.90	2.35	-	0.81	- 0.106	2.177	28.272	- 2.883
D31	26.06	2.23	-	0.83	- 0.320	4.645	20.283	1.195
D32	28.64	2.10	1.11	-	- 0.035	1.260	28.838	- 2.916

TABLE 31. Specimens with Flat Ends. Steel (A)

Axial compressive strain ε_z	Circumferential strain ε_θ	Effective strain $\bar{\varepsilon}$	Volume fraction of voids f_v
1.20	0.65	1.21	0.015
1.32	0.74	1.34	0.028
0.74	0.40	0.75	0.010
0.94	0.53	0.96	0.024
1.63	0.75	1.60	0.015
1.31	0.69	1.32	0.022
0.35	0.17	0.35	-
0.99	0.53	1.00	0.014
0.41	0.30	0.63	0.011
0.77	0.52	0.74	0.007
1.10	0.58	0.88	0.017
1.18	0.75	1.15	0.023

TABLE 31. Specimens with 10° cone angle. Steel (A)

Axial compressive strain ε_c	Circumferential strain ε_θ	Effective strain $\bar{\varepsilon}$	Volume fraction of voids f_v
1.27	0.73	1.33	0.027
1.21	0.74	1.24	0.026
1.09	0.75	1.12	0.017
1.04	0.64	1.13	0.014
1.00	0.58	1.08	0.020
0.97	0.52	1.02	0.012
0.94	0.52	0.96	0.020
0.72	0.38	0.70	0.010
0.69	0.37	0.68	0.005
0.36	0.17	0.30	-

TABLE 31. Specimens with 30° Cone Angle. Steel (A)

Axial compressive strain ε_c	Circumferential strain ε_θ	Effective strain $\bar{\varepsilon}$	Volume fraction of voids f_v
1.30	0.66	1.32	0.021
1.03	0.64	1.10	0.010
1.19	0.60	1.23	0.023
0.91	0.47	0.95	0.017
0.77	0.42	0.80	0.010
0.51	0.28	0.40	-
0.49	0.25	0.52	-
0.28	0.17	0.29	-
0.17	0.10	0.11	-
0.96	0.52	0.99	-
1.05	0.58	1.10	0.009

TABLE 32. Specimens with flat ends. Steel (B)

Axial compressive strain ε_c	Circumferential strain ε_θ	Effective strain $\bar{\varepsilon}$	Volume fraction of voids f_v
1.71	0.77	1.68	0.020
1.57	0.83	1.58	0.025
0.85	0.39	0.84	0.025
0.38	0.22	0.39	-
0.85	0.45	0.86	-
0.52	0.25	0.52	-
0.68	0.43	0.71	0.015
0.83	0.29	0.79	0.008
1.19	0.62	1.19	0.029
0.89	0.53	0.92	0.015
1.75	0.74	1.70	0.018
1.38	0.63	1.36	0.020
0.38	0.16	0.37	-
1.03	0.57	1.05	0.020
0.65	0.36	0.66	0.013
1.55	0.80	1.55	0.015
1.00	0.45	0.98	0.018

TABLE 32. Specimens with 10° cone angle Steel (B)

Axial compressive strain ε_c	Circumferential strain ε_θ	Effective strain $\bar{\varepsilon}$	Volume fraction of voids f_v
1.33	0.71	1.29	0.016
1.15	0.66	1.10	0.022
1.06	0.63	1.13	0.018
1.26	0.62	1.38	0.029
0.81	0.53	0.89	0.013
0.95	0.40	0.90	0.012
0.63	0.33	0.68	0.015
0.67	0.30	0.65	0.017
0.29	0.27	0.45	0.017

TABLE 32. Specimens with 30^{o} cone angle Steel (B)

Axial compressive strain ε_c	Circumferential strain ε_θ	Effective strain $\bar{\varepsilon}$	Volume fraction of voids f_v
1.41	0,88	1.51	0.028
1.29	0.82	1.39	0.030
1.37	0.81	1.48	0.016
1.38	0.80	1.45	0.010
1.50	0.73	1.47	0.020
1.55	0.68	1.45	0.023
1.20	0.68	1.28	0.027
1.18	0.66	1.23	0.010
1.13	0.57	1.09	0.010
1.01	0.54	0.96	0.012
0.75	0.31	0.73	0.015
0.70	0.29	0.63	0.009
0.34	0.27	0.40	-

TABLE 33. Specimens with flat ends. Steel (C)

Axial compressive strain ε_c	Circumferential strain ε_θ	Effective strain $\bar{\varepsilon}$	Volume fraction of voids f_v
0.69	0.37	0.70	
0.78	0.43	0.79	
0.37	0.23	0.38	
0.78	0.35	0.76	
0.76	0.46	0.79	
0.98	0.53	0.99	
0.21	0.14	0.22	
0.69	0.28	0.67	
0.76	0.38	0.76	
0.91	0.37	0.88	
1.01	0.51	1.01	
0.76	0.31	0.74	
0.92	0.37	0.89	
0.86	0.38	0.84	
1.08	0.60	1.10	
0.76	0.49	0.80	
0.70	0.65	0.82	
0.79	0.48	0.82	

TABLE 33. Specimens with 10° cone angle Steel (C)

Axial Compressive strain ε_c	Circumferential strain ε_θ	Effective strain $\bar{\varepsilon}$	Volume fraction of voids f_v
1.19	0.85	1.44	
1.08	0.59	1.11	
0.77	0.44	0.84	
0.77	0.42	0.71	
0.68	0.35	0.59	
0.86	0.35	0.77	
0.79	0.32	0.70	
0.72	0.28	0.50	

TABLE 33. Specimens with 30° cone angle Steel (C)

Axial Compressive strain ε_c	Circumferential strain ε_θ	Effective strain $\bar{\varepsilon}$	Volume fraction of voids f_v
1.08	0.73	1.36	
1.13	0.68	1.38	
1.17	0.60	1.25	
0.79	0.50	0.89	
0.84	0.49	0.90	
1.03	0.50	1.10	
0.75	0.43	0.76	
0.95	0.37	0.93	
0.47	0.24	0.44	

ACKNOWLEDGMENTS

I wish to express my very sincere appreciation for the encouragement and guidance given to me by my supervisors, Professor K.Sachs and Professor J.T. Barnby.

My thanks are due to Professor W.O. Alexander, former head of Department, to Professor I.L. Dillamore, Head of Department, to the staff in the Department of Metallurgy and Materials at the University of Aston and to the staff of the G.K.N. Group Technological Centre at Wolverhampton for their kind help.

I am very grateful to the Sudan Industrial Research and Consultancy Institute for the financial support and to my wife for her encouragement and patience.

Appendix I

The Calibration of the QTM for particle counting.
Objective x40
Optics x1·0
Eyepiece x10
Scale = 24 cms. on the screen = 0·1 mms.

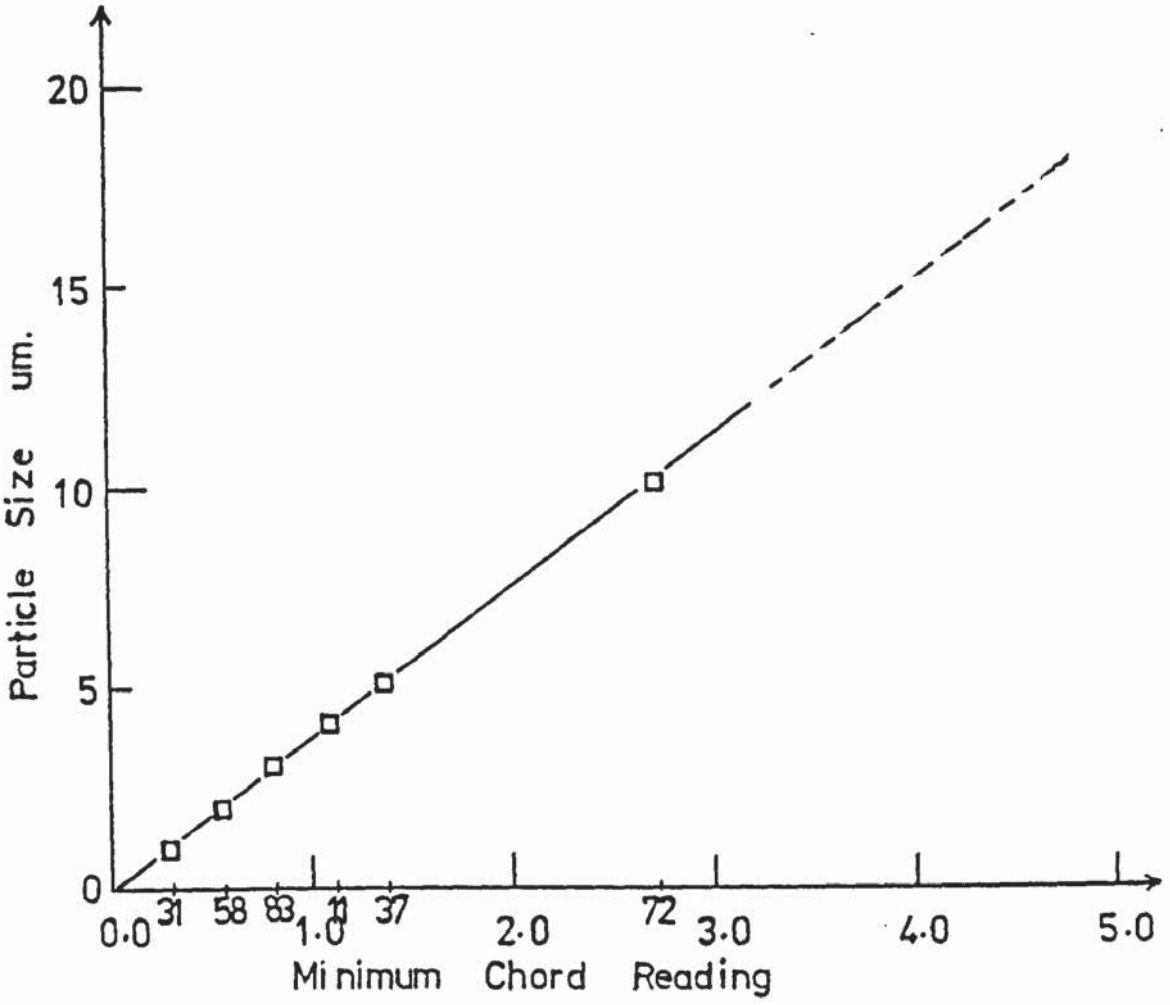

FIG. 86.

APPENDIX I

Programme (1)

Q.T.M. 720, calibration to count sulphides in steels D.

RM1

1PP = ?

0.217 *

FRAME = ?

444000.000

FIELDS

30.000 *

DIST H.F.

1.085 µm.
1.953
3.038
3.906
4.991
6.076
8.029
9.982

DIST AREA

0.235
0.424
0.659
0.848
1.083
1.818
1.742
2.166

APPENDIX I

Programme (2)

Q.T.M. 720, calibration to count oxides in steels D.

```
RM1

1PP = ?
                    0.217 *
FRAME = ?
              444000.000
FIELDS
                   30.000 *
DIST H.F.
                    1.085 µm.
                    1.953
                    4.991
                    9.982
                   14.973
                   19.964
                   30.380
                   39.060
DIST AREA
                    0.235
                    0.424
                    1.083
                    2.166
                    3.249
                    4.332
                    6.592
                    8.476
```

APPENDIX I

2.0 Particle Size-Distribution Measurements

The measurements of the Q.T.M. can be corrected to represent the particles size-distribution in terms of volume as follows:- (38)

(a)The particles are assumed to be uniform spheres of diameter (d_{mean}), randomly distributed in the specimen. When they are examined and measured under the QTM on a polished cross-section through the sample, they reveal circular areas of carbides with diameters varying from (0) to (d_{mean}).

(b) Considering a cube of unit dimensions cut from the sample, if a cross-section parallel to one of the cube faces is examined, the average number of particles per unit area (N_S) equal the number of particles per unit volume (N_V) times the probability (p) that the plane would intersect a single sphere positioned at random within the unit cube.

(c) Since, of the various possible positions for the cross-sectional plane over the unit length from top to bottom of the cube, only those positions existing over the length (d_{mean}) would lead to the plane intersecting the sphere, the probability of intersecting a single sphere is just (d_{mean}) and

$N_s = N_V \times p = N_V \times d_{mean}$

where, d_{mean} can be taken as the mean value of the particle diameters.

The volume fraction of particles $f_o = N_V \times V$ where,

V = volume of a single particle, and $f_o = N_V \times \frac{\pi d^3}{6}$

Therefore, in the corrected histograms of N_V against d^3

- the areas under the curves represent the volume fraction of particles f_o.

3.0 The relationship between the volume fraction of particles f_o(second-phase) and the interparticle spacing (λ) is derived as:

Let volume fraction of second-phase particles = f_o

$(1 - f_o)$ = volume fraction of the matrix.

The ratio of the volume fractions of matrix to second-phase particles equals the ratio of the particles' spacing to their size.

i.e. $(1 - f_o) / f_o = \lambda / d_{mean}$

This ratio corrected for the three-dimension measurements gives :

$$[\lambda / d_{mean}] = {}^{2}/_{3} [(1 - f_o) / f_o]^{1/2}$$

APPENDIX II

1.0 Stresses in Plastic Yielding (27, 69, 70)

When three unequal Principal stresses ($\sigma_1 \neq \sigma_2 \neq \sigma_3$) act on a point, it is a triaxial state of stress. If two stresses are equal, it is a cylindrical state of stress. If all the three stresses are equal it is hydrostatic or spherical state of stress.

1.1 Stress Deviators

Material can withstand very large hydrostatic stresses (σ'') without plastic deformation; incompressible isotropic body is not deformed by hydrostatic stresses.

The part of the total stress which is effective in producing plastic deformation is known as the stress deviator (σ'), where:

$$\sigma_1 = \sigma_1' + \sigma_1'' \; ; \quad \sigma_2 = \sigma_2' + \sigma_2'' \; ; \quad \sigma_3 = \sigma_3' + \sigma_3''$$

and, $\sigma_1' + \sigma_2' + \sigma_3' = 0$

Therefore,

$$\sigma_1'' + \sigma_2'' + \sigma_3'' = \sigma_1 + \sigma_2 + \sigma_3$$

1.2 Yielding Criteria

The Von Mises yield criteria is suitable because it expresses the strain energy of distortion, where the strain energy of distortion (U_o') equals the total energy (U_o) minus the strain energy of volume change (U_o'').

In the elastic range :-

The strain energy of distortion U_o' is;

$$U_o' = (1+\nu)/6E\left[(\sigma_1 - \sigma_2)^2 + (\sigma_2 - \sigma_3)^2 + (\sigma_3 - \sigma_1)^2\right]$$

where ν = Poisson's ratio

E = Young's Modulus

The strain energy of volume change U_o'' is:-

$$U_o'' = 1/2\ \sigma_1'' e_1'' + 1/2\ \sigma_2'' e_2'' + 1/2\ \sigma_3'' e_3''$$

$$U_o'' = 1/2\ \sigma_{hyd.}(e_1 + e_2 + e_3)$$

where $\sigma_{hyd} = 1/3\ [\sigma_1 + \sigma_2 + \sigma_3]$ = hydrostatic component of stress or average stress

$(e_1 + e_2 + e_3)$ = volumetric strain

With no volume change, the distortion energy criteria can be written as:

$$Y = 1/(2^{1/2})[(\sigma_1 - \sigma_2)^2 + (\sigma_2 - \sigma_3)^2 + (\sigma_3 - \sigma_1)^2]^{1/2} \ldots\ldots (1)$$

where Y = yield strength in simple tension

This Von Mises criterion is also preferred because its equation represents the critical value of the octahedral shear stress (τ_{oct}).

2.0 Octahedral Shear Stress and Shear Strain

The octahedral shear stresses are important in the theory of plasticity. They are the stresses acting on the faces of the three dimensional octahedron which has the geometric property that the faces of the plane make equal angles ($54^o\ 44'$) with each of the three principal directions of the stress. (and cosine $54^o\ 44' = 1/\sqrt{3}$).

The stress on each octahedron face can be resolved into:-

(a) A normal octahedron stress (σ_{oct}) which is equal to the hydrostatic component of the total stress i.e. $\sigma_{oct} = \sigma_{hyd}$ = This stress cannot deform the material.

(b) An octahedral shear stress lying in the octahedral plane and is given as:-

$$\tau_{oct.} = 1/3[(\sigma_1 - \sigma_2)^2 + (\sigma_2 - \sigma_3)^2 + (\sigma_3 - \sigma_1)^2]^{1/2} = \frac{2^{1/2}}{3} Y \ldots\ldots (2)$$

and this is the stress responsible for the yielding and the

plastic deformation. Its equation is the same as the one derived from the strain energy of distortion.

The octahedral strains are referred to the same dimensional octahedron as the octahedral stresses. The octahedral linear strain is given by $\varepsilon_{oct} = 1/3[\varepsilon_1+\varepsilon_2+\varepsilon_3]$

and the octahedral shear strain (γ_{oct}) is given by:

$$\gamma_{oct.} = 2/3\,[(\varepsilon_1-\varepsilon_2)^2+(\varepsilon_2-\varepsilon_3)^2+(\varepsilon_3-\varepsilon_1)^2]^{1/2} \qquad \ldots\ldots(3)$$

3.0 Invariants of Stress and Strain

The invariant functions of stress and strain yield the same stress-strain curve for different tests.. The octahedral stresses and strains are invariant functions. Also the effective or significant stress and strain ($\bar{\sigma},\bar{\varepsilon}$) are invariant functions.

The effective stress $\bar{\sigma} = \frac{1}{\sqrt{2}}[(\sigma_1-\sigma_2)^2+(\sigma_2-\sigma_3)^2+(\sigma_3-\sigma_1)^2]^{1/2} \ldots\ldots(4)$

The effective strain $\bar{\varepsilon} = \frac{\sqrt{2}}{3}[(\varepsilon_1-\varepsilon_2)^2+(\varepsilon_2-\varepsilon_3)^2+(\varepsilon_3-\varepsilon_1)^2]^{1/2} \ldots\ldots(5)$

when the axes co-ordinates correspond to the principal directions.

APPENDIX III

Definitions and properties of the sphere, the ellipsoid, the circle, the ellipse and the oval curves. (12, 59, 76, 106)

A. The Sphere

1. The sphere is the Locus of points at a given distance from a given point.

2. The equation of sphere in cartesian co-ordinates is, $x^2 + y^2 + Z^2 = r^2$ and for a sphere of unit radius the equation is : $x^2 + y^2 + Z^2 = 1$

3. The area of the sphere of radius r is : $A = 4\pi r^2$

4. The volume of the sphere is : $V = 4/3\,\pi r^3$

B. The Ellipsoid

1. The ellipsoid is the surface of the rotation of an ellipse.

2. The surface is given by the equation : $\frac{x^2}{a^2} + \frac{y^2}{b^2} + \frac{z^2}{c^2} = 1$

C. The Circle

1. The circle is the Locus of points on a plane at a given distance from a fixed point called the centre.

2. The equation of the circle is : $x^2 + y^2 = r^2$

3. The circumference of the circle radius r is (perimeter) $= 2\pi r$

4. The area of the circle is $A = \pi r^2$ and of all the closed plane curves of a given perimeter, the circle encloses the greatest area. (76)

D. The Ellipse (59, 72)

1. The ellipse is the locus of points the sum of the distances of which from two fixed points is constant, as in Fig.(87).

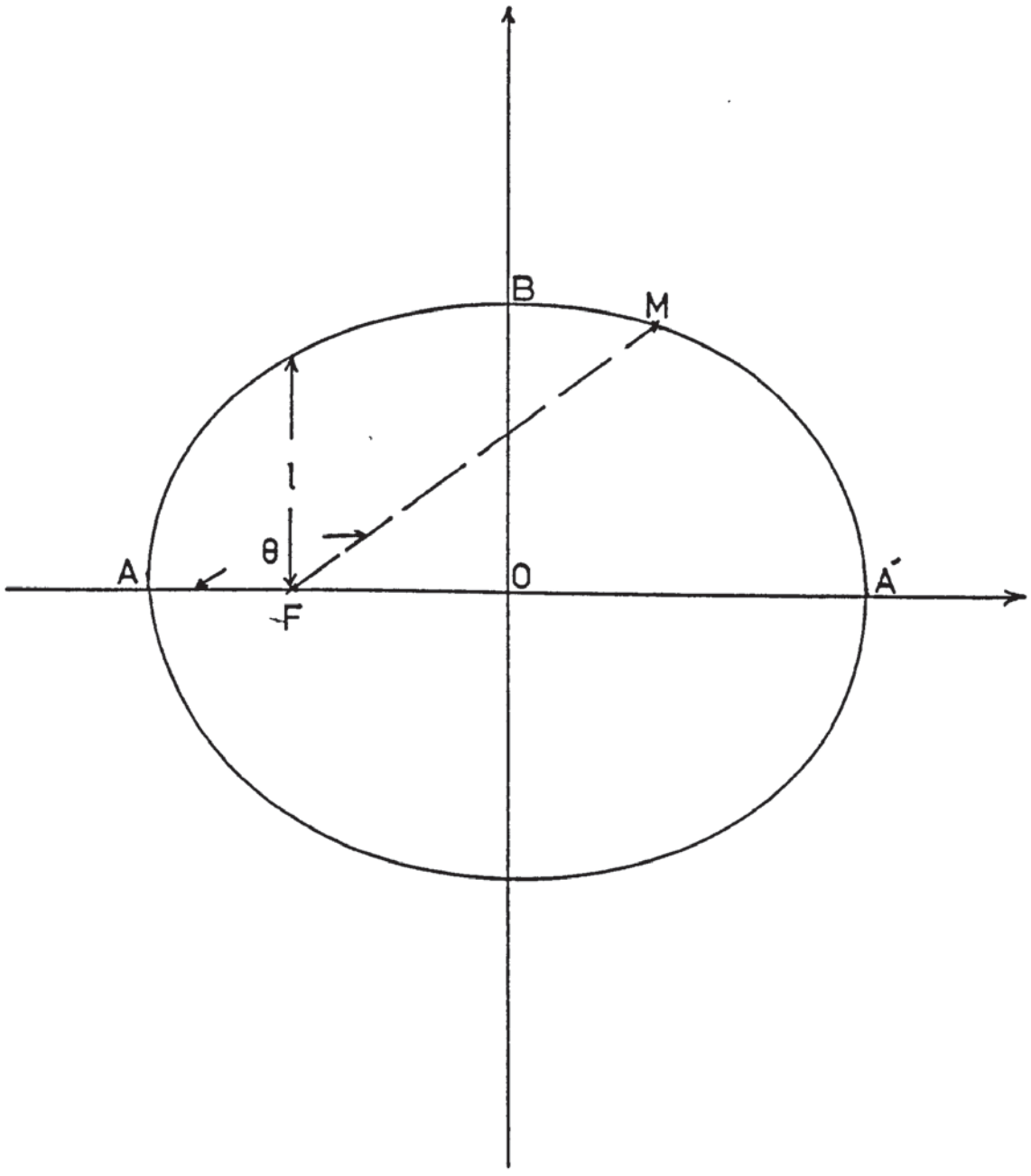

ELLIPSE

FIG. 87.

Where point M is a variable on the circumference of the ellipse, points F and F' are the fixed points and are called the focii of the ellipse, and FM + MF' = 2a = constant. The length FF' = 2c = the focal length.

2. The cartesian equation of the ellipse with its axes taken as the co-ordinate axis and the origin at O is :

$$\frac{x^2}{a^2} + \frac{y^2}{b^2} = 1$$

where : 2a = the major axis of the ellipse

2b = the minor axis of the ellipse

The polar equation of the ellipse is : $l/r = 1 + e\cos\theta$

where, from Fig. (87), l = FL = semi-latus rectum of the ellipse.

r = FM = the distance from the focus to a variable point.

e = the eccentricity of the ellipse and it is the ratio of the focal length to the major axis (i.e. $e = \frac{c}{a}$)

Also $b^2 = a^2(1 - e^2)$ and $l = a(1 - e^2)$

3. The circumference of the ellipse is, perimeter = p

$$p = \pi/2\,[3(a+b) - (a+3b)^{1/2}(3a+b)^{1/2}] \qquad \text{.....(Fig.)}$$

4. The area of the ellipse is, $A = \pi ab$.

E. The Relation between the Ellipse and the Circle

The ellipse can be defined as a compressed circle, as in Fig. (88). In this Figure AA' and DD' are mutually perpendicular diameters of the circle centre O and radius a, equal line-segments OB and OB' of length b ($b<a$) are taken on radii OD and OD' respectively. Then from each point P on the circle a perpendicular is dropped onto the diameter AA'. On this perpendicular a segment NM is laid off from the foot N, so that,

$$NM/NP = b/a$$

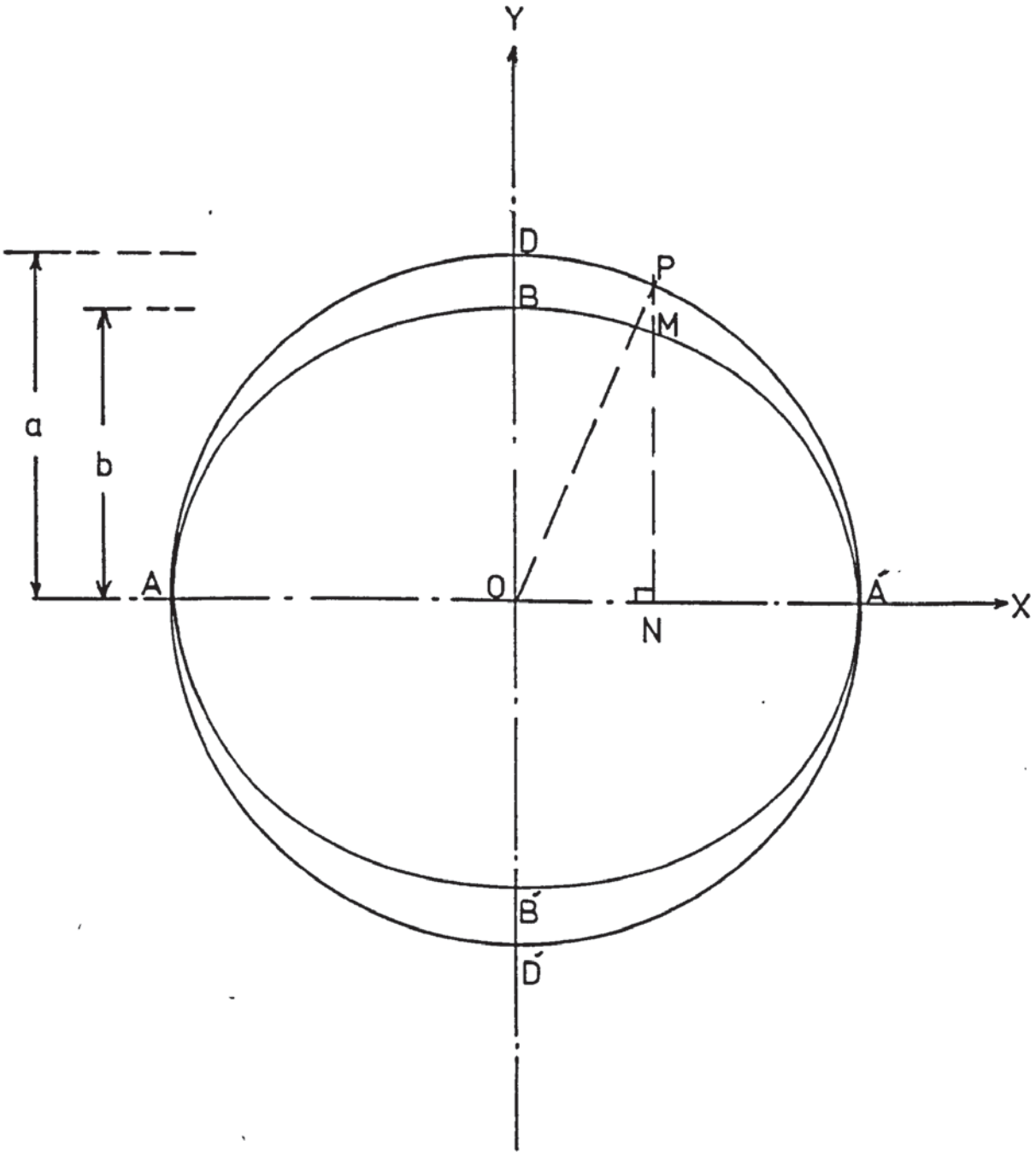

Ellipse and Auxiliary Circle

FIG. 88.

that NM : NP = b : a

This construction transforms every point P on the circle into a corresponding point M lying on the same perpendicular PN. NM is obtained from NP by reduction in the same ratio ($k = {}^{b}/a$), i.e. k is called the coefficient of compression.

A transformation of this kind is termed uniform compression. The line (curve) ABA'B' into which the circle has been transformed by uniform compression is an Ellipse.

In an analogous way as above, the ellipse can be compressed non-uniformly to produce an oval curve. The transformation is similar to that of Fig. (88), but with variable coefficients of compressions k_1, k_2, ...,... This is shown in Fig. (89).

F. The Construction of the Negative Pedals of the Circle

An alternative method of producing the ellipse and oval curve from the circle as above is to construct the negative pedals of the circle. (58, 59).

1. The definition of the negative pedals

Let S be any curve and F be a fixed point. If P is a variable point on the curve S, and a line is drawn through P at right angles to FP, the envelope of this line is the negative pedal of the curve S with respect to the fixed point F.

2. The Method of construction of the negative pedals

In Fig. (90) variable points P_1, P_2, ...,P_m, are taken on the circumference of the circle with diameter AA' and centre O. Perpendiculars to FP_1, FP_2, ...,FP_n are dropped from P_1, P_2, ...,P_n. The curve passing through M_1, M_2,...M is the first negative pedal of the circle and it is an ellipse

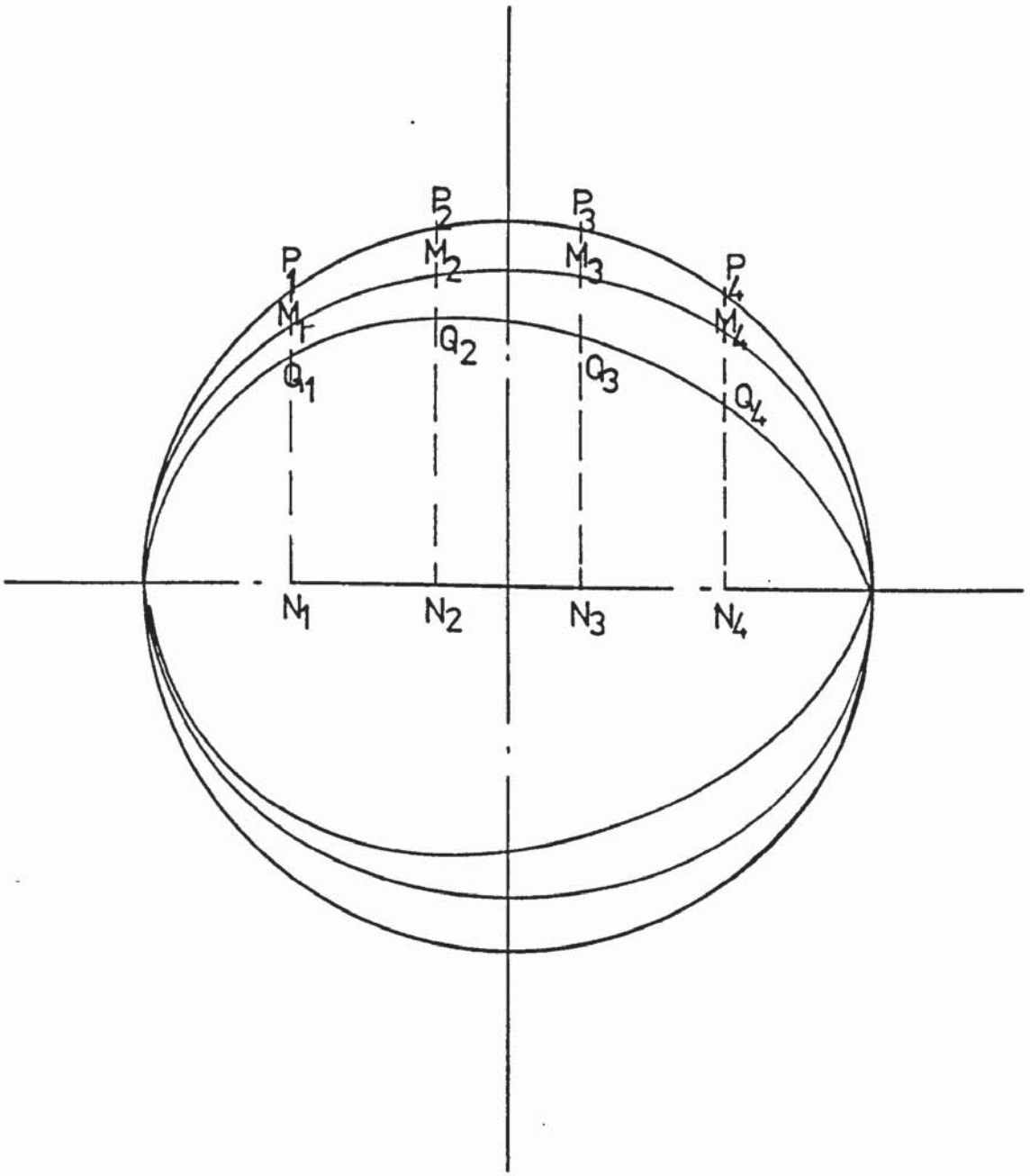

$$\frac{N_1Q_1}{M_1N_1}=k_1 > \frac{N_2Q_2}{M_2N_2}=k_2 > \frac{N_3Q_3}{M_3N_3}=k_3 > \frac{N_4Q_4}{M_4N_4}=k_4$$

Circle, Ellipse and Oval

FIG. 89.

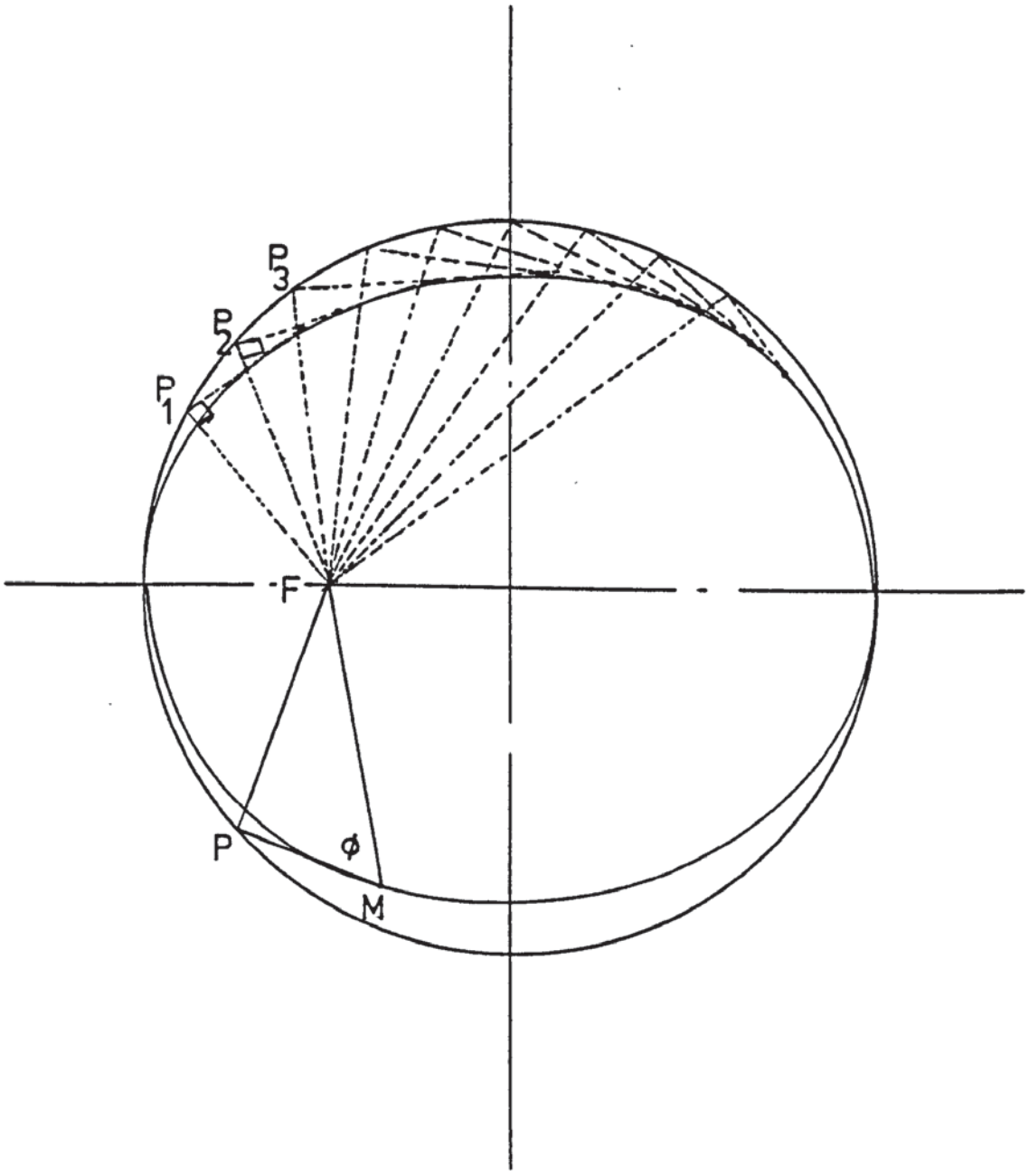

The Construction of the Negative Pedal of the Circle.

FIG.90.

with point F as its focus point.

The construction is continued for the second negative pedal of the circle which is the first pedal of the ellipse as in Fig.(91). The result is an oval curve. In this construction Fig.(91) angle FMP = angle FQM. The shape of these first and second negative pedals depends on the position of the fixed point F; that is, they depend on the value of the eccentricity of the ellipse.

Constructions of negative pedals for different values of the eccentricity of the ellipse are shown in Figs.(91, 92 and 93).

G. Properties of the Oval Curve

The constructions of the second negative pedals of the circle in Figs.(91, 92 and 93) give two different shapes of oval curves for different values of the eccentricity of the ellipse as follows:

1. When the eccentricity of the ellipse is $e \leq 0.5$, the oval is on the major axis of the ellipse.

2. When the eccentricity is $e > 0.5$, the oval curve has a node and two cusps. Where the node is a double point with distinct tangents, and the cusp is a double point with coincident tangents.

The properties of this oval with node and cusps are studied overleaf.

3. The cartesian equation of this oval curve is derived as follows:-

From Fig. (94)

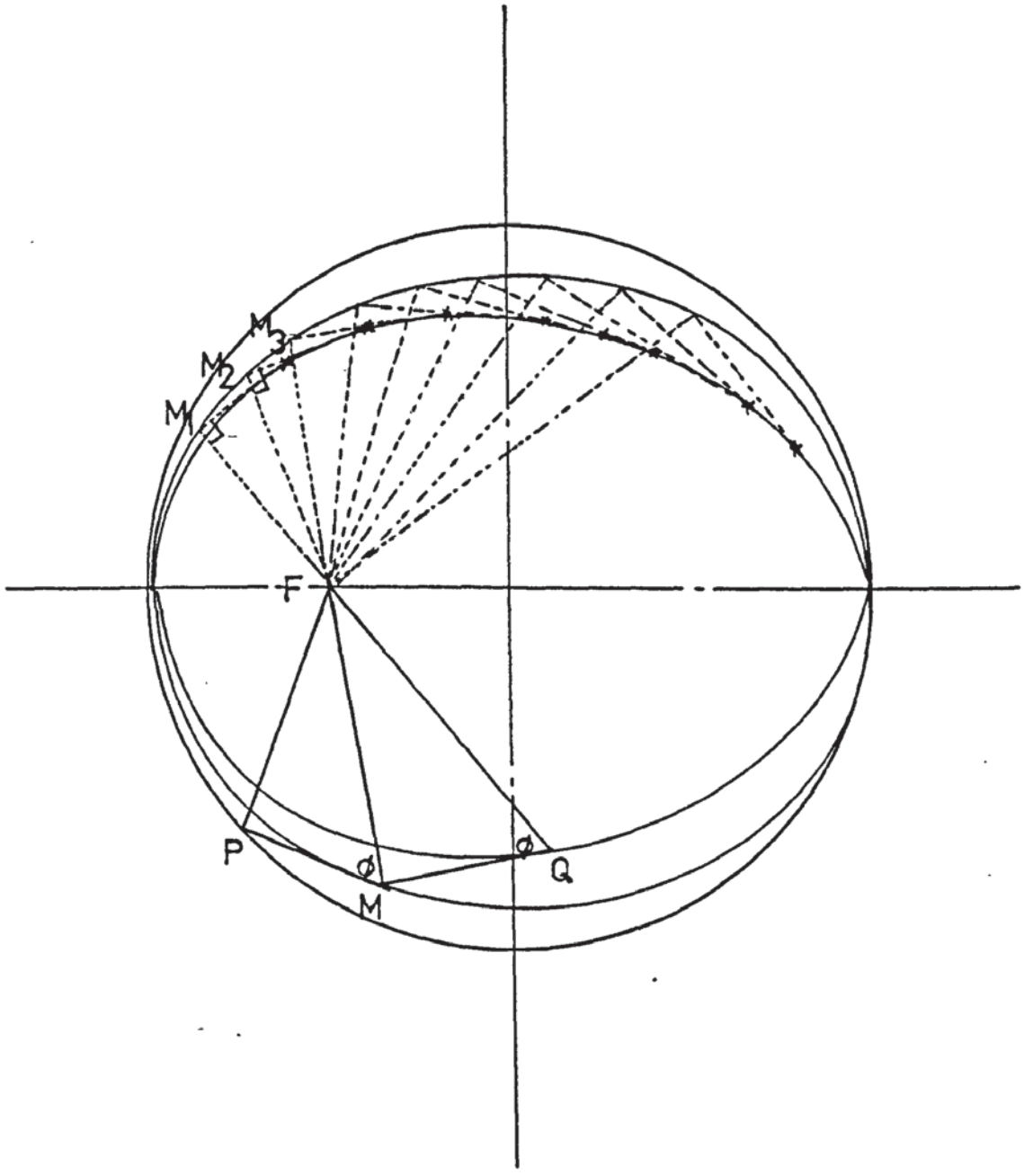

The Construction of the Negative Pedal of the Ellipse.
The Eccentricity of the Ellipse, e=0·5

FIG·91.

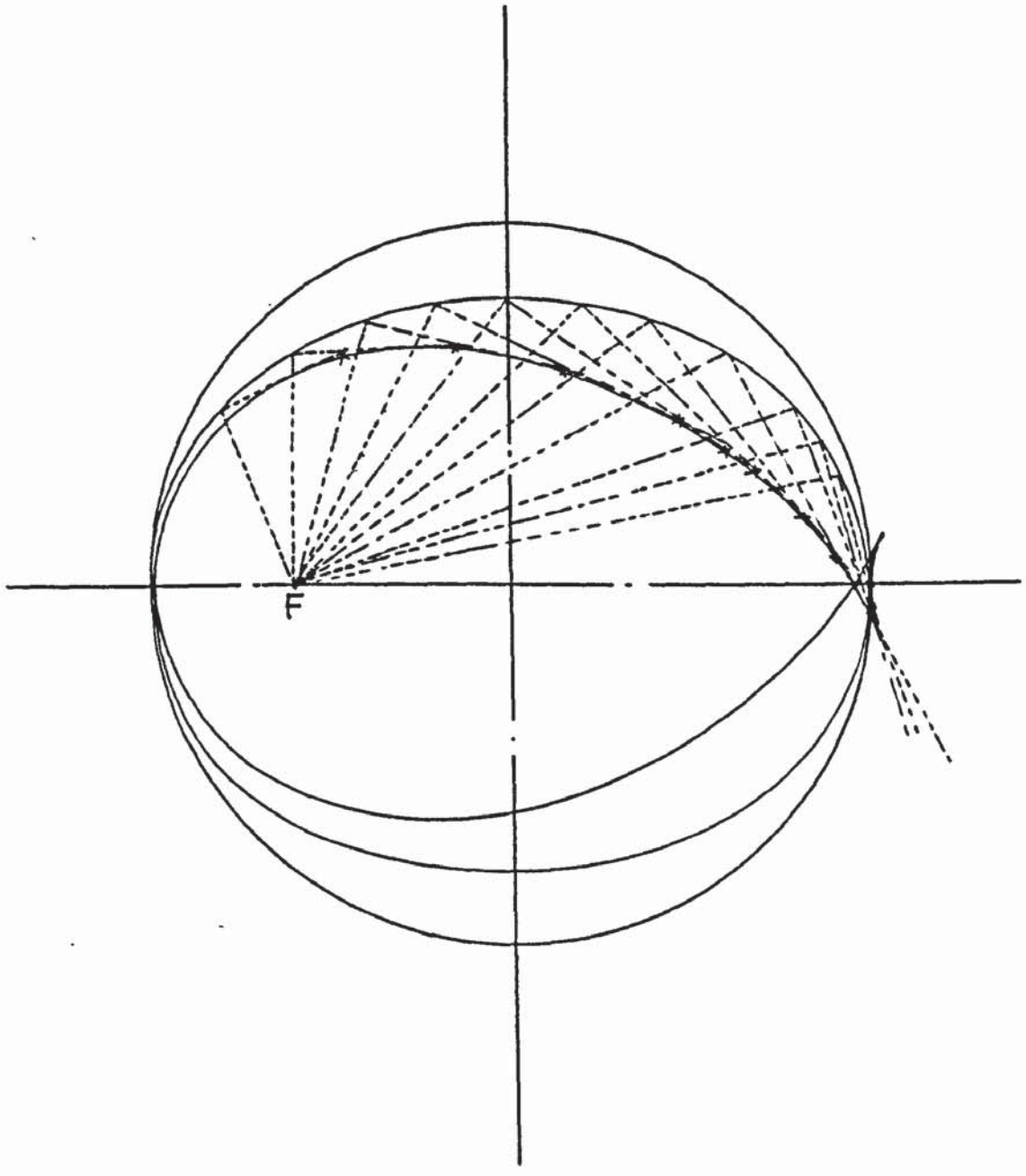

The Construction of the Negative Pedal of the Ellipse.
The Eccentricity of the Ellipse = 0·6

FIG·92.

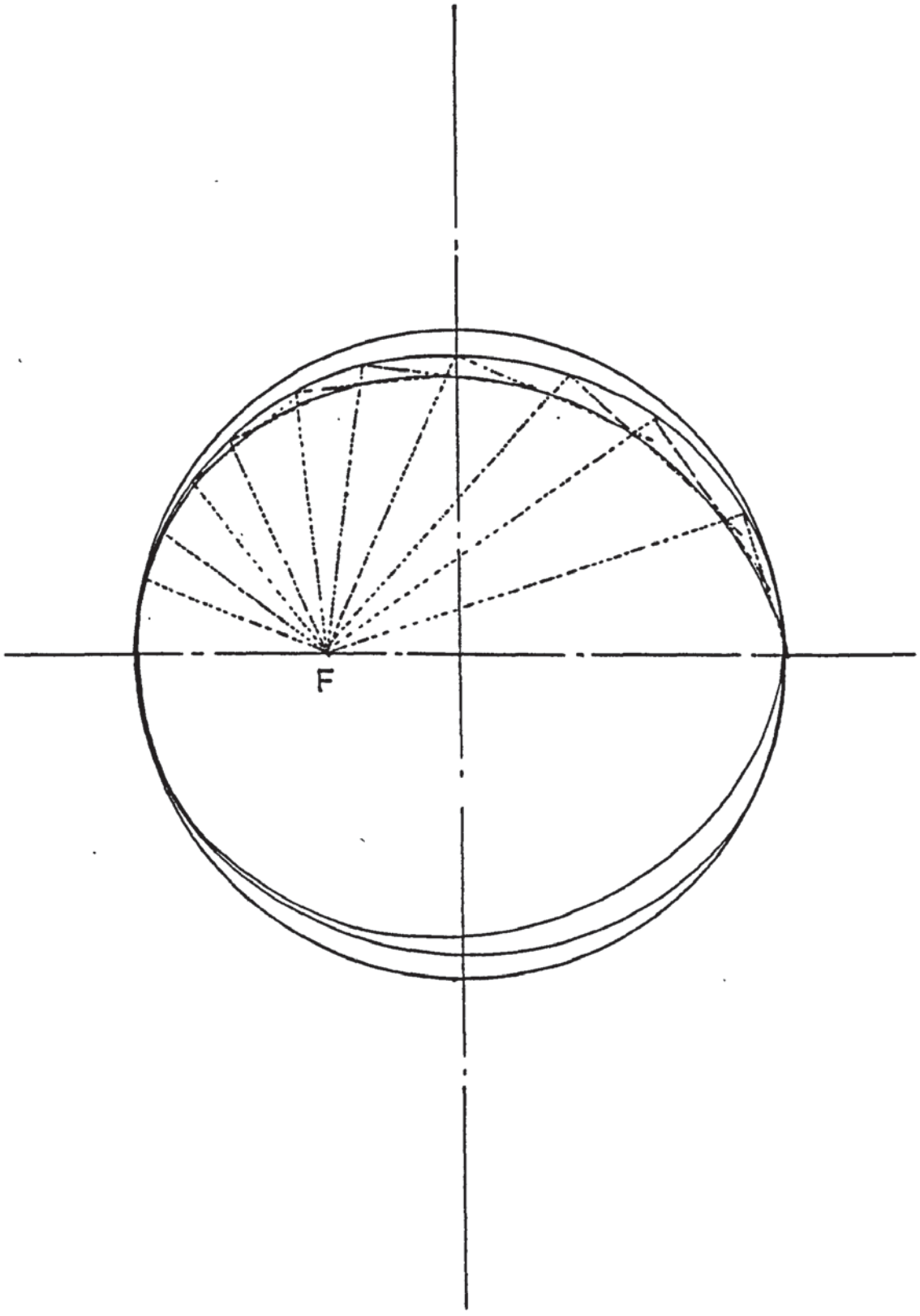

The Construction of the Negative Pedal of the Ellipse.
The Eccentricity of the Ellipse, $e = 0.4$

FIG. 93.

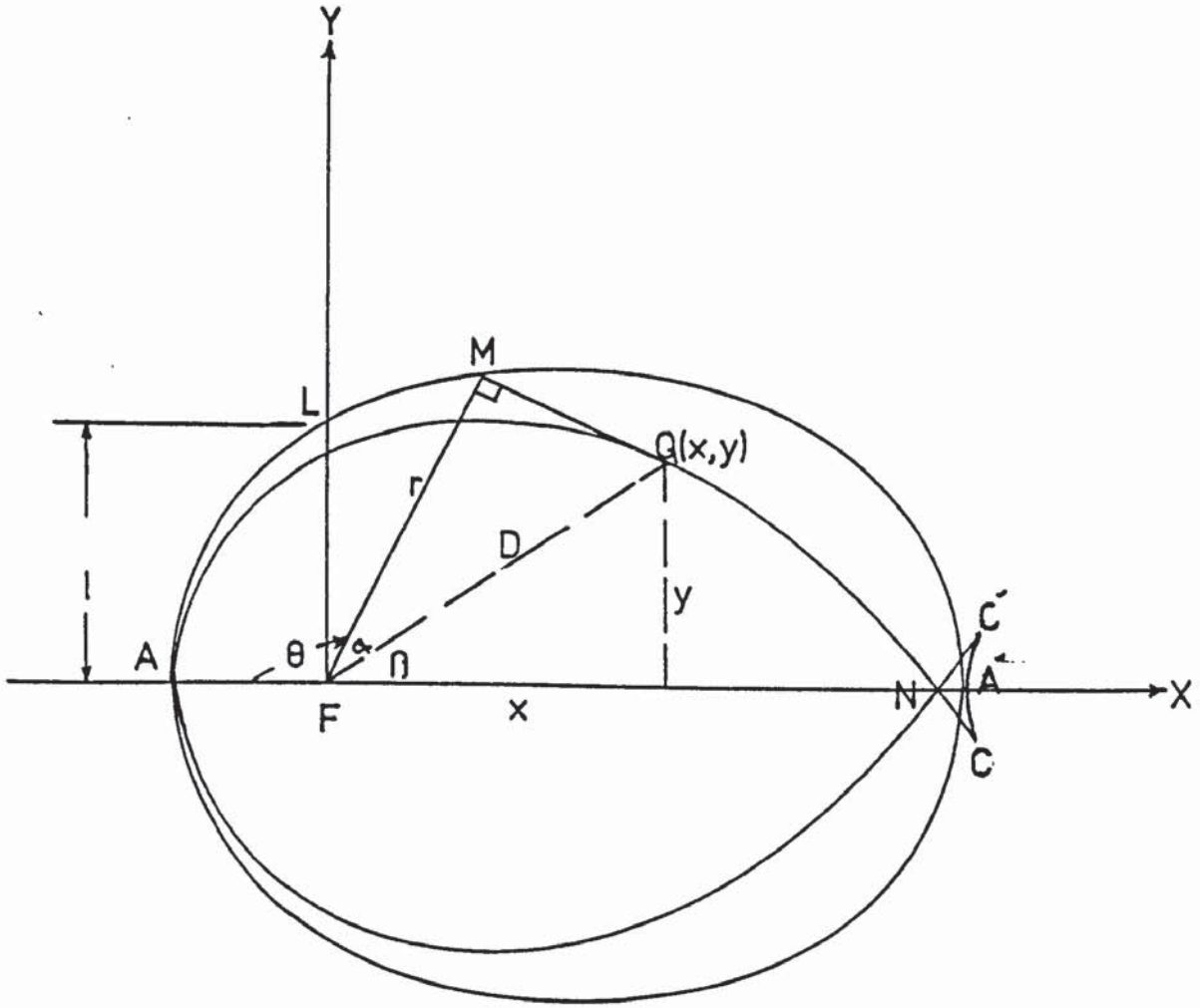

FIG. 94.

angle $\alpha = 180^\circ - (\theta + \beta)$

$x = D \cos \beta$

$y = D \sin \beta$

$r = D \cos \alpha$

$r = -D\cos(\theta + \beta)$

$r = x \cos\theta + y \sin \theta$

Substituting for from the polar equation of the ellipse in D.(2)

$$x \cos\theta + y \sin \theta = l / (1 + e \cos \theta) \qquad \ldots\ldots(1)$$

differentiating w,r,t, θ

$$y \cos \theta - x \sin \theta = (le \sin \theta) / (1 + e \cos \theta)^2 \qquad \ldots\ldots(2)$$

Adding and subtracting these two equations (1) and (2) rearranging the parametric equations for the oval curve are obtained as:

$$x = l(\cos \theta + e \cos 2\theta) / (1 + e \cos \theta)^2 \qquad \ldots\ldots(3)$$

and

$$y = l(\sin\theta + e \sin 2\theta) / (1 + e \cos \theta)^2 \qquad \ldots\ldots(4)$$

The cartesian equation is obtained by eliminating θ, as;

$$(x^2+y^2)(1-e^2)^3 + 2e^2x^2(x^2+y^2)(1-e^2)^2 + e^4x^2(x^2+y^2)(1-e^2)(10+8e^2) + l^2(x^2+y^2)(8e^4+20e^2-1) - l(2l-ex)^3 + (1-e^2)(2l-ex)^4 = 0 \qquad \ldots\ldots(5)$$

The equation is a fourth degree and the oval is a cartesian quartic.

4. From Fig. (95) the angles at the node are the angle between the tangent and radius vector to the point of

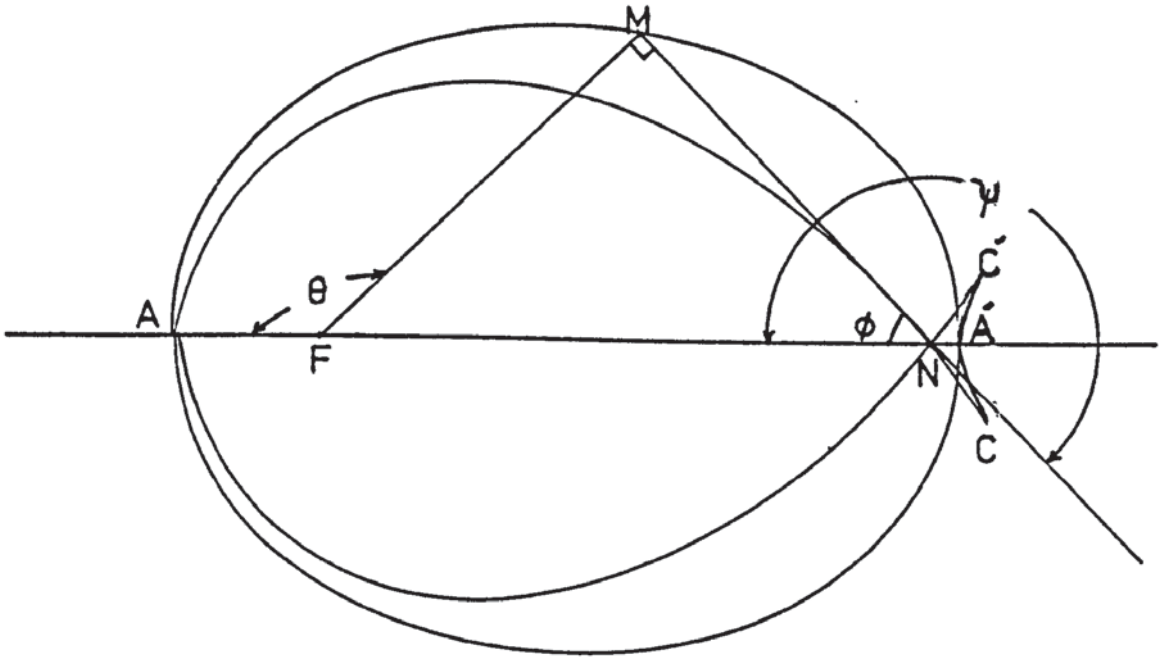

FIG. 95.

tangency = $\psi_N = 180 + \phi$ where ϕ is the inclination to the tangent and equals

$$\phi = \theta - 90$$

therefore $\psi_N = \theta + 90$

Also from Fig. (96) considering neighbouring points M, M' on the ellipse and lines MQ, M'Q at right angles to FM and FM' respectively

$$\cot \phi = (1/r)\left(\frac{dr}{d\theta}\right)$$

differentiating the polar equation $[r = l/(1+e\cos\theta)]$

w. r. t. θ,

then $\frac{dr}{d\theta} = (le\sin\theta)/(1+e\cos\theta)^2$

and $\cot\phi = (1/r)\left(\frac{dr}{d\theta}\right) = e\sin\theta/(1+e\cos\theta)$

substituting ψ_N for θ and ϕ

$$\cot\psi_N = -e\cos\psi_N/(1+e\sin\psi_N)$$

$$\psi_N = \sin^{-1}\left(-\frac{1}{2e}\right)$$

The radius of curvature at the node is $\rho_N = 4l(4e^2-1)$

The values of ψ_N and ρ_N for different values of the eccentricity of the ellipse are given in table below:

eccentricity e	0.9	0.8	0.7	0.6	0.5	0.4	0.3	0.2	0.1
ψ_N	215°	220°	225°	230°	270°	Imaginary angle			
	Real angle								
ρ_N	positive				0.0	negative			

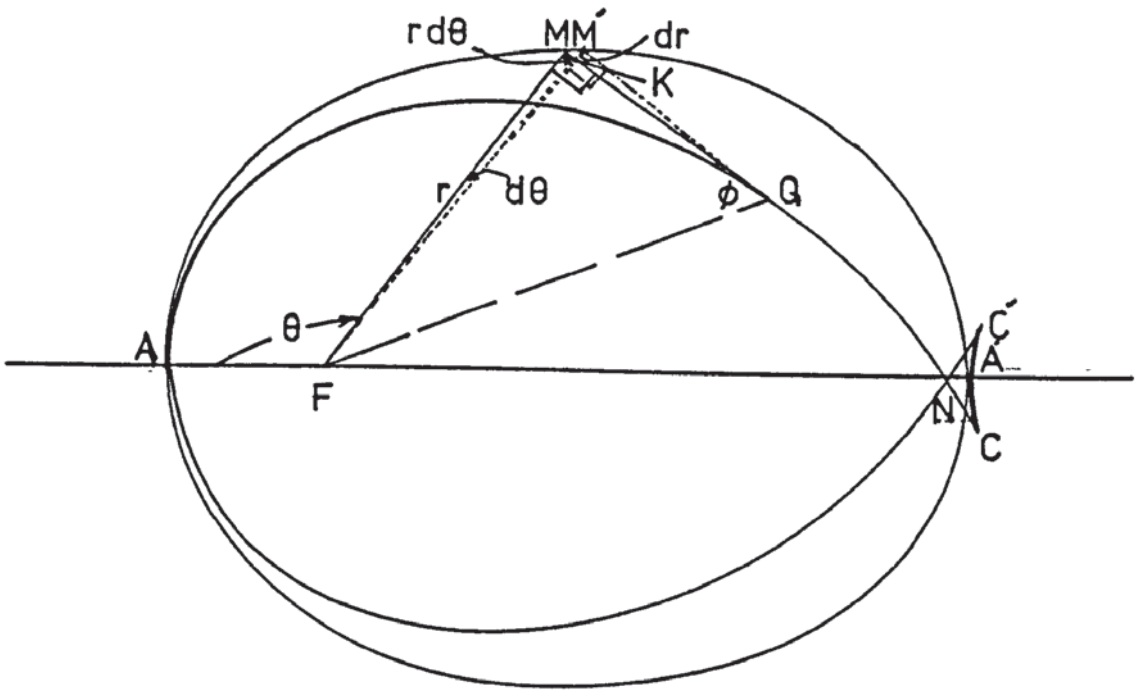

FIG.96.

H. Construction of Negative Pedals on Deformed Single Crystals

1. Deformation of single crystals (44, 48, 49, 84)

The fact that macroscopic plastic flow does not destroy the crystal structure entirely, limits the deformation modes to those which conserve the crystal structure i.e. slip and twinning.

2. Twinning (44, 49)

The x - Fe crystals are cubic, but for the purpose of presenting the twinning process, it is convenient to consider a spherical element within the crystal as in Fig. (97). a diametral section represents the twinning plane T. In this Figure, the upper half of the sphere is distorted into the twinned position with respect to the lower half. (84).

If s is the amount of shear, then the original co-ordinates of the point P (x, y, z) on the surface of the upper hemisphere becomes P' (x', y', z') by the transformation, $x' = x$, $y' = y + sx$ $z' = z$. The movement of the Y- co-ordinates is proportional to its distance from the plane $x = 0$. Thus the equation of the sphere becomes, $(s^2+1)x^2+y^2+2sxy+z^2=1$ ....(Fig.) which is the equation of an ellipsoid.

The projection of this ellipsoid on the plane $z = 0$ is:

$$(s^2+1)x^2+2sxy+y^2=1 \qquad \text{.....(Fig.)}$$

which is an ellipse. Therefore, the geometry of the twinning deformation in Fig. (97) can be projected into two dimensions as shown in Fig. (98). In this Figure there are two planes that have the same dimensions after the deformation as before it. The first is the twinning plane, defined by the normal vector T; it

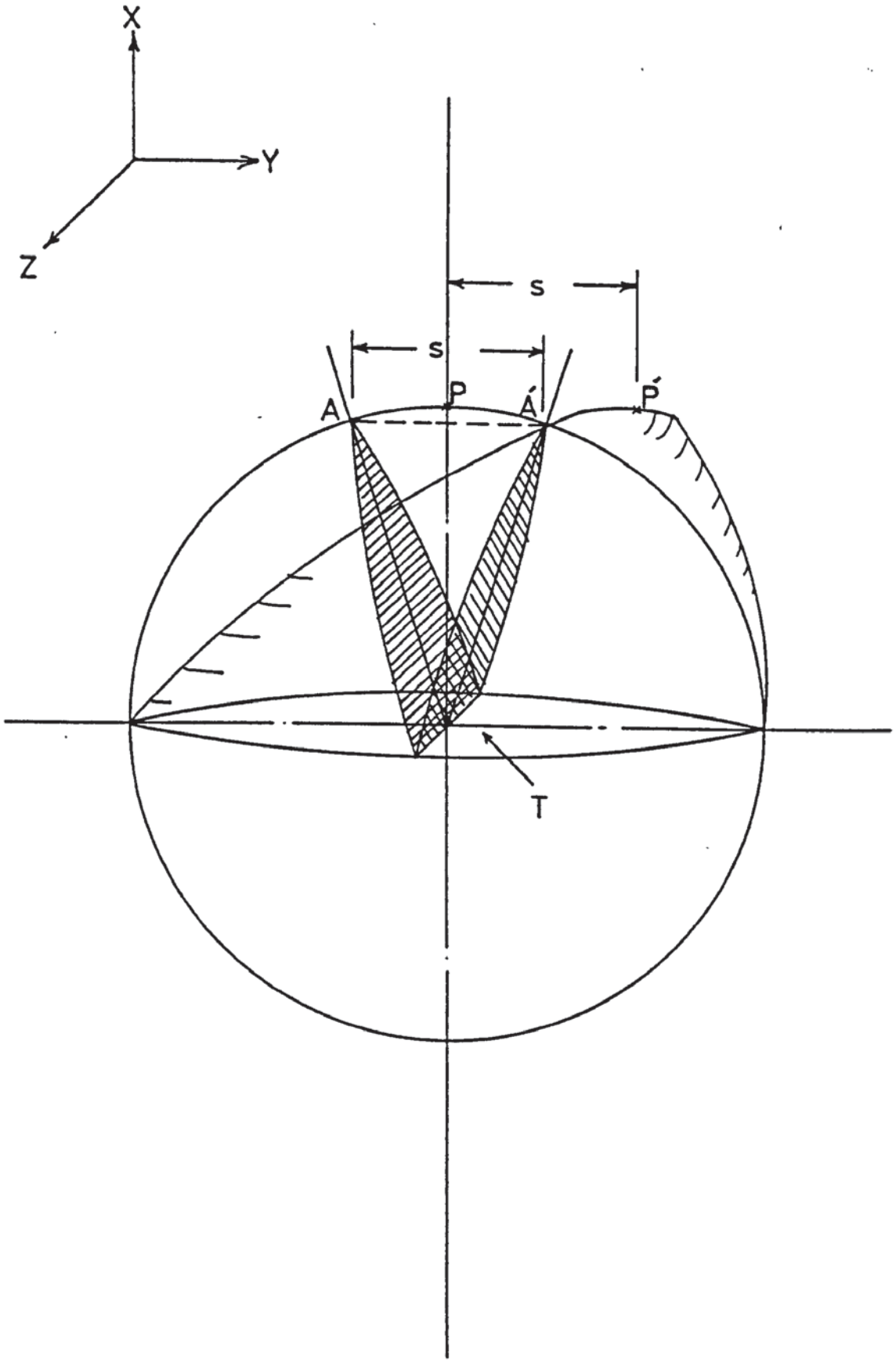

Twinning.

FIG.97.

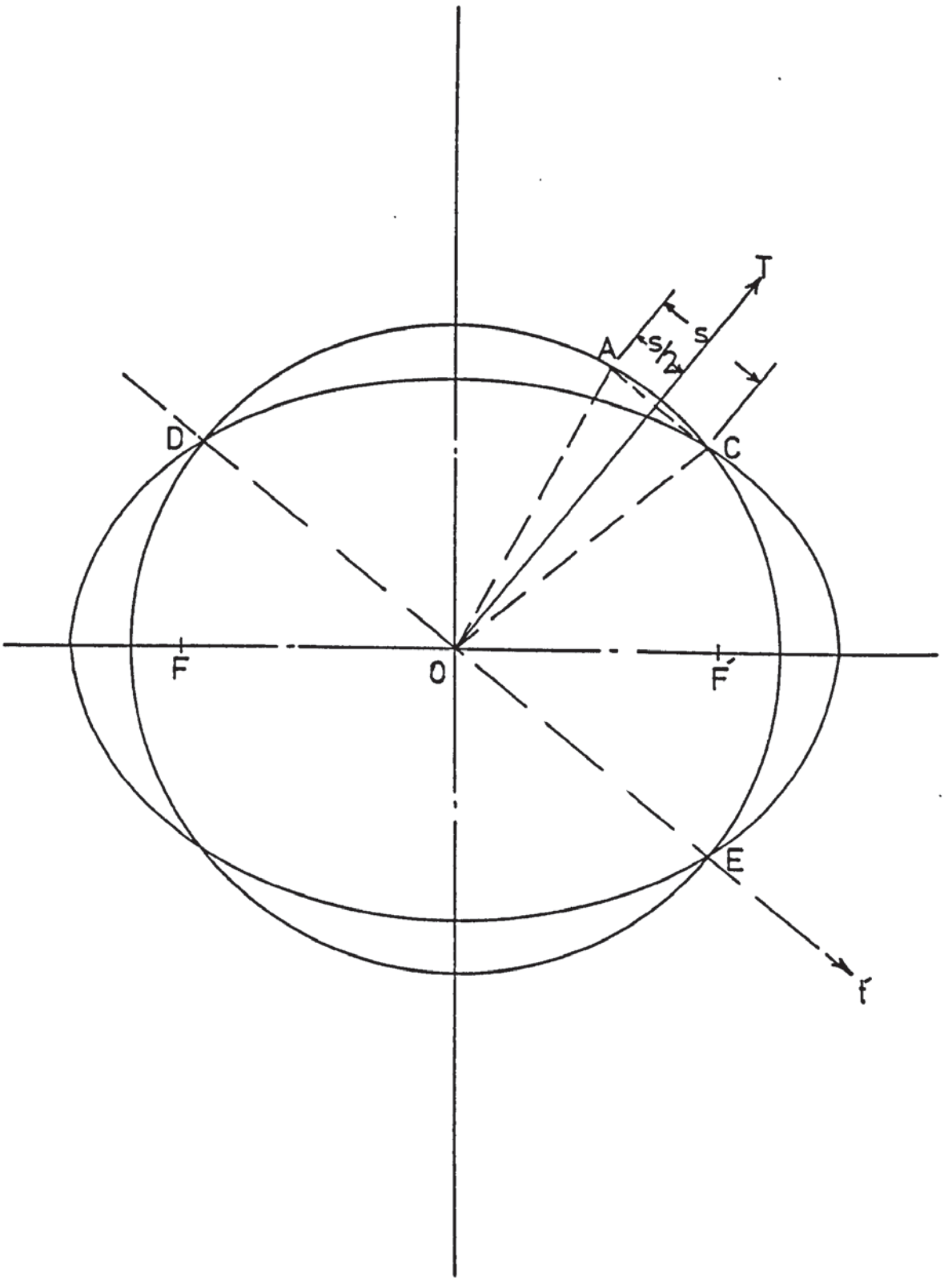

FIG. 98.

contains the twinning direction t. So, the displacement that is defined by the shear s occurs parallel to the twinning plane, leaving its position and shape undisturbed.

The deformation ellipse intersects the undeformed circle at the point C and this defines another undeformed plane whose trace is OC. Its initial position is OA. Therefore, during this twinning point A has actually moved to point C, a displacement (s) parallel to the twinning plane DOE.

(3) Uniform Deformation

Deformation by slipping is more common than by twinning. In slipping, the distortion is uniform, and this uniform deformation can be represented by a transformation from a circle to an ellipse similar to that of twinning as shown in Fig.(99). In this Figure, points A and G move to points B and H respectively during slipping.

(4) Construction of the Negative Pedals of Circles

For the purpose of representing the uniform deformation geometry in its exact dimensions, and to locate the exact displacements of points A and G to points B and H respectively, the following method of construction is used.

The uniform distortion of a spherical crystal gives an ellipsoid of the same volume. This is projected into two dimensions as a circle deformed uniformly to an ellipse of the same area. And the geometric representation of uniform deformation is drawn to the exact dimensions of circles and ellipses of equal areas but with different values of the eccentricity of the ellipses. This drawing is given in Fig. (100). In these figures, the perpendiculars to AB and GH

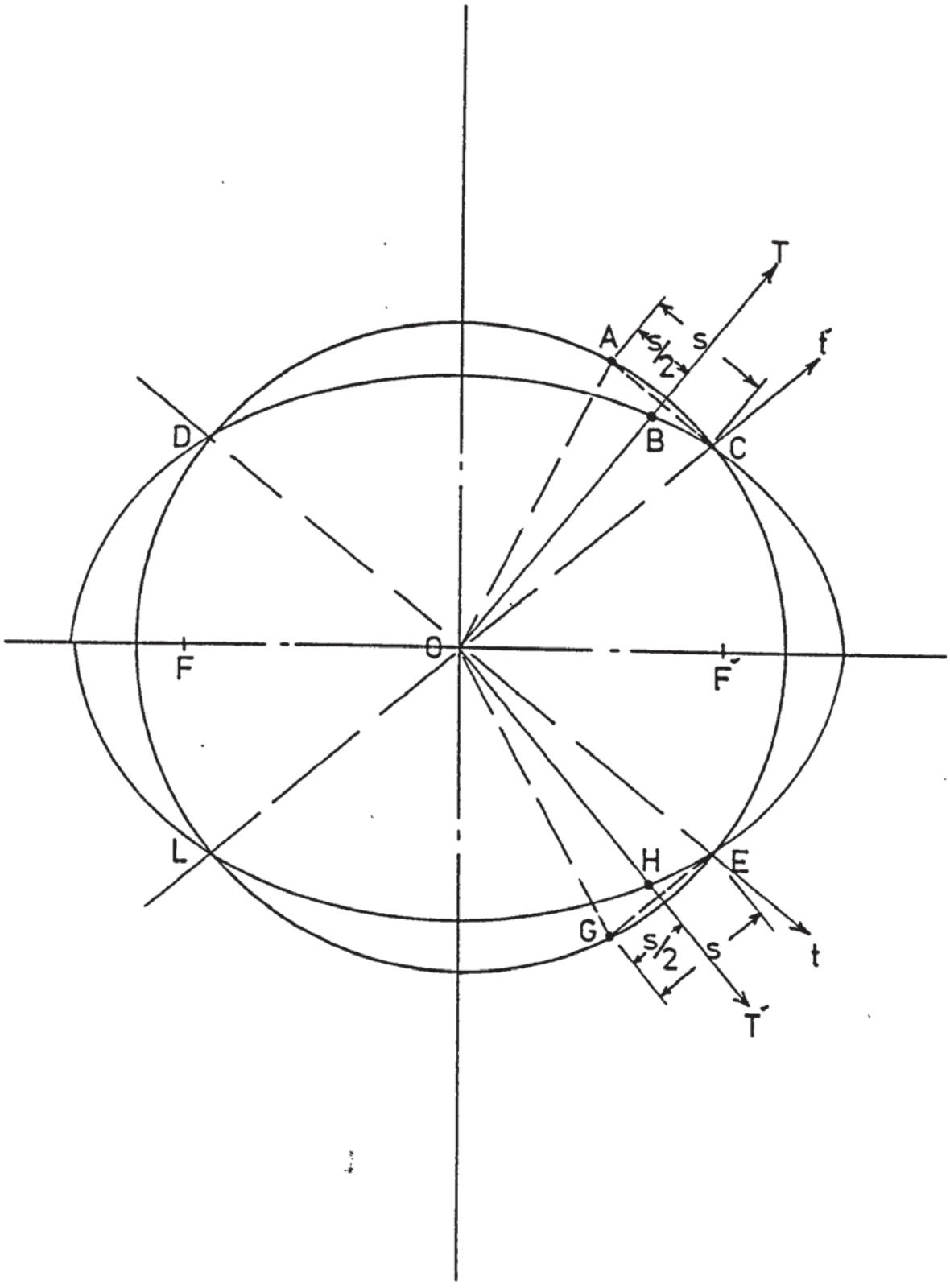

FIG. 99.

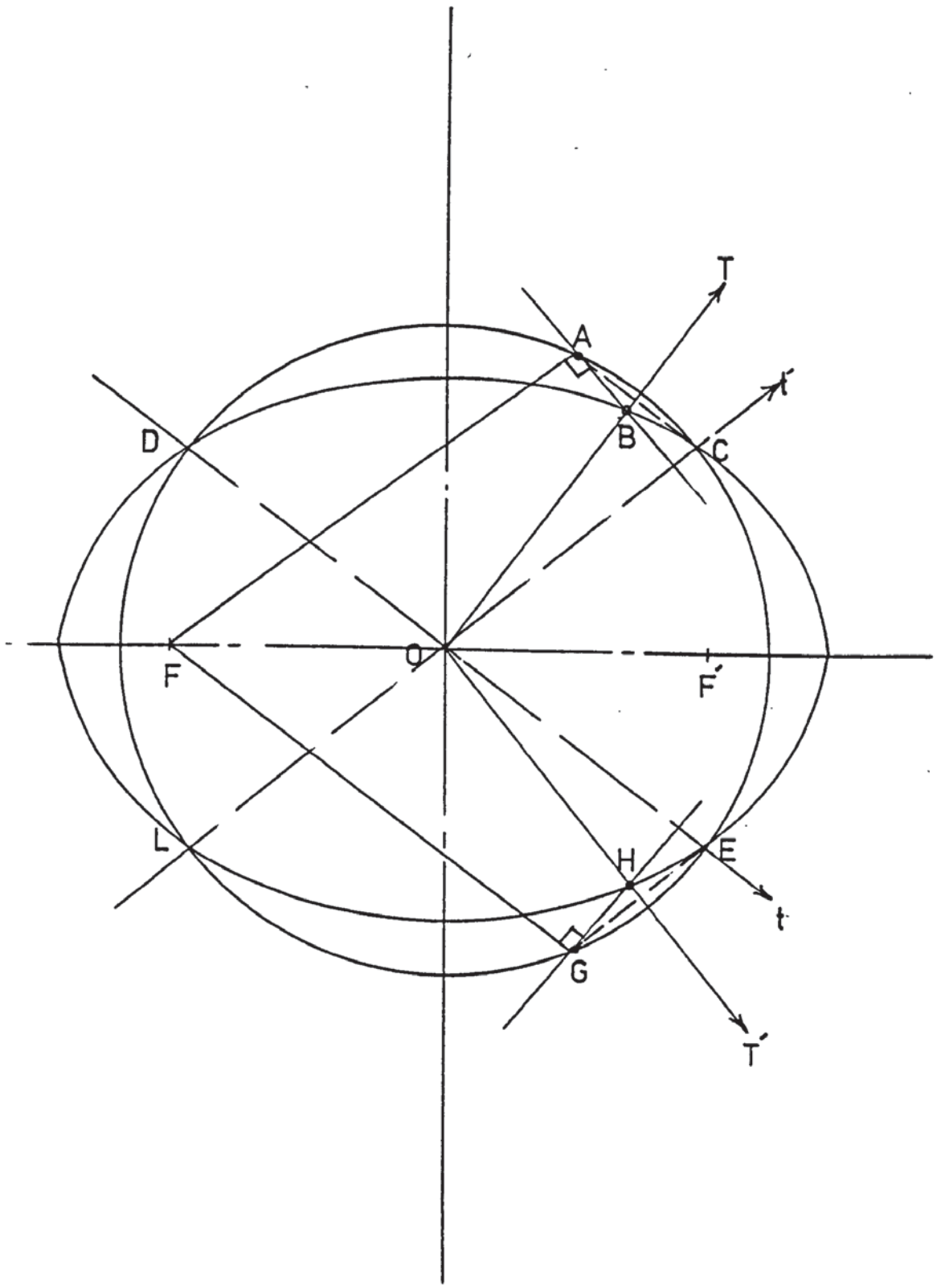

FIG·100·

at points A and G pass through F, the focus of the ellipse. This is the construction of the first negative pedal of the circle. Therefore, the actual uniform deformation and flow of points within the single crystal follows the construction of the first negative pedal of the circle.

APPENDIX IV

Calculations of Volume Fraction of Voids and Particles

The measurements from the photographs produced by (SEM) can be corrected for the statistical errors as follows:- (39,46)

(a) The area of an individual void or particle is

$a = (2\pi R^2)/3$ for uniform circular

$a = (\pi R_m^2)/3$ for non-uniform or irregular

From these, the mean area $\bar{a}$ of the individual void or particle the standard deviation and the variance (σ_a) are calculated.

(b) The areal fraction $A_f = (Ma \times \bar{a}) / A$ .....(1)

where A = the total area of the field (photograph)

(c) The voids or particles are assumed to occur as discrete and randomly distributed in three dimensions. Therefore, the variance in sampling the sub-area and accounting for the form of the structure is given by the equation : (46)

$$[\sigma_{A_f}/A_f]^2 = (1/M_a)[(\sigma_a/a)+1] \quad \text{.....(2)}$$

This equation gives the first statistical correction for the deviation of areal fraction from the true volume fraction.

(d) The fraction of points falling on the voids or particle

$N_f = N_p/N$

where N_p = number of points falling on voids or particles

N = Total number of points on the grid.

There is a possibility that no points on the grid fall on a sub-area of a void or a particle. Therefore, the total number of points falling, is a binomial distribution and the

variance is given by equation: (47)

$$[\sigma_{N_f}/N_f]^2 = (1/N_p)(1-A_f)+(\sigma_{A_f}/A_f)^2 \qquad \ldots\ldots\ldots$$

This equation gives the second statistical correction for the use of point count in place of a direct measurement.

The error in N_f is obtained as error = $(\sigma_{N_f}^{1/2})/M_a$

The volume fraction f_o = $\bar{N}_{f\ \text{expected}}$ where,

$\bar{N}_{f\ \text{expected}}$ = $N_{f\ \text{calculated}}$ $\pm$ error in N_f

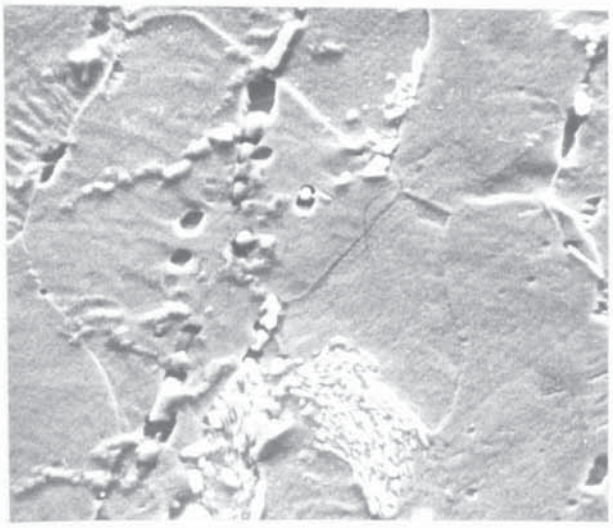

(a) Atypical micrograph on which voids and carbides were made, Magnification 2K,

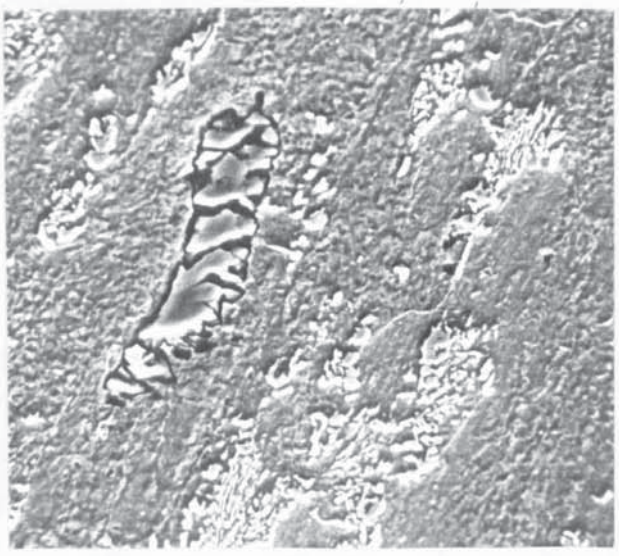

(b) Atypical micrograph on which voids and inclusions were made, Magnification 1.5K,

STEEL B

REFERENCES

1. Allen, P.N.
Fracture. "Conference on the atomic mechanisms of fracture" held in Swanpscott, Massachusetts, April 1959, p.123, 3d. Averback B.L. et al. John Wiley & Sons, Inc., New York. Chapman & Hall Ltd., London.

2. Allen, P.N., Rosenfield, R.
Dislocation Dynamics, May 1967, McGrawlHill.

3. Amit K. Ghosh. Met. Trans. 7A, 523, 1976.

4. Argon, A.S. JIM, & Needleman, A. Met Trans., 6A, 815, 1975.

5. Argon, A.S. & Safozlu, R. Met. Trans., 6A, 825 & 839, 1975.

6. Averbach, B.L., Felbeck, D.K., Hahn, G.T., Thomas D.A.
Fracture, Conference on the atomic mechanicms of fracture, held in Swanpscott, Massachusetts, April 1959. John Wiley & Sons.Inc., New York, Chapman & Hall Ltd., London.
(Low, J.R., p.68 and Stroh, A.N., p.117).

7. Barker, T.J. & Charles, J.A. JISI, 210, 680 & 702, 1972.

8. Barker, T.J. & Charles, J.A., JISI, 211, 197, 1973.

9. Barnby, J.T. Acta Met., 15, 903, 1967.
10. Barnby, J.T., Met.Soc.Jnl., 3, 155, 1969.

11. Barnell, D.M. & Tetelman, A.S., J.Mech.Phys.Solids, 14, 329, 1966.

12. Basset, A.B., Elementary Treatise on Cubic and Quartic Curves, Cambridge, 1901.

13. Bell, G.A. Aust. J.App.Sci., 9, 236, 1958.

14. Bestwick, R.D.W., GKN, unpublished.

15. Bilby, B.A., Bullough, R. & Smith, E., Proc.Roy.Soc., A.231, 253, 1955.

16. Bilby, B.A., Cotterall, A.H. & Swinden, R.H.
Proc.Roy.Soc., A.272, 304, 1973.

17. Bilby, B.A. & Eshelby, J.D., Fracture, edited by Liebowitz, H. 1968. Volume 1, Microscopic & Macroscopic Fundamentals. Sh.2, p.99. Academic Press, New York.

18. Bjorn-Invar Klevebring, Scand.J.Metallurgy, 5, 63, 1976.

19. Branson, J.R., Sheet Metal Industries. 49, 467, 1972.

20. Bridgman, P.W. "Large Plastic Flow and Fracture", McGraw Hill, New York, 1952.

21. Brown, L.M. & Embury, J.D., 1973, Microstructure & design of alloys. Institue of Metal., paper 33.

22. Brown, L.M. 1975, "The mechanics & physics of Fracture". Churchill College, Cambridge. Initiation and growth of voids by plastic flow near second-phase particles.

23. Chiangm C.H., J. Strain Analysis, 5, 110, 1970.

24. Chou, Y.T., Acta Metall. 13, 779, 1965.

25. Clupp, P.B., Sheet Metal Industries, 43, 6, 1966.

26. Cox, T.B., & Low, J.T. Met.Trans., 5, p.1947, 1974.

27. Dieter, G.E., Jr, Mechanical Metallurgy, 1961. McGraw-Hill, New York, Toronto, Lond

28. Dundurs, J & Mura, T., J.Mech.Solids, 12, 177, 1964.

29. Elam, C.F., Distortion of Metal Crystals, Oxford, 1935.

30. Erasmus, L.A., Metallurgia & Metal Forming, 47, 94, 1975.

31. Eshelby, J.D., Frank, F.C. & Nabarro, F.R.N., Phil.Mag, 42, 351, 1951.

32. Feldman, H.D., Dr.Ing. "Cold Forging of Steel", Hutchinson, Scientific & Technical, London, 1959.

33. Feldman, H.D., Sheet Metal Industries, 38, 8, 1961.

34. Forging Equipment, Material & Particles, Metal & Ceramics Information Centre, October 1973.

35. Fredriksson, H. & Hillert, M., JISI, 209, 109, 1971.

36. Fredricksson, H & Hillert, M. Scand.J. Metallurgy, 2, 125, 1973.

37. Friedel, J. "Dislocations", Pergamon Press, Oxford, 1964.

38. Fullmann, R.L., Trans. A.I.M.E., J.Meta., 197, 447, 1953.

39. Gladmann, T. & Woodhead, J.H. JISI, 194, 189, 1960.

40. Gladmann, T., Holmes B, & Ivor, I.D. "Effect of second-phase particles on the mechanical properties of steel", I.S.I., London, 1971.

41. Goodier, J.N., J.Appl.Mech., 22, 39, 1955.

42. Griffiths, F., Sheet Metal Industries, 38, 123, 1961.

43. Gurland, J. & Plateau, J. Trans. ASM 56, 442, 1963..

44. Hall, E.O., Twinning. Butterworth, London, 1954.

45. Hart, E.W., Acta Met., 15, 351, 1967.

46. Hilliard, J.E., & Cahn, J.W. Trans. AIME., 221, 344, 1961.

47. Hobdell, A.C., Metallurgia & Metal Forming, 36, 17, 1969.

48, Honeycombe, R.W.K., The Plastic Deformation of Metals. Edwards Arnold (Publishers) Ltd., 1968.

49. John J. Gilman. Micromechanics of Flow in Solids. McGraw Hill, 1969.

50. Jonas, J.J. and Bandelet, B. Acta Met., 25, 43, 1977.

51. Joubert, F.L. & Valentin, G.H. Eng. Fract. Mech., 8, 669, 1976.

52. Kare Hallen, Int.J.Mech.Sci., 17, 369, 1975.

53. Keeler, S.P. Sheet Metal Industries, 45, 633, 1986.

54. Kudo, H., & Aoi, J. Japan Soc. Technol. Plast. 8, 17, 1967.

55. Kuhn, H.A. & Lee P.W., Met.Trans., 2, 3197, 1971.

56. Lindly, T.G., Oates, G. & Richards G.E., Micro- and Macromechanical Models of Carbide Cracking in Ferrite/Carbide Steel. ISI publication, 1971, p.54.

57. Liu, C.T. & Gurland J. Trans. ASM, 61, 156, 1968.

58. Lockwood, E.H. The Mathematical Gazette, 41, 254, 1957.

59. Lockwood, E.H. A Book of Curves. Cambridge, 1963.

60. Lubahn, J.D. & Schnectady, N.Y. Trans. ASME, 1, 111, 1957.

61. "Manganese Sulphide Inclusions in Steel". Proceedings on an International Symposium 7 - 8 Nov. 1974. Port Chester, New York. American Society for Metals. Edited by John I. de Barbadillo and Edwin Snape. "No.6 in the Materials Metalworking Technology Series".

62. Martinet, C. Metallurgia & Metal Forming, 39, 21, 1972.

63. McDermott, R.P. & Bramley, A.N. Metallurgia & Metal Forming, 41, 127, 1974.

64. McClintock, F.A., J.App Mech., 35, 363, 1968.

65. Mechanisms and Control of Crack Growth, B.C.C., First Report. 1st July - Dec. 31st, 1974.

66. Michihiko Nagumo et al. Steel for Cold Forging, Nipton Steel. Technical Report Overseas, No.3., June 1973.

67. Motor Business, 2nd Quarter, 1974.

68. Muskhelishivili, N.I. "Some Basic Problems of the Mathematical Theory of Elasticity". 3rd Edition, Translated by Radok, J.R., Groningen, Holland, 1953.

69. Nadai, A., J.App.Phys., 8, 205, 1937.

70. Nadai, A. "Theory of Flow and Fracture of Solids". Vol.III, 1963. McGraw-Hill, New York, Toronto, London.

71. Neuber, H. "Theory of Notch Stresses, principles for exact calculation of strength, with reference to structural form and material". Translated from a publication of Springer-Verlag. Berlin, Gottinger, Heidelberg, 1958.

72. Nichols, J. Sheet Metal Industries, 45, 306, 1968.

73. Nilsson, S. Langebor , R. & Sandstromm R. Metal Science, 9, 223 & 226, 1975.

74. Nilsson, S., Sandstrom, R. & Langeborg, R. Scand. J. Metallurgy, 4, 89, 1975.

75. Orowan, E. Proc. Phys. Sco., 52, 8, 1940.

76. Pedoe, D. "Circles", Pergamon, London, New York, Paris. 1957.

77. Percival, Barker, K. Metallurgia & Metal Forming, 40. 273, 350, 1973.

78. Peterson, R.E., "Stress Concentration Design Factors", John Wiley & Sons Inc., New York, 1953.

79. Rice, J.E. & Tracey, D.M. J.Mech.Phys.Solids, 17, 201, 1969.

80. Pearce, R. & Drinkwater, I.C. Sheet Metal Industries, 45, 751, 1968.

81. Sachs, H. & Lubahn, J.D. Trans. ASM, 41, 125, 1943.

82. Sachs, G., Lubahn, J.D., & Ebert L.J. Trans. ASM, 33, 340, 1944.

83. Sachs, G., Lubahn, J.D. & Ebert L.J. Trans. ASM., 34, 517, 1945.

84. Schmid & Boas, "Plasticity of Crystals", Hughes F.A. & Co. Ltd., London, 1950.

85. Segal & Charles, Metals Technology, 4, 177, 1977.

86. Sen, S.K., Metallurgia & Metal Forming, 40 154. 1973.

87. Smith, E. & Barnby, J.T. Metal Science, J., 1, & 56, 1967.

88. Smith, E. Acta Metall., 14, (p.556, p.985, 0.991), 1966

89. Smith, E. J.Mech.Phys.Solids, 16, 163, 1968.

90. Spikes, R.H. Sheet Metal Industries, 40, 581, 1963.

91. Sten Bergh, Jernkontorets Annaler, 146, 914, 1962.

92. "Strength & Ductility of Metals at Elevated Temperatures and Metallurgical Changes". Symposium held in New York, N.Y., June 1952, Special Technical Publication No.128, ASTM Philadelphia, Pa. 1953.

93. Stroh, A.N. Proc. Roy.Soc., A. 223, 404, 1954.

94. Stroh, A.N. Proc. Roy. Soc,, A, 232, 548, 1955.

95. Stroh, A.N., Advances in Physics, 6, 418, 1957.

96. Tetelman, A.S. & McEvily, A.J. "Fracture of Structural Materials". John Wiley & Sons Inc., New York, London, Sydney. p.38, 1967.

97. Thomason, P.F., Int.J.Mech.Sci., 10, 501, 1968.

98. Thomason, P.F., J.Inst.Met., 96, 360, 1968.

99. Thomason, P.F., Int. J.Mech.Sci.,11, 187, 1969.

100. Thomason, P.F., Int.J.Frac.Mech., 7, 409, 1971.

101. Tipnis, V.A. & Cook, N.H., Trans.ASME, J.Basic Eng., 89, 538, 1967.

103. "Towards Improvement in Ductility", Koyto International Conference. 25 Oct. 1971.

103 Toya, M. J.Mech.Phys. Solids. 24, 1, 1976.

104. Tsuyoshi Inoue & Shushi Kinoshita. "Microstructure & Design of Alloys". Paper 32, Institute of Metals, 1973.

105. Volker Weis. Fracture. Edited by Liebowitz, H., Volume III, "Notch Analysis of Fracture", Ch.3, p.227. Academic Press, New York, 1968.

106. Vygodsky M. "Mathematical Handbook". Mir Publishers, Moscow, 1971.